A Study on Gain Enhancement of Leaf-Shaped Bowtie Slot Antennas Array for Use in Quasi-Millimeter Wave Frequency Band

By

Hor Mangseang

A dissertation submitted in partial fulfillment of the requirement for the degree of

Doctor of Information Science and Technology

Wireless Technology and EMC Research Laboratory

Graduate School of Information Science and Technology

Hokkaido University

January 27th, 2022

Doctoral Committee: _____

Acknowledgement

This research was carried out in Wireless Technology and EMC Research Laboratory, Graduate School of Information Science and Technology, Hokkaido University.

I would like to express my deep and sincere gratitude to my esteem research supervisors, Associate Professor Manabu Yamamoto, and Assistant Professor Takashi Hikage for his invaluable guidance throughout this research. His dynamism, vision, sincerity, and motivation have deeply inspired me. Both professors have taught me the methodology to carry out the research and to present the research works as clearly as possible. It was a great privilege and honor to work and study under his guidance. I am extremely grateful for what both professors have offered me. I would like to thank both professor for his friendship, empathy, and great sense of humor. I would like to extend my thanks to emeritus professor Toshio Nojima for his warmly welcome and giving me invaluable advice.

I am extremely grateful to my parents for their love, caring and sacrifices for educating and preparing me for my future. Also, I express my thanks to my older sisters for their support and encouragement.

I would like to thank to my friends and research colleagues, Tetsuya Sekiguchi, Takuma Makanae, Tatsuro Shigihara, Jintao Sun, Naoya Yamamoto, and other students in the Laboratory for their constant encouragement and humor. I would like to thank Tetsuya Sekiguchi for his supports during the first week when I arrived Sapporo. I would like to express my special thanks to Tatsuro Shigihara and Naoya Yamamoto for helping me when I have problems with official documents during my stay in Sapporo, explaining me antenna fabrication process and teaching me Japanese language.

I would like to send my deep gratitude to JICA (Japan International Cooperation Agency) for giving me this precious opportunity to continue my PhD in Hokkaido University, Japan. I would like to thank all JICA officers in Sapporo Head Quarter for their supports. I would like to thank to staff in Graduate School of Information Science and Technology for their supports.

Finally, I would like to thank to all the people who have supported me to complete the research work directly or indirectly.

Abstract

This thesis dissertation proposes to design a high gain antenna structure with a wide bandwidth. The antenna structure is designed to operate within quasi-millimeter wave frequency band.

The demand of high data rate transfer through wireless communication medium has been surging. Mobile users need a high-speed data transfer for daily usage such as high-resolution video stream and gaming. Due to the scarcity of spectrum within microwave frequency band, millimeter wave frequency band has been proposed and explored for potential application. 28GHz frequency band is more favorable and expected to significantly use in future 5G communication. High-gain antenna is required to compensate large propagation attenuation of millimeter wave frequency band. To increase coverage area and capacity of the overhanging station, large number of antennas are required to install. To efficiently use the overhanging with such a distributed antenna system, the antenna frequency must be shared regardless of frequency band. Therefore, wideband antenna is required to use in such a distributed antenna system.

To have a high gain antenna structure, array configuration is promising technique. In this research, leaf-shaped bowtie slot antenna, which contains a wide impedance bandwidth characteristic of self-complementary antenna, has been adopted as radiating element of linear array configuration. In addition, leaf-shaped bowtie slot antenna has high gain and wide gain bandwidth characteristics. Moreover, leaf-shaped bowtie slot antenna and its feeding circuit have low profile which is suitable for large scale array structure. In this research, a linear array of 4 leaf-shaped bowtie slot antenna has been proposed for use within quasi-millimeter wave frequency band. In addition, two structures of feeding circuit have been used with the slot antennas array configuration. First structure is feeding circuit with microstrip line and conductor probe, which is used as connection between microstrip line and ground plane vicinity of radiating slot element. Second structure is the feeding circuit with quarter wavelength matching circuit.

Partially Reflecting Surface (PRS) has been used as gain enhancement technique, which is based on multiple reflecting, to increase gain of planar and aperture slot antenna. Based on PRS concept, dielectric superstrate with high relative permittivity has been applied as gain enhancement technique of aperture slot antenna. Therefore, in this research, gain enhancement technique based on dielectric superstate reflector has been applied to further increase gain in addition to array configuration technique. In this research, two layers of dielectric superstrate have been proposed to use as gain enhancement technique. This technique is considered as low cost, effective and efficient technique.

The results and discussions which is obtained from this research are summarized as following, and the significance of this research is clarified.

Chapter 1 describes the background and outline of this research.

Chapter 2 Computational electromagnetic is briefly discussed. In addition, the Finite Difference Time Domain method is the main topic for discussion. However, only a small part of Finite Difference Time Domain is discussed. This review is helping to comprehensively use the commercial simulation (software) Sim4Life in an effective and efficient way.

Chapter 3 describes the background of leaf-shaped bowtie slot antenna for use in ultra-wideband communication systems (UWB). In this research, instead of microstrip tapered line matching circuit, quarter-wavelength matching circuit has been proposed and designed as feeding circuit of leaf-shaped bowtie slot antenna for use in UWB systems. As the results, impedance bandwidth of the antenna structure has been increased by around 9% in terms of fractional bandwidth, which is wider than the impedance bandwidth of antenna structure fed by microstrip tapered line.

Chapter 4 describes the background of leaf-shaped bowtie antenna for use in millimeter wave frequency band. Since feeding circuit of leaf-shaped bowtie antenna is unsuitable for large scale array, an array of 4 leaf-shaped bowtie slot antennas has been proposed for use in millimeter wave frequency band, in this research. Since leaf-shaped bowtie slot antenna has bi-directional radiation pattern, a flat reflector has been placed under dielectric substrate to make radiation pattern unidirectional. Two structures of feeding circuit have been used with linear array of 4 leaf-shaped bowtie slot antennas. First feeding circuit structure consists of microstrip line, conductor probe and microstrip tapered line. Conductor probe is used as connection between microstrip line and ground plane vicinity of radiating slot. Tapered line is used as impedance matching at input port. The leaf-shaped bowtie slot antennas array, which is fed by first feeding circuit structure, offers 490MHz of impedance bandwidth and 13.17dBi of maximum actual gain. Second feeding circuit structure consists of quarter wavelength matching circuit which is used as impedance matching. The leaf-shaped bowtie slot antennas array, which is electromagnetically fed by the second feeding circuit structure, offers 1.68GHz of impedance bandwidth and 13.7dBi of maximum actual gain. Therefore, the second feeding circuit structure consisting of quarter wavelength matching circuit offers a wider impedance bandwidth. To improve the performance of leaf-shaped bowtie slot antenna array, another feeding circuit structure is designed. The third feeding circuit structure consists of quarter wavelength matching circuit and microstrip taper line. The impedance bandwidth occupies frequency range of 26GHz to 28.21GHz with maximum actual gain of around 15.8dBi. The antenna structure offers wider impedance bandwidth and higher actual, although the impedance bandwidth doesn’t satisfy the target frequency band of 27GHz to 29GHz.

Chapter 5 describes the background of gain enhancement technique. In addition, this research proposes to use two layers of dielectric superstrate as gain enhancement technique for leaf-shaped bowtie slot antennas array structures which are designed in Chapter 4. After two superstrate layers have been arranged on top of slot antennas array, which is fed by the first feeding circuit structure, impedance bandwidth has been widened and actual gain has been increasing. The obtained impedance bandwidth is about 1.22GHz, and maximum actual

gain is about 20.5dBi. However, after two superstrate layers have been arranged on top of the second antenna structure, impedance bandwidth has been narrowed and actual has been increased. The obtained impedance bandwidth is about 1.45GHz and maximum actual gain is about 19dBi. The impedance bandwidth of the second antenna structure is wider than that of the first antenna structure although there is destructive effect from two superstrate layers. However, the maximum actual gain of the second antenna structure is about 1.5dB smaller than that of the first structure. To further investigate the gain enhancement of leaf-shaped bowtie slot antenna for use in millimeter wave frequency band, antenna structure, whose feeding circuit consists of quarter wavelength matching circuit and microstrip tapered line, is used as primary radiator. With one superstrate layer, the antenna structure offers higher actual gain around 18.5dBi, and wider impedance bandwidth which occupies frequency range of 27GHz to 29.15GHz. With two superstrate layers, the antenna structure offers higher actual gain around 20dBi, and wider impedance bandwidth which occupies frequency range of 27GHz to 29GHz. Therefore, the antenna structures satisfy the targeted frequency band 27GHz to 29GHz.

Chapter 6 describes the validation of proposed antenna structures which have been designed in Chapter 3 and Chapter 5. The protype of single slot antenna electromagnetically fed by quarter wavelength matching circuit has been fabricated. The antenna characteristics have been measured and compared with simulated results. The prototype of slot antennas array structure, whose feeding circuit is conductor probe and microstrip line, with two superstrate layers has been fabricated and antenna characteristics have been measured and compared with simulated results. The simulated and measured results are in a good agreement although there is small discrepancy.

Chapter 7 is a conclusion and summarizes of the results of the entire thesis dissertation. The quarter wavelength matching circuit does improve the impedance bandwidth of leaf-shaped bowtie slot antenna. Two layers of superstrate is considered as an effective and efficient technique to design high gain and wide bandwidth antenna structure. In addition, the superstrate layers can be used as cover of the antenna structure. The proposed antenna structure in this research offers wide impedance bandwidth and higher actual gain with wide −3dB gain bandwidth. Therefore, the proposed antenna structure in this research is applicable for 28GHz band (27GHz to 29GHz) and contribute to future 5G communication.

List of Figures

List of Tables

Table of Contents

CHAPTER 1
Introduction

1.1 Research Background

The use of mobile data for smartphone application and mobile pocket Wi-Fi has rapidly increased during last decade. User has demanded more high-speed data rate for daily life usage such as high-quality video streaming, gaming, and video conferencing [1]. The use of mobile data is projected to significantly grow by 2030 [2][3]. To comply with this unprecedented growth, millimeter wave frequency spectrum has been proposed and explored for potential application in future 5th generation communication (5G). To increase capacity and coverage area, many antennas are installed and distributed in the base station. To use efficiently and effectively the hanging over at base station, the antenna at base station must be shared regardless of frequency band. Therefore, wide band antenna is required for this application. Although millimeter wave frequency spectrum can solve the data rate requirement from mobile users, millimeter frequency suffer a high attenuation in atmosphere [3]. Table1. 1 shows major results in 5G radio technology trials (press releases) [4].

Table1. 1 List of 5G Radio Technology Test Trials

Press release date (year/month/day)	Test results	Trial Partner
2015/03/03	Successful reception of data at over 4.5 Gbit/s using the 15 GHz band	Ericsson
2015/03/03	Successful reception of data at over 2 Gbit/s using the 70 GHz band	Nokia
2015/11/26	Successful communication tests at over 2 Gbit/s in real environments with commercial equipment using the 70 GHz band	Nokia
2015/11/26	Successful data communication receiving over 2.5 Gbit/s in a high-speed mobile environment traveling at approximately 60 km/h using the 28 GHz band	Samsung
2016/2/22	Successful multi-user 5G communication trial achieving capacity over 20 Gbit/s in an outdoor environment using the 15 GHz band	Ericsson
2016/5/24	Successful real-time 5G transmission of 8K video using the 70 GHz band	Nokia
2016/11/16	High-speed, high-capacity communication achieved between 23 terminals distributed in an outdoor environment, totaling 11.29 Gbit/s, using the 4.5 GHz band	Samsung
2016/11/16	High-speed, high-capacity communication achieved between 23 terminals distributed in an outdoor environment, totaling 11.29 Gbit/s, using the 4.5 GHz band	Huawei
2017/11/2	Successful field trial of 5G ultra-reliable, low-latency communication (URLLC) using the 4.5 GHz band	Huawei
2017/11/2	Successful trial increasing spectral efficiency using the world's first smartphone-sized NOMA chip set	MediaTek
2017/11/6	Successful 5G trials for implementing connected cars in the Odaiba area using the 28 GHz band	Toyota, Ericsson, Intel
2018/4/23	Successful 5G wireless communication trials in an ultra-high-speed environment of 300 km/h using the 28 GHz band	NEC
2018/5/23	Successful 5G wireless communication with multiple mobile terminals, reducing interference using cooperative beamforming among 4.5 GHz base stations	NEC
2018/7/25	Successful 5G communication for connected cars using "vehicle glass mounted antenna" and using the 28 GHz band	AGC, Ericsson
2018/11/22	Successful field trial of 27 Gbit/s communication using the 28 GHz band	Mitsubishi Electric
2019/5/29	Successful communication using a glass antenna for 5G terminals using the 28 GHz band	AGC, Ericsson

1.1.1 Millimeter Waver Frequency Band and Frequency Allocation

Considering the global development, 3GPP started to define 5G operating bands aiming to provide the first set of specifications. New frequency bands, 3.3-4.2GHz, 4.4-5GHz, 24.25-29.5GHz, and 37-40GHz, are considered for 5G [5]. Some of existing LTE bands around 1.7GHz, 2GHz and 2.5GHz and several bands below 1GHz. Three frequency bands have been allocated in Japan for 5G: the 3.7GHz band (3.6-4.1GHz), 4.5GHz band (4.5-4.6GHz), and the 28GHz band (27.0-29.5GHz) [6]. The 3.7GHz band and 4.5 GHz band are called sub-6 bands and the 28GHz band is called millimeter wave (mm-Wave) band. The sub-6 bands each feature a 100MHz bandwidth per operator within Japan's 5G frequencies. Compared with Long Term Evolution (LTE), they enable wideband usage and can achieve the same coverage as the LTE 3.5GHz band [6].

On the other hand, the millimeter wave band has been allocated 400MHz for each operator in Japan [6]. The mm-Wave band is significantly different from the frequencies which are used by LTE. The expectations of mm-Wave are so high for the spot-like rollout of services based on transmission speeds of several Gbit/s through the ultra-wideband allocation. In general, the higher is the frequency the more difficult is wave propagation. The use of the 3.7GHz band and 28GHz band has already begun in various countries, and from the perspective of the future terminal support, roaming support, etc., these bands should be effectively in rolling out high-speed and large capacity services reflecting the unique features of 5G. The plan is to execute a commercial rollout that will make maximum use of the strengths of each of these frequency bands based on the features of those frequencies, coexistence with existing operators, and global trends.

Table1. 2 Frequency allocation of sub-6G and 28GHz band

	3.7GHz band	4.5GHz band	28GHz band
Allocated frequencies	3.6-4.1GHz (500 MHz bandwidth)	4.5-4.6 GHz (100 MHz bandwidth)	27.0-28.2 GHz 29.1-29.5 GHz (1.6 GHz bandwidth)
Allocated Bandwidth	100 MHz bandwidth/operator	100 MHz bandwidth/operator	400 MHz bandwidth/operator
Use of Massive MIMO	Used in MIMO multiplexing		Coverage extension by beamforming
Use with other systems	Satellite systems	Airplane radar altimeter	Satellite systems
Overseas trends	China, Korea, Europe, United State	Planned for future use by China	United States, Korea

1.1.2 Antenna for Millimeter Wave Frequency Band

Historically, wireless standards typically evolve in a decade, the same trend may or may not continue in the future. In the migration from 2G to 3G and from 3G to 4G, there is not much modification in hardware, especially in antenna part. The frequencies band of 2G, 3G and 4G are not much difference. The critical parts which were changed are software and

network architecture. However, in the case of migration from 4G to 5G, both manufacture and service provider must redesign both the hardware and software and network architecture.

So far, the antenna specific to base stations are not commonly reported. Coplanar Strip line CPS fed antennas are introduced in [7]. The radiation patterns are stable across wide band. However, gain of the proposed antenna structure in [7] is within 8-10dB at the frequency range of 22-28GHz, which is not high enough. At 28GHz band, attenuation of the radiation in free space is up to 7dB/km. Therefore, a higher gain antenna is required. From Figure1. 1, the feed of the antenna should be re-designed to match the standard microstrip feed, so that the antenna structure in [7] is difficult to use in real practice.

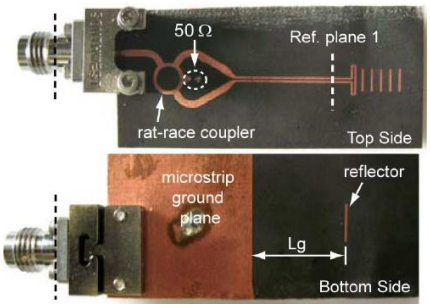

Figure1. 1 Coplanar Strip-line CPS fed antennas [7]

Log-periodic dipole antenna design has been introduced in [8]. Gain of the proposed antenna is from 6dBi to around 13.5dBi at frequency range of 20GHz to 40GHz. However, within 27GHz to 29GHz, gain of antenna is not high enough. A tilted parasitic is proposed in [9] for gain enhancement; however, gain of the antenna is from 6.8dB to 7.4dB at frequency of 27GHz to 29GHz, which is not high enough. In addition, the transition for waveguide to microstrip line make the antenna structure difficult to integrate with other devices.

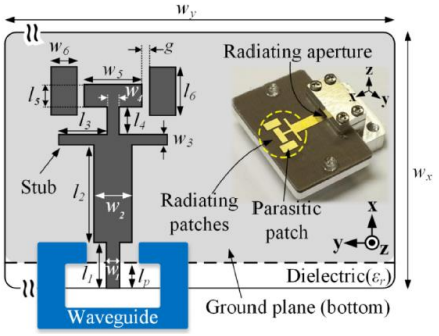

Figure1. 2 Tilted combine beam antenna [9]

Various research articles on dense dielectric patch arrays have been proposed in [10][11]. The antenna array reported in [10] incorporates a multi-layered dielectric substrate which is designed to feed high dielectric constant (ε_r=82) resonator antenna. Another superstrate is

also integrated to primary radiator to enhance gain in the broadside. Since the aperture coupling was standard dielectric superstrate, EBG unit cells were integrated periodically to suppress the surface wave modes, thus increasing radiation efficiency. The structure of antenna in [10] is more complex because many techniques are added up to enhance gain over wide frequency band. However, the gain of antenna is from 12-17dBi over frequency range of 26GHz to 30GHz.

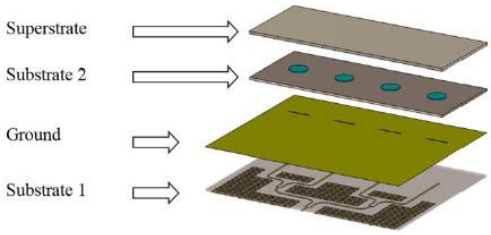

Figure1. 3 Dense dielectric patch array with improve radiation pattern characteristics [10]

Leaky wave antennas have been demonstrated in [12], where the beam tilted is observed for shift in the frequency of operation, which might be unsuitable for commercial deployment. Also, leaky wave antennas suffer from scanning loss when the beam is scanning away from the broadside. Sidelobe suppression technique have been proposed in [13][14][15] by parasitic patch and designing the aperture for phase-error correction when the beam is tilted away from the broadside. Circular polarized designs are proposed in [16][17][18][19]. However, gain of antennas in [16][17] is from 4.5-7dBi and −3dB gain bandwidth is narrow. Gain of antennas in [18][19] are from 13dBi-16dBi. Antennas in [18][19] incorporate multi-layer dielectric substrate. In addition, the waveguide-to-SIW transition make antenna structure more complicated.

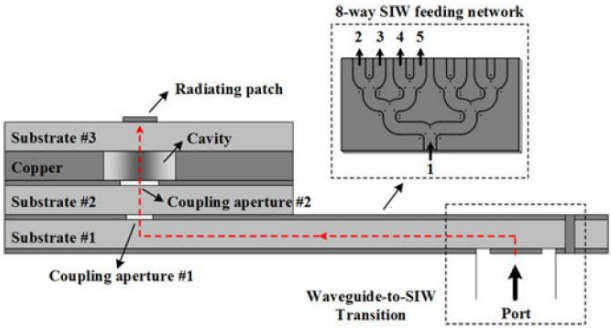

Figure1. 4 Substrate integrated waveguide antenna array for millimeter wave application

A printed ridge gap waveguide feeding method is proposed in [20][21]. The surface waves are minimal in this architecture because of a lack of dielectric between the top metal plane and the ground plane, which function as an electromagnetic bandgap structure. However, the antenna structure which is introduced in [20] is composed of multi-layer substrate which is difficult to fabricate and integrate with other devices.

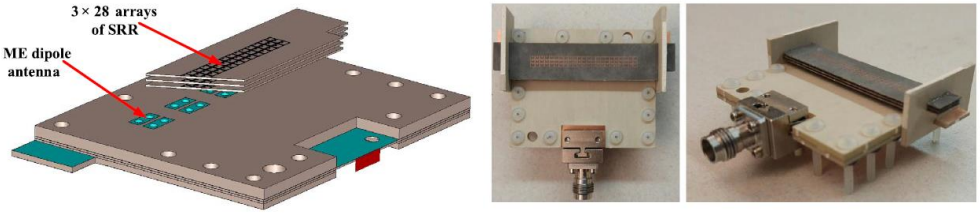

Figure1. 5 Schematic of configuration of 1×4 ME dipole antenna with array of SRR unit-cells

A series-fed array with low sidelobe level is proposed in [22][23]. Even though, the radiation patterns and broadside are stable in the frequency band of 24.5-30GHz, the waveguide to microstrip transition increase the complexity of the design. All metallic tapered slot antenna with an impedance bandwidth of 22.5-32 GHz is proposed in [24]. The insertion loss is minimal because of the absence of lossy dielectrics. The end-fire gain of the compact 1×4 array is 12-15dBi. The transition from the end launch connector to the all-metallic structure would be challenging to design. Variants of tapered slot antennas are proposed in [25][26][27].

1.2 Objective of Thesis

Among proposed frequency bands for 5G, 28GHz band is expected to be used dramatically. The mm-Wave band can offer high data transfer rate; however, the mm-Wave band suffer a great loss in the atmosphere. Therefore, antenna with high gain characteristics must be used in mm-Wave band. In addition, impedance bandwidth of the antenna must be wide enough to be useful in 5G application. From the previous section 1.1.2, the proposed antenna for mm-Wave band has some draw backs which must be improved. Some antennas have high gain, but they suffer narrow bandwidth. Some antennas have wide band and gain is stable over a wide frequency; however, their gain is still not high. Some antennas have high gain and wide band, but they have a complicated structure. Therefore, this research would like to propose antenna structure which has high gain, wide band, and simple structure. The model of proposed antenna is analyzed by numerical analysis in commercial simulation software and the prototype of proposed antenna structures are fabricated to validate the analysis results. Through out of this thesis, discussion problems are listed as below:

- Finite Difference Time Domain Analysis (FDTD)
- Quarter wavelength matching circuit used as feeding circuit of reflector backed leaf-shaped bowtie slot antenna
- Leaf-shaped bowtie slot antenna for use in millimeter wave frequency band
- Linear array of leaf-shaped bowtie slot antenna for use in millimeter wave frequency band

- Gain enhancement of leaf-shaped bowtie antenna slot antenna array for use in millimeter wave frequency band

1.3 Content and Structure of Thesis

In this thesis, contents are organized as following. In Chapter 1, research background and purpose of the thesis are discussed. Chapter 2 discusses about numerical method for electromagnetic. Finite Different Time Domain (FDTD) will be mainly discussed. Some basic equations and parameters of FDTD are shown. In addition, the use of FDTD method to analyze antenna characteristics over wide frequency band is discussed. In Chapter 3, leaf-shaped bowtie, and leaf-shaped bowtie slot antenna for use in ultra-wideband communication systems. Quarter wavelength matching circuit is proposed to use as feeding circuit of leaf-shaped bowtie slot antenna instead of microstrip tapered line. Chapter 4 discusses about leaf-shaped bowtie slot antenna for millimeter wave band. In this Chapter, characteristics of both single slot element and slot antennas array are discussed. In Chapter 5, gain enhancement of leaf-shaped bowtie slot antenna is discussed. Chapter 5 discusses mainly about the use of dielectric superstrate to enhance gain of the slot antennas array. In Chapter 6, Measured results of proposed antennas prototype are shown and comparison between simulated and measured results are discussed. In Chapter 7, the conclusion of this thesis is drawn.

CHAPTER 2
Wideband Antenna Analysis Using FDTD

2.1 Abstract

In Chapter 2, Computational electromagnetic is briefly discussed. In addition, the Finite Different Time Domain method is the main topic for discussion. However, only a small part of Finite Different Time Domain is discussed. Therefore, only methods that are used to calculate characteristics of antenna is briefly reviewed. The structural of Chapter 2 are arranged as following. Firstly, the fundamental of FDTD equations are presented. From the fundamental FDTD, the updating equations for 3 dimensional problems are discussed. Then, the basic parameters in FDTD are shown. In addition, the absorbing boundary condition that is used in FDTD method is shortly presented. Finally, type of voltage source, S-parameter, and near-to-far field conversion are briefly discussed. The contents throughout Chapter 2 are based on reference [28]. The purpose of reviewing FDTD in this chapter is to show the background of numerical analysis in this research. However, the Finite Different Time Domain method in commercial simulation software (sim4Life) is used [29]. By understanding the theoretical concept of FDTD, it helps to comprehend the operation in the commercial simulation software. In addition, it helps to utilize the commercial software effectively and efficiently.

2.2 Overview of Computational Electromagnetic Methods

Computational electromagnetic (CEM) has evolved rapidly during the past decade. The commonly used CEM methods today can be classified into two main categories. The first category is based on differential equation methods (DE), and the second category is based on integral equation methods (IE). Both methods are solutions of Maxwell's equations and the boundary conditions in accordance with the problems to be solved. The DE method provides approximation solution for differential equation as finite differences. The IE method provides solution for integral equation in terms of finite sums.

Most numerical electromagnetic analysis has taken place in the frequency domain. However, time harmonic behavior is assumed from the frequency domain response. Frequency domain solution was more popular than time domain because a frequency domain approach is more suitable for obtaining analytical solutions for canonical problems, which are used to verify the numerical method for generating data for real-world applications. Furthermore, the experimental hardware available for making measurements in past years was largely confined to the frequency domain approach.

The development of faster and more powerful computational resources allowed for more advanced time-domain CEM models. Differential equation methods in time domain

approaches are focused more than integral equation. Finite Difference Time Domain (FDTD) method is time domain approaches for CEM application. FDTD is easier to formulate and to adapt in computer simulation model without complex mathematics. They also provide more physical insight to the characteristics of the problems.

2.2.1 Overview of FDTD Method

The FDTD method has been more popular as a tool for solving Maxwell's equations. FDTD is based on simple formulations that do not require complex asymptotic or Green's functions. Although FDTD solves problems in time domain, it can provide frequency domain response over wideband using Fourier transform. FDTD can handle composite geometries consisting of different type of materials including dielectric, magnetic, frequency-dependent, non-linear, and anisotropic materials. The FDTD technique is easy to implement using parallel computation algorithms. These features of the FDTD method have made it most attractive technique of CEM for many microwave devices and antenna applications. FDTD has been used to solve numerous types of problems arising as in the following:

- Scattering, radar cross-section
- Microwave circuits, waveguides, fiber optics
- Antenna (radiation, impedance)
- Propagation
- Medical application and so on

2.2.2 Formulation of FDTD Method

FDTD algorithm is constructed from Maxwell's time-domain equations. The differential time-domain Maxwell's equations needed to specify the field behavior over time are:

$$\nabla \times \vec{H} = \frac{\partial \vec{D}}{\partial t} + \vec{J} \quad \text{(a)} \quad \text{Equation2. 1}$$

$$\nabla \times \vec{E} = -\frac{\partial \vec{B}}{\partial t} - \vec{M} \quad \text{(b)}$$

$$\nabla \cdot \vec{D} = \rho_e \quad \text{(c)}$$

$$\nabla \cdot \vec{B} = \rho_m \quad \text{(d)}$$

Where $\vec{E}$ is the electric field strength vector in volts per meter, $\vec{D}$ is the electric displacement vector in coulombs per square meter, $\vec{H}$ is the magnetic field strength vector in amperes per meter, $\vec{B}$ is the magnetic flux density vector in webers per square meter (tesla), $\vec{J}$ is the electric current density vector in amperes per square meter, $\vec{M}$ is the magnetic current

density vector in volts per square meter, ρ_e is the electric charge density in coulombs per cubic meter and ρ_m is the magnetic charge density in webers per cubic meter.

Constitutive relations are necessary to supplement Maxwell's equations and characterize the material media. Constitutive relations for linear, isotropic, and nondispersive materials can be written as:

$$\vec{D} = \varepsilon\vec{E} \quad \text{(a)} \quad \text{Equation2. 2}$$
$$\vec{B} = \mu\vec{H} \quad \text{(b)}$$

To derive FDTD equations, only curl equations in Maxwell's equation are needed. The current density is decomposed into conduction current density and impressed current density. The Maxwell's curl equation can be rewritten as following:

$$\nabla \times \vec{H} = \frac{\partial \vec{D}}{\partial t} + \overrightarrow{J_c} + \overrightarrow{J_\iota} \quad \left(\overrightarrow{J_c} = \sigma^e \vec{E}\right) \qquad \text{Equation2. 3}$$

$$\nabla \times \vec{E} = -\frac{\partial \vec{B}}{\partial t} - \overrightarrow{M_c} - \overrightarrow{M_\iota} \quad \left(\overrightarrow{M_c} = \sigma^m \vec{H}\right) \qquad \text{Equation2. 4}$$

Where $\overrightarrow{J_\iota}$ and $\overrightarrow{M_\iota}$ represent electric current source and magnetic current source, respectively. Each Maxwell's curl equation can be decomposed into three scale equations for three-dimension space as in the following:

$$\frac{\partial E_x}{\partial t} = \frac{1}{\epsilon_x}\left(\frac{\partial H_z}{\partial y} - \frac{\partial H_y}{\partial z} - \sigma_x^e E_x - J_{ix}\right) \quad \text{(a)} \quad \text{Equation2. 5}$$

$$\frac{\partial E_y}{\partial t} = \frac{1}{\epsilon_y}\left(\frac{\partial H_x}{\partial z} - \frac{\partial H_z}{\partial x} - \sigma_y^e E_y - J_{iy}\right) \quad \text{(b)}$$

$$\frac{\partial E_z}{\partial t} = \frac{1}{\epsilon_z}\left(\frac{\partial H_y}{\partial x} - \frac{\partial H_x}{\partial y} - \sigma_z^e E_z - J_{iz}\right) \quad \text{(c)}$$

$$\frac{\partial H_x}{\partial t} = \frac{1}{\mu_x}\left(\frac{\partial E_y}{\partial z} - \frac{\partial E_z}{\partial y} - \sigma_x^m H_x - M_{ix}\right) \quad \text{(d)}$$

$$\frac{\partial H_y}{\partial t} = \frac{1}{\mu_y}\left(\frac{\partial E_z}{\partial x} - \frac{\partial E_x}{\partial z} - \sigma_y^m H_y - M_{iy}\right) \quad \text{(e)}$$

$$\frac{\partial H_z}{\partial t} = \frac{1}{\mu_z}\left(\frac{\partial E_x}{\partial y} - \frac{\partial E_x}{\partial x} - \sigma_z^m H_z - M_{iz}\right) \quad \text{(f)}$$

Material parameters $\epsilon_x, \epsilon_y, and\ \epsilon_y$ are related to electric field components $E_x, E_y, and\ E_z$ through electric flux density $D_x = \varepsilon_x E_x$, $D_y = \varepsilon_y E_y$, $and\ D_z = \varepsilon_z E_z$, respectively. Material parameters μ_x, μ_y, μ_y are related to magnetic field components H_x, H_y, $and\ H_z$ through magnetic flux density $B_x = \mu_x H_x$, $B_y = \mu_y H_y$, $and\ B_z = y_z H_z$, respectively.

The scalar equations of Maxwell's curl equation are approximated by using finite differences. The derivative of a function $f(x)$ at point x can be written as:

$$f'(x) = \lim_{\Delta x \to 0} \frac{f(x+\Delta x) - f(x)}{\Delta x} \qquad \text{Equation2. 6}$$

The derivative of $f(x)$ can be approximated in three formulas as following:

forward difference formula: $f'(x) \approx \frac{f(x+\Delta x) - f(x)}{\Delta x}$

backward difference formula: $f'(x) \approx \frac{f(x) - f(x-\Delta x)}{\Delta x}$

central difference formula: $f'(x) \approx \frac{f(x+\Delta x) - f(x-\Delta x)}{\Delta x}$

2.2.3 FDTD updating equations for three-dimensional problems

Yee originated a set of finite-difference equations for the time domain Maxwell's curl equations systems in 1966. Time domain Maxwell's curl equations can be represented in discrete form, both in space and time, employing the second order accurate central difference formula. From the previous section, the electric and magnetic field components are sampled at discrete positions both in time and space. The FDTD technique divides the three-dimension problem geometry into cells to form a grid. Figure2. 1 illustrates an FDTD grid composed of ($N_x \times N_y \times N_z$) cells. A unit cell of this grid is called Yee cell. Using rectangular Yee cells, a stepped or "staircase" approximation of the surface and internal geometry of the structure of interest is made with a space resolution set by the size of the unit cell.

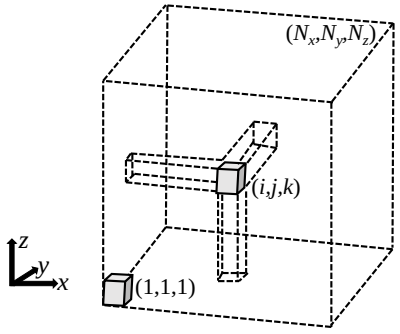

Figure2. 1 A three-dimensional FDTD computational space composed of ($N_x \times N_y \times N_z$).

The discrete spatial positions of the field components have a specific arrangement in the Yee cell, as demonstrated in Figure2. 2. The electric field vector components are placed at the center of the edges of Yee cells and are oriented parallel to the respective edges, and the magnetic field vector component are placed at the centers of the faces of the Yee cells and are oriented normal to the respective faces. This provides a simple picture of three-dimensional space being filled by an interlinked array of Faraday's law and Ampere's law contours. It can be easily noticed in the Figure2. 2 that each magnetic field vector is

surrounded by four electric field vectors that are curling around the magnetic field vector, thus simulating Faraday's law. Similarly, if the neighboring cells are added to the picture, it would be apparent that each electric field vector is surrounded by four magnetic field vectors that are curling around the electric field vector, thus simulating Ampere's law.

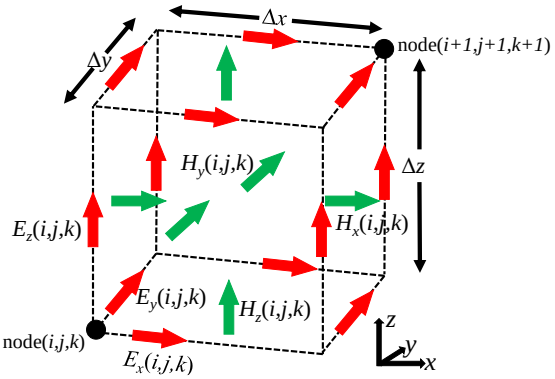

Figure2. 2 Arrangement of field components on a Yee cell indexed as (*i*, *j*, *k*).

Figure2. 2 shows indices of the field components, which are indexed as (i, j, k), associated with a cell indexed as (i, j, k). For a computation domain composed of uniform Yee cells having dimension Δx in *x* direction, Δy in *y* direction, Δz in *z* direction, the actual positions of the field components with respect to an origin coinciding with the positions of the node (1, 1, 1) can easily be calculated as:

$$E_x(i,j,k) \Rightarrow \left((i-0.5)\Delta x, (j-1)\Delta y, (k-1)\Delta z\right) \quad \text{(a)} \quad \text{Equation2. 7}$$

$$E_y(i,j,k) \Rightarrow \left((i-1)\Delta x, (j-0.5)\Delta y, (k-1)\Delta z\right) \quad \text{(b)}$$

$$E_z(i,j,k) \Rightarrow \left((i-1)\Delta x, (j-1)\Delta y, (k-0.5)\Delta z\right) \quad \text{(c)}$$

$$H_x(i,j,k) \Rightarrow \left((i-1)\Delta x, (j-0.5)\Delta y, (k-0.5)\Delta z\right) \quad \text{(d)}$$

$$H_y(i,j,k) \Rightarrow \left((i-0.5)\Delta x, (j-1)\Delta y, (k-0.5)\Delta z\right) \quad \text{(e)}$$

$$H_x(i,j,k) \Rightarrow \left((i-0.5)\Delta x, (j-0.5)\Delta y, (k-1)\Delta z\right) \quad \text{(f)}$$

The FDTD algorithm samples and calculates the fields at discrete time instants; however, the electric and magnetic field components are not sampled at the same time instants. For a time-sampling period Δt, the electric field components are sample at time instants 0, Δt, $2\Delta t$, ..., nΔt ...; however, the magnetic field components are sampled at time instants $\frac{1}{2}\Delta t$, $(1+\frac{1}{2})\Delta t$, ..., $(n+\frac{1}{2})\Delta t$, ... Therefore, the electric field components are calculated at integer time steps, and magnetic field components are calculated at half-integer time steps. Electric field and magnetic field are offset from each other by $\frac{1}{2}\Delta t$. The field components need to be referred not only by their spatial indices which indicate their position in space but also by

their temporal indices, which indicate their time instants. Therefore, a superscript notation is adopted to indicate the time instant. For instance, the *z* component of an electric field vector positioned at ((*i*−1) Δ*x*, ((*j*−1) Δ*y*, ((*k*−0.5) Δ*z)* and sampled at time instant nΔ*t* is referred to $E_z^n(i,j,k)$. Similarly, the *y* component of a magnetic field vector positioned at ((*i*−0.5) Δ*x*, ((*j*−1) Δ*y*, ((*k*−1) Δ*z)* and sampled at time instant $(n+\frac{1}{2})\Delta t$ is referred to as $H_z^{n+1/2}(i,j,k)$.

The material parameters (permittivity, permeability, electric, and magnetic conductivity) are distributed over FDTD grid and are associated with field components; therefore, they are indexed the same as their respective field components. For instance, Figure2. 3 illustrates the indices for the permittivity and permeability parameters. The electric conductivity is distributed and indexed the same as the permittivity and the magnetic conductivity is distributed and indexed the same as the permeability.

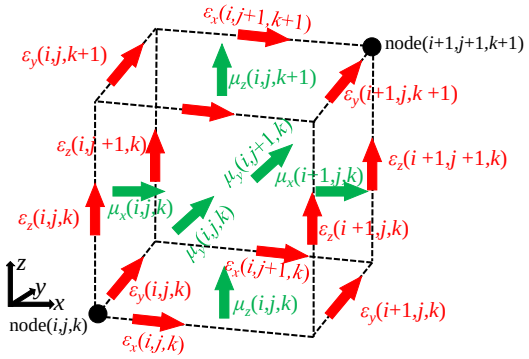

Figure2. 3 Material parameters indexed on Yee cell.

Having adopted an indexing scheme for the discrete samples for field components in both time and space, Maxwell's equations that are given in scalar form can be expressed in terms of finite differences. For instance, consider again:

$$\frac{\partial E_x}{\partial t} = \frac{1}{\varepsilon_x}\left(\frac{\partial H_z}{\partial y} - \frac{\partial H_y}{\partial z} - \sigma_z^e E_z - J_{iz}\right) \qquad \text{Equation2. 8}$$

The derivatives in this equation can be approximated by using the central difference formula with the position of $E_z\ (i,j,k)$ being the center point for the difference formula in space and time instant $(n+\frac{1}{2})\Delta t$ as being the center point in time. Considering the field component positions given in Figure2. 4, the approximation equation can be written as in the following:

$$\frac{E_x^{n+1}(i,j,k)-E_x^n(i,j,k)}{\Delta t} = \frac{1}{\varepsilon_x(i,j,k)}\frac{H_z^{n+\frac{1}{2}}(i,j,k)-H_z^{n+\frac{1}{2}}(i,j-1,k)}{\Delta y} - \frac{1}{\varepsilon_x(i,j,k)}\frac{H_y^{n+\frac{1}{2}}(i,j,k)-H_y^{n+\frac{1}{2}}(i,j,k-1)}{\Delta z} - \frac{\sigma_x^e(i,j,k)}{\varepsilon_x(i,j,k)}E_x^{n+\frac{1}{2}}(i,j,k) - \frac{1}{\varepsilon_x(i,j,k)}J_{ix}^{n+\frac{1}{2}}(i,j,k) \qquad \text{Equation2. 9}$$

From the above equation, the electric field are defined at integer time step on the left-hand side of the equation. However, on the right-hand side of the equation, the electric field is defined at time instant $(n+\frac{1}{2})\Delta t$, that is $E_x^{n+\frac{1}{2}}(i,j,k)$. Therefore, this term can be written as the average of the terms at time instants $(n+1)\Delta t$ and $n\Delta t$ as following:

$$E_x^{n+\frac{1}{2}}(i,j,k) = \frac{E_x^{n+1}(i,j,k)+E_x^{n}(i,j,k)}{2} \qquad \text{Equation2. 10}$$

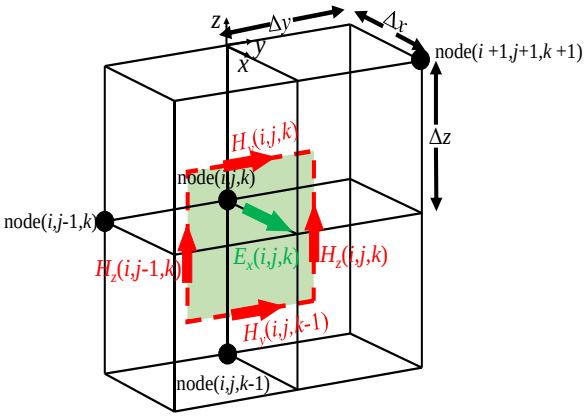

Figure2. 4 Field components around $E_x(i, j, k)$

Rearrange the approximation equation by using the term above such that the terms $E_x^{n+1}(i,j,k)$ is kept on the left side and the rest of terms are moved to the right side of the equation as following:

$$\frac{2\varepsilon_x(i,j,k)+\Delta t\sigma_x^e(i,j,k)}{2\varepsilon_x(i,j,k)}E_x^{n+1}(i,j,k) = \frac{2\varepsilon_x(i,j,k)-\Delta t\sigma_x^e(i,j,k)}{2\varepsilon_x(i,j,k)}E_x^{n}(i,j,k) + \frac{\Delta t}{\varepsilon_x(i,j,k)\Delta y}\left(H_z^{n+\frac{1}{2}}(i,j,k) - H_z^{n+\frac{1}{2}}(i,j-1,k)\right) - \frac{\Delta t}{\varepsilon_x(i,j,k)\Delta y}\left(H_y^{n+\frac{1}{2}}(i,j,k) - H_z^{n+\frac{1}{2}}(i,j,k-1)\right) - \frac{\Delta t}{\varepsilon_x(i,j,k)\Delta y}J_{ix}^{n+\frac{1}{2}}(i,j,k) \qquad \text{Equation2. 11}$$

$$E_x^{n+1}(i,j,k) = \frac{2\varepsilon_x(i,j,k)-\Delta t\sigma_x^e(i,j,k)}{2\varepsilon_x(i,j,k)+\Delta t\sigma_x^e(i,j,k)}E_x^{n}(i,j,k) + \frac{2\Delta t}{(2\varepsilon_x(i,j,k)+\Delta t\sigma_x^e(i,j,k))\Delta y}\left(H_z^{n+\frac{1}{2}}(i,j,k) - H_z^{n+\frac{1}{2}}(i,j-1,k)\right) - \frac{2\Delta t}{(2\varepsilon_x(i,j,k)+\Delta t\sigma_x^e(i,j,k))\Delta z}\left(H_y^{n+\frac{1}{2}}(i,j,k) - H_y^{n+\frac{1}{2}}(i,j-1,k)\right) - \frac{2\Delta t}{2\varepsilon_x(i,j,k)+\Delta t\sigma_x^e(i,j,k)}J_{ix}^{n+\frac{1}{2}}(i,j,k) \qquad \text{Equation2. 12}$$

$$E_y^{n+1}(i,j,k) = \frac{2\varepsilon_y(i,j,k)-\Delta t\sigma_y^e(i,j,k)}{2\varepsilon_y(i,j,k)+\Delta t\sigma_y^e(i,j,k)}E_y^n(i,j,k) + \frac{2\Delta t}{(2\varepsilon_y(i,j,k)+\Delta t\sigma_y^e(i,j,k))\Delta z}\left(H_z^{n+\frac{1}{2}}(i,j,k) - H_z^{n+\frac{1}{2}}(i,j,k-1)\right) - \frac{2\Delta t}{(2\varepsilon_y(i,j,k)+\Delta t\sigma_y^e(i,j,k))\Delta x}\left(H_y^{n+\frac{1}{2}}(i,j,k) - H_y^{n+\frac{1}{2}}(i-1,j,k)\right) - \frac{2\Delta t}{2\varepsilon_y(i,j,k)+\Delta t\sigma_y^e(i,j,k)}J_{iy}^{n+\frac{1}{2}}(i,j,k)$$ Equation2. 13

$$E_z^{n+1}(i,j,k) = \frac{2\varepsilon_z(i,j,k)-\Delta t\sigma_z^e(i,j,k)}{2\varepsilon_z(i,j,k)+\Delta t\sigma_z^e(i,j,k)}E_z^n(i,j,k) + \frac{2\Delta t}{(2\varepsilon_z(i,j,k)+\Delta t\sigma_z^e(i,j,k))\Delta x}\left(H_y^{n+\frac{1}{2}}(i,j,k) - H_y^{n+\frac{1}{2}}(i-1,j,k)\right) - \frac{2\Delta t}{(2\varepsilon_z(i,j,k)+\Delta t\sigma_z^e(i,j,k))\Delta y}\left(H_x^{n+\frac{1}{2}}(i,j,k) - H_x^{n+\frac{1}{2}}(i,j-1,k)\right) - \frac{2\Delta t}{2\varepsilon_z(i,j,k)+\Delta t\sigma_z^e(i,j,k)}J_{iz}^{n+\frac{1}{2}}(i,j,k)$$ Equation2. 14

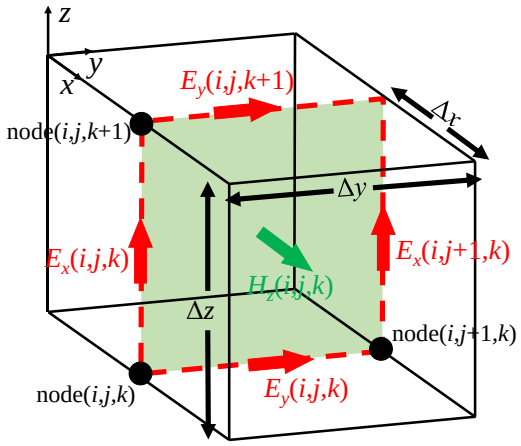

Figure2. 5 Field components around H_x(i, j, k)

The Equation2. 14 shows the updated value of electric field of the current time instant is depending on the previous time instant. This equation is called an FDTD updating equation of electric field. The updating equation of magnetic field equation can be written from Maxwell's curl equation as following:

$$\frac{\partial H_x}{\partial t} = \frac{1}{\mu_x}\left(\frac{\partial E_y}{\partial z} - \frac{\partial E_z}{\partial y} - \sigma_x^m H_x - M_{ix}\right)$$ Equation2. 15

$$\frac{H_x^{n+\frac{1}{2}}(i,j,k)-H_x^{n-\frac{1}{2}}(i,j,k)}{\Delta t} = \frac{1}{\mu_x(i,j,k)}\frac{E_y^n(i,j,k+1)-E_y^n(i,j,k)}{\Delta z} - \frac{1}{\mu_x(i,j,k)}\frac{E_z^n(i,j+1,k)-E_z^n(i,j,k)}{\Delta y} - \frac{\sigma_x^m(i,j,k)}{\mu_x(i,j,k)}H_x^n(i,j,k) - \frac{1}{\mu_x(i,j,k)}M_{ix}^n(i,j,k)$$ Equation2. 16

$$H_x^{n+\frac{1}{2}}(i,j,k) = \frac{2\mu_x(i,j,k)-\Delta t\sigma_x^m(i,j,k)}{2\mu_x(i,j,k)+\Delta t\sigma_x^m(i,j,k)} H_x^{n-\frac{1}{2}}(i,j,k) + \frac{2\Delta t}{(2\mu_x(i,j,k)+\Delta t\sigma_x^m(i,j,k))\Delta z} E_y^n(i,j,k+1) - E_y^n(i,j,k) - \frac{2\Delta t}{(2\mu_x(i,j,k)+\Delta t\sigma_x^m(i,j,k))\Delta y} E_z^n(i,j+1,k) - E_z^n(i,j,k) - \frac{2\Delta t}{2\mu_x(i,j,k)+\Delta t\sigma_x^m(i,j,k)} M_{ix}^n(i,j,k)$$ Equation2. 19

$$H_x^{n+\frac{1}{2}}(i,j,k) = \frac{2\mu_x(i,j,k)-\Delta t\sigma_x^m(i,j,k)}{2\mu_x(i,j,k)+\Delta t\sigma_x^m(i,j,k)} H_x^{n-\frac{1}{2}}(i,j,k) + \frac{2\Delta t}{(2\mu_x(i,j,k)+\Delta t\sigma_x^m(i,j,k))\Delta z} E_y^n(i,j,k+1) - E_y^n(i,j,k) - \frac{2\Delta t}{(2\mu_x(i,j,k)+\Delta t\sigma_x^m(i,j,k))\Delta y} E_z^n(i,j+1,k) - E_z^n(i,j,k) - \frac{2\Delta t}{2\mu_x(i,j,k)+\Delta t\sigma_x^m(i,j,k)} M_{ix}^n(i,j,k)$$ Equation2. 20

$$H_y^{n+\frac{1}{2}}(i,j,k) = \frac{2\mu_y(i,j,k)-\Delta t\sigma_y^m(i,j,k)}{2\mu_y(i,j,k)+\Delta t\sigma_y^m(i,j,k)} H_y^{n-\frac{1}{2}}(i,j,k) + \frac{2\Delta t}{\left(2\mu_y(i,j,k)+\Delta t\sigma_y^m(i,j,k)\right)\Delta x} E_y^n(i+1,j,k) - E_y^n(i,j,k) - \frac{2\Delta t}{\left(2\mu_y(i,j,k)+\Delta t\sigma_y^m(i,j,k)\right)\Delta z} E_z^n(i,j,k+1) - E_z^n(i,j,k) - \frac{2\Delta t}{2\mu_y(i,j,k)+\Delta t\sigma_y^m(i,j,k)} M_{iy}^n(i,j,k)$$ Equation2. 17

$$H_z^{n+\frac{1}{2}}(i,j,k) = \frac{2\mu_z(i,j,k)-\Delta t\sigma_z^m(i,j,k)}{2\mu_z(i,j,k)+\Delta t\sigma_z^m(i,j,k)} H_y^{n-\frac{1}{2}}(i,j,k) + \frac{2\Delta t}{(2\mu_z(i,j,k)+\Delta t\sigma_z^m(i,j,k))\Delta y} E_x^n(i,j+1,k) - E_x^n(i,j,k) - \frac{2\Delta t}{\left(2\mu_y(i,j,k)+\Delta t\sigma_y^m(i,j,k)\right)\Delta x} E_x^n(i+1,j,k+1) - E_x^n(i,j,k) - \frac{2\Delta t}{2\mu_y(i,j,k)+\Delta t\sigma_y^m(i,j,k)} M_{iz}^n(i,j,k)$$ Equation2. 18

The Equation2. 20 shows the updated value of magnetic field of the current time instant is depending on the previous time instant. This equation is called an FDTD updating equation of magnetic field. From these updating equations above, the algorithm of FDTD can be drawn as following:

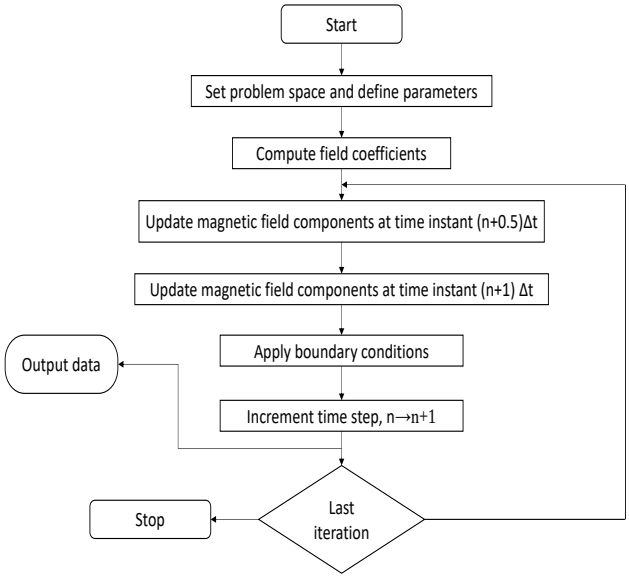

Figure2. 6 Explicit FDTD procedure

2.2.4 Basic Parameters in FDTD Method

The finite-different time-domain (FDTD) algorithm samples the electric and magnetic fields at discrete points both in time and space. The choice of the period of sampling (Δt in time, Δx, Δy, Δz in space) must comply with certain restrictions to guarantee the stability of the solution. Furthermore, the choice of this parameters determines the accuracy of the solution. This section focuses on the stability analysis. First, the stability concept is illustrated using a simple partial differential equation (PDE) in space and time domain. Next, the Courant-Friedrichs-Lewy (CFL) condition for the FDTD method is discussed.

An important issue in designing a time domain numerical algorithm is the stability condition. To understand the stability concept, let's start with a simple wave equation:

$$\frac{\partial u(x,t)}{\partial t} + \frac{\partial u(x,t)}{\partial x} = 0 \quad u(x, t = 0) = u_0(x) \qquad \text{Equation2. 21}$$

Where $u(x,t)$ is the unknown wave function and $u_0(x)$ is the initial condition at $t=0$. Using the PDE knowledge, the equation can be analytically solved:

$$u(x,t) = u_0(x - t) \qquad \text{Equation2. 22}$$

A time domain analytical scheme can be developed to solve above wave equation. First, $u(x,t)$ is discretized in both time and space domains:

$$x_i = i\Delta x \ , i = 0, 1, 2, \ldots$$

$$t_n = n\Delta t,\ n = 0, 1, 2, \ldots$$
$$u_i^n = u(x_i, t_n).$$

If Δx and Δt are space and time cell size. Then, the finite-difference scheme is used to compute the derivatives, the following equation is obtained:

$$\frac{u_i^{n+1} - u_i^{n-1}}{2\Delta t} + \frac{u_{i-1}^n - u_{i+1}^n}{2\Delta x} = 0$$
$$u_i^{n+1} = u_i^{n-1} + \frac{\Delta t}{\Delta x}(u_{i+1}^n - u_{i-1}^n)$$
$$u_i^{n+1} = u_i^{n-1} + \lambda(u_{i+1}^n - u_{i-1}^n)$$

The stability of numerical scheme of the above equation is depending on the value of λ. In the same way, the numerical stability of the FDTD method is determined by CFL condition, which require that the time increment Δt has specific bound relative to the lattice space increments, such that

$$\Delta t \leq \frac{1}{c\sqrt{\frac{1}{(\Delta x)^2} + \frac{1}{(\Delta y)^2} + \frac{1}{(\Delta z)^2}}} \qquad \text{Equation2. 23}$$

Where c is the speed of light in free space. The equation can be rewritten as

$$c\Delta t \sqrt{\frac{1}{(\Delta x)^2} + \frac{1}{(\Delta y)^2} + \frac{1}{(\Delta z)^2}} \leq 1$$

For the cubical spatial grid where $\Delta x = \Delta y = \Delta z$, the CFL condition reduces to

$$\Delta t \leq \frac{\Delta x}{c\sqrt{3}}$$

In the case where value of $\Delta x, \Delta y, \Delta z$ are not equal, the smallest value of among those three parameters is the dominant factor controlling the maximum time step and the maximum time step allowed is always smaller than $min(\Delta x, \Delta y, \Delta z)/c$

2.2.5 Absorbing Boundary Condition in FDTD Method

The computational storage space is finite; therefore, the finite-difference time-domain (FDTD) problem space size is finite and needs to be truncated by special boundary conditions. In some CEM techniques, perfect electric conductor (PEC) is used boundary condition. However, many CEM problems such as scattering, and radiation require the boundary condition which is equivalent to open space. The types of boundary conditions that simulate electromagnetic wave propagating continuously beyond the computational space are called ***absorbing boundary conditions*** **(ABCs).** However, if the absorbing boundary conditions is imperfect, the numerical reflected electromagnetic wave will be created. Therefore, the

corrupted computational results will occur after certain amount of simulation time. Many types of ABCs have been introduced. However, the perfectly matched layer (PML), which is proposed by Berenger [30][31], has been the most robust ABCs in comparison with other techniques in the past. PML is a finite-thickness special medium surrounding the computational space based on fictitious constitutive parameters to create a wave-impedance matching condition, which is independent of the angles and frequencies of the wave incident on this boundary. The theory and implementation of the PML boundary condition are illustrated as following:

The modified Maxwell's equations have 12 field components instead of the original six components. These modified equations are separated into 6 equations for electric field and 6 equations for magnetic field. Modified equations for electric field are written as following:

$$\varepsilon_0 \frac{\partial E_{xy}}{\partial t} + \sigma_{pey} E_{xy} = \frac{\partial (H_{zx} + H_{zy})}{\partial y} \quad \text{(a)} \quad \text{Equation2. 24}$$

$$\varepsilon_0 \frac{\partial E_{xz}}{\partial t} + \sigma_{pez} E_{xz} = -\frac{\partial (H_{yx} + H_{yz})}{\partial z} \quad \text{(b)}$$

$$\varepsilon_0 \frac{\partial E_{yx}}{\partial t} + \sigma_{pex} E_{yx} = -\frac{\partial (H_{zx} + H_{zy})}{\partial x} \quad \text{(c)}$$

$$\varepsilon_0 \frac{\partial E_{yz}}{\partial t} + \sigma_{pez} E_{yz} = \frac{\partial (H_{xy} + H_{xz})}{\partial z} \quad \text{(d)}$$

$$\varepsilon_0 \frac{\partial E_{zx}}{\partial t} + \sigma_{pex} E_{zx} = \frac{\partial (H_{yx} + H_{yz})}{\partial x} \quad \text{(e)}$$

$$\varepsilon_0 \frac{\partial E_{zy}}{\partial t} + \sigma_{pey} E_{zy} = -\frac{\partial (H_{xy} + H_{xz})}{\partial y} \quad \text{(f)}$$

Modified equations for magnetic field are written as following:

$$\mu_0 \frac{\partial H_{xy}}{\partial t} + \sigma_{pmy} H_{xy} = -\frac{\partial (E_{zx} + E_{zy})}{\partial y} \quad \text{(a)} \quad \text{Equation2. 25}$$

$$\mu_0 \frac{\partial H_{xz}}{\partial t} + \sigma_{pmz} H_{xz} = \frac{\partial (E_{yx} + E_{yz})}{\partial z} \quad \text{(b)}$$

$$\mu_0 \frac{\partial H_{yz}}{\partial t} + \sigma_{pmz} H_{yz} = -\frac{\partial (E_{yx} + E_{yz})}{\partial z} \quad \text{(c)}$$

$$\mu_0 \frac{\partial H_{yx}}{\partial t} + \sigma_{pmx} H_{yx} = \frac{\partial (E_{zx} + E_{zy})}{\partial x} \quad \text{(d)}$$

$$\mu_0 \frac{\partial H_{zy}}{\partial t} + \sigma_{pmy} H_{zy} = \frac{\partial (E_{xy} + E_{xz})}{\partial y} \quad \text{(e)}$$

$$\mu_0 \frac{\partial H_{zx}}{\partial t} + \sigma_{pmx} H_{zx} = -\frac{\partial (E_{yx} + E_{zy})}{\partial x} \quad \text{(f)}$$

Then the matching condition for a three-dimensional PML is given by

$$\frac{\sigma_{pex}}{\varepsilon_0} = \frac{\sigma_{pmx}}{\mu_0}, \qquad \frac{\sigma_{pey}}{\varepsilon_0} = \frac{\sigma_{pmy}}{\mu_0}, \qquad and \ \ \frac{\sigma_{pez}}{\varepsilon_0} = \frac{\sigma_{pmz}}{\mu_0}$$

If a three-dimensional FDTD problem space is attached with adequate thickness of PML media as shown in Figure2.7 the outgoing wave will be absorbed without any undesired

numerical reflection. The PML regions must be assigned appropriate conductivity values satisfying the matching condition; the positive and negative x boundaries of PML regions have nonzero σ_{pex} and σ_{pmx}, the positive and negative x boundaries of PML regions have nonzero σ_{pey} and σ_{pmy}, the positive and negative x boundaries of PML regions have nonzero σ_{pez} and σ_{pmz} values as illustrated in Figure2. 7. The coexistence of nonzero values of σ_{pex} , σ_{pmx}, σ_{pey} , σ_{pmy} , σ_{pez} , and σ_{pmz} is required at the PML overlapping regions. By applying the finite difference schemes to the modified Maxwell's equations, the FDTD field updating equations for the three-dimensional PML regions can be obtained.

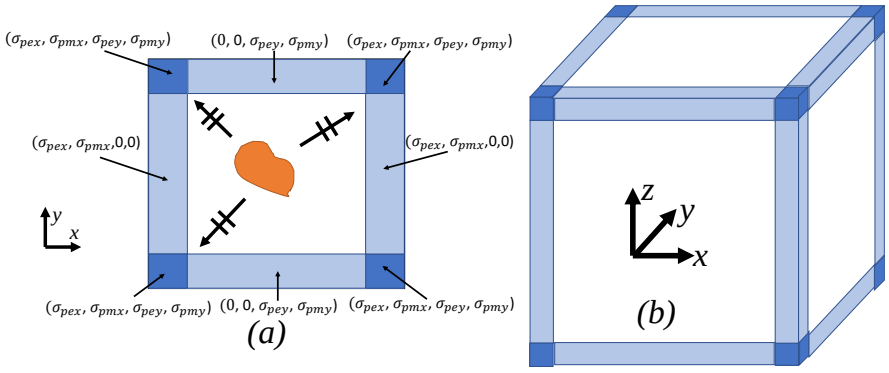

Figure2. 7 (a) 2-dimensional and (b) 3-dimensional PML regions

2.3 Antenna Characteristics Evaluation by Using FDTD Method

2.3.1 Gaussian pulse

Sources are necessary components of finite-difference time-domain (FDTD) simulation and their types vary depending on the type of problem under consideration. Usually, sources are separated into two types: (1) near, such as the voltage and current sources, and (2) far, such as the incident fields appearing in scattering problems. In any case, a source excites electric and magnetic field with a waveform as a function of time. The type of waveform can be selected specific to the problem under consideration. However, some limitations of the FDTD method should be kept in mind while constructing the source wave forms to obtain a valid and accurate simulation result.

A source waveform should be chosen such that its frequency spectrum includes all the frequencies of interest for the simulation, and it should have a smooth turn-on and turn-off to minimize the undesired effects of high-frequency components. A sine and cosine function are a single-frequency waveform, whereas other waveforms such as Gaussian pulse, time derivative of Gaussian pulse, and cosine-modulated Gaussian pulse are multiple frequency waveforms. The type and parameters of the waveforms can be chosen based on the frequency spectrum of the waveform interest.

Running an FDTD simulation will yield numerical results for a dominant frequency as well as for other frequencies in the spectrum of the finite sinusoidal excitation. However, the sinusoidal waveform is not an appropriate choice if simulation results for a wideband of frequencies are sought. The frequency spectrum of the source waveform determines the range of frequencies for which valid and accurate results can be obtained. As the frequency increases, the wavelength decreases and becomes comparable to the cell size of the problem space. If the cell size is too large compared with fraction of a wavelength, the signal at that frequency cannot be sampled accurately in space. Therefore, the highest frequency in the source waveform spectrum should be chosen such that the cell size is not larger than a fraction of the highest frequency wavelength. For many applications, setting the highest-frequency wavelength larger than 20 cell size is sufficient for a reasonable FDTD simulation. A Gaussian waveform is the best choice for a source waveform, since it can be constructed to contain all frequencies up to the highest frequency that is tied to cell size by a factor. This factor, which is the proportion of the highest frequency wavelength to the unit cell size, is referred as *number of cells per wavelength* n_c. A Gaussian waveform can be written as a function of time as:

$$g(t) = e^{-\frac{t^2}{\tau^2}} \qquad \text{Equation2. 26}$$

Where τ is a parameter that determine the width of the Gaussian pulse both in the time domain and the frequency domain. The Fourier transform of a Gaussian waveform is also a Gaussian waveform, which can be expressed as function of frequency as:

$$G(w) = \tau\sqrt{\pi}e^{-\frac{\tau^2 w^2}{4}} \qquad \text{Equation2. 27}$$

The highest frequency that is available out of an FDTD calculation can be determined by the accuracy parameter number of cells per wavelength such that

$$f_{max} = \frac{c}{\lambda_{min}} = \frac{c}{n_c \Delta s_{max}}$$

Where c is the speed of light in free space, Δs_{max} is the maximum of the cell dimensions ($\Delta x, \Delta y, or\ \Delta z$), and λ_{min} is the wavelength of the highest frequency in free space. Once the highest frequency in the spectrum of the frequency domain Gaussian waveform is determined, it is possible to find a τ that constructs the corresponding time-domain Gaussian waveform.

2.3.2 S-Parameter calculation

Scattering parameters (S-parameters) are used to characterize the response of radio frequency and microwave circuits, and they are more commonly used than other types of network parameters (Y-parameters, and Z-parameters) because they are easier to measure

and work with at high frequencies. S-parameters are based on the power wave concept. The incident and reflected power waves a_i and b_i associated with port *i* are defined as following:

$$a_i = \frac{V_i + Z_i \times I_i}{2\sqrt{|Re\{Z_i\}|}} \quad , \quad b_i = \frac{V_i - Z_i^* \times I_i}{2\sqrt{|Re\{Z_i\}|}} \qquad \text{Equation2. 28}$$

Where V_i and I_i are the voltage and the current flowing into the i^{th} port of a junction and Z_i is the impedance looking out from the i^{th} port as illustrated in Figure2. 8. In general, Z_i is complex; however, in most of the microwave's applications it is real and equal to 50Ω. Then the S-parameters matrix can be expressed as:

$$\begin{bmatrix} b_1 \\ b_2 \\ \vdots \\ b_N \end{bmatrix} = \begin{bmatrix} S_{11} & S_{12} & \cdots & S_{1N} \\ S_{21} & S_{22} & \cdots & S_{2N} \\ \vdots & \vdots & \ddots & \vdots \\ S_{N1} & S_{N2} & \cdots & S_{NN} \end{bmatrix} \times \begin{bmatrix} a_1 \\ a_2 \\ \vdots \\ a_N \end{bmatrix} \qquad \text{Equation2. 29}$$

The subscripts *mn* indicate output port number, *m*, and input port number, *n*, of the scattering parameter S_{mn}. If only the port n is excited while all other ports are terminated by matched loads, the output power wave at port *m*, b_m, and the input power wave at port *n*, a_n, can be used to calculate S_{mn} using:

$$S_{mn} = \frac{b_m}{a_n} \qquad \text{Equation2. 30}$$

This technique can be applied to FDTD simulation results to obtain S-parameters for an input port *n.* A multiport circuit can be constructed in an FDTD problem space where all ports are terminated by matching loads and only the reference port *n* is excited by a source.

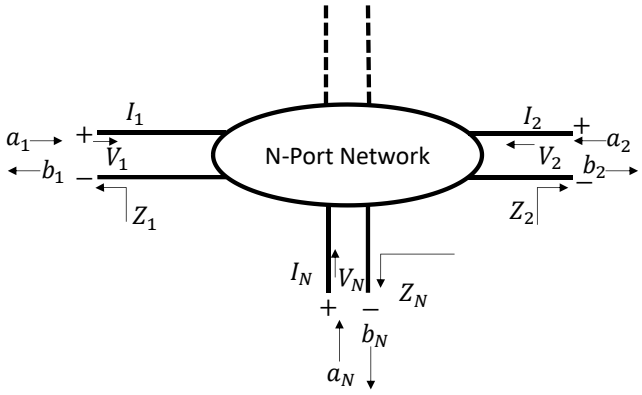

Figure2. 8 An N-port Network

2.3.3 Near to Far-Field Conversion

In finite-difference time-domain (FDTD) method is used to compute electric and magnetic fields within a finite space around an electromagnetic object (the near-zone

electromagnetic fields). In many applications, such as antennas and radar cross-section, it is necessary to find the radiation or scattered field in the region that far away from an antenna or scatterer. With the FDTD technique, the direct evaluation of the far field calls for an excessively large computational domain, which is practical in applications. Instead, the far-zone electromagnetic fields are computed from the near-field FDTD data through a near-field to far-field (NF-FF) transformation technique. A simple condition for the far field is defined as following:

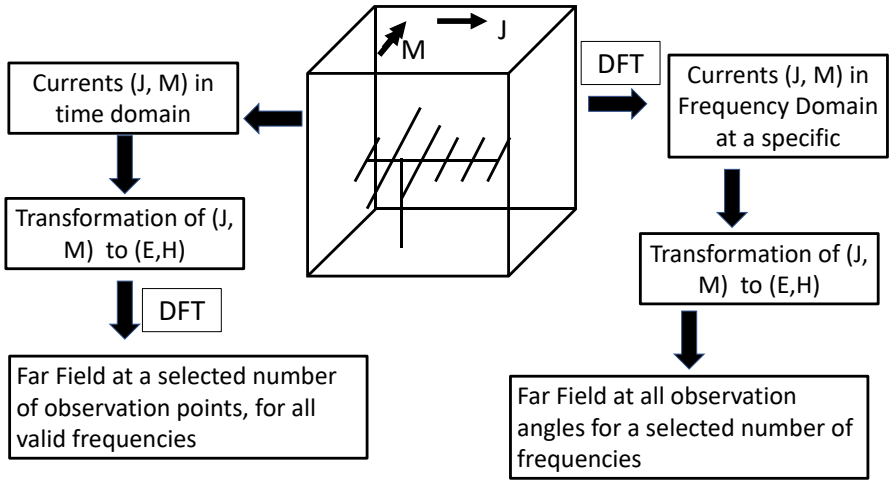

Figure2. 9 Two paths of the near-field to far-field transformation techniques are implemented to achieve different computation objective

$$kR \gg 1 \Longrightarrow \frac{2\pi R}{\lambda} \gg 1 \qquad \text{Equation2. 31}$$

Where R is the distance from radiator to the observation point, k is the wave number in free space, and λ is the wavelength. For an electrically large antenna such as a parabolic reflector, the aperture size D is often used to determine the far-field condition:

$$r > \frac{2D^2}{\lambda} \qquad \text{Equation2. 32}$$

Where r is the distance from the center of the antenna aperture to the observation point (r, θ, ϕ) can be expressed as:

$$\vec{E}(r,\theta,\phi) = \frac{e^{-jkr}}{4\pi r}\vec{F}(\theta,\phi) \qquad \text{(a)} \qquad \text{Equation2. 33}$$

$$\vec{H} = \hat{r} \times \frac{\vec{E}}{\eta_0} \qquad \text{(b)}$$

Where η_0 is the wave impedance of free space and $\vec{F}(\theta,\phi)$ is a term determining the angular variations of the far-field pattern of electric field. Thus, the radiation pattern of the antenna is only a function of the angular position (θ,ϕ) and is independent of the distance r.

In general, the near-field to far-field transformation technique is implemented in a two-step procedure. First, an imaginary surface is selected to enclose the antenna, as shown in Figure. The currents $\vec{J}$ and $\vec{M}$ on the surface are determined by the computed $\vec{E}$ and $\vec{H}$ field from the currents is equivalent to the radiation field from the antenna. Next, the vector potentials $\vec{A}$ and $\vec{F}$ are used to compute the radiation fields from the equivalent currents $\vec{J}$ and $\vec{M}$. The far-field conditions are used in the derivations to obtain the appropriate analytical formulas.

Compare with the direct FDTD simulation that requires a mesh extending many wavelengths from the object, a much smaller FDTD mesh is needed to evaluate the equivalent currents $\vec{J}$ and $\vec{M}$. Thus, it is much more computationally efficient to use this near-field to far-field transformation technique.

According to different computation objectives, the transformation technique can be applied in both the time and frequency domains, as shown in Figure2. 9. When transient or broadband frequency-domain results are required at a limited number of observation angles, the left path in Figure2. 9 is adopted. For these situations, the time-domain transformation is used and the transient far-zone fields at each angle of interest are stored while updating the field components.

In contrast, when the far fields at all observation angles are required for a limited number of frequencies, the right path in Figure2. 9 is adopted. For each frequency of interest, a running discrete Fourier transform (DFT) of the tangential fields (surface currents) on a closed surface is updated at each time step. The complex frequency-domain currents obtained from the DFT are then used to compute the far-zone fields at all observation angles through the frequency-domain transformation.

The surface equivalence theorem was introduced in 1936 by Sckelkunoff and is now widely used in electromagnetic and antenna problems. The basic idea is to replace the actual source such as antennas or scatterers with fictitious surface currents on a surrounding closed surface.

Within a specific region, the fields generated by an arbitrary source are $(\vec{E}, \vec{H})$. An imaginary surface S is selected to enclose all the sources and scattering objects, as shown in Figure2. 10. Outside the surface S is only free space. An equivalent problem is set up in Figure2. 10 where the fields outside the surface S remain the same but inside the surface S are set to zero. It is obvious that this setup is feasible because the fields satisfy Maxwell's equations both inside and outside the surface S. To comply with the boundary conditions on the surface, equivalent surface currents must be introduced on S:

$$\vec{J}_s = \hat{n} \times \left(\vec{H}^{out} - \vec{H}^{in}\right) = \hat{n} \times \vec{H} \quad \text{(a)} \qquad \text{Equation2. 34}$$

$$\vec{M}_s = -\hat{n} \times \left(\vec{E}^{out} - \vec{E}^{in}\right) = -\hat{n} \times \vec{E} \quad \text{(b)}$$

It is worthwhile to emphasize that Figure2. 10 have the same fields outside the surface S but different fields inside the surface S. If the field values on the surface S in the original problem Figure2. 10 can be accurately obtained by some means, the surface currents in Figure2. 10 can be determined from equation. Then the fields at any arbitrary far observation point in Figure2. 10 can be readily calculated from the vector potential approach. Based on the uniqueness theorem, are the only solution of the problem in Figure2. 10. According to the relations between Figure2. 10, the computed fields outside the surface S are also the solution for the original problem. The implementation of the surface equivalence theorem simplifies the far-field calculation. In the original Figure2. 10 problem, materials with different permittivity and permeability may exist inside the surface S. Thus, a complex Green's function needs to be derived to calculate the radiating field. In the problem Figure2. 10, the fields inside the surface are zero, and the permittivity and permeability can be set the same as the radiating field. The key point of the equivalent theorem implementation is to accurately obtain the equivalent currents on the imaginary surface S. In the FDTD simulation, the surface currents can be readily computed from the following procedure.

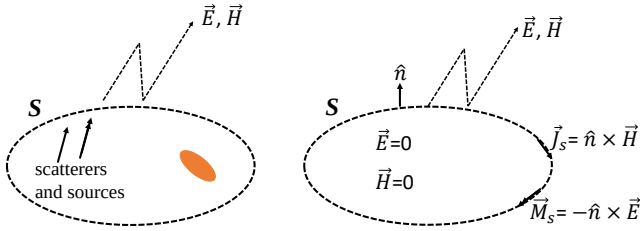

Figure2. 10 Surface equivalent theorem

First, a closed surface is selected around the antennas or scatterers, as shown in Figure2. 11. The selected surface is usually a rectangular box that fits the FDTD grid. It is set between the analyzed objects and the outside absorbing boundary. The location of the box can be defined by corners: lowest coordinate (*li*, *lj*, *lk*) corner and upper coordinate (*ui*, *uj*, *uk*) corner. It is critical that all the antennas or scatterers must be enclosed by this rectangular box so that the equivalent theorem can be implemented. It is also important to have this box in the air buffer area between all objects and the first interface of the absorbing boundary.

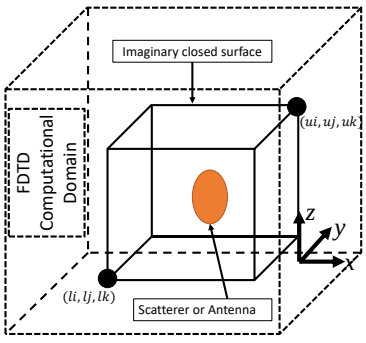

Figure2. 11 An imaginary surface is selected to enclose the antennas or scatterers

Once the imaginary closed surface is selected, the equivalent surface currents are computed next. There are six surfaces of the rectangular box, and each surface has four scalar electric and magnetic currents, as shown in Figure2. 12. For the top surface, the normal direction is $\hat{z}$. From the equivalent surface currents are calculated as:

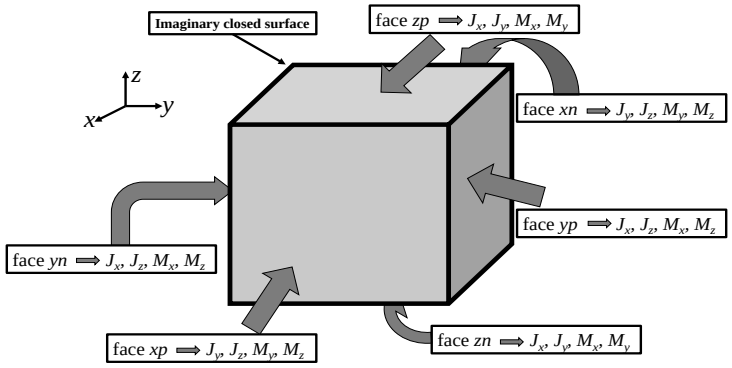

Figure2. 12 Equivalent surface current on imaginary closed surface

$$\vec{J_S} = \hat{z} \times \vec{H} = \hat{z} \times \left(\hat{x}H_x + \hat{y}H_y + \hat{z}H_z\right) = -\hat{x}H_y + \hat{y}H_x \qquad \text{Equation2. 35}$$

$$\vec{M_S} = -\hat{z} \times \vec{E} = -\hat{z} \times \left(\hat{x}E_x + \hat{y}E_y + \hat{z}E_z\right) = \hat{x}E_y - \hat{y}E_x \qquad \text{Equation2. 36}$$

The scalar surface currents can be obtained:

$$\vec{J_S} = \hat{x}J_x + \hat{y}J_y \Rightarrow J_x = -H_y, J_y = H_x \qquad \text{Equation2. 37}$$

$$\vec{M_S} = \hat{x}M_x + \hat{y}M_y \Rightarrow M_x = E_y, M_y = -E_x \qquad \text{Equation2. 38}$$

Note that the E and H fields used in Equation2. 37 and Equation2. 38 are computed form the FDTD simulation. For a time-domain data are used directly. For a frequency-domain far-field calculation, a DFT needs to be carried out to obtain the desired frequency components of the fields. Similar methodology is used to obtain the surface currents on the other five surfaces.

On the bottom surface,

$$\vec{J_S} = \hat{x}J_x + \hat{y}J_y \Rightarrow J_x = H_y, J_y = -H_x \qquad \text{(a)} \qquad \text{Equation2. 39}$$

$$\vec{M_S} = \hat{x}M_x + \hat{y}M_y \Rightarrow M_x = -E_y, M_y = E_x \qquad \text{(b)}$$

On the left surface,

$$\vec{J_S} = \hat{x}J_x + \hat{z}J_z \Rightarrow J_x = -H_z, J_z = H_x \qquad \text{(a)} \qquad \text{Equation2. 40}$$

$$\vec{M_S} = \hat{x}M_x + \hat{z}M_z \Rightarrow M_x = E_z, M_z = -E_x \qquad \text{(b)}$$

On the right surface,

$$\vec{J}_S = \hat{x}J_x + \hat{z}J_z \Rightarrow J_x = H_z, J_z = -H_x \quad \text{(a)} \qquad \text{Equation2. 41}$$

$$\vec{M}_S = \hat{x}M_x + \hat{z}M_z \Rightarrow M_x = -E_z, M_z = E_x \quad \text{(b)}$$

On the front surface,

$$\vec{J}_S = \hat{y}J_y + \hat{z}J_z \Rightarrow J_y = -H_z, J_z = H_y \quad \text{(a)} \qquad \text{Equation2. 42}$$

$$\vec{M}_S = \hat{y}M_y + \hat{z}M_z \Rightarrow M_y = E_z, M_z = -E_y \quad \text{(b)}$$

On the back surface,

$$\vec{J}_S = \hat{y}J_y + \hat{z}J_z \Rightarrow J_y = H_z, J_z = -H_y \quad \text{(a)} \qquad \text{Equation2. 43}$$

$$\vec{M}_S = \hat{y}M_y + \hat{z}M_z \Rightarrow M_y = -E_z, M_z = E_y \quad \text{(b)}$$

To obtain complete source currents for the far-field calculation, Equation2. 39 to Equation2. 43 must be calculated at every FDTD cell on the equivalent closed surface. It is preferable that the magnetic and electric currents should be located at the same position, namely, the center of each Yee's cell surface that touches the equivalent surface S. Because of the spatial offset between the components of the E and H field locations on Yee's cell, averaging of the field components may be performed to obtain the value of the current components at the center location. The obtained surface currents are then used to compute the far-field pattern in the next section.

The obtained equivalent surface currents are used to calculate the far-field radiation pattern, antenna polarization, and radiation efficiency. The first thing in the frequency-domain calculation is to convert the time-domain FDTD data into frequency-domain data using the DFT. For example, the surface current J_y in Equations above can be calculated as following:

$$J_y(u, v, w; f_1) = H_x(u, v, w; f_1) = \sum_{n=1}^{N_{steps}} H_x(u, v, w; n) e^{-j2\pi f_1 n \Delta t} \Delta t \qquad \text{Equation2. 44}$$

Where (u, v, w) is the index for the space location, and n is the time step index. N_{steps} is the maximum number of the time steps used in the time-domain simulation. Similar formulas can be applied in calculating other surface currents. Therefore, the frequency-domain patterns are calculated after all the time steps of the FDTD computation is finished. For a cubic imaginary box with $N \times N$ cells on each surface, the total required storage size for the surface currents is $4 \times 6 \times N_2$. Note that the frequency-domain data in equation have complex values. If radiation patterns at multiple frequencies are required, a gaussian pulse excitation is used in the FDTD simulation. For each frequency of interest, the DFT in Equation2. 44 is performed with corresponding frequency value. One round of FDTD

simulation is capable to provide surface currents and radiation patterns at multiple frequencies.

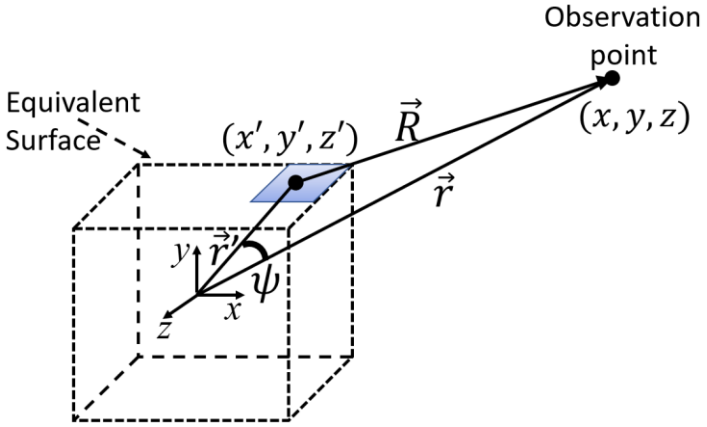

Figure2. 13 The equivalent surface current source and far field

For radiation problems, a vector potential approach is well developed to compute the unknown far fields from the known electric and magnetic currents. A pair of vector potential is defined as following:

$$\vec{A} = \frac{\mu_0 e^{-jkR}}{4\pi R}\vec{N} \qquad \text{(a)} \qquad \text{Equation2. 45}$$

$$\vec{F} = \frac{\varepsilon_0 e^{-jkR}}{4\pi R}\vec{L} \qquad \text{(b)}$$

where

$$\vec{N} = \int_S \vec{J}_s e^{-jkr'cos(\psi)} dS' \qquad \text{(a)} \qquad \text{Equation2. 46}$$

$$\vec{L} = \int_S \vec{M}_s e^{-jkr'cos(\psi)} dS' \qquad \text{(b)}$$

As illustrated in Figure2. 13, the vector $\vec{r} = r\hat{r}$ denotes the position of the observation point (*x*, *y*, *z*), whereas the vector $\vec{r}' = r'\hat{r}'$ denotes the position of source point (*x'*, *y'*, *z'*) on the surface S. The vector $\vec{R} = R\hat{R}$ is between the source point and the observation point, and the angle ψ respresnts the angle between $\vec{r}$ & $\vec{r}'$. In the far-field calculation, the distance R is approximated by

$$R = \sqrt{r^2 + (r')^2 - 2rr'cos(\psi)} = \begin{cases} r - r'cos(\psi) & for\ the\ phase\ term \\ r & for\ the\ amplitude\ term \end{cases} \qquad \text{Equation2. 47}$$

The computation of the components of E and H in the far fields can then be obtained using the vector potentials, which are expressed as:

$$E_r = 0 \quad \text{(a)} \qquad \text{Equation2. 48}$$
$$E_\theta = -\frac{jke^{-jkr}}{4\pi r}\left(L_\phi + \eta_0 N_\theta\right) \quad \text{(b)}$$
$$E_\phi = +\frac{jke^{-jkr}}{4\pi r}\left(L_\theta - \eta_0 N_\theta\right) \quad \text{(c)}$$
$$H_r = 0 \quad \text{(d)}$$
$$H_\theta = +\frac{jke^{-jkr}}{4\pi r}\left(N_\phi - \frac{L_\theta}{\eta_0}\right) \quad \text{(e)}$$
$$H_\theta = -\frac{jke^{-jkr}}{4\pi r}\left(N_\theta + \frac{L_\phi}{\eta_0}\right) \quad \text{(f)}$$

When the closed surface S is chosen as in Figure2. 10, the equivalent surface currents are computed based on Equation2. 39 to Equation2. 41, and the DFT in Equation2. 44 is performed to obtain frequency-domain components, the auxiliary function N and L are calculated as:

$$N_\theta = \int_S \left(J_x cos(\theta)cos(\phi) + J_y cos(\theta)sin(\phi) - J_z sin(\theta)\right)e^{jkr' cos(\psi)}dS' \qquad \text{Equation2. 49}$$

$$N_\phi = \int_S \left(-J_x sin(\phi) + J_y cos(\phi)\right)e^{jkr' cos(\psi)}dS' \qquad \text{Equation2. 50}$$

$$L_\theta = \int_S \left(M_x cos(\theta)cos(\phi) + M_y cos(\theta)sin(\phi) - M_z sin(\theta)\right)e^{jkr' cos(\psi)}dS' \qquad \text{Equation2. 51}$$

$$L_\phi = \int_S \left(-M_x sin(\phi) + M_y cos(\phi)\right)e^{jkr' cos(\psi)}dS' \qquad \text{Equation2. 52}$$

By substituting the Equation2. 49 − Equation2. 52 into the Equation2. 48, the far-field pattern can be obtained at any observation point (r, θ, ϕ).

The E and H fields which are calculated in Equation are linearly polarized (LP) components. In some antenna applications such as satellite communications, it is desired to obtain circularly polarized (CP) field components. This can be done through unit vector transformations between LP and CP components, such that:

$$\hat{\theta} = \hat{\theta} - j\frac{\hat{\phi}}{2} + \hat{\theta} + j\frac{\hat{\phi}}{2} = \frac{\hat{E}_R}{\sqrt{2}} + \frac{\hat{E}_L}{\sqrt{2}} \qquad \text{Equation2. 53}$$
$$\hat{\phi} = \hat{\theta} + j\frac{\hat{\phi}}{2j} - \hat{\theta} - j\frac{\hat{\phi}}{2j} = \frac{\hat{E}_L}{j\sqrt{2}} - \frac{\hat{E}_R}{j\sqrt{2}}$$

Where $\hat{E}_R$ and $\hat{E}_L$ are unit vectors for the right-hand circular polarized (RHCP) field and left-hand circularly polarized (LHCP) field. Substituting Equation2. 53 into Equation2. 48, we obtain

$$\vec{E} = \hat{\theta}E_\theta + \hat{\phi}E_\phi = \left(\frac{\hat{E}_R}{\sqrt{2}} + \frac{\hat{E}_L}{\sqrt{2}}\right)E_\theta + \left(\frac{\hat{E}_L}{j\sqrt{2}} - \frac{\hat{E}_R}{j\sqrt{2}}\right)E_\phi \quad \text{(a)} \qquad \text{Equation2. 54}$$
$$= \hat{E}_R\left(\frac{E_\theta}{\sqrt{2}} - \frac{E_\phi}{j\sqrt{2}}\right) + \hat{E}_L\left(\frac{E_\theta}{\sqrt{2}} + \frac{E_\phi}{j\sqrt{2}}\right) = \hat{E}_R E_R + \hat{E}_L E_L$$

$$E_R = \frac{E_\theta}{\sqrt{2}} - \frac{E_\phi}{j\sqrt{2}} \quad \text{(b)}$$
$$E_L = \frac{E_\theta}{\sqrt{2}} + \frac{E_\phi}{j\sqrt{2}} \quad \text{(c)}$$

The magnitudes of the RHCP component *(E_R)* and the LHCP component (E_L) are then obtained. The axial ratio is defined to describe the polarization purity of the propagating waves and is calculated as follows:

$$AR = -\frac{|E_R|+|E_L|}{|E_R|-|E_L|} \qquad \text{Equation2. 55}$$

For an LP (Linear Polarized) wave, AR goes to infinity. For RHCP wave $AR = -1$ and for an LHCP wave $AR = 1$. For a general elliptically polarized wave, $1 \leq |AR| \leq \infty$. Other expressions for direct computation of the AR from the far-field components E_θ and E_ϕ are given in

$$AR = 20\,log_{10}\left(\frac{\left[\frac{1}{2}\left(E_\phi^2+E_\theta^2+\left[E_\theta^4+E_\phi^4+2E_\theta^2E_\phi^2cos(2\delta)\right]^{\frac{1}{2}}\right)\right]^{\frac{1}{2}}}{\left[\frac{1}{2}\left(E_\phi^2+E_\theta^2+\left[E_\theta^4+E_\phi^4-2E_\theta^2E_\phi^2cos(2\delta)\right]^{\frac{1}{2}}\right)\right]^{\frac{1}{2}}}\right) \qquad \text{Equation2. 56}$$

And

$$R = 20\,log_{10}\left(\frac{|E_\phi|^2 sin^2(\tau)+|E_\theta|^2cos^2(\tau)+|E_\phi||E_\phi|cos(\delta)sin(2\tau)}{|E_\phi|^2 sin^2(\tau)+|E_\theta|^2cos^2(\tau)-|E_\phi||E_\phi|cos(\delta)sin(2\tau)}\right) \qquad \text{Equation2. 57}$$

Where

$$2\tau = tan^{-1}\left(\frac{2|E_\phi||E_\phi|cos(\delta)}{|E_\theta|^2-|E_\phi|^2}\right)$$

δ is the phase difference between E_θ and E_ϕ.

The radiation efficiency is a very important indication for the effectiveness of an antenna which can also be obtained using the FDTD technique. First, the radiation power of antenna is obtained by applying the surface equivalence theorem to obtain:

$$P_{rad} = \frac{1}{2}Re\left\{\int_S \vec{E}\times\vec{H}^*\cdot\hat{n}dS'\right\} = \frac{1}{2}Re\left\{\int_S \vec{J}*\times\vec{M}\cdot\hat{n}dS'\right\} \qquad \text{Equation2. 58}$$

The delivered power to an antenna is determined by the product of the voltage and current provided from the voltage source and can be expressed as:

$$P_{del} = \frac{1}{2}Re\{V_s(\omega)I_s^*(\omega)\} \qquad \text{Equation2. 59}$$

Where $V_s(\omega)$ and $I_s(\omega)$ represent the Fourier transformed values of the source voltage and current. The antenna's radiation efficiency η_a is then defined as:

$$\eta_a = \frac{P_{rad}}{P_{del}} \qquad \text{Equation2. 60}$$

Summary

The Finite Difference Time Domain Method has been briefly discussed. The basic equations such as Maxwell's curl equations and finite difference equations are shown in Chapter 2. From these equations, the finite difference of electric field and magnetic field are created. The representation of electric and magnetic field in space and time are also shown, which is equivalent to the grid systems in commercial simulation software. In addition, important components which are used to calculate the characteristics of antenna are also shown. Concepts of Finite Difference Time Domain Methods, which are briefly discussed in Chapter 2, will be used as basis to comprehend and to unitize the commercial simulation software (sim4Life) effectively and efficiently.

CHAPTER 3
Leaf-Shaped Bowtie Antenna for UWB Application

3.1 Abstract

In Chapter 3, characteristics of wideband antenna will be presented. In addition, concept of self-complementary antenna, which is basic of wideband antenna, will be shortly discuss. From this concept, leaf-shaped bowtie antenna, which is a finite shape of self-complementary antenna, is briefly reviewed. Furthermore, leaf-shaped bowtie slot antenna which is complementary structure of leaf-shape bowtie antenna will also be discussed. Both single and array configuration of leaf-shaped bowtie and leaf-shaped bowtie slot antenna, which has been designed for use in UWB communication systems, are presented. Finally, instead of using microstrip tapered line as feeding circuit, quarter wavelength matching circuit has been proposed to as feeding-circuit of leaf-shaped bowtie slot antenna.

3.2 Introduction of Self-Complementary Antenna

An antenna with a self-complementary structure has a constant input impedance, independently of the source frequency and shape of the structure. The practical realization of such a structure, and an explanation of the remarkable principle of constant impedance, were accomplished by Yatsuto Mushiake [32]. So far, various types of self-complementary structures have been developed successively. The principle of self-complementary antennas has been introduced into the investigation of extremely broad-band, or frequency-independent antennas, which leads to the development of log-periodic antenna and log-periodic dipole array. The intensive development studies were carried out at Tohoku University and other institutions in Japan, to investigate other types of self-complementary antenna.

In this connection, it should be noted that the log-periodic structure does not automatically ensure frequency-independent characteristics for antennas, as explained in The IEEE Standard Dictionary of Electrical and Electronics Terms, although self-complementary structures and their modifications do guarantee the constant impedance of antenna. This mean that the broadband characteristics of the log-periodic antenna have their origin not in the log-periodic shape, but rather those aspects of the shape that are derived from the self-complementary antenna. However, since the self-complementary property of antenna focused extremely on broad-band nature of its radiation properties, information about the radiation characteristics of other existing antenna must be considered of practical broad-band antennas are to be developed. In addition, self-complementary antennas have infinitely extended structures; therefore, it must be truncated in order to use in real application. Thus, the reduction of the effects of truncation is very important in practice. Experimental “hardware designs” studies are therefore usually needed for this purpose.

Properly arranged log-periodic structures have various well-known merits as extremely broadband antennas. Reduction of truncation effects, mentioned above, can be achieved satisfactorily for log-periodic structures, as for other cases of "teeth-type" array structures in general. The self-complementary planar structure is the shape of the original sheet structure which is identical to the shape of its complementary planar structure. In other words, the self-complementary structure is a structure that is complementary to the original structure itself. As a natural consequence of the self-complementary configuration of the structure, the input impedance Z_1 of the original structure is identical to that of its complementary structure Z_2, and they have a common value Z that is:

$$Z_1 = Z_2 = Z \qquad \text{Equation3. 1}$$

$$Z = \frac{Z_0}{2}$$

$$Z_0 = 120\pi \quad (free\ space\ impedance)$$

$$Z_1 = Z_2 = \frac{120\pi}{2} = 60\pi$$

Therefore, the input impedance of self-complementary antenna is equal to half of free space which is $Z \approx 60\pi \approx 188\Omega$. The input impedance of the self-complementary planar structure is always constant whatever the source frequency and shape of the structure. Therefore, the constant-impedance property of self-complementary structures provides an important and effective technological guidance principle for development and investigations of extremely broad-band practical antenna. In practice, the principle can be extended from the basic structure to various other case having rather more complicated structure. For this reason, the fundamental Principle of self-complementary can be extensively applied in a broad sense. Some examples of self-complementary antennas corresponding to the two fundamental types are shown in Figure3. 1 and Figure3. 2. The structures in Figure3. 1 (a) and Figure3. 2 (b) are rotationally symmetric, and they work as balanced-type constant-impedance antennas. In contrast, the structure in Figure3. 2 is axially symmetric, and it works as an unbalanced-type constant-impedance antenna.

Figure3. 1 Balanced type of self-complementary planar antenna (Z≈60π)

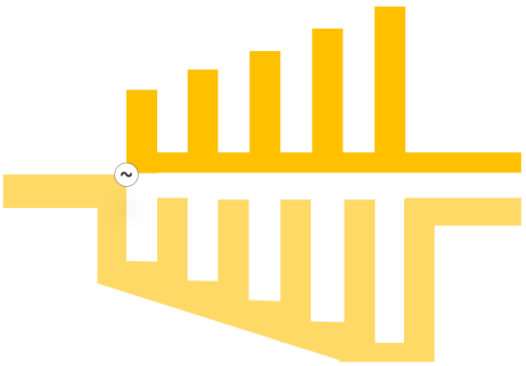

Figure3. 2 Unbalance type of self-complementary planar antenna (Z≈60π)

3.3 Double-Sided Leaf-Shaped Bowtie Antenna for UWB Application

Double-sided leaf-shaped bowtie slot antenna has been proposed in [33]. The antenna structure has omnidirectional over the frequency range of 3.0GHz to 11.5GHz. The purpose of using doble-sided leaf-shaped bowtie antenna in [33] instead of dipole is to achieve wideband characteristics. The design of antenna element is based on the theory of self-complementary. The infinite structure of ideal self-complementary is truncated into a practical radiating element. If self-complementary is maintained around the feeding point of radiating elements, various kinds of shapes can be adopted for the truncated part of the radiating element. Therefore, leaf-shaped element was designed. Two leaf-shaped elements are arranged on upper and lower surfaces of a dielectric substrate. Each element is excited by a tapered microstrip line. From both simulated and measured results, −10dB impedance bandwidth occupies frequency range of 4.5GHz to 15.0GHz. The realized gain is −1dBi to 3dBi over the frequency range of 3.0GHz to 11.5GHz. This bandwidth fulfills the UWB bandwidth approved by FCC.

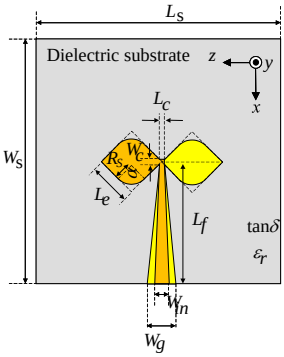

Antenna parameters

W_s[mm]	L_s[mm]	h[mm]	ε_r	$\tan\delta$
40	55	0.762	2.17	0.0009

R_s[mm]	α[deg]	L_e[mm]	W_c[mm]	L_c[mm]
7.1	90	12	0.2	0.2

W_{in}[mm]	W_g[mm]	L_f[mm]	L_a
2.4	12	45	$2\sqrt{2}L_e$

Figure3. 3 Leaf-shaped bowtie antenna with microstrip tapered line as feeding circuit

Double-sided leaf-shaped bowtie antenna with flat reflector has been proposed in [34]. The purpose of adding flat reflector is to make radiation pattern unidirectional. However, the −3dB gain bandwidth are depending on the separation between reflector and dielectric

substrate. The optimization of separation between reflector and dielectric substrate are performed with Finite Different Time Domain analysis (FDTD) to determine the separation which realize the widest −3dB gain bandwidth. The −3dB gain bandwidth is defined as the relative bandwidth between the two frequencies at which the antenna gain degrades by 3dB from the maximum gain. The requirement for achieving a practical UWB antenna is that the null in the gain does not exist in the desired bandwidth. The separation between dielectric substrate and flat reflector is chosen from 3mm to 15mm with sampling point of 1mm. To minimize the diffraction effect from the reflector edges as much as possible, the reflector dimensions W_{ref} and L_{ref} are both set to 300mm, which is about three times longer than the wavelength at 3.1GHz. The maximum bandwidth of 96% is obtained at the separation of 9mm to 10mm.

The maximum gain of the antenna without reflector is 3.4dBi, whereas the maximum gain of antenna with reflector is 7.8dBi. The maximum gain has been improved around 4.4dB by placing the reflector with a separation of 9mm under dielectric substrate. The dimension of reflector is chosen to be larger than antenna substrate is to avoid any degradation caused by the diffraction wave.

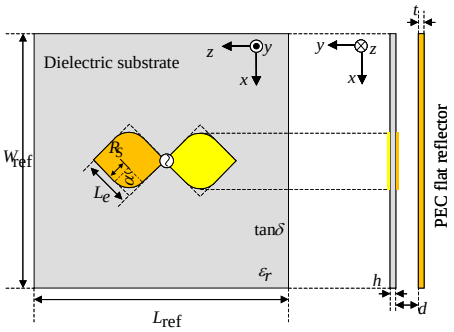

Figure3. 4 Reflector backed leaf-shaped bowtie antenna with delta-gap as feeding source

In the previous configuration, the delta-gap feed model was employed for FDTD calculations. Since the delta-gap feed model is an idealized feeding technique, a practical feeding circuit is needed to supply power to the antenna [34].

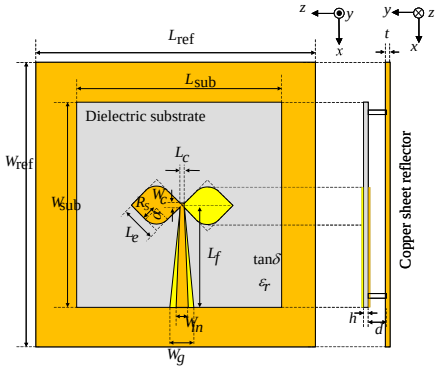

Figure3. 5 Reflector backed leaf-shaped bowtie antenna with microstrip tapered line feeding

Double-sided leaf-shaped bowtie antenna backed by a mushroom-type electromagnetic band gap (EBG) has been proposed in [35]. The flat reflector from the previous model has been replaced by EBG. The EBG reflector is composed of a periodic 9×9 array of square patches printed on a dielectric substrate having the thickness of *h*. Each patch is connected to the ground plane through metal via whose diameter is *r*. The dimension and substrate permittivity of EBG are the same as those of the antenna substrate. The parameters of the radiating elements and feeding circuit are optimized for operating in the UWB frequency band (3.1-10.6GHz) which is the same as the previous case. The performances of the double-sided leaf-shaped bowtie antenna backed by the EBG reflector are evaluated by the FDTD analysis and measurements. The measured reflection coefficient is less than −10dB over the frequency range from 6.4 to 9.0GHz. On the other hand, the simulated reflection coefficient is larger than −10dB around 7.5GHz to 9.0GHz. Unidirectional radiation patterns are obtained over the frequency band of 5GHz to 9GHz. On the other hand, the deterioration of the radiation patterns in both E-planes and H-planes are observed at 10GHz. Especially, the H-plane pattern contains many lobes and nulls. To investigate the mechanism for the deterioration of the radiation patterns, current distributions on the patches of the EBG reflector are simulated. For this case, unwanted radiation pattern is generated by the patches of the EBG reflector. This results in the degradation of the radiation pattern described above.

The maximum gain of about 10dBi is obtained at 7.5GHz. −3dB gain bandwidth occupies the frequency range from 6GHz to 8.7GHz, which is about 2.7GHz gain bandwidth. It is found in [35] that the reflection phase of the EBG at these frequencies are 135° and -45°, respectively. These results imply that the −3dB gain bandwidth can be estimated by finding the frequency region of the reflection phase in the range of 90° ± 45°. It is confirmed that low-profile unidirectional antenna having wideband characteristics can be realized by placing the leaf-shaped bowtie antenna parallel to the EBG reflector at distance of less than a quarter wavelength. The maximum gain of about 10dBi is obtained around the frequency at which the zero-degree reflection phase of EBG occurs.

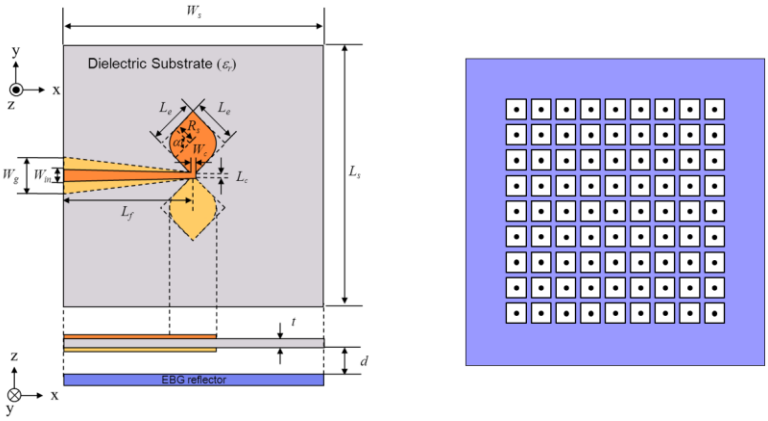

Figure3. 6 Electromagnetic band gaps backed leaf-shaped bowtie antenna

3.4 Array of Double-Sided Leaf-Shaped Bowtie Slot Antenna for UWB Application

An array of 2 double-sided leaf-shaped bowtie antennas has been proposed in [36]. Two double-sided leaf-shaped bowtie antennas are arranged on upper and lower surfaces of a dielectric substrate with thickness h=0.762mm, dielectric constant ε_r=2.17, and tanδ=0.0009. A flat reflector with thickness of 0.5mm is placed under dielectric substrate at separation of 9mm to make radiation pattern unidirectional. The spacing between each antenna element is 18mm. The double-sided leaf-shaped bowtie radiating elements are excited by a tapered microstrip line and microstrip line T-junction. The actual gain of 2 double-sided leaf-shaped bowtie antennas array is from 8.5dBi to 11.5dBi at the maximum radiation direction over the frequency bandwidth of 4.3 to 11.0GHz. The −3dB gain bandwidth is 87% (from 4.3GHz to 11.0GHz). The cross-polarization level is less than 15dB within HPBW in the frequency range of 4.0GHz to 9.0GHz.

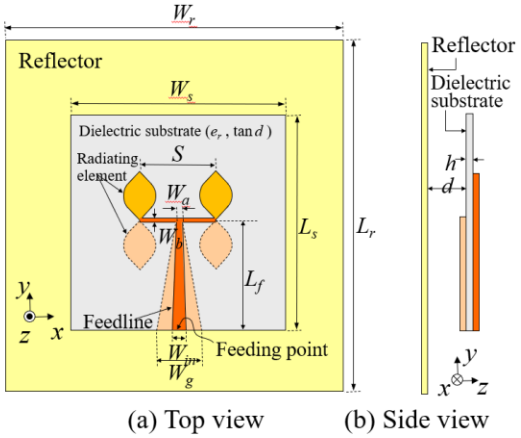

Figure3. 7 Array of 2 leaf-shaped bowtie antenna with reflector

An array of 4 double-sided leaf-shaped bowtie antennas for use in UWB has been proposed in [37]. The purpose of increasing the number of radiating elements is to increase gain in broadside direction. The separation between the antenna substrate and reflector *d* and the element spacing *S* are set to 9mm and 18mm, respectively. From [37], the widest −3dB gain bandwidth was obtained at d=9mm and S=18mm. The double-sided leaf-shaped bowtie antenna are excited by a tapered microstrip line and a two-stage microstrip line T-junction. From [6], the reflection is almost less than −10dB and the measured results and the calculation results are in good agreement. The proposed linear array of 4 double-sided leaf-shaped bowtie antenna can offer actual gain of 10.3dBi to 13.3dBi at maximum radiation direction over the frequency bandwidth of 4.1GHz to 11.0GHz (−3dB gain bandwidth is 91%).

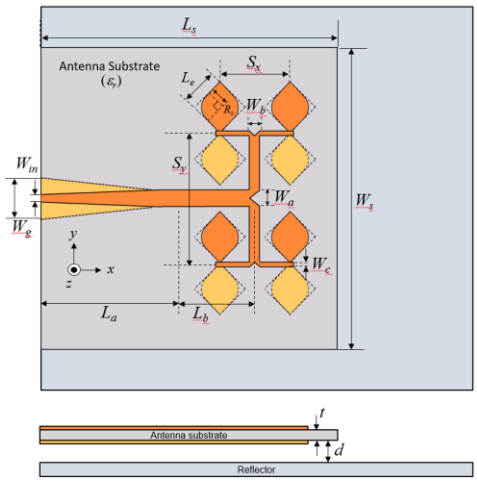

Figure3. 8 Array of 4 leaf-shaped bowtie antenna with reflector

3.5 Leaf-Shaped Bowtie Slot Antenna for UWB Application

Leaf-shaped bowtie slot antenna, which is a complementary structure of double-sided leaf-shaped bowtie antenna, has been proposed in [38] for use in UWB application. In the first place, the antenna having the operating frequency band from 7GHz to 10GHz (UWB high band in Japan) is designed, and its reflection coefficient is evaluated for the case when the feeding point is arranged in the center portion of the antenna. Based on the evaluated results, a feeding circuit for the proposed antenna is designed. Antenna characteristics for the case with the feeding circuit are evaluated with FDTD analysis and measurements to confirm the effective performance of the proposed configuration.

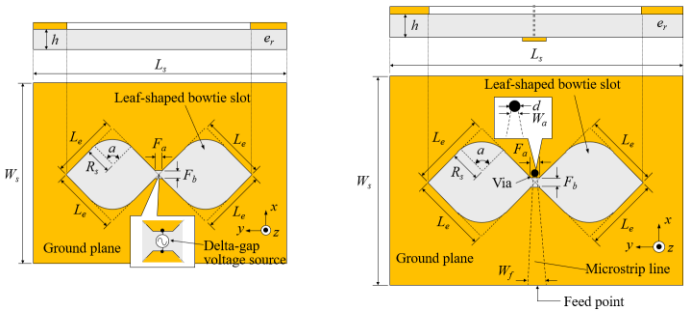

Figure3. 9 Leaf-shaped bowtie slot antenna with delta gap voltage source and microstrip feeding circuit

The actual gain is ranging from 3dBi to 5dBi over the frequency band from 7GHz to 10GHz. By using linearly tapered microstrip line to feed leaf-shaped bowtie slot antenna, the −10dB impedance bandwidth is within frequency range from 6.0GHz to 10.3GHz, and the actual gain ranging from 3dBi to 5dBi over the frequency band from 7GHz to 10GHz is obtained.

Leaf-shaped bowtie slot antenna electromagnetically fed by microstrip line has been proposed in [39] for use over the frequency band of 7GHz-10GHz. In this configuration, electromagnetic coupling has been used to replace conductor probe in the connection between microstrip line and antenna ground plane. A strip conductor of a microstrip line is placed on the bottom side of the dielectric substrate. The feeding point of radiating slot are excited by electromagnetic fields propagating along the microstrip line. The strip conductor is terminated in an open-circuited stub beyond the center portion of the radiating slot. The length L_f of the open-circuited stub is chosen to be approximately a quarter wavelength at the center frequency of the design frequency band in order to realize the efficient excitation of the radiating slot. In this model, a linear tapered microstrip line is employed in order to achieve 50Ω impedance matching between antenna load impedance and input port impedance as shown in [39]. Simulated and measured reflection coefficient of antenna structure is shown in [8]. The measured and calculated results are in good agreement. As for the measured result, the reflection is less than −10dB over the frequency range from 6.0GHz to 12GHz, and the maximum gain of about 7.5dBi is obtained around 9.5GHz.

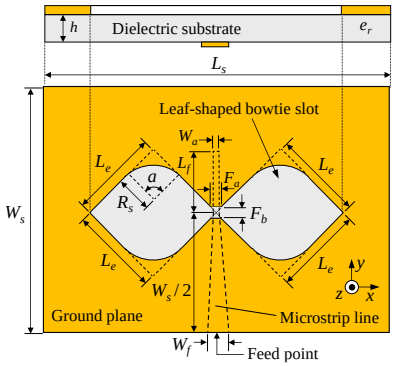

Figure3. 10 Leaf-shaped bowtie slot antenna electromagnetically fed by microstrip line [39]

3.6 Leaf-Shaped Bowtie Slot Antenna Array for UWB Application

An array of 4 leaf-shaped bowtie slot antennas has been proposed in [40] for use over the frequency range of 7GHz-10GHz (UWB high band in Japan). 4 leaf-shaped bowtie slot antennas are linearly aligned along the *x*-axis. The side lengths of the substrate are designed as L_s and W_s. The radiating elements are placed with the separation of *S*. The element spacing of S=24mm is determined that the grating lobes don't appear in the *xz*-plane pattern over the frequency band of 7-10GHz. In the designed antenna array, the corporate feed configuration is employed to excite the radiating elements with the equal amplitude and the equal phase. As shown in Figure3. 11, the antenna feeding circuit is composed of microstrip lines and three pairs of T-junctions. These components are arranged on the bottom side of the dielectric substrate. Over the frequency band of 7-10GHz, the actual gain is 10.7-13.3dBi and 10.1-12dBi for the simulation and measurement, respectively. It is seen that the gain of the antenna array is increased by 5dB in comparison with that of the single element Figure3. 9.

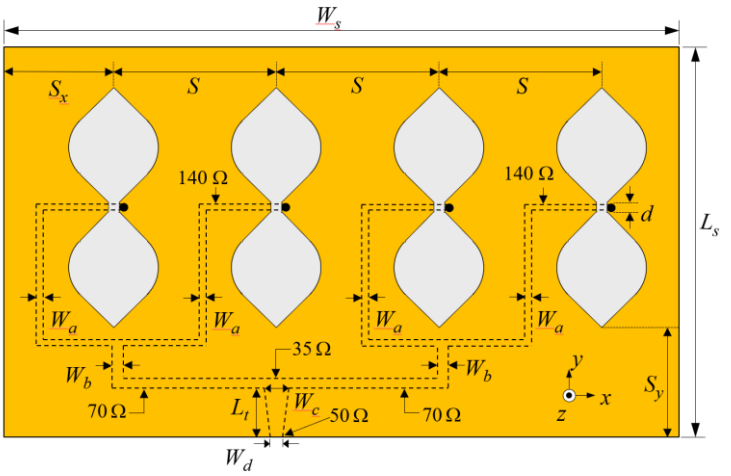

Figure3. 11 Linear array of 4 leaf-shaped bowtie slot antenna

Literature review of research progress of double-sided leaf-shaped bowtie and leaf-shaped bowtie slot antenna from section3.3 to section3.6 show that structure of the leaf-shaped bowtie slot antenna is less complexity than structure of double-sided leaf-shaped bowtie antenna. In structure of double-sided leaf-shaped bowtie antenna, the leaf-shaped element must be printed on both side of dielectric substrate, which could easily cause the error during the fabrication. On the hand, the feeding circuit of the double-sided antenna must be printed on both sides of substrate, which could cause error during fabrication and high complexity in a large-scale array. However, to create leaf-shaped bowtie slot antenna, only one side of dielectric substrate is cut into slot antenna. The feeding circuit is constructed only on the other side of substrate. Both antenna structures offer a high gain over a wide bandwidth although leaf-shaped bowtie slot antenna has more advantages in large scale array. The feeding circuit of leaf-shaped slot antenna can be constructure in the form simple linear microstrip line on the other side of substrate. More importantly, in case of large-scale array structure for use in high frequency, the element size and microstrip line width will be small. Therefore, the fabrication of leaf-shaped bowtie slot antenna is much more convenience that the fabrication of double-sided leaf-shaped bowtie antenna. The possibility of using leaf-shaped bowtie slot antenna at high frequency in array configuration will be further studies.

3.7 Reflector Backed Leaf-Shaped Bowtie Slot Antenna Using Quarter-Wave Transformer

High frequency band of millimeter wave and terahertz band will be utilized to increase transmission data rate and capacity. In order to cover the area with radio waves in these frequency bands that require line of sight communication, it is necessary to use antenna array with a large number of antenna element. In order to efficiently implement such a distributed antenna system in society, it is necessary that the overhanging radio station can be shared regardless of the frequency band, and a wideband antenna is essential for its realization. As wideband antenna can be applied to high frequency bands such as microwave and millimeter-wave bands, dipole antenna has been used in [33][34][41][42]. The leaf-shaped bowtie slot

antenna, whose characteristics have been clarified in [38], has also been used in [40]. Theses antennas are type of self-complementary antenna, which has a constant input impedance regardless of frequency, with finite dimensions. Therefore, these antennas are operating as planar wideband antennas. To create a leaf-shaped bowtie antenna, two squares with side length L_e are rounded at two corners with curve line with radius R_s and are arranged at both sides of dielectric substrate. The leaf-shaped bowtie slot antenna is complementary structure of the leaf-shaped bowtie antenna. These wideband antennas are expected to be applied to overhanging radio stations in the array antenna systems. Leaf-shaped bowtie antenna needs a balanced feeding circuit, and the radiating element and feeding circuits must be arranged on both side of the dielectric substrate, so that the structure is complicated when using in the array structure. Therefore, leaf-shaped bowtie antenna is considered unsuitable for large scale array. In the case of leaf-shaped bowtie slot antenna, radiating slot and feeding circuit can be individually constructed on the front and back of dielectric substrate. Therefore, it is easy to make a large-scale array by using leaf-shaped bowtie slot antenna as radiating element.

The leaf-shaped bowtie slot antenna is bidirectional radiation pattern wideband antenna. However, in the application of distributed antenna systems to overhanging radio stations, it is considered necessary to make them unidirectional. As a method for making a bidirectional antenna to become a unidirectional, a reflector made of plate-shaped conductor is placed on the back of the antenna, and the distance between the reflector and the antenna is set to about a quarter of free space wavelength of the operating frequency, the method of doing this is in [43]. Although the radiation pattern of leaf-shaped bowtie slot antenna can be made unidirectional, the input impedance and radiation characteristics will be narrowed due to the influence of the reflector. Based on the above background, the leaf-shaped bowtie slot antenna with a flat reflector is designed in consideration of the influence of the reflector. Although the reflector is added, the wide band characteristics of various antenna structure is still possible. Since the leaf-shaped bowtie slot antenna has a high input impedance of about 180Ω, a matching circuit is required to obtain matching with general characteristics impedance of 50Ω [44]. In [43][44][45], tapered microstrip line has been use the matching circuit. On the other hand, it is possible to obtain double resonance characteristics by feeding an antenna with high input impedance through a transmission line having a length of about a quarter of wavelength, thereby widening the impedance characteristics. From [46][47], a quarter wavelength matching circuit is adopted as the matching circuit of the leaf-shaped bowtie slot antenna with a reflector.

3.7.1 Structure of Leaf-Shaped Bowtie Slot Antenna

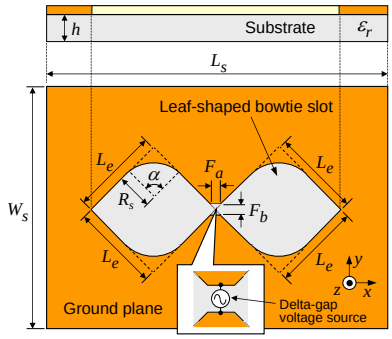

Figure3. 12 Structure of leaf-shaped bowtie slot antenna

Table3. 1 Structural parameters of leaf-shaped bowtie slot antenna

W_s [mm]	L_s [mm]	h [mm]	L_e [mm]	R_s [mm]
30	60	0.76	12,13,14	$0.6L_e$
ε_r [mm]	F_a	F_b [mm]	α [deg.]	
2.17	1.0	1.0	90	

Figure3. 12 shows the structure of the leaf-shaped bowtie slot antenna. A ground conductor plate is provided by substrate with a relative permittivity of ε_r and a thickness of h. This ground conductor plate is provided with an opening (slot element) that operates as radiating element, whose shape is a leaf-shaped bowtie cut with element length L_e and R_s on the ground plane. In order to avoid a short-circuiting, the upper and lower ground conductor surfaces at the center of the slot element, the conductor plate is removed with a $F_a \times F_b$ rectangle at the center of slot element.

In this antenna structure, the lower limit frequency band is determined by the element length L_e of one side of the leaf-shaped bowtie slot element, and it operates in a frequency band higher than this lower limit frequency. Assuming that the free space wavelength at the lower limit frequency of operation is λ_0, the element length L_e of one side of the leaf-shaped bowtie element is given by equation in [34].

$$L_e = \frac{\lambda_0}{4\sqrt{\varepsilon_{re}}} \quad , \quad \varepsilon_{re} \approx \frac{\varepsilon_r + 1}{2} \qquad \text{Equation3. 2}$$

The target antenna operating frequency band is set to 7GHz to 10GHz (comparative bandwidth to the center frequency band of 8.5GHz, 35% factional bandwidth). In order to fully cover this band, lower limit frequency is chosen around 5GHz, and structural parameters are shown as in Table3. 1. The parameter study of element length L_e which is based on reflection coefficient and directivity gain are shown as in following Figure3. 13.

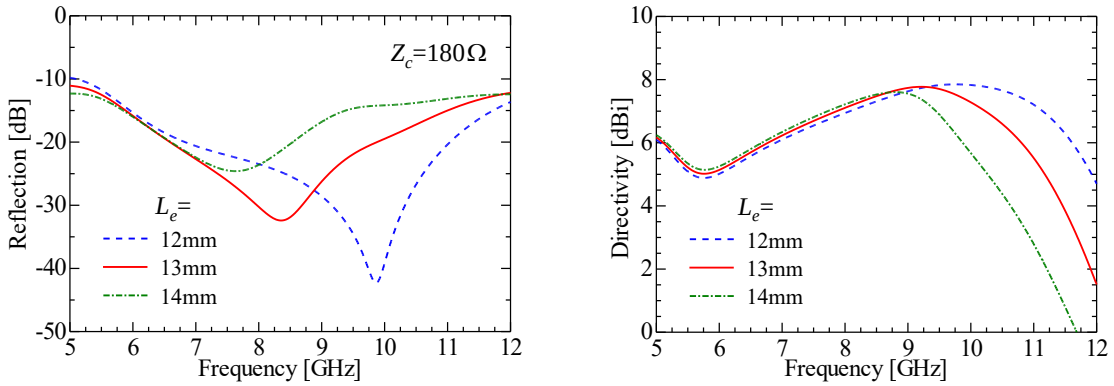

Figure3. 13 Frequency dependence of reflection coefficient amplitude and of directivity of leaf-shaped bowtie slot antenna without reflector by changing L_e

In this structure, the radius of curvature R_s is set to be 60% (R_s=0.6L_e) of the length L_e of one side slot element [44][45]. The operating lower limit frequency corresponding to L_e=12mm, 13mm, and 14mm shown in Table3. 1 are calculated from Equation3. 2 with frequency of 5.0GHz, 4.6GHz, and 4.3GHz, respectively. Regarding to substrate (ground conductor plate) dimension at frequencies where the dimension W_s in E-plane is larger than one wavelength, ripples occur in the shape of the E-plane radiation pattern due to the effect of edge diffraction of the ground conductor plate [44]. In order to avoid the occurrence of E-plane pattern ripple in the designed band, the ground plane dimension W_s is chosen as 30mm which is about one wavelength at the upper limit frequency (10GHz) of the design band. The substrate dimension L_s in the H-plane is chosen to be equal to the two wavelengths (60mm) at the upper limit frequency. The reflection coefficient and directional gain in the maximum direction (+z direction shown in Figure3. 13) of a leaf-shaped bowtie slot antenna with these dimensions are evaluated by FDTD analysis. In the following FDTD analysis, the self-made FDTD analysis program is used. The conductor plate such as antenna and feeding circuit are chosen as perfect conductor. The dielectric loss of the dielectric substrate is not included. In addition, an 8-layer Unsplit PML was placed around the analysis region as absorbing boundary condition, and the antenna to be analyzed is modeled using the unequal-spaced mesh method. The leaf-shaped bowtie element is modeled by staircase approximation with a cell size of Δx=Δy=0.05mm. The analysis area is set as followings. The distance between the surface of the dielectric substrate (ground conductor plate) where the slot element is located and the PML placed above it is 16mm. If there is no reflector, the distance between the bottom surface of dielectric substrate and the PML below the substrate is 16mm. When a reflector is placed on the back of the antenna, distance between reflector and PML placed below is 12mm. The distance between the PML placed around the dielectric substrate and the edge of the substrate is 12 mm in both the case where there is no reflector and the case where the reflector is placed on the back of the antenna. These distances correspond to about 0.3 to 0.4 wavelengths at the lower limit frequency (7 GHz) of the design band and about 0.4 to 0.5 wavelengths at the upper limit frequency (10 GHz). The dimensions of the reflector shall be the same as the dimensions of the dielectric substrate (ground conductor plate). As shown in

Figure3. 12, the delta gap voltage source is employed as excitation source at the center of the leaf-shaped bowtie slot antenna without a reflector. Analysis results from FDTD show that the magnitude of reflection coefficient and of directivity gain in the maximum radiation direction. The frequency characteristics of analysis results are shown in Figure3. 13. The reflection coefficient is calculated with reference impedance of $60\pi \approx 180\Omega$, which is an input impedance of self-complementary antenna. The magnitude of reflection coefficients shown in Figure3. 13 is less than −10dB over the entire target operating frequency band (7GHz to 10GHz) for all slot dimensions of L_e=12mm, 13mm, and 14mm. It can be confirmed that the reflection coefficient is optimized. The reflection coefficient amplitude is minimized near 8.5 GHz, which is the center frequency of the same band, when the slot size is L_e = 13 mm. From the frequency characteristics of the directional gain shown in Figure3. 13, the directivity gain (6.1 to 6.4 dBi) is almost the same for all slot dimensions at 7 GHz, which is the lower limit of the design band, but the characteristic is different at 10 GHz, which is the upper limit of the design band. It can be seen that the larger dimension offers lower gain. Based on the above results, in the following examination, The optimum dimensions of the leaf-shaped bowtie slot antenna are L_e = 13 mm and R_s = 7.8 mm, where magnitude of reflection coefficient is the minimum near the center frequency of 8.5 GHz in the design band and the directivity gain is maximum (7.8 dBi) near the same frequency.

3.7.2 Structure of Leaf-Shaped Bowtie Slot Antenna with Reflector

A leaf-shaped bowtie slot antenna is “bidirectional antenna” that radiates from both sides of the antenna. For practical use, it is necessary to make radiation pattern “unidirectional” that radiates only in one direction. Therefore, the unidirectional radiation is considered by arranging a reflector on the back if the leaf-shaped bowties slot antenna which is designed in previous section3.7.1. The effect of reflector on antenna must be consider, specifically the separation between dielectric substrate and reflector. A method of arranging conductor flat plates as reflectors at appropriate intervals on the back surface of the antenna is widely used [34][41][47][48]. In the case of a bidirectional antenna that operates at a single frequency, the distance between antenna and reflector is chosen around quarter of free space wavelength at operating single frequency [48]. Even a wideband bidirectional antenna such as a leaf-shaped bowtie slot antenna can be made unidirectional by arranging a reflector on the back of antenna. However, since it is a wideband antenna, the distance between the antenna and the reflector cannot be chosen as a quarter of free space wavelength, so that the distance between reflector and substrate must be optimized based on reflection coefficient magnitude and directivity. Sideview of antenna structure with reflector is shown as in following Figure3. 14.

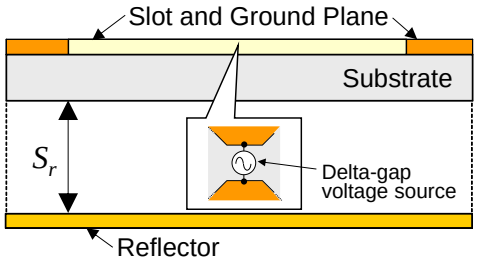

Figure3. 14 Reflector backed leaf-shaped bowtie slot antenna

The analysis results of directivity and reflection coefficient regarding to the separation (S_r) between reflector and antenna substrate are analyzed. The leaf-shaped bowtie slot antenna has the same structure as in section3.7.1. Reflector has the same size as antenna dielectric substrate. The appropriate separation S_r is obtained by performing parameter study based on analysis result of reflection coefficient and directivity from FDTD simulation. In the following numerical simulation (FDTD analysis), it is assumed that the antenna conductor and reflector is lossless material (conductivity is infinite), and the dielectric loss of the substrate is not included.

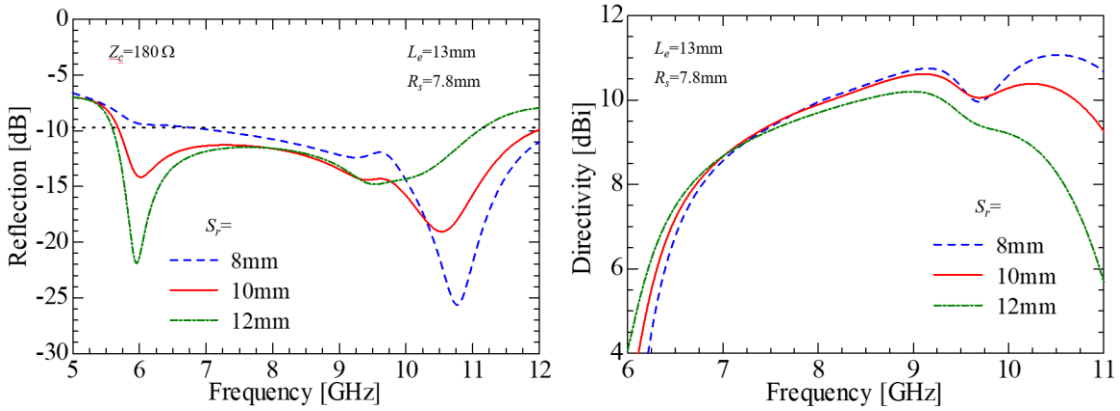

Figure3. 15 Frequency dependence of reflection coefficient amplitude and directivity for leaf-shaped bowtie slot antenna with reference impedance of 180Ω

Based on the examination results in the previous section, the antenna structure shown in Figure3. 12 in which a delta gap voltage source is employed as an excitation source to the center of a leaf-shaped bowtie slot antenna with a reflector whose element dimensions are L_e=13mm and R_s=7.8mm. The frequency characteristics of the reflection coefficient magnitude and the directional gain in the maximum radiation direction when the separation S_r is chosen as 8mm, 10mm, and 12mm are obtained by performing FDTD analysis. The analysis results are shown in Figure3. 15, which are the reflection coefficient is evaluated with reference impedance of 180Ω, as in previous section. The separation S_r of 8mm, 10mm, and 12mm corresponds to a quarter wavelength at 9.4GHz, 7.5GHz, and 6.3GHz, respectively. From Figure3. 15, the magnitude of reflection coefficient when S_r=8mm is larger over the entire design band than when S_r=10mm. In addition, the directivity at the

lower limit frequency of 7GHz of the design band is the same (8.7dBi) regardless of the reflector spacing. In contrast, when S_r is chosen as 12mm, the directivity is decreasing at higher frequency of target band. Based on the above results, S_r=10mm is considered as the most appropriate reflector spacing from the viewpoint of reflection coefficient magnitude and directivity gain in the target band. The directional gain in this case has maximum value of 10.6dBi near 9GHz, which is 1.2dB higher than the maximum gain (7.8dBi) of antenna without reflector as shown in Figure3. 12 in pervious section3.7.1. Regarding to the directional gain shown in Figure3. 15, the gain drops around 9.7GHz. The reason for this drop could be caused by the effect of resonance of the parallel plate structure consisting of the ground conductor surface of the dielectric substrate and the reflector. The resonance frequency f_{mn} when the structure is shown in Figure3. 14 is regarded as a parallel plate resonator is given by the following equation:

$$f_{mn} = \frac{C_0}{2}\sqrt{\left(\frac{m}{L_s}\right)^2 + \left(\frac{n}{W_s}\right)^2} \qquad \text{Equation3. 3}$$

C_0 is the speed of light in free space, L_s and W_s are the dimensions of substrate and reflector, and m and n are positive integer. When L_s=60mm, W_s=30mm, m=0, n=2 in (Equation3. 3), the resonance frequency is 9.9GHz, which is almost equal to the frequency at which the gain drops, so it is caused by arranging the reflector. It is considered that the effect of resonance causes disturbance of radiation directivity, which causes a decrease in gain. As a countermeasure to avoid such a gain decrease, a method of adjusting the ground plane dimension (W_s) is adopted, so that the resonance frequency of the parallel plate structure is outside the design band of the antenna be considered.

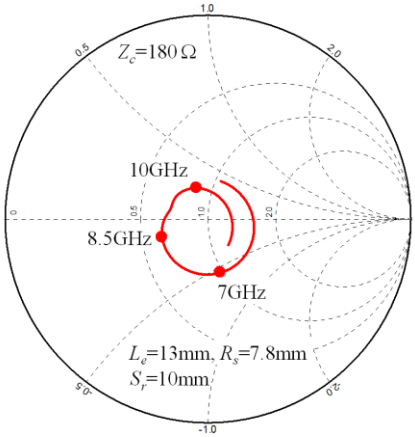

Figure3. 16 Smith chart plot of input impedance of leaf-shaped bowtie slot antenna with reflector (S_r=10mm, reference impedance: 180Ω)

At the end of this section, Figure3. 16 shows the Smith chart display of the input impedance when S_r=10mm. The Figure3. 16 shows the impedance trajectory from 6GHz to 11GHz, with the reference impedance set to 180Ω. From the Figure3. 16, the impedance

locus surrounds the center of the Smith chart. From the above results, the feeding circuit including a matching circuit is required to obtain matching between 180Ω and the general characteristic impedance of 50Ω. Therefore, in the next section, we will consider a feeding circuit that satisfies these conditions.

3.7.3 Design of Feeding Circuit Using Quarter Wavelength Transform as Matching Circuit

Since leaf-shaped bowtie slot antenna with a reflector has a high input impedance of about 180Ω, it is necessary to supply power via a feeding circuit that has matching function with 50Ω, which is a general characteristic impedance. Tapered microstrip lines have been used in past studies as feeding circuit and matching circuit for leaf-shaped bowtie and leaf-shaped bowtie slot antenna [38][39]. This sets the width if the microstrip line on the feeding point side so that the characteristic impedance is 50Ω, while the line width to which the leaf-shaped bowtie element is connected, is set to the high characteristic impedance (140Ω to 180Ω). Since the width of the high-characteristic impedance microstrip line become very narrow, problems such as manufacturing error during antenna manufacturing occurred when the tapered microstrip line was used.

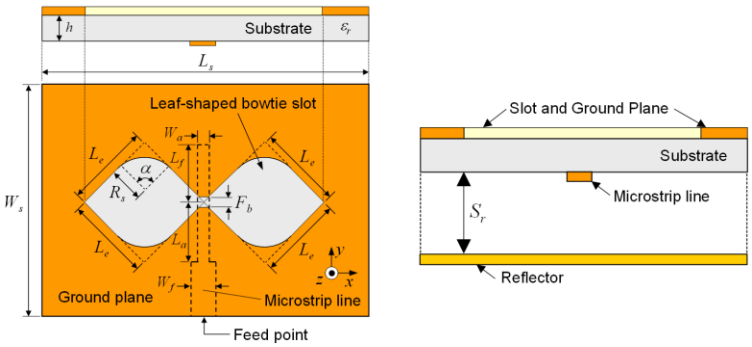

Figure3. 17 Reflector backed leaf-shaped bowtie slot antenna with feed circuit using quarter-wave transformer

A method has been reported in which an antenna with high input impedance is fed via a transmission line having a length of about a quarter of wavelength to obtain double resonance characteristics, thereby achieving matching with 50Ω in wide frequency band [46][47]. These methods are considered to be applicable to a leaf-shaped bowtie slot antenna with reflector. Furthermore, since the width of microstrip line is larger, it is expected that the influence of error during antenna fabrication can be reduced. Based on the above background, a quarter wavelength matching circuit is adopted as matching circuit for the leaf-shaped bowtie slot antenna with reflector. Figure3. 17 shows the structure of a leaf-shaped bowtie slot antenna with a reflector using feeding circuit consisting of a quarter wavelength matching circuit. A microstrip line is additionally placed as a feeding line on the back surface of the dielectric substrate of the leaf-shaped bowtie slot antenna shown in Figure3. 12. In addition, a reflector is placed on the back side of the antenna as in Figure3. 17. Based on the results of the previous

studies, the dimensions of the leaf-shaped bowtie element are chosen as L_e=13mm, R_s=7.8mm, and separation S_r=10mm.

Figure3. 18 shows the configuration of the feeding circuit in the antenna shown in Figure3. 17 and its equivalent circuit. As shown in Figure3. 18, a microstrip line with a width of W_f and a microstrip line with a width of W_a are connected in cascade. The distance from the connection point of these lines to just below the slot element is L_a which operates as quarter wavelength matching circuit. In addition, the line with a width if W_a is terminated and opened at a position L_f away from directly under the slot, which operates as an open stub.

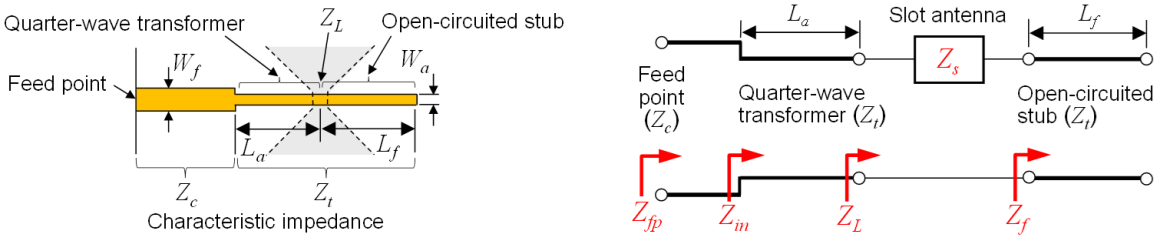

Figure3. 18 Configuration of feeding circuit and its equivalent circuit

Table3. 2 Structural parameters of feeding circuit

W_f [mm]	W_a [mm]	L_a [mm]
2.4 (Z_c=50Ω)	0.8 (Z_t=95Ω)	6.6 (λ_g/4@8.5GHz)

As shown in Figure3. 18, it is assumed that the characteristic impedance of the microstrip line with a width of W_f is Z_c, and the characteristic impedance of the microstrip line with a width of W_a connected to it is Z_t. In addition, as shown in Figure3. 18, the impedance that anticipates the latter line from the connection point between the line of width W_f and the width W_a is Z_{in}, and the impedance that anticipates the open-end side of the line from directly below the slot element is Z_L.

It is assumed that the input impedance of the slot element is Z_s, the impedance that allows for an open stub of length L_f is Z_f, and the impedance that allows for the feeding point at the end of the line with a width of W_f is Z_{fp}. In the equivalent circuit of Figure3. 18, the load impedance of the quarter wavelength matching circuit is Z_L, which is equal to the series composite value of the input impedance Z_s of the slot element and the input impedance of the open stub. If the antenna operates at a single frequency, the length L_f of the open stub is set to be equal to quarter wavelength at the operating frequency. If it is determined, Z_f = 0, so the load impedance Z_L of the matching circuit becomes equal to the input impedance Z_s of the slot element. However, in the case of a wideband antenna such as a leaf-shaped bowtie slot antenna, the stub length L_f cannot be set to simply quarter wavelength, so the issue is how to set the interval. Therefore, in this section, we perform a parameter study to set the stub length L_f.

Table3. 2 shows the structural parameters of the feeding circuit assumed in the following parameter study on stub length. The line width W_f of the feeding point is set to 2.4 mm so that the characteristic impedance of the feeding point is 50Ω. Based on the examination results in the previous section, the load impedance Z_L of the matching circuit is set to 180Ω. Since the characteristic impedance Z_t of the microstrip line operating as a quarter wavelength matching circuit is equal to the geometric mean of the load impedance Z_L and the characteristic impedance Z_c of the feeding point

$$Z_t = \sqrt{180 \times 50} = 95\Omega$$

Therefore, the line width W_a is set to 0.8mm which is equivalent to Z_t=95Ω. The length L_a of a quarter wavelength matching circuit is chosen to be L_a=6.6mm so that it is equivalent to a quarter of wavelength on the line at 8.5GHz, which is the center frequency of the design band.

When the stub length L_f is 6.5mm, 7.5mm, 8.5mm and 9.5mm (corresponding to a quarter wavelength on the line at 8.5GHz, 7.5GHz, 6.6GHz and 6.0GHz, respectively), numerical value of load impedance Z_L shown in the equivalent circuit shown as in Figure3. 18 are evaluated. Figure3. 19 shows the analysis results of load impedance, which is obtained by FDTD simulation, with reference impedance Z_c=180Ω. The impedance trajectory in Smit Chart is shown within 6GHz to 11GHz. The reference plane of the impedance shown in Figure3. 19 is Z_L position (center of the slot element) shown in Figure3. 18. From those four cases of stub length (L_f), the impedance locus exists in a circle with a standing wave ratio of 2 or less over the entire design band (7GHz to 10GHz) when L_f=6.5mm and L_f=7.5mm. The analysis result of input impedance Z_{fp} at the feeding point, when a quarter wavelength matching circuit in Figure3. 18 is used, is obtained by FDTD analysis from the above four cases of four stub lengths.

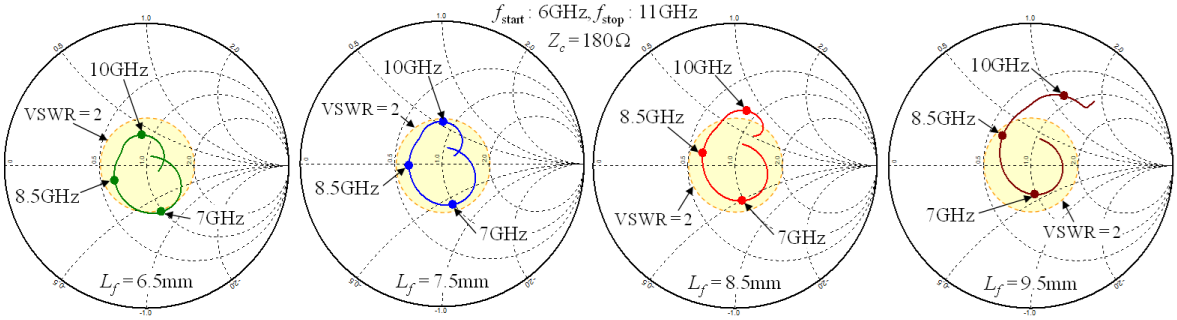

Figure3. 19 Smith chart plot of load impedance Z_L

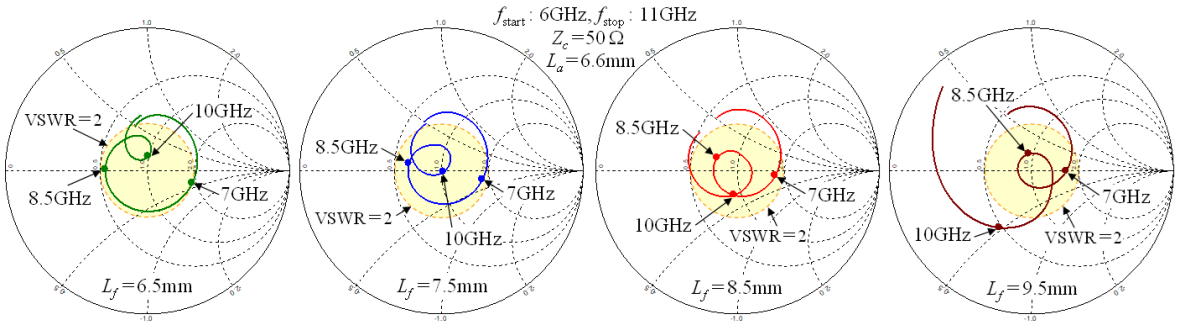

Figure3. 20 Smith chart plot of input impedance at feed point Z_{fp}

Figure3. 20 show the analysis results input impedance at feeding point with the reference impedance of 50Ω. The impedance trajectory is shown in the band of 6GHz to 11GHz. The reference surface of the impedance display in Figure3. 20 is at the input end of the feed line (feed point shown in Figure3. 18). By feeding the high impedance with a quarter wavelength matching circuit as shown in Figure3. 18, the twist of impedance trajectory due to the double resonance characteristic can be formed. From Figure3. 20, The size and position of the twist change depending on the stub length L_f, and the center of the twist and the position of the Smith chart almost coincide with each other in the design band at L_f=8.5mm out of the four cases of stub length L_f.

To evaluate the effect of the quarter wavelength matching circuit, the input impedance of the equivalent circuit shown in Figure3. 18 and slot antenna with reflector shown in Figure3. 17 are combined. The input impedance is obtained by the transmission line theory [49] using the simulation results of impedance Z_s. Figure3. 21 shows Smith chart of analytical results of impedance for the equivalent circuit. The reference impedance of Smith chart in Figure3. 21 is 50Ω, and the impedance trajectory is shown within the band of 6GHz and 11GHz. The impedance Z_s of the slot antenna shown by the solid green line is added in series with the impedance Z_f of the stub (since the stub length L_f is a quarter wavelength at 6.6GHz, it becomes an inductive reactance in the design band of 7GHz to 10GHz). Therefore, the load impedance Z_L of a quarter wavelength matching circuit becomes the locus shown by the solid blue line. It can be seen that Z_L is converted to the input impedance Z_{in} shown by the solid red line by feeding power via a transmission line with a line length (L_a=6.6mm) that a quarter wavelength at the center frequency (8.5GHz). Similar to the result of FDTD analysis shown in Figure3. 20, Z_{in} is a locus with a twist surrounding the center of the Smith chart. For the analysis results in Figure3. 21, it can be confirmed that the input impedance can be widened by feeding power via a quarter wavelength matching circuit.

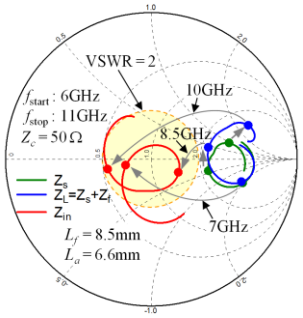

Figure3. 21 Smith chart plot of impedances for equivalent circuit

3.7.4 Evaluation of Antenna Characteristics Fed by a Quarter Wavelength Matching Circuit

Based on the above analysis results, the antenna characteristics with stub length of L_f=8.5m is used. The reflection coefficient and radiation characteristics of leaf-shaped bowtie slot antenna with a reflector using the feeding circuit which is designed in the previous section. Based on the results which have been optimized in the previous section, the structural parameters of the antenna are chosen as in the following Table3. 3.

Table3. 3 Structural parameters of the designed antenna with quarter wave transformer

L_s, W_s [mm]	ε_r, h [mm]	L_e, R_s [mm]	F_a, F_b [mm]	α [deg.]
60,30	2.17, 0.76	13, 7.8	1.0, 1.0	90
S_r [mm]	W_f [mm]	W_a [mm]	L_a [mm]	L_f [mm]
10	2.4	0.8	6.6	8.5

Figure3. 22 shows the frequency characteristic of reflection coefficient magnitude at feeding point and actual gain in the maximum radiation direction (+z direction). In Figure3. 22, the reflection coefficient is evaluated with reference impedance of 50Ω. The maximum magnitude of reflection coefficient is less than −9.7dB (standing wave ratio is equal or less than 2) within the frequency range of 6.8GHz to 10.5GHz (which is about 43% fractional bandwidth). Therefore, the desired frequency band 7GHz to 10GHz is also satisfied. The 10.1dBi of maximum actual gain is obtained at 9GHz. An actual gain of 8.5dBi is obtained at lower bound frequency (7GHz) and 9.5dBi is obtained at upper bound frequency (10GHz) of the desired band.

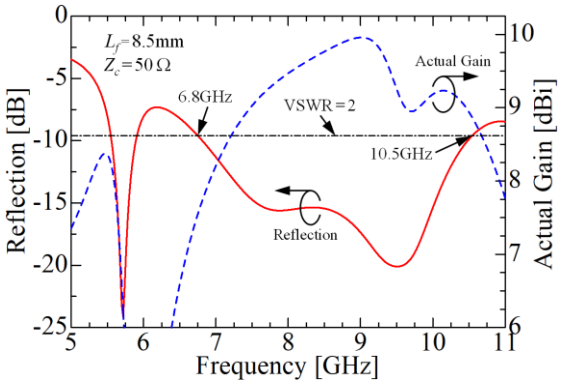

Figure3. 22 Frequency dependence of reflection coefficient amplitude and actual gain evaluated in maximum radiation direction.

Figure3. 23 shows the analysis results of E-plane and H-plane radiation patterns in the design band. The E-plane and H-plane of this antenna correspond to the *yz*-plane and *xz*-plane shown in Figure3. 17, respectively. In addition, the figure shows the result of normalizing the main polarization components (E-plane: E_θ, H-plane: E_ϕ) with maximum gain (value displayed in the 0-degree direction). From the results shown in the Figure3. 23, it can be confirmed that the pattern shape is unidirectional in the designed band. The half-power beamwidth (HPBW) of E-plane pattern is within 63° to 66°, which is almost the same HPBW regardless of the frequency. On the other hand, H-plane has HPBW within 87° at 7GHz, 65° at 8GHz, 52° at 9GHz, and 43° at 10GHz, and it can be seen that the half-power beamwidth is getting narrow as the frequency is getting higher.

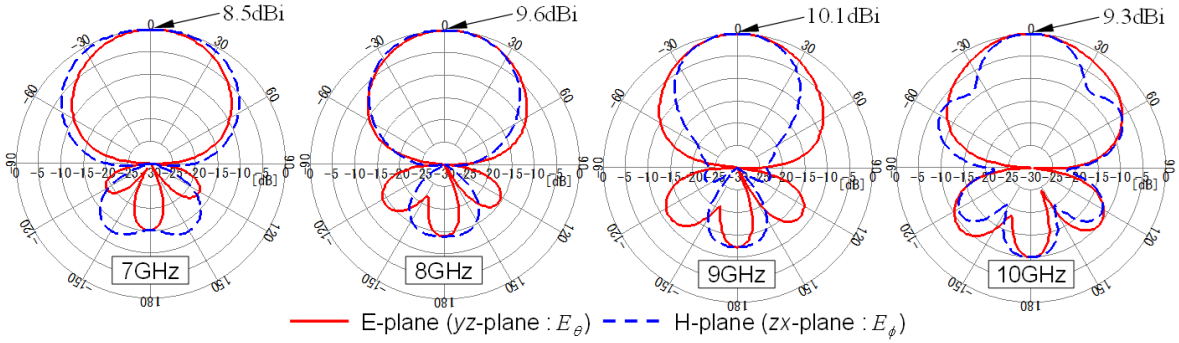

Figure3. 23 Simulated results of E-plane and H-plane pattern

To verify the effectiveness of the feeding circuit using a quarter wavelength matching circuit, the analysis result of the input impedance Z_{fp} at the feeding point, when tapered microstrip is used as matching circuit, is analyzed, and compared. Figure3. 24 shows the comparison of impedance at feeding point of quarter wavelength feeding circuit and tapered line feeding circuit, with the reference impedance of 50Ω. The impedance trajectory is shown in band of 6GHz and 11GHz.

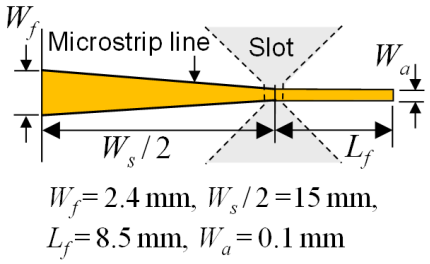

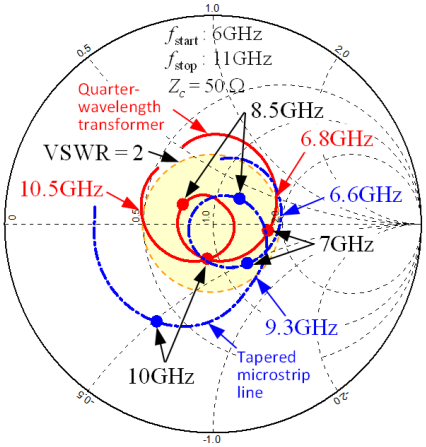

Figure3. 24 Smith chart plot of input impedance at feed point for the case when tapered microstrip line is employed

The solid red line is the impedance locus when a quarter wavelength matching circuit is used, and the frequency band with standing wave ratio of less than or equal to 2 is 6.8GHz to 10.5GHz (fractional bandwidth: 43%). On the other hand, the blue dash line is the impedance locus when a tapered microstrip line is used, and the frequency band with a standing wave ratio of less than or equal to 2 is within 6.6GHz and 9.3GHz (fractional bandwidth: 34%). From the above results, it is possible to widen the bandwidth by about 9% in terms of fractional bandwidth, confirming the effectiveness of the power supply circuit using a quarter wavelength matching circuit. In the above analysis characteristics, the dimension (F_a, F_b shown in Figure3. 12) of the part where the conductor plate was removed from the center of the slot were chosen as F_a=F_b=1mm. Since this part intersects with the microstrip line, the dimension of F_a and F_b are expected to effect of the input characteristics such as input impedance and reflection coefficient. Therefore, Figure3. 25 shows the results of the analysis reflection coefficient when F_a and F_b are changed. The Figure3. 25 shows the analysis results when F_a=F_b=1mm, 0.4mm, 1.6mm, and 2.4mm. When F_a and F_b are getting smaller, the operational band is getting wider. However, the magnitude of reflection coefficient is increasing near the center frequency (8.5GHz) of the design band. The best matching near the center frequency is when F_a=F_b=2.4mm, although the operational impedance bandwidth is narrower. From the analysis results in Figure3. 25, the impedance bandwidth does change depending on the dimensions of F_a and F_b.

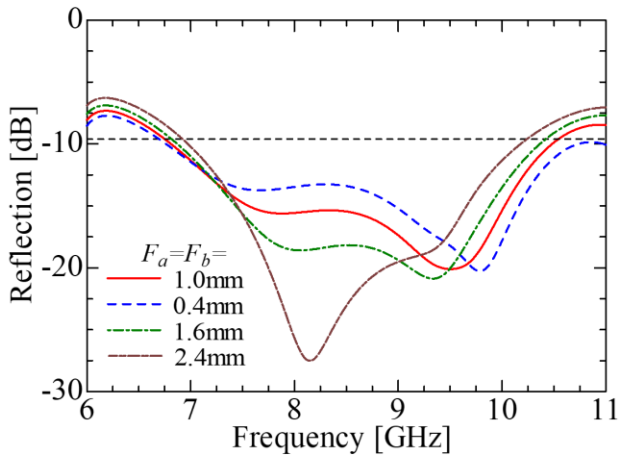

Figure3. 25 Reflection coefficient amplitude comparison when the dimensions of the slot center are changed

Summary

From Chapter 3, a research progress of leaf-shaped bowtie and leaf-shaped bowtie slot antenna have been briefly discussed. The antenna characteristics are evaluated by performing Finite-Difference Time-Domain in commercial simulation software. Leaf-shaped bowtie and leaf-shaped bowtie slot antenna have offered a high performance over a wide frequency band. More importantly, performance of leaf-shaped bowtie and leaf-shaped bowtie slot antenna are sufficient for ultra-wide band (UWB) systems. In addition to the previous studies of leaf-shaped bowtie slot antenna, quarter wavelength feeding circuit has been employed instead of microstrip tapered line. By using quarter wavelength feeding circuit, the impedance bandwidth of antenna structure has been improved. The comparison of antenna impedance bandwidth between structure with tapered microstrip line and with quarter wavelength transformer have been discussed. In addition to impedance bandwidth improvement, quarter wavelength feeding circuit also make the fabrication easier. By using quarter wavelength feeding circuit, the width at the end of microstrip line is larger than that of microstrip tapered line. Therefore, the error from fabrication process is less likely happening.

CHAPTER 4
Leaf-Shaped Bowtie Antenna for Use in Millimeter Wave Band

4.1 Abstract

In Chapter 4, some antenna structures, which have been proposed for used in 28GHz band, are briefly discussed. In addition, the use of leaf-shaped bowtie antenna in 28GHz band are also discussed. The proposed leaf-shaped bowtie antennas for millimeter wave frequency are mostly in an array configuration because mm-wave systems required high gain antenna structures to compensate atmospheric attenuation. However, an array of leaf-shaped bowtie antenna might have a complicated structure of feeding circuit because feeding mechanism of each radiating element requires balance feeding circuit on both sides of dielectric substrate. However, leaf-shaped bowtie slot antenna which is the complementary structure of leaf-shaped bowtie antenna, may have a simple feeding circuit. The feeding circuit of leaf-shaped bowtie slot antenna is constructed only one side of dielectric substrate. In addition, the leaf-shaped bowtie slot antenna can also be excited electromagnetically from microstrip line which is terminated by an opened circuit. Therefore, Chapter 4 will primarily discuss about the leaf-shaped bowtie slot antenna array for use in 28GHz frequency band. Two structure of feeding circuit will be proposed in this research. The first structure is the feeding circuit with microstrip line and conductor probe. The second structure is feeding circuit as quarter wavelength matching circuit. Actual gain and magnitude of reflection coefficient will be evaluated by FDTD methods in commercial simulation software. From FDTD analysis results, Actual gain and −10dB impedance bandwidth will be optimized.

4.2 Planar Type Antenna for Millimeter Wave Frequency Band

A high gain low-profile circular polarized substrate integrated waveguide cavity antenna is proposed in [50]. To construct the antenna, the planar bottom-layer square cavity is constructed by metallic via arrays with diameter of D and spacing of P with total length L_c on substrate with thickness = 20mil. The feeding probe is used to excite the cavity. The antenna gain is about 16dBi and −10dB impedance bandwidth is within 27GHz to 28.5GHz. From [50], the fabrication of the antenna structure is complicated. More importantly, the feeding point the structure is not a standard microstrip line. Therefore, the antenna structure is difficult to be integrated with other devices.

In [12], a leaky-wave antenna (LWA) is demonstrated and developed at Ka-band based on the proposed half-mode substrate integrated waveguide (HWSIW). The center symmetry plane of an SIW can be equivalently regarded as a magnetic wall when it operates with its dominant mode (TE_{10}-like mode). The proposed LWA has a transition between 50Ω microstrip line and HMSIW is used for impedance matching with a width of W_t and a length

L_t. To improve the return loss, a section of HMSIW with gradually tapered width from W1 to W2 is adopted. The antenna is terminated by a 50Ω matching load. The substrate thickness has a noticeable impact on the far-field radiation pattern. In H-plane, there is a beam other than the main one emerging due to the small substrate thickness compared to the guided wavelength. The leakage effect is mainly related to the width of the HMSIW. The operational frequency band is within 25-28GHz. However, the disadvantage of the antenna structure in [12] is that it has more than one beam and the radiation beams are not in broad side.

In [15], a compact, broadband, planar array antenna with Omni-directional radiation in horizontal plane is proposed for the 26 GHz fifth generation (5G) broadcast applications. The antenna element is composed of two dipoles and a substrate integrated cavity (SIC) as the power splitter. The two dipoles are placed side-by-side at both sides of the SIC, and they are compensated with each other to form an omni-directional pattern in horizontal plane. By properly combing the resonant frequencies of the dipoles and the SIC, a wide impedance bandwidth from 24 to 29.5GHz is achieved. Based on the dual-port structure, an eight-element array with an enhanced gain of over 12dBi is designed and prototyped.

4.3 Double-Sided Leaf-Shaped Bowtie Antenna for Millimeter Wave Band

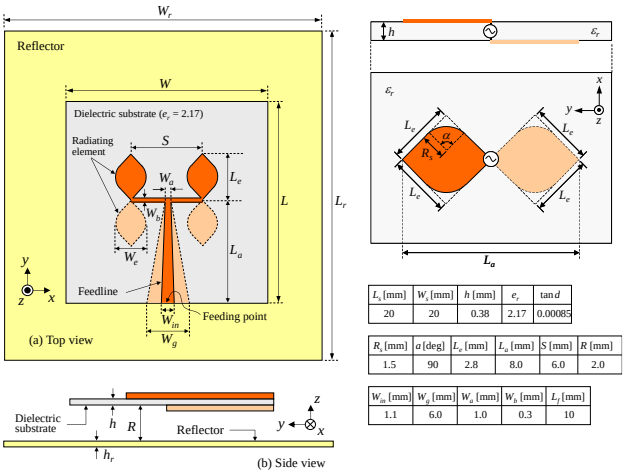

L_s [mm]	W_s [mm]	h [mm]	ε_r	tan d
20	20	0.38	2.17	0.00085

R_s [mm]	a [deg]	L_e [mm]	L_a [mm]	S [mm]	R [mm]
1.5	90	2.8	8.0	6.0	2.0

W_m [mm]	W_g [mm]	W_a [mm]	W_b [mm]	L_f [mm]
1.1	6.0	1.0	0.3	10

Figure4. 1 An array of 2 leaf-shaped bowtie antennas for millimeter wave frequency band [51]

The Federal Communications Commission (FCC) has allocated the quasi-millimeter wave band of 22GHz to 29GHz for radar applications. As the practical use of UWB radar systems, short-range (SR) automotive radar operating in the quasi-millimeter wave band has been receiving more interest in recent years. In [51], An array of two double sided leaf-shaped bowtie antennas with flat reflector, which is type of UWB with unidirectional radiation characteristic and high gain, has been proposed for use in quasi-millimeter wave band of 22GHz to 29GHz. Two-pairs of leaf-shaped radiating element has been printed on top and bottom sides of a substrate. The side length of the square shape is denoted by L_e. The radiating

elements are excited by a feeding circuit consisting of a tapered microstrip line and a parallel strip line T-junction. To obtain unidirectional radiation characteristics, a flat reflector is placed underneath the antenna substrate. The separation between the substrate and the reflector is denoted by *d*. The antenna structure in Figure4. 1 offers the actual gain of 8dBi to 10dBi.

An array of 4 double-sided leaf-shaped bowtie antennas has been proposed in [52] for use in quasi-millimeter wave band. The array antenna is backed by a mushroom-type electromagnetic band gap (EBG) substrate which is designed such that the array operates at the frequency band from 22GHz to 29GHz. Four pairs of radiating elements are printed on top and bottom sides of a dielectric substrate having the thickness of h, relative permittivity of ε_r. The side lengths of the substrate are designed as L_s and W_s. The spacing between each radiating element are S_x and S_y in *x*-and *y*-directions, respectively. Each radiating elements of the array are excited by a feeding circuit consisting of a tapered microstrip line and a parallel strip line T-junction. The antenna substrate is placed parallel to a mushroom-type EBG substrate at a distance of d. The EBG reflector is composed of a periodic array of square patches printed on a grounded dielectric substrate having the thickness of h. The size of EBG reflector is the same as those of the antenna substrate. The EBG substrate is designed such that the 0° reflection phase for the normal incidence of the plane wave on the substrate is achieved at around 26GHz. The −10dB impedance bandwidth occupies the frequency range of 24.2GHz to 25.2GHz and 28.2GHz to 29GHz. Actual gain is within 13dBi to 15dBi over the frequency range of 24GHz to 26GHz, and within 14.5dBi to 15.2dBi over frequency of 28GHz to 29GHz.

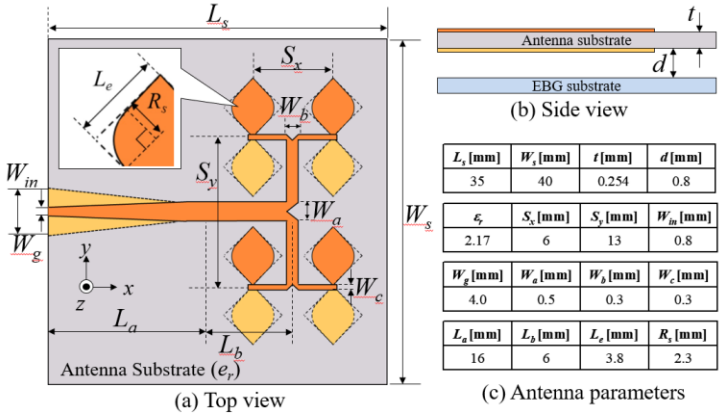

L_s [mm]	W_s [mm]	t [mm]	d [mm]
35	40	0.254	0.8

ε_r	S_x [mm]	S_y [mm]	W_{in} [mm]
2.17	6	13	0.8

W_g [mm]	W_a [mm]	W_b [mm]	W_c [mm]
4.0	0.5	0.3	0.3

L_a [mm]	L_b [mm]	L_e [mm]	R_s [mm]
16	6	3.8	2.3

Figure4. 2 Array of 4 leaf-shaped bowtie antenna backed by EBG reflector for using in mm-wave frequency band

A planar array of 16 double-sided leaf-shaped bowtie slot antennas has been proposed in [53] for use within frequency range of 22GHz to 30GHz. Eight pairs of two-element subarray are printed on top and bottom sides of a dielectric substrate having the thickness of h, relative permittivity of ε_r. In each subarray, a leaf-shaped bowtie antenna is adopted as the

radiating elements. This antenna is designed by rounding the corner of the square copper sheet with the curvature radius of R_s. The side length of the square shape is denoted by L_e. The radiating elements are excited with equal amplitude and phase by a series feed network based on a parallel strip line. A parallel feed network based on a microstrip line is employed to excite the subarray antennas with the equal amplitude and the qual phase. Microstrip and parallel strip lines are connected through tapered balun for the purpose of realizing the impedance matching. To obtain unidirectional radiation pattern, a flat reflector having the same dimension as those of the antenna substrate is placed underneath the antenna array. The spacing between each radiating element along *x*-axis is L_x=8.5mm and along *y*-axis is L_y=9mm. The separation between antenna substrate to reflector is d=3.0mm. Characteristics of the designed array antenna are evaluated by the FDTD analysis and measurements. As for the reflection coefficient, the simulated results are bellow −8dB over the band of 22-30GHz. Over the frequency band of 22-30GHz, the actual gain is 12.3-19.4dBi and 19.7-14.2dBi for the simulation and measurement, respectively.

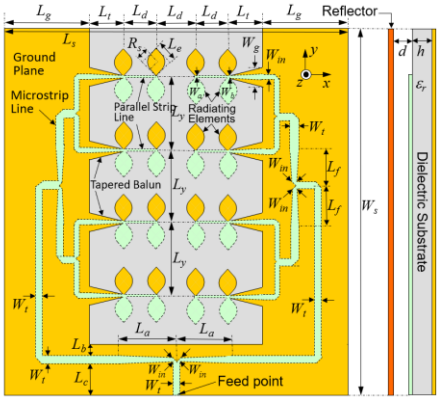

Figure4. 3 Configuration of 16-element leaf-shaped bowtie antenna array

From section4.2, most of proposed antenna structure has low gain and complicated fabrication method. The fabrication methods of antenna proposed in section4.2 mostly are involving multilayer substrate and substrate integrated waveguide. From section4.3, double-sided leaf-shaped bowtie antennas array can offer high gain over a wide bandwidth. However, double-sided leaf-shaped bowtie antenna requires feeding circuit on both sides of dielectric substrate, which is difficult to use in large scale arrays for high gain antenna structure. In addition, large scale feeding circuit will generate high conductor loss for operation within millimeter wave frequency band. On the hand, leaf-shaped bowtie slot antenna is a complement structure which can offer high gain over a wide bandwidth. In addition, the feeding circuit is required on only one side of dielectric substrate. Therefore, the feeding circuit is less complexity. From above reasons, leaf-shaped bowtie slot antenna is proposed to use in millimeter wave frequency band in this research.

4.4 Leaf-Shaped Bowtie Slot Antenna with Feeding Circuit as Microstrip Line and Conducting Probe for Use in Millimeter Wave Frequency Band

4.4.1 Characteristic of Single Slot Antenna

So far, the leaf-shaped bowtie slot antenna has not been proposed to use for millimeter wave yet. In this research, the leaf-shaped bowtie slot antenna is proposed for use in quasi-millimeter wave. The advantage of leaf-shaped bowtie slot antenna is that it has low profile for both antenna structure and feeding circuit. The structure of single leaf-shaped bowtie slot antenna is shown as in the following Figure4. 4 and the structural parameter of single leaf-shaped bowtie slot antenna is shown in Table4.1.

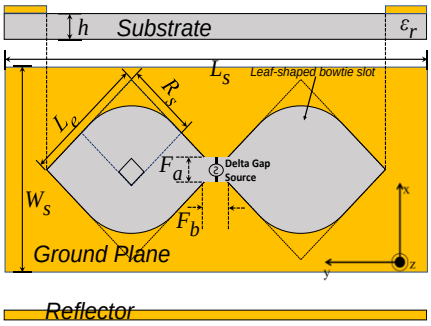

Figure4. 4 Structure of single leaf-shaped bowtie slot antenna

Table4. 1 Structural parameters of single leaf-shaped bowtie slot antenna designed for use with 27-29*GHz*

L_s	R_s	L_a	W_s	F_a	F_b	h	ε_r
2.8mm	1.7mm	20mm	10mm	0.6mm	0.6mm	0.38mm	2.17

To create the leaf-shaped bowtie slot antenna as shown in Figure4. 4, a layout of square shape is firstly drawn a ground plane of a dielectric substrate. The length of the square shape is L_e which is chosen by following the equation. Then, the corner of the square slot is rounded by curve line with radius R_s at right angle (α=90°). In this research, the relative permittivity of substrate and thickness are ε_r=2.17 and h=0.38mm which is the ultra-thin substrate. The dissipation factor of dielectric substrate is tanδ=0.00085.

$$L_e = \frac{\lambda_0}{4\sqrt{\varepsilon_{re}}} \quad ; \quad \varepsilon_{re} = \frac{\varepsilon_r + 1}{2}$$

In this research, the element length L_e is chosen as L_e=2.8mm so that the proposed antenna structure can operate over the frequency range of 27GHz to 29GHz which is the 28GHz band in Japan. In addition, the radius of the curve line R_s is chosen as 0.6L_e=1.7mm.

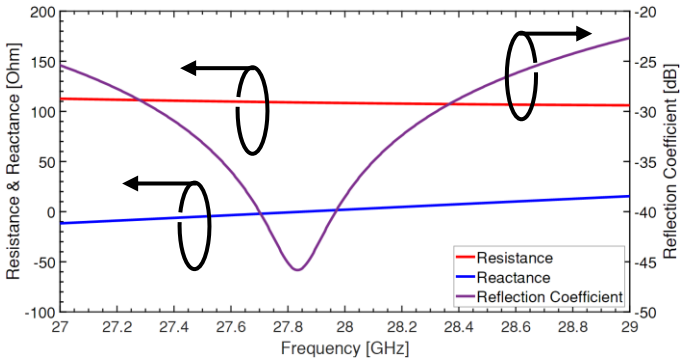

Figure4. 5 Antenna impedance (resistance & reactance) and reflection coefficient (Z_{ref}=120Ω)

Figure4. 5 shows impedance (real and imaginary part) and magnitude of reflection coefficient with reference impedance of 50Ω. From Figure4. 5, the antenna resistance is almost constant over the frequency range of 27GHz to 29GHz. The characteristics of single antenna are studied by changing element length L_e. In this study, the antenna characteristics are evaluated by performing finite-difference time domain analysis in commercial simulation software (Sim4Life). In FDTD simulation, delta gap is employed to excite gaussian signal with center frequency of 28GHz and bandwidth of 2GHz, so that the characteristics are analyzed over the frequency range of 27GHz to 29GHz. Parameters of FDTD simulation are set as in the following Table4. 2:

Table4. 2 FDTD simulation setting for single slot antenna

		Δx	Δy	Δz
Grid Size	Substrate	0.05mm	0.05mm	0.02mm
	Ground	0.05mm	0.05mm	0.02mm
	Padding	10mm	10mm	10mm
Absorbing Boundary		10-layer UPML (Uniaxial Perfectly Matched Layer)		
Simulation Time		150 periods		

In FDTD simulation setting, padding is the separation between antenna structure to absorbing boundary condition. 10mm padding is about one free space wavelength at 28GHz. In this simulation, actual gain of single antenna is evaluated with sampling frequency of 0.05GHz. The antenna reflection coefficient is calculated with the reference impedance of 110Ω. The element length is changed in order to optimized both actual gain in $+z$-direction and −10dB impedance bandwidth.

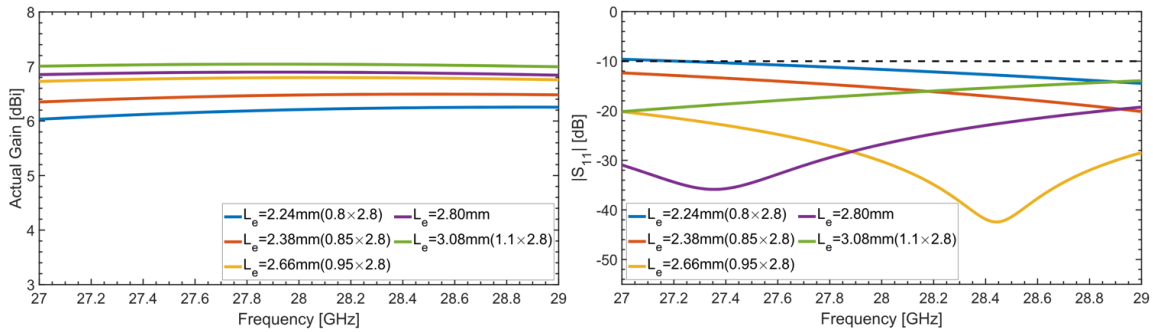

Figure4. 6 Frequency dependence of actual gain and $|S_{11}|$ by changing element length (L_e)

From Figure, the element length is decreased from 5%, 15%, and 20% and it is increased from 10%. The actual gain of the single antenna element is decreasing after element length is decreased; however, the actual gain is increasing after element length is increased. On the other hand, magnitude of reflection coefficient is also depending on the element length. The element length that offers small magnitude of reflection coefficient is L_e=2.8mm, and L_e=2.66mm. With L_e=2.66mm, the single antenna offers smaller actual gain than that of L_e=2.8mm. Therefore, the optimum element length for single slot antenna with delta gap feeding is L_e=2.8mm. The radiation pattern of single slot antenna with L_e=2.8mm are shown as in Figure4. 7 and Figure4. 8 which evaluated at frequency of 27GHz, 28GHz and 29GHz.

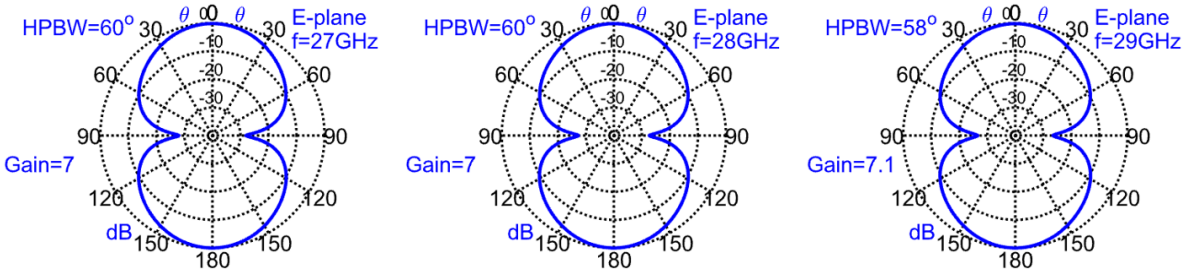

Figure4. 7 E-plane pattern of single slot antenna with delta gap as feeding

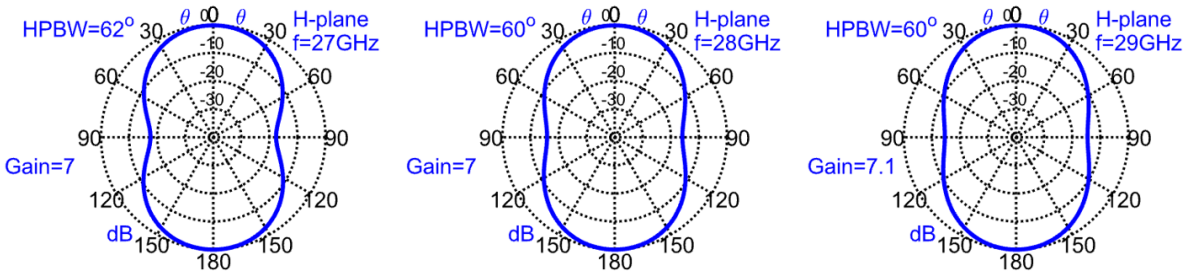

Figure4. 8 H-plane pattern of single slot antenna with delta gap as feeding

As shown in Figure4. 7 and Figure4. 8, the radiation pattern characteristic of single slot antenna is bi-directional radiation pattern. To obtain high gain and unidirectional radiation pattern, a reflector is placed under the substrate at distance of S_r=2.5mm which is about a

quarter wavelength at 28GHz frequency band. The structure of antenna with reflector is shown as in Figure4. 4. The characteristics of the slot antenna with reflector are shown as following Figure4. 9:

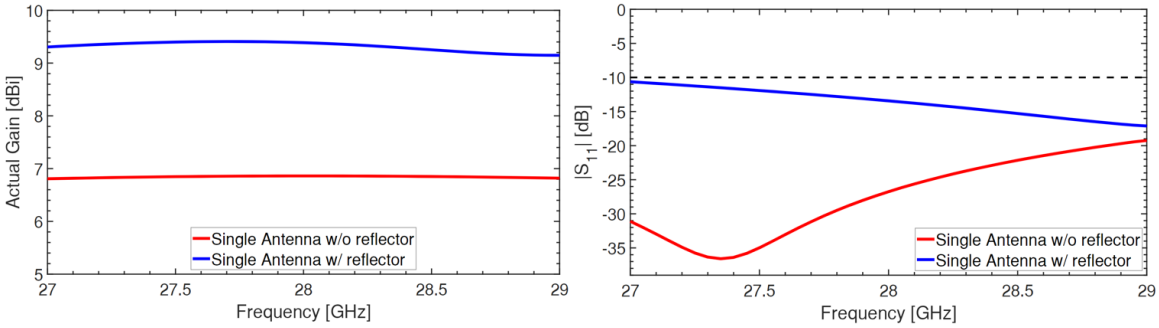

Figure4. 9 Frequency dependence of actual gain and $|S_{11}|$ of antenna with and without reflector

Simulation setting of FDTD is the same as the previous section. Actual gain is evaluated with sampling frequency of 0.05GHz. Reflection coefficient is calculated with reference impedance of 110Ω. From Figure4. 9, actual gain has increased around 2.5dB after a reflector is placed under the dielectric substrate. On the other hand, magnitude of reflection coefficient has also increased. However, magnitude of reflection coefficient is less than −10dB over the frequency range from 27GHz to 29GHz. The radiation pattern results are shown as in the following Figure4. 10 and Figure4. 11. In addition, both radiation pattern of slot antenna without reflector and slot antenna with reflector are compared. The radiation pattern of both E-plane and H-plane are evaluated at frequency of 27GHz, 28GHz, and 29GHz.

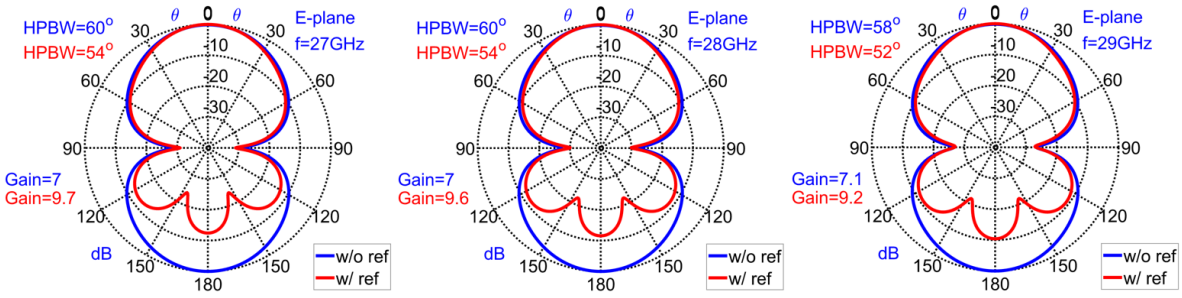

Figure4. 10 E-plane pattern of single slot antenna with and without reflector

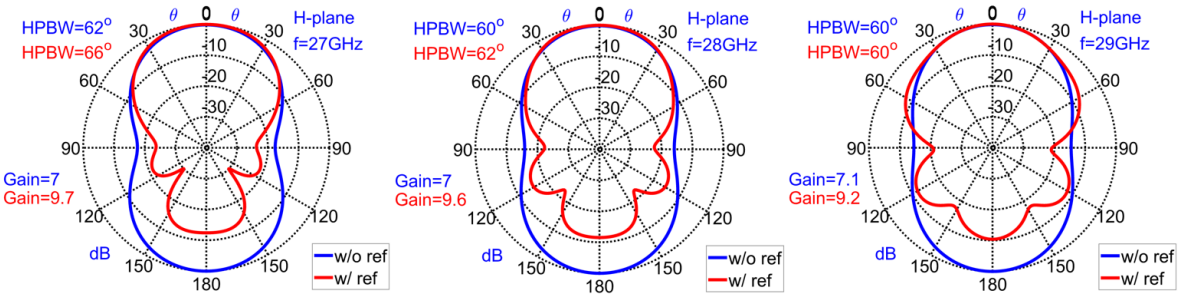

Figure4. 11 H-plane pattern of single slot antenna with and without reflector

From Figure4. 10 and Figure4. 11, the unidirectional radiation pattern is obtained after reflector is used. Maximum gain has increased within 2.7dB to 2.1dB. Half Power Beamwidth is within 57° to 55° along E-plane and within 64° to 60° along H-plane. In +z-direction, the radiation pattern of slot antenna without reflector and slot antenna with reflector have slightly different half-power beamwidth.

4.4.2 Single Leaf-Shaped Bowtie Slot Antenna Fed by Microstrip Line and Conductor Probe

From [38][40], the feeding circuit of leaf-shaped bowtie slot antenna is a tapered microstrip line which is connected to conductor probe at the end of the line. The conducting post is connected to ground plane vicinity of the leaf-shaped bowtie slot antenna. In [38], the tapered microstrip line is employed to achieve 50Ω impedance matching. In this research, the feed line of leaf-shaped bowtie slot antenna is microstrip line which is connected to conductor probe at the end of microstrip line. The conductor probe is serving as connection between slot antenna ground plane vicinity and microstrip line. The width of microstrip line is W_{in}=0.2mm which has characteristic impedance of about 110Ω at 28GHz. The diameter of the conducting post is D_{probe}=1mm. The structure of single leaf-shaped bowtie slot antenna with feeding circuit and the structural parameter are shown in Figure4. 12 and Table4. 3, respectively.

Table4. 3 Structural parameters of slot antenna with microstrip line and conductor post

L_s	R_s	L_a	W_s	F_a	F_b	h	D_{probe}	W_{in}	ε_r
2.8mm	1.7mm	20mm	10mm	0.6mm	0.6mm	0.38mm	1mm	0.2mm	2.17

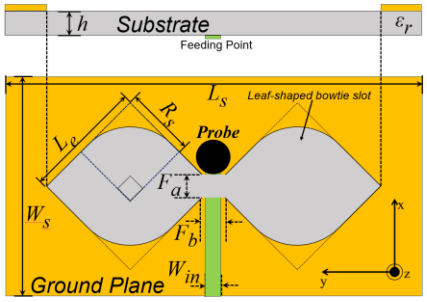

Figure4. 12 Single leaf-shaped bowtie slot antenna with microstrip line and conductor post

Characteristics of the single leaf-shaped bowtie slot antenna with feeding circuit as microstrip line and conductor probe are evaluated by performing FDTD analysis in commercial simulation software. In FDTD simulation, delta gap, which is placed at the edge between microstrip line and ground plane, is employed to excite gaussian signal with center frequency of 28GHz and bandwidth of 2GHz, so that the characteristics are analyzed over the frequency range of 27GHz to 29GHz. In FDTD simulation, ground plane and feeding circuit are chosen PEC. In addition, loss tangent of dielectric substrate is not included.

Therefore, the materials are considered as lossless. Parameters of FDTD simulation are set as in the following Table4. 4:

Table4. 4 FDTD simulation setting for slot antenna with microstrip line

		Δx	Δy	Δz
Grid Size	Probe	0.05mm	0.05mm	0.02mm
	Feed Line	0.05mm	0.05mm	0.02mm
	Padding	10mm	10mm	10mm
Absorbing Boundary		10-layer UPML (Uniaxial Perfectly Matched Layer)		
Simulation Time		150 periods		

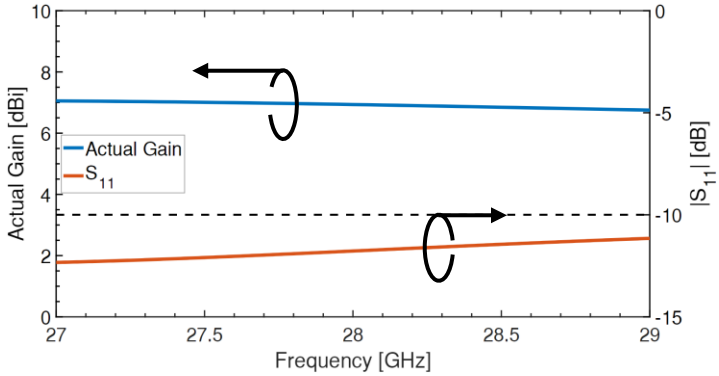

Figure4. 13 Actual gain and $|S_{11}|$ of antenna structure with feed line (Z_{ref}=120Ω)

Figure4. 13 show actual gain and reflection coefficient of the single slot antenna which is shown in Figure4. 12. The actual gain is calculated with sampling frequency of 0.05GHz, and the reflection coefficient is calculated with reference impedance of 110Ω. After using microstrip line and conductor probe as feeding circuit, the antenna actual gain is between 7dBi to 6.8dBi and the −10dB impedance bandwidth is within 27GHz to 29GHz. Comparing the analysis results in Figure4. 13 and in Figure4. 6 with the case of L_e=2.8mm, the actual gains are almost in the same range. However, the reflection coefficient magnitude of antenna structure with microstrip line is higher than that of antenna structure without microstrip line. The radiation patterns of the slot antenna are shown as in the following Figure4. 14 and Figure4. 15. The radiation patterns are evaluated at frequency of 27GHz, 28GHz, and 29GHz. Comparing between Figure4. 14 and Figure4. 7 and between Figure4. 15 and Figure4. 8, HPBW of radiation pattern of sot antenna with feed line is slightly wider than that of slot antenna without feedline. In addition, maximum gain in +z-direction of slot antenna with feedline is also slightly higher than that of without feedline. This discrepancy may be caused by the radiation of microstrip feeding line.

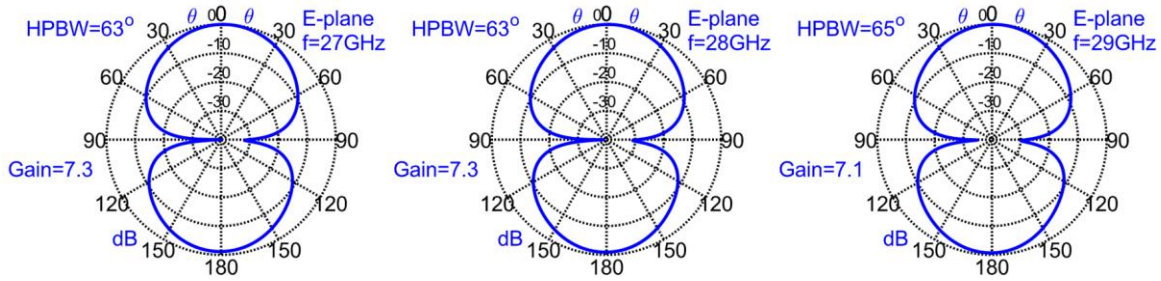

Figure4. 14 E-plane of antenna structure with feed line

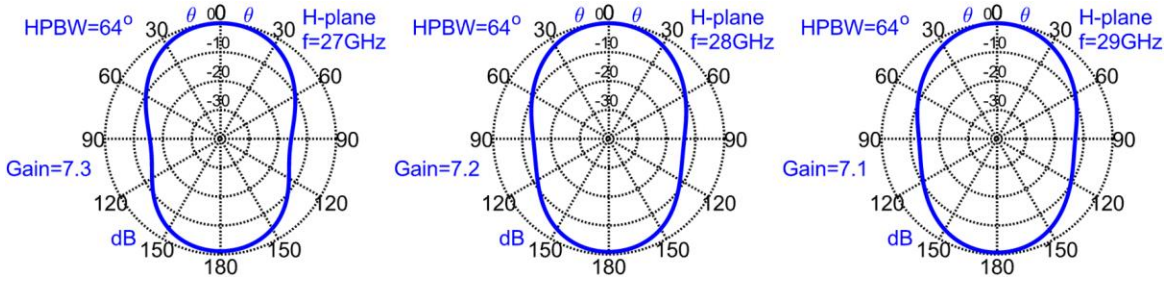

Figure4. 15 H-plane of antenna structure with feed line

4.4.3 Array of Leaf-Shaped Bowtie Slot Antenna Fed by Microstrip Line and Conductor Probe

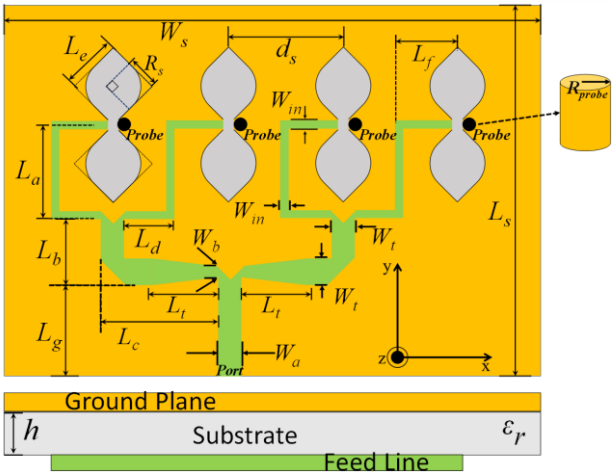

Figure4. 16 An array of 4 leaf-shaped bowtie slot antennas

4 leaf-shaped bowtie slot antennas with element length L_e=2.7mm and rounded by a curve line with radius R_s=1.7mm, which is designed the same as Figure4. 12, is adopted as radiating slot of the linear array along E-plane. The antenna ground plane is printed on a dielectric substrate with relative permittivity of ε_r=2.17 and with thickness of h=0.38mm. The structure of linear array of 4 leaf-shaped bowtie slot antennas is shown as in the following Figure4. 16. The structural parameters are shown as in Table4. 5.

Table4. 5 Structural parameters of an array of 4 leaf-shaped bowtie slot antennas

W_s	L_s	L_a	L_b	L_g	L_d	L_t	d_s
58	34	6.6	2.8	7.5	3.9	5.5	8.4
L_f	W_a	W_b	W_t	W_{in}	R_{probe}	L_c	h
3.6	1	0.3	0.8	0.2	0.5	8.3	0.38

Element spacing between neighboring radiating slot is varied to investigate the actual gain and −10dB impedance bandwidth. The antenna characteristics are evaluated by performing FDTD simulation in commercial simulation software. In FDTD simulation, grid size is chosen as Δx=0.05mm, Δy=0.05mm, and Δz=0.02mm. 10-layer uniaxial perfectly match layer is employed as absorbing boundary condition. Padding between absorbing boundary condition and antenna structure is 10mm. The antenna characteristics are analyzed within the frequency range of 27GHz to 29GHz. The reflection coefficient is calculated with reference impedance of 50Ω. Actual gain are evaluated with sampling frequency of 0.05GHz. Actual gain and reflection coefficient are show as in following Figure4. 17.

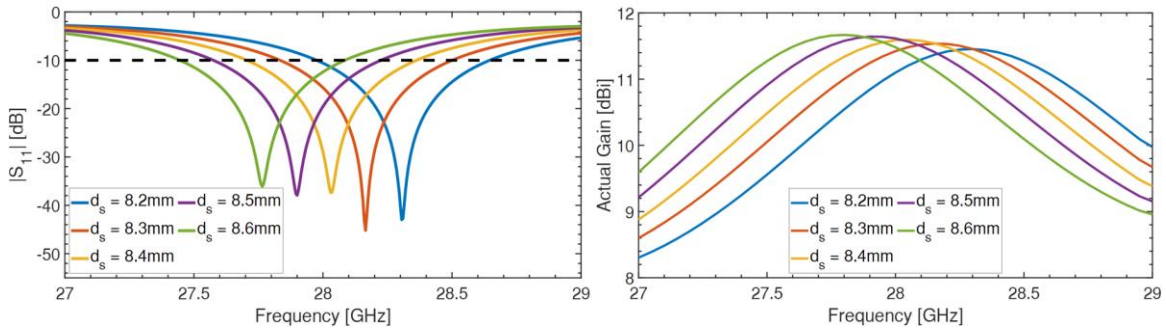

Figure4. 17 $|S_{11}|$ and actual gain by changing element spacing (d_s)

From the analysis results in Figure4. 17, −10 impedance bandwidth is slightly changed versus element spacing d_s. However, the resonance frequency is shifting from high frequency to low frequency when element spacing is changed from small to large. The 28GHz resonance frequency is obtained when the element spacing is chosen as d_s=8.4mm. The same case as −10dB impedance bandwidth, the maximum actual gain and −3dB impedance bandwidth are slightly changing versus element spacing d_s. Comparing to analysis results of Figure4. 12, actual gain has increased around 4.5dB.

As leaf-shaped bowtie slot antenna has bi-directional radiation pattern, a flat reflector is placed at separation of S_r=2.5mm which is about a quarter of free space wavelength at 28GHz. The element spacing d_s is changed in order to investigate the actual gain and −10dB impedance bandwidth. Figure4. 18 shows side view of leaf-shaped bowtie slot antenna array with a flat reflector. Figure4. 19 shows analysis results of actual gain and reflection coefficient magnitude which is calculated with reference impedance of 50Ω.

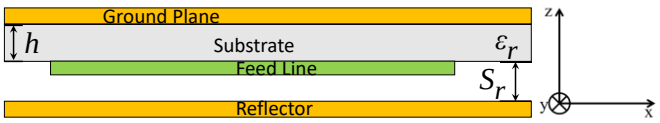

Figure4. 18 Side view of slot array antenna with reflector

The reflection coefficient and actual gain are slightly changing versus element spacing d_s. The same scenario as previous case, the resonance frequency is shifting from high frequency to low frequency when element spacing is changed from small to large. The 28GHz resonance frequency is obtained when the element spacing is chosen as d_s=8.4mm. The same case as −10dB impedance bandwidth, the maximum actual gain and −3dB impedance bandwidth are slightly changing versus element spacing d_s.

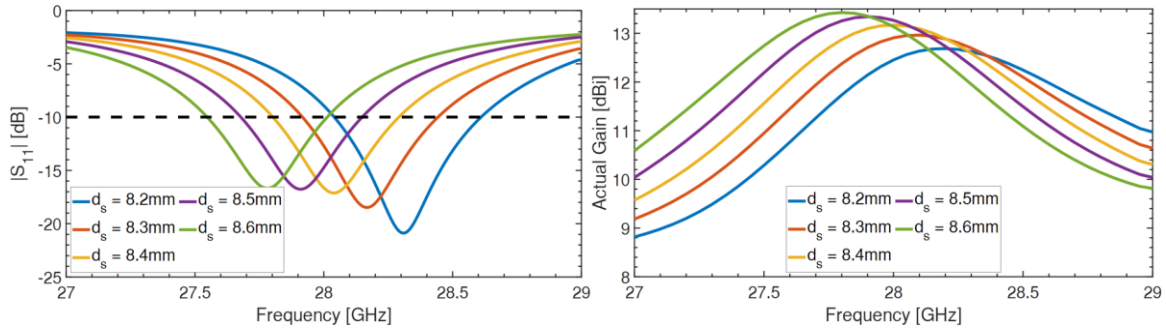

Figure4. 19 $|S_{11}|$ and actual gain of leaf-shaped bowtie slot antenna array with reflector by changing element spacing d_s

In addition, the effect of S_r on actual gain and −10dB impedance bandwidth are investigated. The separation between substrate and reflector (S_r) is varied from 2mm to 6mm. Actual gain and reflection coefficient are evaluated by performing FDTD analysis in commercial simulation software. In FDTD simulation, grid size is chosen as Δx=0.05mm, Δy=0.05mm, and Δz=0.02mm. 10-layer uniaxial perfectly match layer is employed as absorbing boundary condition. The antenna characteristics are analyzed within the frequency range of 27GHz to 29GHz. The reflection coefficient is evaluated with reference impedance of 50Ω. Actual gain are evaluated with sampling frequency of 0.05GHz. The analysis results of actual gain and reflection coefficient are shown as in following Figure4. 20.

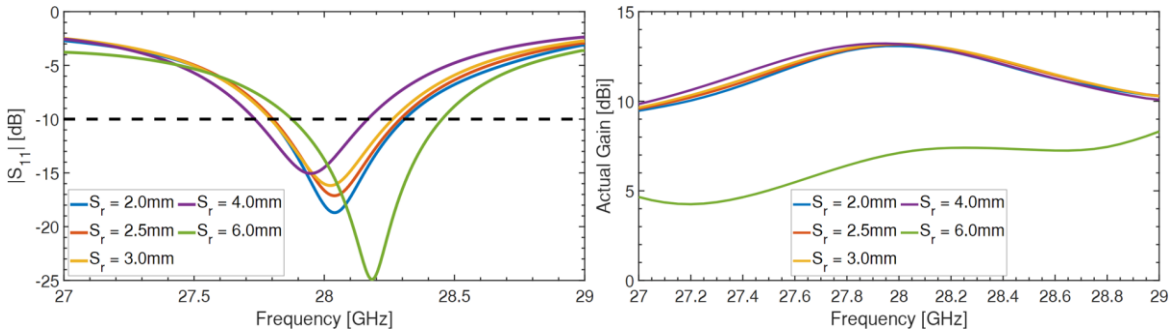

Figure4. 20 $|S_{11}|$ and actual gain of slot antenna array with reflector by changing separation S_r

From the analysis results in Figure4. 20, actual gain is slightly changing when S_r is changed with 2mm to 4mm.When S_r is chosen as 6mm, actual gain is the lowest. Magnitude of reflection coefficient is slightly changing for S_r=2, 2.5, 3mm. However, resonant frequency is shifting for S_r=4, 6mm. It can be concluded that both optimum actual gain and −10dB impedance bandwidth are obtained when S_r is chosen to be 2.5mm. Therefore, the optimum antenna element spacing d_s and separation between substrate and reflector is d_s=8.4mm, and S_r=2.5mm, respectively. Actual gain and reflection coefficient comparison between slot antenna array without reflector and with reflector are shown as in the following Figure4. 21.

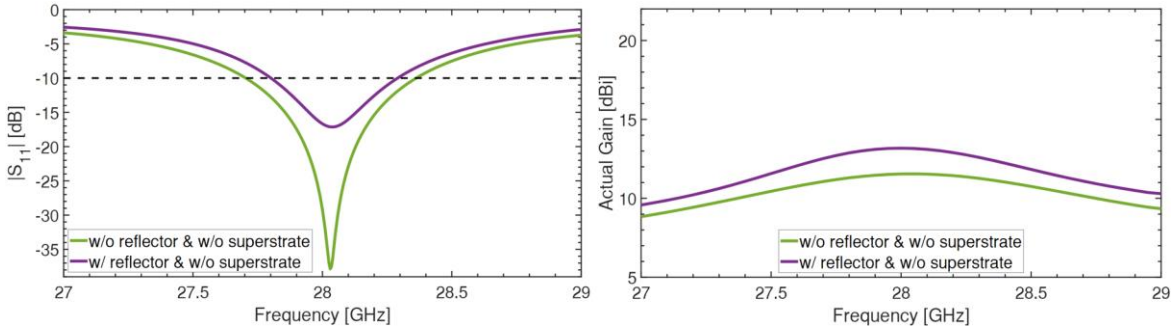

Figure4. 21 $|S_{11}|$ and actual gain comparison of antenna structure with and without reflector (Z_{ref}=50Ω)

From the analysis results in Figure4. 21, −10dB impedance bandwidth of slot antennas array without reflector occupies frequency range of 27.7GHz to 28.36GHz which is about 660MHz. However, −10dB impedance bandwidth is decreasing after a flat reflector is employed. The −10dB impedance bandwidth of the slot antenna array with reflector occupies the frequency range of 27.8GHz to 28.29GHz which is about 490MHz. Therefore, −10dB impedance bandwidth decreases around 170MHz. From the analysis results in Figure4. 21, the slot antennas array without reflector has maximum actual gain of 11.5dBi and −3dB gain bandwidth occupies frequency range of 27GHz to 29GHz. In addition, the slot antennas array with reflector has maximum actual gain of 13.17dBi and −3dB gain bandwidth occupies frequency range of 27.17GHz to 29GHz. Therefore, maximum actual gain of the slot

antennas array increases around 1.62dBi after a flat reflector is used. However, −3dB gain bandwidth decreases around 170MHz.

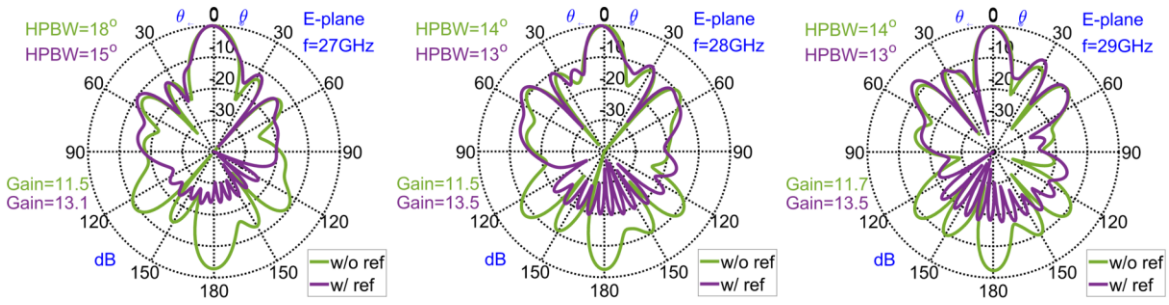

Figure4. 22 E-plane comparison between antenna structure with and without reflector

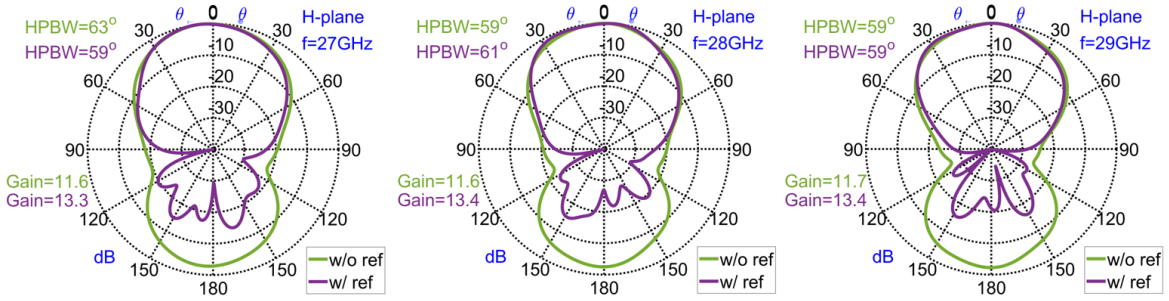

Figure4. 23 H-plane comparison between antenna structure with and without reflector

Figure4. 22 and Figure4. 23 show analysis results of radiation pattern along E-plane and H-plane. The numerical results of radiation pattern are evaluated at frequencies of 27GHz, 28GHz, and 29GHz. Without reflector, the slot antennas array has bidirectional radiation pattern. Half-power beamwidth (HPBW) along E-plane is 18° at 27GHz, and 14° at 28GHz and 29GHz. HPBW along H-plane is 63° at 27GHz and 59° at 28GHz and 29GHz. Maximum sidelobe level is −10dB at 27GHz and −8dB at 28GHz and 29GHz along E-plane. Unidirectional radiation pattern is obtained, after a flat reflector is used. HPBW of the slot antenna array with reflector is 59° at 27GHz, 61° at 28GHz, and 59° at 29GHz along H-plane. Maximum sidelobe level along E-plane is −10dB at 27GHz, −8dB at 28GHz and −7dB at 29GHz. In +z direction, the HPBW and sidelobe level of slot antennas array with and without reflector are slightly different.

4.5 Leaf-Shaped Bowtie Slot Antenna Electromagnetically Fed by Microstrip Line for Use in Millimeter Wave Frequency Band

From the previous section, the feeding circuit of single leaf-shaped bowtie slot is normal microstrip line connecting with conductor probe. In this section, the feeding circuit of the single leaf-shaped bowtie slot antenna is coupling between microstrip line and antenna feed point which is at the center of the slot antenna. The microstrip line is terminated by opened circuit line whose length is about a quarter of free space wavelength at 23GHz. Leaf-shaped bowtie slot antenna has high input impedance. In previous research [39], microstrip taper line has been used to convert from antenna load impedance to a 50Ω standard feeding microstrip line. In section3.7, quarter wavelength matching circuit has been used to convert from antenna load impedance to 50Ω standard microstrip line for use in UWB communication systems. As the results, the impedance bandwidth of the single slot antenna has been improve comparing to microstrip tapered line. In this section, quarter wavelength matching circuit is used to transform from antenna load impedance to 50Ω standard microstrip line and 50Ω connector for use in millimeter wave frequency band. Firstly, the antenna impedance is calculated by performing FDTD in commercial simulation software. To analyze the impedance over a wide frequency band, delta-gap is employed to excite a gaussian voltage source. The center frequency and bandwidth of gaussian signal is 30GHz and 20GHz bandwidth. In this structure, the element length L_e is set to 4mm which is designed for the frequency band of 23GHz-33GHz. The structure and impedance of single antenna are shown as in the following Figure4. 34. The structural parameters are shown as in Table4. 6.

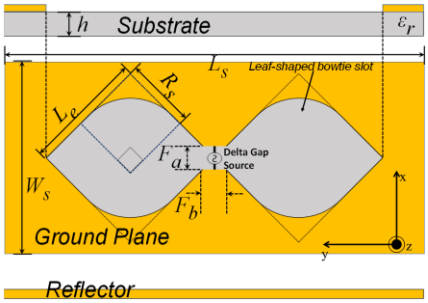

Figure4. 24 Structure of single slot antenna with delta gap

Table4. 6 Structural parameters of single slot antenna for use with quarter wavelength feeding circuit

L_s	R_s	L_a	W_s	F_a	F_b	h	ε_r
4.0mm	2.4mm	20mm	10mm	0.6mm	0.6mm	0.38mm	2.17

From the simulation results, the resistance of single slot antenna without reflector is within 150Ω to 190Ω over the frequency range of 23GHz to 33GHz. After a reflector is placed under the single slot antenna, the impedance of single slot antenna is changed. The resistance of slot antenna is around 100Ω within frequency of 23GHz to 30GHz. Therefore, reflector has effect on antenna impedance.

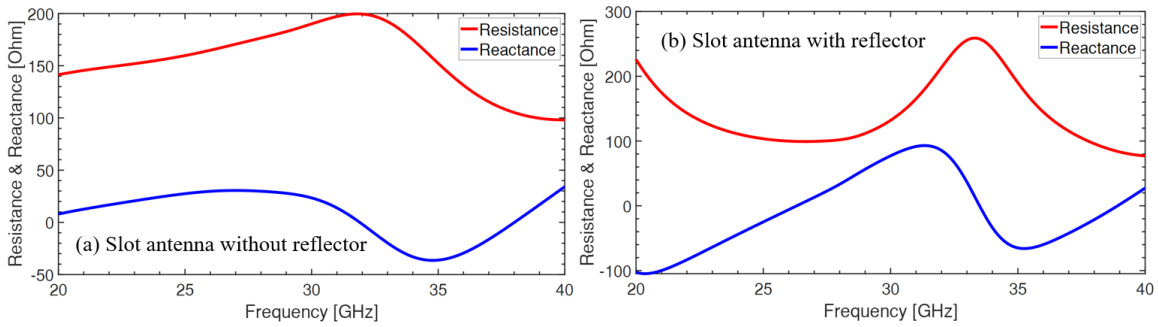

Figure4. 25 Impedance of slot antenna structure with and without reflector

4.5.1 Single Leaf-Shaped Bowtie Slot Antenna Electromagnetically Fed by Microstrip Line

As described above, the antenna characteristics having the stable resistance over the frequency 23GHz to 30GHz. Feeding circuit has been added to the antenna structure to connect to standard connector. The structure of feeding circuit, which is a quarter wavelength matching circuit, is shown as in following Figure4. 26.

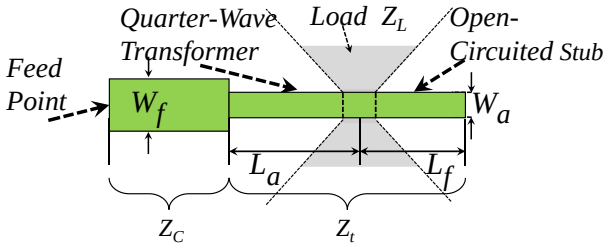

Figure4. 26 Structure of quarter wavelength transformer

The transformer impedance is calculated with antenna's load impedance Z_L=100Ω as in the following equation:

$$Z_c = 50\Omega \ , \quad Z_L = 100\Omega$$
$$Z_t = \sqrt{Z_c Z_L} = \sqrt{50 \times 100}$$
$$Z_t = 70\Omega$$
$$Z_t \cong 70\Omega \rightarrow W_a = 0.7mm$$

The single leaf-shaped bowtie slot antenna structure with quarter wavelength matching circuit is shown in the Figure4. 27. The antenna structural parameters are the same as in Table4. 6. In addition, the single leaf-shaped bowtie slot antenna is backed by a flat reflector to make radiation pattern unidirectional.

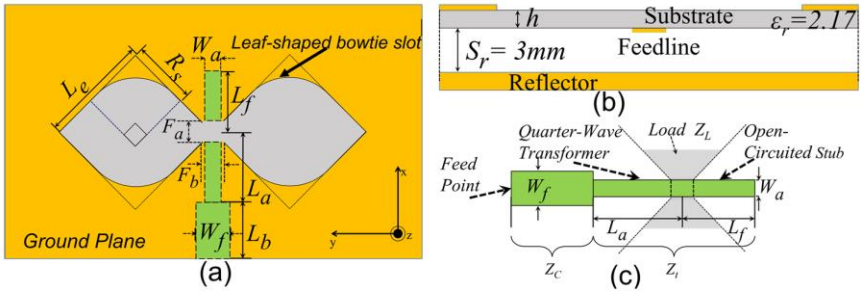

Figure4. 27 Structure of single slot antenna with quarter wavelength feeding circuit

The reflection coefficient of single slot antenna is depending on the width of microstrip line (W_f & W_a). The antenna characteristics are evaluated by performing FDTD analysis in commercial simulation software. In FDTD simulation, grid size is setting as Δx=0.05mm, Δy=0.05mm, and Δz=0.02mm. In the simulation, ground plane, feeding line, and reflector are chosen as PEC. The loss tangent of dielectric substrate is not included in the simulation. Therefore, materials of antenna structure are considered as lossless material. Separation between antenna structure to absorbing boundary in all direction are chosen as 10mm which is about one free space wavelength at frequency of 28GHz. In addition, 10-layer of uniaxial perfectly matched layer is used as the absorbing boundary condition. To analyze antenna characteristics over a wide frequency band, gaussian pulse are excited by line source (delta gap) which is set at the edge of microstrip line and antenna ground plane.

The center frequency of gaussian pules is 30GHz and the bandwidth is 20GHz.Therefore, the antenna characteristics such as reflection coefficient and actual gain are evaluated over the frequency range of 20GHz to 40GHz. The actual gain is evaluated with the sampling frequency of 0.05GHz. As shown in Figure4. 27, the quarter wavelength matching circuit is used as feeding circuit; therefore, the antenna impedance bandwidth is highly depending on the parameter of the quarter wavelength matching circuit. To optimize the impedance bandwidth of the antenna, the parameters such as L_f and W_f are varied. The analysis results of impedance bandwidth of antenna structure by changing the parameters above are shown as in the following Figure4. 28. The reflection coefficient is calculated with reference impedance of 50Ω.

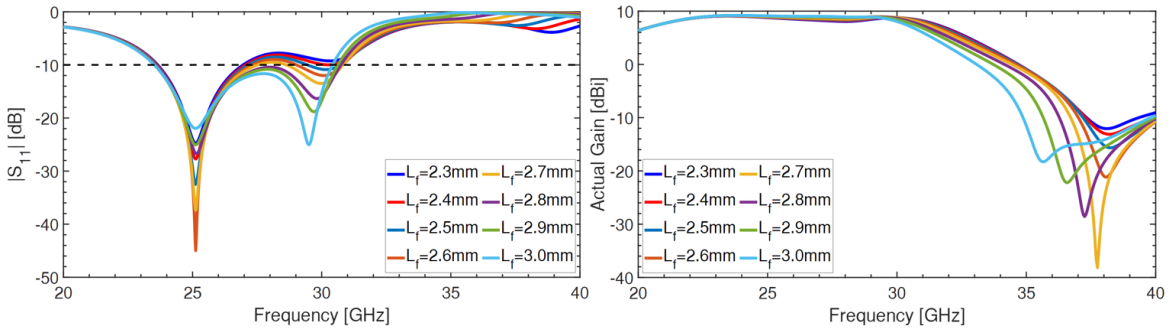

Figure4. 28 $|S_{11}|$ and actual gain of leaf-shaped bowtie slot antenna with reflector by changing L_f

The microstrip line that is used to excite electromagnetic wave at center of the leaf-shaped bowtie slot antenna is terminated by opened circuit line. The length of the opened circuit line L_f is varied from 2.3mm to 3.0mm to investigate the performance of −10dB impedance bandwidth and actual gain of single slot antenna element. From the analysis results in Figure4. 28, the impedance bandwidth is slightly changing versus L_f. From Figure4. 28, the optimum impedance bandwidth is obtained when L_f is chosen as 2.8mm with −10dB impedance bandwidth of 7GHz occupying the frequency range of 23.5GHz to 30.5GHz. On the other hand, antenna actual gain is almost constant versus L_f over the frequency band. In addition, W_f and W_a are also changed to investigate the actual gain reflection coefficient. The analysis results of the antenna characteristics are shown as in Figure4. 29.

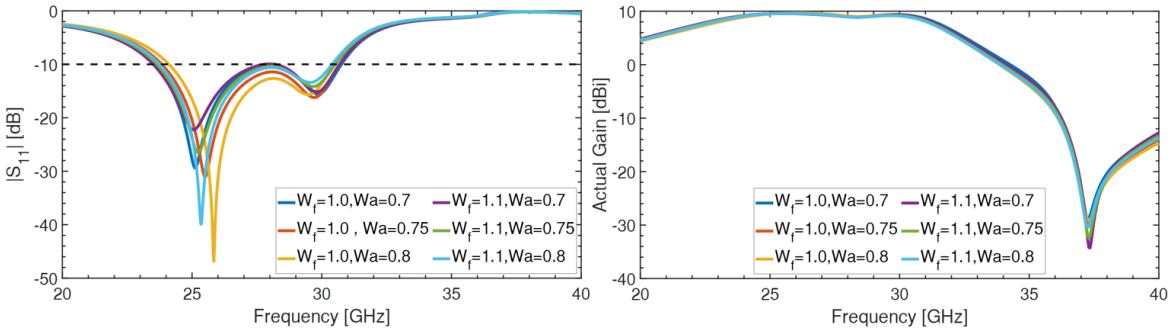

Figure4. 29 $|S_{11}|$ and actual gain of leaf-shaped bowtie slot antenna with reflector by changing W_f & W_a

From the analysis results in Figure, the optimum results of impedance bandwidth and actual gain are obtained with condition of W_f=1.1 and W_a=0.7. Therefore, the optimum parameter of feeding circuit for single leaf-shaped bowtie slot antenna is L_f=2.8mm, W_f=1.1mm, W_a=0.7mm.

Over the desired frequency band 23GHz-33GHz, the −10dB impedance bandwidth of antenna structure is within 23.48GHz−30.68GHz. On the other hand, actual gain doesn't vary when L_f is varied. The maximum actual gain in +z-direction is 9.6dBi, and actual gain is stable over operational impedance bandwidth (23.48GHz−30.68GHz).

4.5.2 Array of Leaf-Shaped Bowtie Slot Antenna Electromagnetically Fed by Microstrip Line and Quarter Wavelength Matching Circuit

From the optimized structure of the previous section (Figure4. 27), linear array of 4 leaf-shaped bowtie slot antennas is designed to increase gain of the antenna structure. The feeding circuit is printed on the bottom the substrate. In this structure, relative permittivity of substrate is ε_r=2.17 and dissipation factor $tan\delta$=0.00085. At center portion of the slot, each radiating element are excited by electromagnetic field propagating on microstrip line which is terminated by opened circuit stub. The length of opened circuit stub is about a quarter of free space wavelength at 28GHz. In addition, quarter wavelength matching circuit is used to

convert from antenna load impedance to 50Ω microstrip line. From the 50Ω microstrip line, each microstrip line are joined in pairs through T-junction connection. From the T-junction connection, quarter wavelength matching circuit is used to transform from 50Ω parallel connection line to 50Ω line. At the end, another T-junction is used to join the 50Ω line and transform to the 50Ω input port. Since the leaf-shaped bowtie slot antenna has bi-directional radiation pattern as shown in the previous section, a flat reflector is placed at a distance S_r under the dielectric substrate. The separation S_r is chosen to optimize both actual gain and −10dB impedance bandwidth. The structure of array of leaf-shaped bowtie slot antenna electromagnetically fed by microstrip line is shown as in the following Figure4. 30. The structural parameters are shown in the Table4. 7.

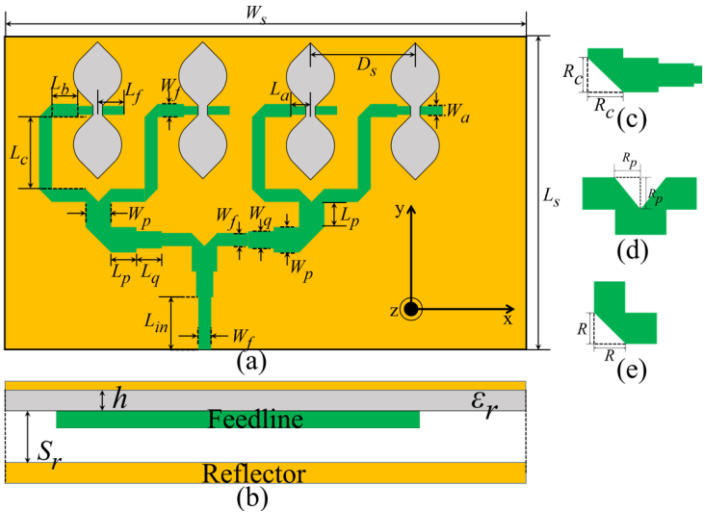

Figure4. 30 Linear array of 4 leaf-shaped bowtie slot antenna with quarter wavelength feeding circuit

Table4. 7 Structural parameters linear array of 4 leaf-shaped bowtie slot antenna with quarter wavelength feeding circuit

W_s	L_s	h	$\boldsymbol{L_f}$	L_a	W_f
50mm	45mm	0.38mm	**2.7mm**	2.0mm	1.1mm
W_a	W_p	W_q	L_p	Lq	L_c
0.7mm	2.6mm	1.5mm	2mm	2mm	8mm
L_{in}	L_b	$\boldsymbol{D_s}$	R	$\boldsymbol{R_c}$	R_p
5mm	1.5mm	**8.5mm**	0.7mm	**2.9mm**	1.2mm

As the element spacing between adjacent radiating slot $\boldsymbol{D_s}$ is getting smaller, the length of opened circuit line $\boldsymbol{L_f}$ is also slightly decreasing to keep the gap between the 50Ω microstrip line. The impedance bandwidth of antenna structure in Figure4. 30 is highly depending on cutting ratio at right-angel bend and at T-junction. The cutting ratio is described as in Appendix. To improve impedance matching, cutting ratio and value of $\boldsymbol{L_f}$ must be adjusted when the element spacing is changed. The value that is more sensitive is cutting ration η_{Rc} which is calculated from $\mathbf{R_c}$. The structural parameters, which are adjusted versus element spacing $\mathbf{D_s}$, are shown as in Table4. 8.

Table4. 8 Variation of L_f and R_c depending on D_s to improve impedance matching

D_s	8.5mm	8.4mm	8.3mm	8.2mm	8.1mm	8.0mm
L_f	2.7mm	2.7mm	2.5mm	2.5mm	2.5mm	2.3mm
R_c	2.9mm	2.9mm	2.8mm	2.8mm	2.8mm	2.8mm

The antenna characteristics are evaluated by performing FDTD analysis in commercial simulation software. In FDTD simulation, grid size is set as Δx=0.05mm, Δy=0.05mm, Δz=0.02mm. 10-layer uniaxial perfectly matched layer is used as absorbing boundary condition. Separation between antenna structure to absorbing boundary condition is 10mm in all direction except in −z-direction. The separation between reflector to absorbing boundary condition is 5mm. In this structure dielectric loss tangent is not included. Ground plane, feeding circuit, and reflector are chosen as PEC. Therefore, the materials in antenna structure are considered as lossless material. Line source (delta gap) is placed at input port (the edge between ground plane and microstrip line) to excite gaussian waveform with center frequency of 28GHz and bandwidth of 2GHz. Therefore, the antenna characteristics are analyzed over the frequency range of 27GHz to 29GHz which is 28GHz band in Japan. The analysis results of actual gain and reflection coefficient are shown as in Figure4. 31. Actual gain of the slot antenna is evaluated with sampling frequency of 0.05GHz. The reflection coefficients are calculated with reference impedance of 50Ω. The element spacing D_s are changed to get optimized actual gain and −10dB impedance bandwidth.

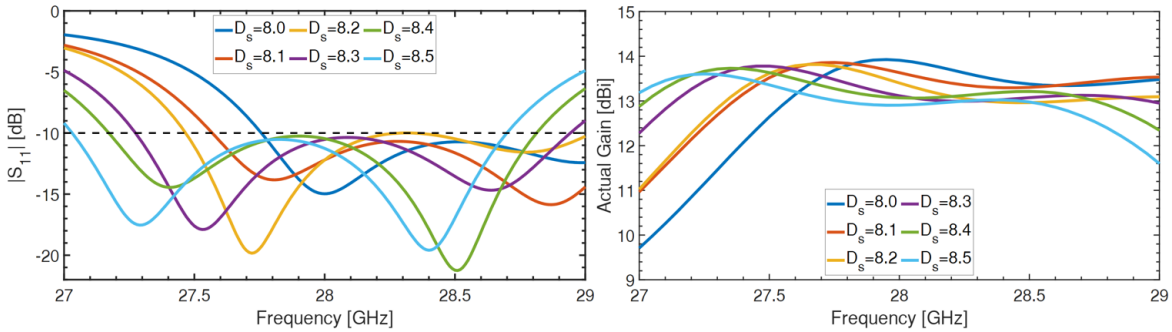

Figure4. 31 $|S_{11}|$ *and actual* leaf-shaped bowtie slot antennas array with quarter wavelength feeding circuit by changing D_s

The antenna element spacing are changing within 8.0mm to 8.5mm. From the analysis results, the impedance bandwidth and actual gain are shown in Figure4. 13 and summarized in Table4. 9:

Table4. 9 Summary of $|S_{11}|$ and actual gain in Figure4. 31

Spacing	−10dB Impedance Bandwidth	Actual Gain (dBi)
D_s=8.0mm	27.76 GHz − 29GHz	9.7dBi – 13.9dBi
D_s=8.1mm	27.57 GHz − 29GHz	10.9dBi – 13.8dBi
D_s=8.2mm	27.47 GHz − 29GHz	11.0dBi – 13.8dBi
D_s=8.3mm	27.27 GHz – 28.95GHz	12.2dBi – 13.7dBi
D_s=8.4mm	27.17 GHz – 28.8GHz	12.3dBi – 13.7dBi
D_s=8.5mm	27.03 GHz – 28.7GHz	11.5dBi – 13.6dBi

From the analysis results in Figure4. 31 and Table4. 9, the −10dB Impedance Bandwidth and Actual gain are slightly changing versus the element spacing D_s. However, the element spacing that offers a maximum −10dB impedance bandwidth is D_s=8.3mm.

In addition, the separation between reflector and substrate is also changed in order to investigate the performance of actual gain and reflection coefficient. In this structure, the element spacing between each radiating slot is chosen as D_s=8.3mm. FDTD method is used to analyze the antenna characteristics. Simulation setting of FDTD is the same as that of the previous section.

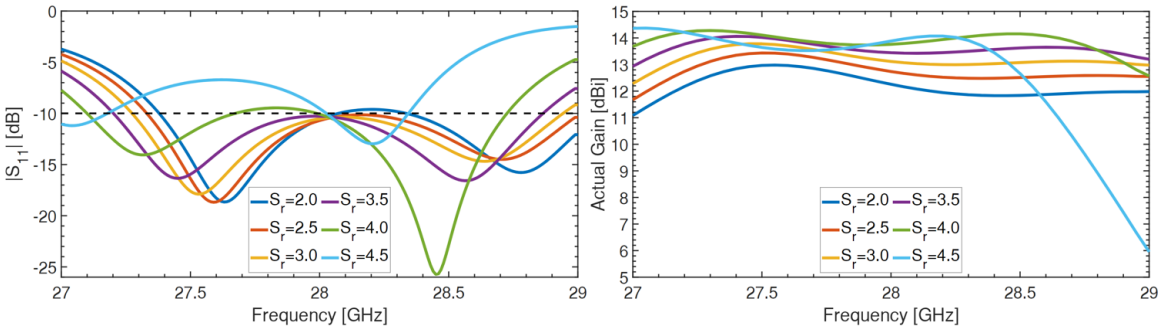

Figure4. 32 $|S_{11}|$ *and actual* leaf-shaped bowtie slot antennas array with quarter wavelength feeding circuit by changing D_s

The separation (S_r) between flat reflector and substrate are changing between 2.0mm to 4.5mm. The sampling point is 0.5mm. Actual gains are evaluated with sampling frequency of 0.05GHz. Reflection coefficients are calculated with reference impedance of 50Ω. From the analysis results which is shown in Figure4. 32, the −10dB impedance bandwidth and actual gain versus separation S_r are summarized as in Table4. 10.

Table4. 10 Summary of $|S_{11}|$ and actual gain in Figure4. 32

Separation (S_r)	−10dB Impedance Bandwidth	Actual Gain
S_r=2mm	27.38−28.07GHz & 28.35−29GHz	11−12.9dBi
S_r=2.5mm	27.33−29GHz	11.6−13.4dBi
S_r=3mm	27.27−28.95GHz	12.2−13.7dBi
S_r=3.5mm	27.2GHz−28.86GHz	13−14dBi
S_r=4mm	27.1−27.67GHz & 28−28.72GHz	12.5−14.2dBi
S_r=4.5mm	27.1−27.18GHz & 28.03−28.34GHz	6−14.3dBi

From the analysis results, the separation between reflector and dielectric substrate is chosen as S_r=3mm to optimize the actual gain and −10dB impedance bandwidth. Therefore, the proposed antenna structure is designed with element spacing between each radiating element is D_s=8.3, and the separation between reflector and dielectric substrate is S_r=3mm. The radiation patterns of the designed antenna are shown as in the following Figure4. 33 and Figure4. 34.

From the analysis results of radiation pattern, the proposed antenna offers a unidirectional radiation pattern. Half-Power Beamwidth of the antenna is within 20° to 25°

along E-plane and within 48° to 52° along H-plane over the frequency band of 27GHz to 29GHz. The maximum cross polarization level is around −20dB along both E-plane and H-plane. Side lobe level at lower frequency is lower than side lobe level at higher frequency. Maximum sidelobe level is −12dB at 27GHz, −10dB at 28GHz and −7dB at 29GHz.

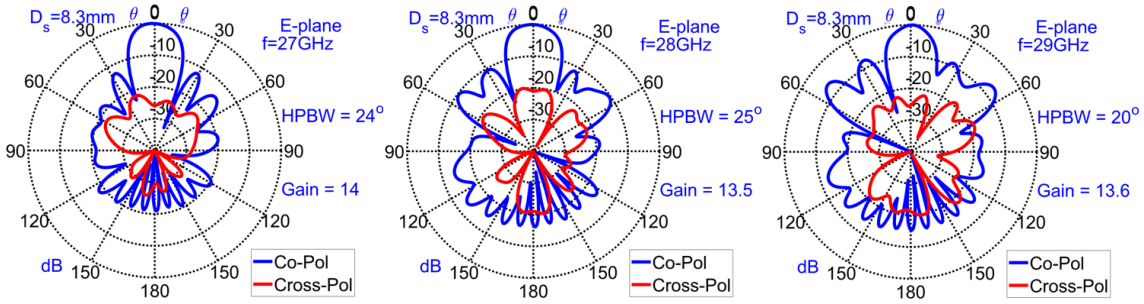

Figure4. 33 E-plane pattern of slot antennas array with quarter wavelength feeding circuit with D_s=8.3mm

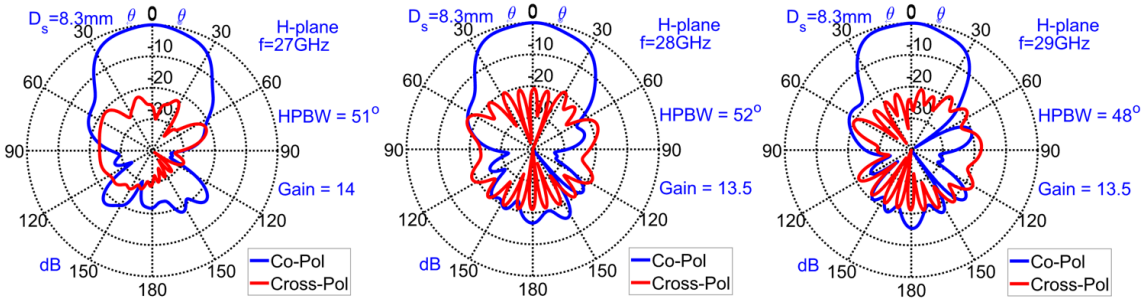

Figure4. 34 H-plane pattern of slot antennas array with quarter wavelength feeding circuit with D_s=8.3mm

In addition to antenna characteristics analysis, dielectric loss and conductor loss are investigated by performing FDTD in commercial simulation software. The dielectric loss is included by using loss tangent tanδ=0.00085. To include conductor loss, ground plane and feeding circuit are treated as lossy metal in FDTD simulation. The conductivity of lossy metal is chosen the same as the conductivity of copper (Cu). In FDTD simulation, grid size and boundary condition are chosen the same as in the previous section4.5.2. The analysis results are shown as in the following Figure4. 35.

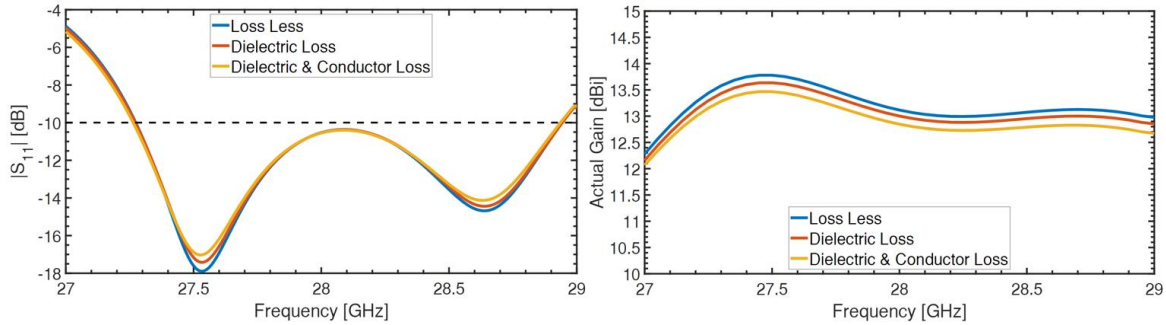

Figure4. 35 Comparison of dielectric and conductor loss of slot antennas array with quarter wavelength feeding circuit

From FDTD analysis results, −10dB impedance bandwidth are in the same band after dielectric loss and conductor are considered in the simulation. However, actual gain of the antenna structure is slightly decreasing after dielectric and conductor loss are considered. The actual gain is decreasing around 0.15dB after only dielectric loss is considered. Moreover, the actual gain is decreasing around 0.3dB after both dielectric loss and conductor loss are considered.

4.5.3 Array of Leaf-Shaped Bowtie Slot Antenna Electromagnetically Fed by Quarter Wavelength Matching Circuit and Microstrip Tapered Line

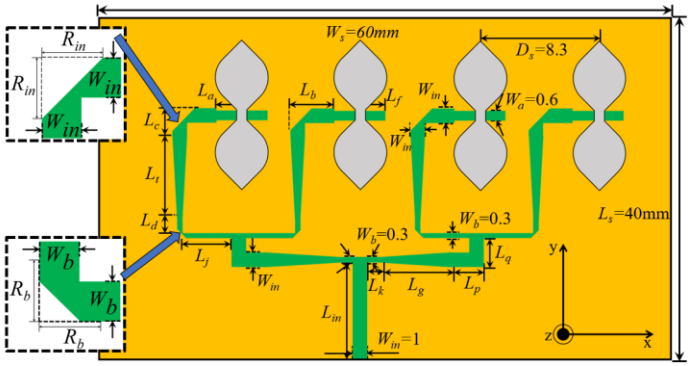

Figure4. 36 Structure of leaf-shaped bowtie slot antenna array electromagnetically fed by quarter wavelength matching circuit and microstrip tapered line

From the previous structure, microstrip tapered line is used instead of quarter wavelength matching circuit at the T-junction. To have balance of impedance within feeding circuit, microstrip tapered line is used to transform from 50Ω of slot antenna feed line to 100Ω line and from 50Ω of T-junction to 100Ω line. To improve impedance matching, the right-angle bending is used in the feeding circuit. Structural parameters of the slot antenna array are shown as in following table.

Table4. 11 structural parameters of slot antenna array with quarter wavelength matching circuit and tapered line

L_a	L_b	L_f	W_{in}	W_a	L_c
2mm	2.55mm	2.1mm	1mm	0.6mm	2.3mm
L_t	L_d	L_j	L_{in}	W_b	L_q
5.5mm	2mm	2.5mm	7.75mm	0.3mm	3mm
L_p	L_g	L_k	R_b	R_{in}	
3mm	4mm	1.3mm	0.3mm	1.6mm	

From the antenna structure as shown in Figure4. 36, the actual gain and reflection $|S_{11}|$ are evaluated by using FDTD in commercial simulation software. The same as previous structure, relative permittivity of substrate is ε_r=2.17 and thickness h=0.38mm. The dissipation factor (loss tangent) $tan\delta$=0.00085. To have unidirectional radiation pattern, a flat reflector is arranged at S_r=2.5mm under the substrate.

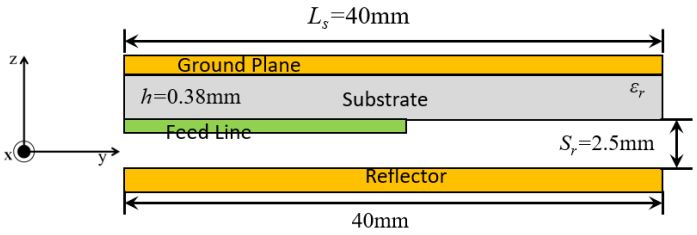

Figure4. 37 side view of slot antenna array with flat reflector

Actual gain is evaluated with sampling frequency of 0.05GHz, reflection coefficient is calculated with reference impedance of 50Ω. To optimize maximum actual gain and impedance bandwidth, antenna element spacing is varied within 8.1mm to 8.5mm. The analysis results of actual gain and impedance bandwidth are shown as in following Figure.

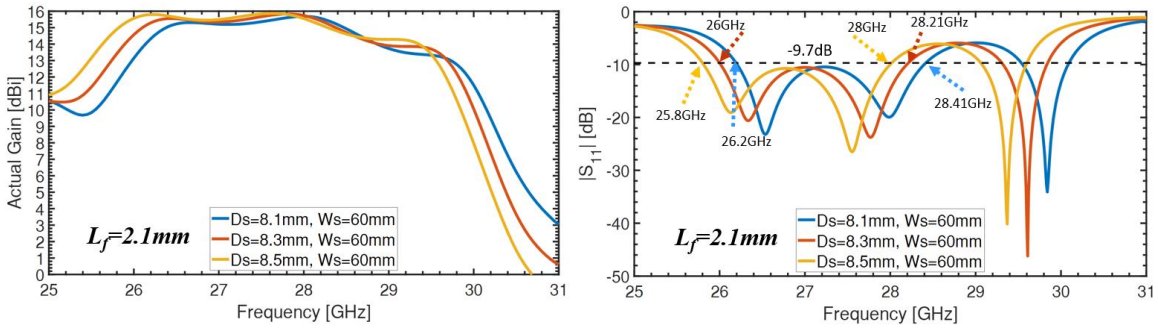

Figure4. 38 Analysis results of actual gain and reflection coefficient

From the comparison of analysis results of actual gain and reflection coefficient, the impedance bandwidth is shifting to lower frequency when D_s is getting larger and higher frequency when D_s is getting smaller. The actual gain is almost the same for each case of element spacing. However, the optimum element spacing is chosen as D_s=8.3mm.

The impedance bandwidth occupies the frequency range of 26GHz to 28.21GHz which is about 2.21GHz. The maximum actual gain is around 15.8dBi and gain bandwidth is within 25.62GHz to 29.7GHz. Comparing to antenna structure in Figure4. 30, the actual is higher, and the impedance bandwidth is wider.

From the radiation pattern analysis in Figure4. 39, the side lobe level in E-plane is less than −10dB within frequency ranges of 26GHz to 29GHz which is operational impedance bandwidth. The maximum actual gain in broadside direction is around 15.9dB at 28GHz. In H-plane, the cross-polarization in H-plane is less than −15dB within 26GHz to 29GHz. Comparison to analysis results in Figure4. 33 and Figure4. 34, the slide lobe level in Figure4. 39 is lower and the beamwidth is smaller.

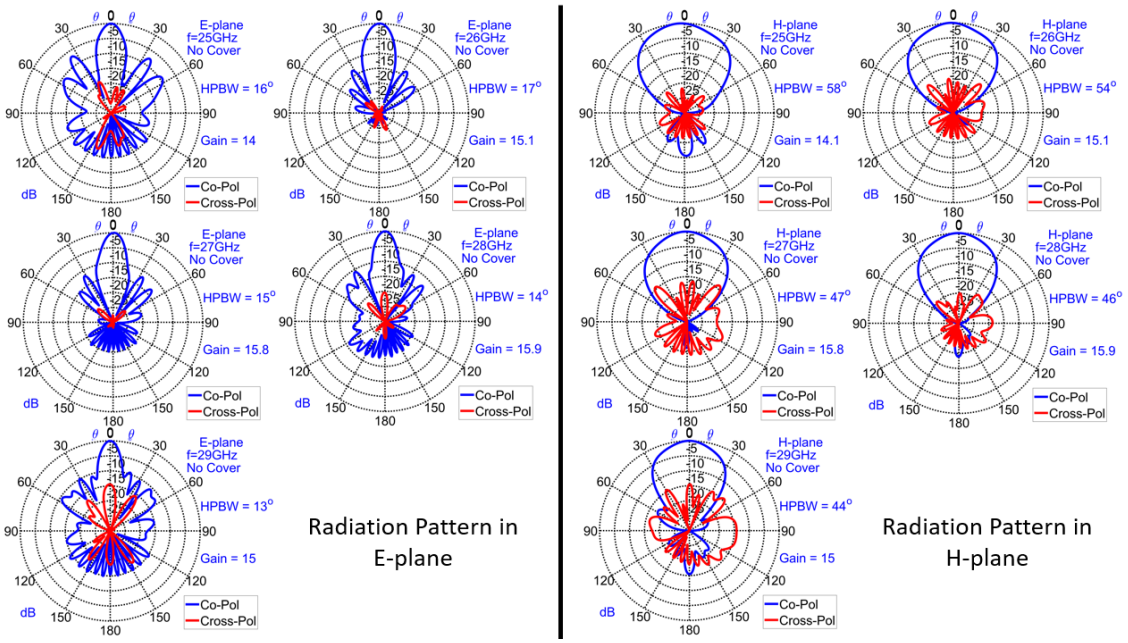

Figure4. 39 Radiation pattern of leaf-shaped bowtie slot antenna electromagnetically fed by quarter wavelength matching circuit and microstrip tapered line

Summary

In Chapter 4, the research progress of leaf-shaped bowtie antenna for use in millimeter wave frequency band has been briefly discussed. In addition, leaf-shaped bowtie slot antenna is proposed and designed for use in millimeter wave frequency band in this research. The antenna characteristics are evaluated within frequency band of 27GHz to 29GHz which is 28GHz band in Japan. Two structures of leaf-shaped bowtie slot antennas array are designed and optimized to achieve maximum impedance bandwidth and actual gain. The first structure is the slot antennas array having normal microstrip line and conductor post as feeding circuit. The second structure is the slot antennas array having quarter wavelength matching circuit as feeding circuit. From analysis results in Chapter 4, the actual gain of the second structure is higher than that of the first structure. In addition, the impedance bandwidth of the second structure is also wider than that of the first structure. On the other hand, microstrip tapered line is used to replace quarter wavelength matching circuit at T-junction. To have balance of impedance within feeding circuit, other tapered lines are used from antenna feed line. As the results, a wider impedance bandwidth and higher actual gain are obtained. Moreover, the fabrication process of second structure is also easier than the fabrication process of the first structure and the second structure.

CHAPTER 5

Gain Enhancement of Leaf-Shaped Bowtie Slot Antenna Array for Use in Millimeter Wave Frequency Band

5.1 Abstract

In Chapter 5, gain enhancement technique is proposed to apply to two structures of leaf-shaped bowtie slot antennas array which are designed and optimized in Chapter 4. Chapter 5 are organized as following. The principal concept of gain enhancement from multiple reflection between partially reflecting surface (PRS) is briefly discussed. In addition, gain enhancement by using frequency selective surface is also briefly discussed. From these two concepts, the gain enhancement of slot antenna by using superstrate layer is also shortly discussed. The application of two superstrate layers to enhance gain of leaf-shaped bowtie slot antenna for ultra-wide band (UWB) is also shown. In this research, two layers of dielectric superstrate are proposed to enhance gain of leaf-shaped bowtie slot antenna array for use in millimeter wave frequency band. The optimization of dielectric superstrate layer will perform to obtain maximum actual gain and −10dB impedance bandwidth. In addition, effect of dielectric loss and conductor loss are also investigated. Finally, the application of leaf-shaped bowtie slot antenna in beam scanning is introduced in this research.

5.2 Overview of Gain Enhancement of Planar Antenna

In [54], multiple reflection of electromagnetic wave between two planes has been studied, and the increase in directivity that results by placing a partially reflecting sheet in front of an antenna with a reflecting screen is investigated at a wavelength of 3.2cm. A large, plane, conducting screen placed behind an antenna is serving as a shield against backward radiation and affecting depending on its spacing and the forward pattern. Improved directivity in the normal direction is possible only to a limited degree because the illumination of reflecting screen is not optimum and the rays reflected from more distance zones produce, in part, out-of-phase contributions. Improved illumination and increase in directivity, and therefore gain, can be obtained by adding a partially reflecting sheet in front of the antenna and parallel to the reflecting sheet in front of the antenna and parallel to the reflecting screen, causing multiple reflections between the sheet and screen. The distance between the sheet and screen must be such that the partial rays projected through the sheet into space have equal phase in the normal direction.

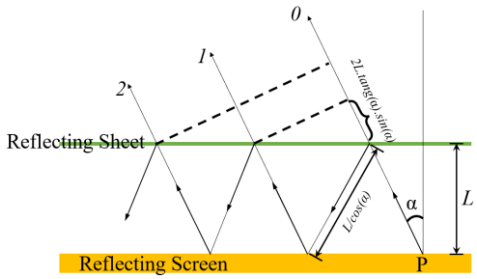

Figure5. 1 Multiple reflection betweeen screen (Reflector) and sheet (PRS)[54]

If antenna is located in front of, or in the plane of, a conducting screen, its radiation can be imagined as originating in a point P of the screen with element pattern $f(\alpha)$ (Figure5. 1). A partially reflecting screen introduces multiple reflections with decreasing amplitudes between these two planes. Let the reflection coefficient of the sheet be $pe^{j\psi}$. Assuming no transmission losses, the amplitude of the direct ray 0 is proportional to $\sqrt{1-p^2}$; the amplitude of the once reflected ray 1 is proportional to $p\sqrt{1-p^2}$; etc. The **electric field intensity** in the Fraunhofer zone consists of the vector sum of these partial rays, and for an infinite screen and sheet we may write:

$$E = \sum_{n=0}^{\infty} f(\alpha)\, E_0 p^n \sqrt{1-p^2} e^{i\Theta_n} \qquad \text{Equation5. 1}$$

The phase angle Θ_n is composed of the phase variations during reflections from the completely reflecting screen and partially reflecting sheet, and also of the path difference of the partial rays. An additional phase shift occurs when a partial ray passes through the sheet, but since this is the same for all rays it need not be considered. From Figure5. 1, the phase difference between ray 1 and ray 0 could be derived as following:

$$\Theta_1 = \frac{2\pi}{\lambda} 2l(tan\alpha)(sin\alpha) - \frac{2\pi}{\lambda}\frac{2l}{cos\alpha} - \pi + \psi \quad \text{Equation5. 2}$$

Between ray 2 and ray 0 as

$$\Theta_2 = \frac{2\pi}{\lambda} 4l(tan\alpha)(sin\alpha) - \frac{2\pi}{\lambda}\frac{4l}{cos\alpha} - 2\pi + 2\psi \quad \text{Equation5. 3}$$

Which somewhat transformed, gives

$$\Theta_n = n\Phi = n\left[-\frac{4\pi}{\lambda} l(cos\alpha) - \pi + \psi\right] \quad \text{Equation5. 4}$$

Since $p < 1$, we obtain

$$\sum_{n=0}^{\infty} \left(pe^{i\Phi}\right)^n = \frac{1}{1-pe^{i\Phi}} \qquad \text{Equation5. 5}$$

Inserting this expression in equation 5.1, The absolute value of field strength becomes

$$|E| = |E_0| f(\alpha) \sqrt{\frac{1-p^2}{1+p^2-2p\cos\Phi}} \quad \text{Equation5. 6}$$

The power pattern is therefore

$$S = \frac{1-p^2}{1+p^2-2p\cos(\psi-\pi-\frac{4\pi}{\lambda}l\cos\alpha)} \quad \text{Equation5. 7}$$

It is considered that the amplitude p and the phase ψ of the sheet reflection coefficient are a function of the angle of incidence α. Maximum power in the direction of $\alpha = 0°$ is obtained when:

$$\psi - \pi - \frac{4\pi}{\lambda} l = 0 \quad \text{Equation5. 8}$$

And hence the equation determining the resonance distance L_r of the sheet is

$$L_r = \left(\frac{\psi_0}{360} - 0.5\right)\frac{\lambda}{2} + N\frac{\lambda}{2} \quad \text{Equation5. 9}$$

With ψ_0 expressed in degrees and N=0, 1, 2, 3, etc. The phase angle for a sheet with inductive field impedance is in the second quadrant, and for a capacitive sheet, in the third quadrant

In [55], a high gain planar antenna has been investigated, using an optimized partially reflecting surface (PRS) placed in front of a waveguide aperture in a ground plane. The antenna performance is initially related to the reflection characteristics of the PRS array following an approximate analysis. The partial reflection can be obtained from periodic arrays, also known as frequency selective surfaces (FSSs), which are customarily used for filtering electromagnetic waves. These are arrays of conducting elements (or apertures in a conducting plane). Typically, they exhibit total reflection (patches) or transmission (apertures) at the resonant frequency, and they are partially reflecting at frequencies near resonance.

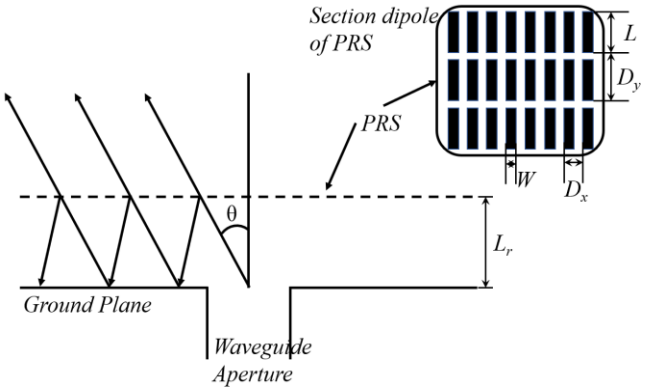

Figure5. 2 Schematic of aperture waveguide antenna and dipole of PRS [55]

Thus far a simple ray theory has been used, based on multiple reflections between the screen and ground plane, to produce the radiation pattern. Both the PRS and the ground plane are assumed to be infinite. In practice, however, the coupling field will be non-uniform across the antenna's surface and therefore, for a high gain and good efficiency, the finite size of the antenna needs to be accounted for. In addition, both the radiation pattern and surface currents will be affected by the diffracted field near the antenna edges.

The antenna was initially analyzed using ray theory approach. The principle of the analysis is like the resonant optical cavity theory. The antenna structure resembles that of a simple Fabry-Perot interferometer, where the reflecting surfaces are now replaced by a highly reflective PRS and a ground plane $\left(R_{gr}=1,\ \varphi_{gr}=-\pi\right)$. The reflection characteristics of the PRS vary with frequency in contrast to the frequency independent response of the partially metallized surfaces used in the interferometer. The schematic diagram of the antenna, using a partially reflective array, is shown in Figure5. 2. An open-ended rectangular waveguide, placed within the ground plane, is used as the primary antenna since it is simple and has adequate bandwidth. The antenna function can be described as following. Waves emerging from the primary antenna travel long paths as a result of multiple reflections between the ground plane and the PRS. A phase shift is introduced by the path length, the total reflection on the ground plane and also by the phase of the reflection coefficient of the PRS. The transmitted power can be calculated by the interference of the wave partially transmitted through the PRS. The sum of the transmitted rays yields an analytic formula for the power pattern, given by the formula as in following:

$$P(\theta)=\frac{\left[1-R^2(\theta)\right]}{1+R^2(\theta)-2R(\theta)\,cos\left[\phi(\pi)-\pi-\frac{4\pi L_r}{\lambda_0}\right]}F^2(\theta) \qquad \text{Equation5. 10}$$

Where:

$R(\theta)e^{j\varphi(\theta)}$ is the complex reflection coefficient of the PRS as a function of θ

λ_0 is the free space wavelength

$F(\theta)$ is the radiation pattern of the primary antenna

L_r is the resonant distance (distance between the PRS and the ground plane)

Maximum power at boresight is obtained when: $\phi(0)-\pi-\frac{4\pi L_r}{\lambda_0}=2N\pi$ or

$L_r=\left(\frac{\phi(0)}{\pi}-1\right)\frac{\lambda_0}{4}+N\frac{\lambda_0}{2}$ where $N=0,1,2,\ldots$ Equation5. 11

An infinite size PRS and ground plane has been assumed. Inserting Equation5. 10 into Equation5. 11 and taking $\theta=0°$, yield an expression for the boresight gain relative to the primary antenna, as a function of the magnitude of the reflection coefficient:

$$G=\frac{P}{F}=\frac{1+R}{1-R} \qquad \text{Equation5. 12}$$

A simple formula for the half-power fractional bandwidth (BW), calculated for a highly reflecting surface with frequency independent reflection characteristics:

$$BW = \frac{\Delta f_{1/2}}{f_0} = \frac{\lambda}{2\pi L_r}\frac{1-R}{\sqrt{R}} \qquad \text{Equation5. 13}$$

From Equation5. 12, Gain (G) increase considerably with R, and high gain can be obtained with highly reflective screen. However, from Equation5. 13, BW decreases as R increases, and the narrower bandwidth is expected for resonant distance beyond the first one. In addition, as *N* increases the sidelobes become higher.

A way to increase both the gain and bandwidth of this resonant structure is to optimize the reflection characteristics (magnitude and phase) of the PRS by using Equation5. 11 and Equation5. 12. The resonant distance L_r is a function of the operating frequency and the reflection coefficient of the PRS. It has been a fixed value for a certain operating frequency of the antenna. Rearranging the phase condition from Equation5. 11 shows that for maximum gain within a certain frequency range the phase of the reflection coefficient of the PRS must satisfy the following relationship:

$$\phi(0) = \frac{4\pi L_r}{c} f - (2N-1)\pi \qquad \text{Equation5. 14}$$

Therefore, a linear increasing (with frequency) phase response will result in maximum gain within a certain frequency range. The maximum gain will be determined from the magnitude of the reflection coefficient, which should ideally be constant as indicated from Equation5. 12. Under these two conditions high gain and wide bandwidth can be obtained. Therefore, [54][55] gain of the whole antenna structure is physically depending on the separation between PRS and ground plane (L_r).

In [56], bandwidth and gain of resonant cavity antenna has been enhanced by applying two high permittivity dielectric layers as superstrates. The approach is based on creating two cavity corresponding to two operating frequency bands that combine to form a single wide band of operation. [56] The proposed technique is capable of enhancing the bandwidth from 9% of the single superstrate RCA to 17.9% of the two superstrate RCA, with only 0.1dB reduction of the maximum directivity (17.5dBi). The presented design method can be replicated for any RCA with any directivity level and type of primary feeding. In [56], two main aspects are presented. First aspect, a step-by-step and non-iterative method to calculate the structure variables needed to enhance the bandwidth is presented, which is short process to analyses the PRS. Second aspect is the better understanding of the physical insight behind the improvement of bandwidth. Each variable of the structure is comprehensively digested with regard to its influence into the overall antenna performance. Although the optimization process in [56] is in short process, the concept for designing PRS (Dielectric Superstrates) is still finding the optimized parameter of magnitude and phase of reflection coefficient of PRS (Dielectric Superstrates). In [56], relative permittivity, and thickness of superstrate, and

distance between each superstrate layers and between ground plane have been tuned to the optimum reflection coefficient of PRS (Dielectric Superstrates). Therefore, the optimum gain and −3dB gain bandwidth can be realized. In [56], the antenna structure, which is used as primary source, is a standard Ku-band waveguide (WR-62). The antenna has high profile, and it is difficult to be integrated with other devices.

In [57], gain enhancement and bandwidth improvement of a 2×2 square dense dielectric patch antenna using a holey superstrate are proposed. The aperture-coupled antenna is fed by a conventional power divider. A dielectric superstrate layer is utilized to enhance the antenna gain. Moreover, by drilling a set of identical circular holes in the superstrate layer, the antenna bandwidth is improved, and the sidelobe level is decreased. The proposed antenna is fabricated and tested. The prototype yields an impedance bandwidth of 15.35% from 26.5 to 30.8GHz. The proposed antenna exhibits a flat measured gain of about 16dBi over all the bandwidth with a high simulated radiation efficiency of 92%. Furthermore, the sidelobe levels of the antenna are −15.8dB and −21dB in the E-plane and H-plane, respectively. In [57], dense dielectric patches were fabricated with a length Lp=4.1mm and a height Hp=0.15mm with relative permittivity of 82. The dense dielectric patches are printed on a Rogers Duroid 6002 substrate (top layer) with thickness h_1=20mil (ε_r=2.94 and $tan\delta$=0.0009). The bottom substrate is Rogers RT 3010 with the same thickness as the top substrate. The two substrates have the same length and width (L=W=20mm). A 50-Ω conventional power divider is located on the bottom side of the bottom substrate. Moreover, the aperture-coupling feed method is used to excite the 2×2 DD patch antenna array. The coupling slot in the common ground plane between the two layers has a length L_s=2.55mm and width W_s=0.25mm. Furthermore, a superstrate dielectric layer with a relative permittivity of 10.2 and thickness h_s=0.64mm is designed and applied over the 2×2 dense dielectric patch antenna array with a distance d=5.32mm above the array. In addition, dielectric superstate layer is perforated by a set of identical periodical circular holes of diameter D (with period P) placed along x-axis and y-axis. From structure in [57], the antenna elements are fabricated from dense dielectric with high relative permittivity which is not easy to fabricate by using etching and engraving method. In addition, the antenna structure needs two layers substrate to design feeding circuit, this process is also complicated. In return, the antenna structure has offered a wide impedance bandwidth which occupies the frequency range from 26.5GHz to 30.8GHz. However, the antenna structure has offered a maximum realized gain of 16dBi which is not high enough.

5.3 Gain Enhancement of Leaf-Shaped Bowtie Slot Antenna Array for UWB Application

In [58], Gain of linear array of 4 leaf-shaped bowtie slot antennas has been enhanced by using 2 layers of dielectric superstrate. In [58], the antenna structure has been designed for use in Ultra-Wide Band frequency band (UWB high band). In [58], the radiating slots are cut on a ground plane of a dielectric substrate with thickness of h=0.76mm and relative

permittivity of ε_r=2.17. The relative permittivity of dielectric superstrate is ε_{rs}=10.7. In [58], the corporate feed is used to excite the four slot antennas with equal amplitude and equal phase. Antenna feeding circuit is composed of microstrip lines and three pairs of T-junctions. These components are arranged on the bottom side of the dielectric substrate. The ends of the microstrip lines are connected to the slot antennas by conductor probe with the diameter of *d*. To realize unidirectional radiation pattern, a metal flat reflector is placed underneath the antenna substrate with the separation of S_r. For the gain enhancement, two layers of identical dielectric superstrate are placed above the slot antenna array. The location of superstrate layers is adjusted to get the optimum actual gain and −10dB impedance bandwidth. The reflection for the case with dielectric superstrate is below −10dB over the frequency band of 7.8−8.9GHz and 9.5−9.6GHz, which correspond to the fractional bandwidth of 13% and 1%, respectively. It is seen that the operating bandwidth is increased by placing the dielectric superstrate in front of the antenna array. The maximum actual gain for the case with the dielectric superstrate is 19.5dBi and 19.7dBi are observed at two frequencies of 8.2GHz and 9.6GHz, respectively. The −3dB bandwidth with respect to the peak gain is 7.7−8.6GHz and 9.4−9.8GHz, which correspond to the fractional bandwidth of 11% and 4%, respectively.

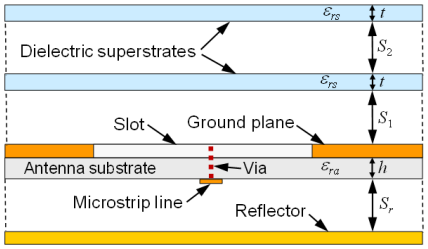

h[mm]	ε_{ra}	S_1[mm]	S_2[mm]
60	2.17	18	20
S_r[mm]	ε_{rs}	t[mm]	
12	10.7	1.5	

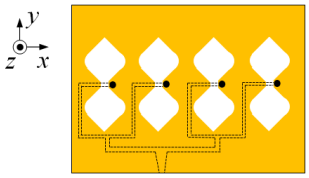

Figure5. 3 Gain enhancement of leaf-shaped bowtie slot antenna array for use in UWB systems [58]

5.4 Gain Enhancement of Leaf-Shaped Bowtie Slot Antenna Array for Use in mm-Wave Band

In this research, dielectric superstrate layer has been employed to enhance gain of leaf-shaped bowtie slot antennas array for use in millimeter wave frequency band. The linear array of 4 leaf-shaped bowtie slot antennas, which are designed and optimized in section 4.4.2 and section 4.5.2, are used in the enhancement procedure.

5.4.1 Gain Enhancement of Leaf-Shaped Slot Antenna Array Fed by Microstrip Line and Conductor Probe

A. Antenna structure with one layer of dielectric superstrate

Linear array of leaf-shaped bowtie slot antenna, whose radiating slot has element length L_e=2.7mm, is used as first case study for gain enhancement. The antenna structure has been

designed and optimized as in section 4.4.2 Figure4. 16 and Figure4. 18. To investigate effect of dielectric superstrate on actual gain and reflection coefficient of the slot antennas array, one layer of dielectric superstrate has been placed on the top of antenna ground plane. The structure of the slot antennas array with one layer of dielectric superstrate is shown as in the following Figure5. 4.

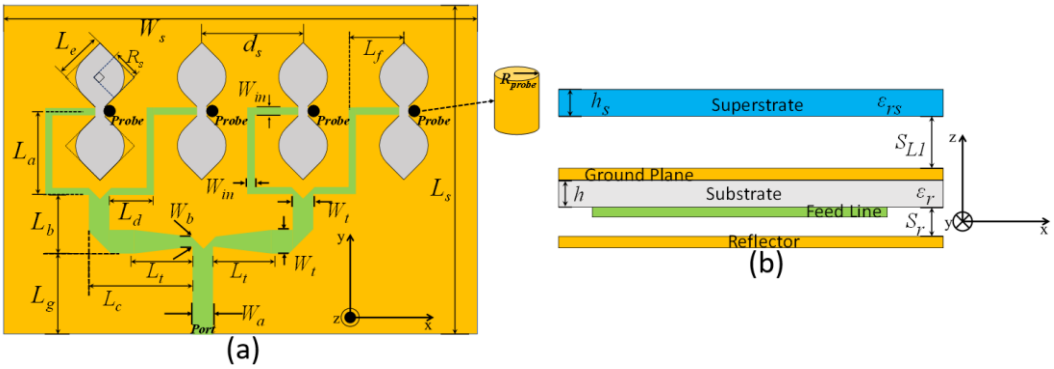

Figure5. 4 Leaf-shaped bowtie slot antenna array with 1 layer of dielectric superstrate.

From Figure5. 4, the separation between superstrate layer and the antenna ground's plane is presented by S_{L1}. The relative permittivity of dielectric superstrate is ε_{rs}=10.2, with dielectric loss tangent $tan\delta$=0.0023. The thickness of dielectric superstrate is h_s=0.6mm. After a dielectric superstrate layer is placed on top antenna ground plane, a resonant cavity is also created. The thickness of resonant cavity is the separation between superstrate layer and ground plane (S_{L1}). The antenna characteristics such as gain, and reflection coefficient are highly depending on the thickness of the cavity which is the separation S_{L1}. Therefore, the antenna characteristics are highly depending on the location of dielectric superstrate layer. To obtain the optimum actual gain and −10dB impedance bandwidth, the location of superstrate layer is shifted along *z*-axis. The antenna characteristic such as actual gain and reflection coefficient are evaluated by using FDTD analysis in commercial simulation software. In FDTD simulation setting, grid size is chosen as Δx=0.05mm, Δy=0.05mm, and Δz=0.02mm for dielectric substrate, and Δz=0.05mm for dielectric superstrate layer. 10-layer uniaxial perfectly matched layer is used as absorbing boundary condition. The separation between antenna structure to absorbing boundary condition is 10mm in all direction, except in −z-direction. The distance between reflector to absorbing boundary condition is 5mm. Line source (delta gap source) has been placed at edge of microstrip line and ground plane to excite gaussian signal with center frequency of 28GHz and 2GHz bandwidth. Dielectric loss and conductor loss are not included in this simulation. The analysis results of actual gain and reflection coefficient by changing location of dielectric superstrate layer are shown as in following Figure5. 5. The actual gain is calculated over the frequency range of 27GHz to 29GHz with the sampling frequency of 0.05GHz. The reflection coefficient is calculated with reference impedance of 50Ω.

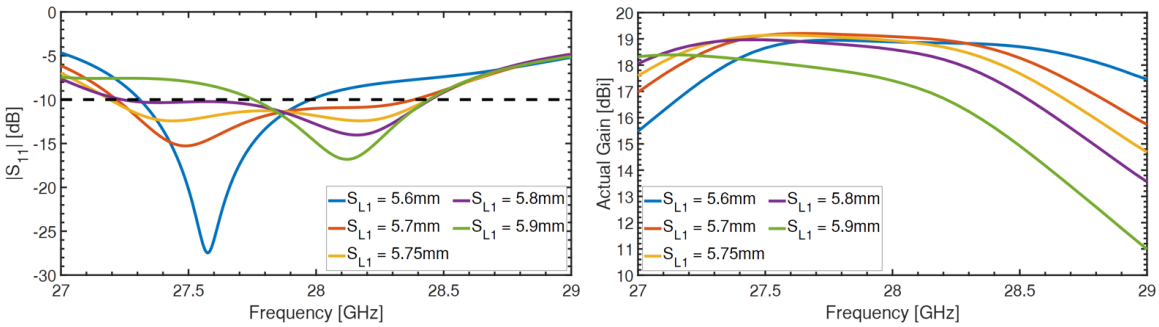

Figure5. 5 Actual gain and $|S_{11}|$comparison by changing separation S_{L1}.

Table5. 1 summary of −10dB impedance bandwidth and maximum actual gain of Figure5. 5

S_{L1}(mm)	−10dB impedance bandwidth	Maximum actual gain
S_{L1}=5.6	0.66GHz (27.31−27.97GHz)	18.94dBi
S_{L1}=5.7	1.16GHz (27.22−28.38GHz)	19.2dBi
S_{L1}=5.75	1.25GHz (27.19−28.44GHz)	19.14dBi
S_{L1}=5.8	1.2GHz (27.24−28.44GHz)	18.96dBi
S_{L1}=5.9	0.68GHz (27.76−28.44GHz)	18.39dBi

Figure5. 5 shows the comparison of the frequency response of $|S_{11}|$ by changing distance S_{L1}. From the comparison, the maximum −10dB impedance bandwidth, which is about 1.25GHz, is obtained when separation S_{L1} is chosen as 5.75mm. Figure5. 5 shows analysis results of actual gain by changing the separation S_{L1}. The maximum actual gain is obtained at two value of separation S_{L1}(S_{L1}=5.7mm, and S_{L1}=5.75mm). From both results of −10dB impedance bandwidth and actual gain, the optimum separation between antenna ground plane and dielectric superstrate layer S_{L1} is chosen as S_{L1}=5.75mm. Comparison between characteristics of antenna structure with one layer of dielectric superstrate and characteristics of antenna structure without dielectric superstrate layer are shown as in following Figure5. 6.

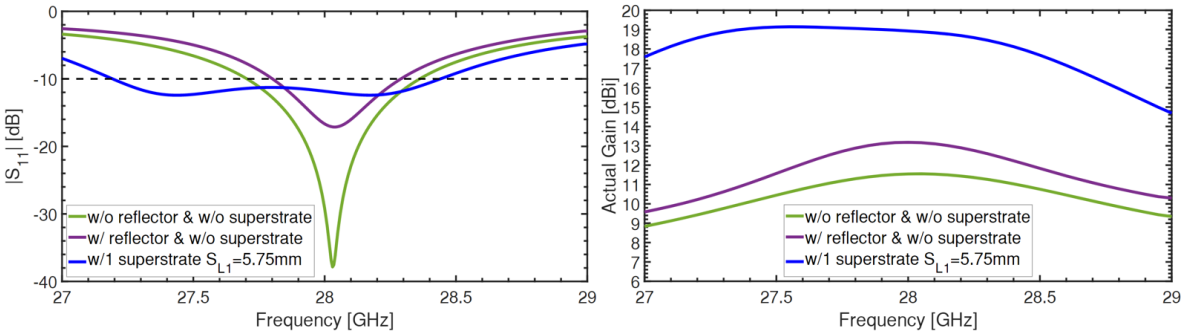

Figure5. 6 Actual gain and $|S_{11}|$ comparison after one layer of superstrate is used.

From Figure5. 6, it can be seen that −10dB impedance bandwidth of the slot antenna array with one layer of dielectric superstrate occupies frequency range of 27.19GHz to 28.44GHz, which is about 1.25GHz. The −10dB impedance bandwidth of the slot antenna array with only reflector occupies frequency range of 27.8GHz to 28.29GHz which is about 490MHz. Therefore, the −10dB impedance bandwidth increases around 780MHz after one

layer of dielectric superstrate is used. In addition, it can be observed that actual gain in +z direction is about 19.14dBi and −3dB gain bandwidth occupies the frequency range of 27GHz to 28.77GHz which is about 1.77GHz gain bandwidth. In addition, the antenna structure with only reflector has maximum actual gain of 13.17dBi and −3dB gain bandwidth occupies frequency range of 27.17GHz to 29GHz which is about 1.83GHz. Therefore, the maximum actual gain has been enhanced around 6dBi. As the results, by using one layer of dielectric superstrate, −10dB impedance bandwidth and actual gain have been enhanced around 780MHz and 6dBi, respectively. In addition, the comparison of actual gain between antenna structure with one layer of superstrate and with only reflector are shown as in the following Figure5. 7 and Figure5. 8.

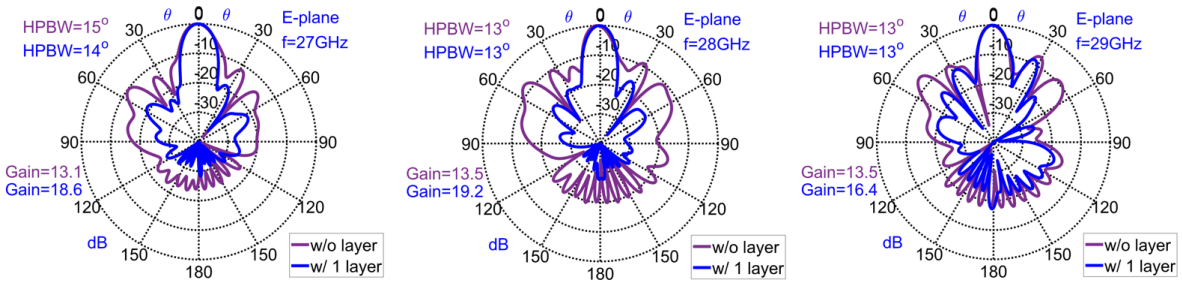

Figure5. 7 E-plane comparison of antenna structure without layer and with one layer.

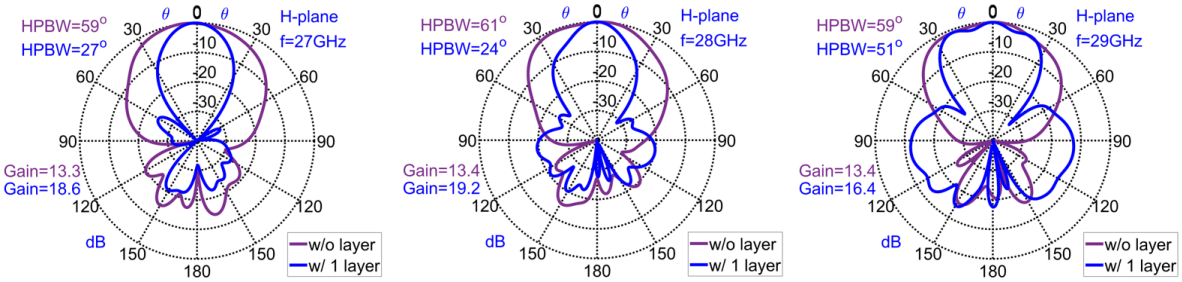

Figure5. 8 H-plane comparison of antenna structure without layer and with one layer.

Figure5. 7 and Figure5. 8 shows the radiation pattern comparison of the antenna structure with one layer of dielectric superstrate and antenna structure with only reflector. The analysis results of radiation pattern are evaluated at 27GHz, 28GHz, and 29GHz. It can be confirmed that radiation pattern has been improved after one layer of dielectric superstrate is used. In E-plane, maximum sidelobe level is −20dB at 27GHz, −16dB at 28GHz, and −10dB at 29GHz. From antenna structure with only reflector, maximum sidelobe level is −10dB at 27GHz, −8dB at 28GHz, and −6dB at 29GHz. Therefore, sidelobe level is decreasing around 10dB at 27GHz, 8dB at 28GHz, and 4dB at 29GHz. HPBW of antenna structure with one layer of dielectric superstrate and with only reflector are slightly different at 27GHz. In H-plane, HPBW is 27° at 27GHz, 24° at 28GHz, and 51° at 29GHz. From antenna structure with only reflector, HPBW is 59° at 27GHz, 61° at 28GHz, and 59° at 29GHz. Therefore, HPBW in H-plane has decreased 32° at 27GHz, 37° at 28GHz, and 8° at 29GHz.

B. Antenna structure with two layers of dielectric superstrate

To further investigate the effect of dielectric superstrate layer on antenna actual gain and reflection coefficient, two layers of dielectric superstrate are arranged on top of antenna ground plane. The characteristic of first layer and second layer are identical. Relative permittivity of dielectric superstrate is ε_{rs}=10.2 and thickness is h_s=0.6mm. The S_{L1} represents separation between ground plane and 1st layer, and S_{L2} represents separation between 1st layer and 2nd layer. Structure of the slot antennas array with two layers of dielectric superstrate is shown as in Figure5. 9.

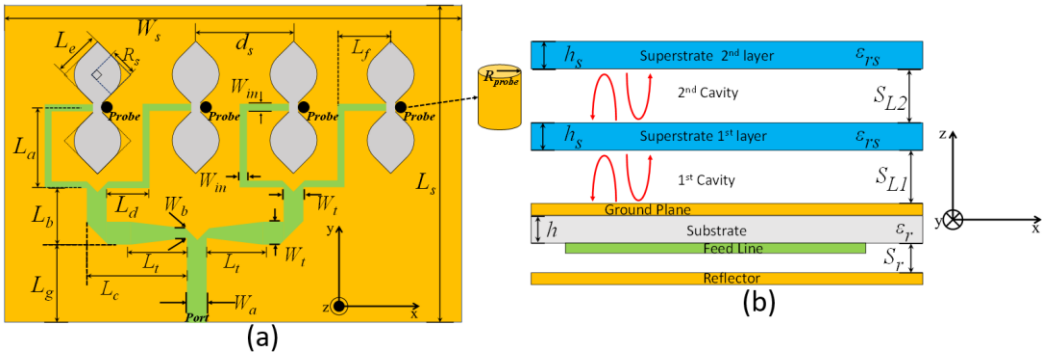

Figure5. 9 Leaf-shaped bowtie slot antenna array with 2 layers of dielectric superstrate.

From Figure5. 9, two resonant cavities are formed after two layers of dielectric superstrate are placed on top of the slot antennas array. First cavity is created between first dielectric superstrate layer and ground plane. Second cavity is created between second dielectric superstrate layer and first dielectric superstrate layer. The performances of antenna characteristic are highly depending on the thickness of resonant cavities which are S_{L1} and S_{L2}. Therefore, the separation S_{L1} and S_{L2} are shifted along *z*-axis and precisely optimized to get maximum performance of actual again and −10dB impedance bandwidth. The antenna characteristic such as actual gain and reflection coefficient are evaluated by using FDTD analysis in commercial simulation software. In FDTD simulation setting, grid size is chosen as Δx=0.05mm, Δy=0.05mm, and Δz=0.02mm for dielectric substrate, and Δz=0.05mm for dielectric superstrate layer. 10-layer uniaxial perfectly matched layer is used as absorbing boundary condition. The separation between antenna structure to absorbing boundary condition is 10mm in all direction, except in −z-direction. The distance between reflector to absorbing boundary condition is 5mm. Line source (delta gap source) has been placed at the edge of microstrip line and ground plane to excite gaussian signal with center frequency of 28GHz and 2GHz bandwidth. Dielectric loss and conductor loss are not included in this simulation. The analysis results of actual gain and reflection coefficient by changing location of dielectric superstrate layer are shown as in following Figure5. 10. The actual gain is calculated over the frequency range of 27GHz to 29GHz with the sampling frequency of

0.05GHz. The reflection coefficient is calculated with reference impedance of 50Ω. The analysis results are summarized as in Table5. 2.

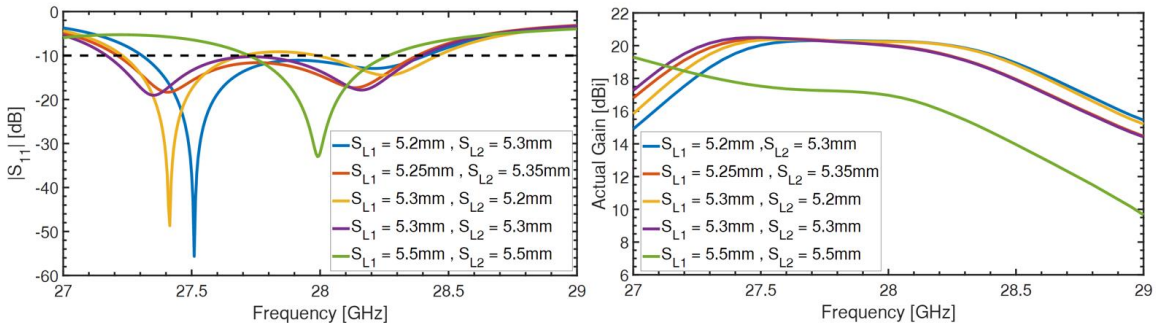

Figure5. 10 Actual gain and $|S_{11}|$ comparison by changing separation S_{L1} & S_{L2}.

Table5. 2 Summary of −10dB impedance bandwidth and maximum actual gain of Figure5. 10

S_{L1} & S_{L2} (mm)	−10dB Impedance Bandwidth	Maximum Actual Gain
S_{L1}=5.2, S_{L2}=5.3	1.1GHz (27.31−28.41GHz)	20.30dBi
S_{L1}=5.25, S_{L2}=5.35	1.16GHz (27.21−28.37GHz)	20.44dBi
S_{L1}=5.3, S_{L2}=5.2	0.47GHz (27.23−27.7GHz) 0.46GHz (27.99−28.45GHz)	20.37dBi
S_{L1}=5.3, S_{L2}=5.3	1.22GHz (27.17−28.39GHz)	20.49dBi
S_{L1}=5.5, S_{L2}=5.5	0.54GHz (27.72−28.26GHz)	19.29dBi

From the analysis results, maximum −10dB impedance bandwidth is obtained at S_{L1}=5.3mm and S_{L2}=5.3mm. The maximum −10dB impedance bandwidth is about 1.22GHz bandwidth. The analysis results also show the actual gain comparison by changing separation S_{L1} and S_{L2}. Maximum actual gain is obtained at S_{L1}=5.3mm, and S_{L2}=5.3mm. The maximum actual gain is around 20.49dBi. Comparison between characteristics of antenna structure with two layers of dielectric superstrate and characteristics of antenna structure without dielectric superstrate layer are shown as in following Figure5. 11.

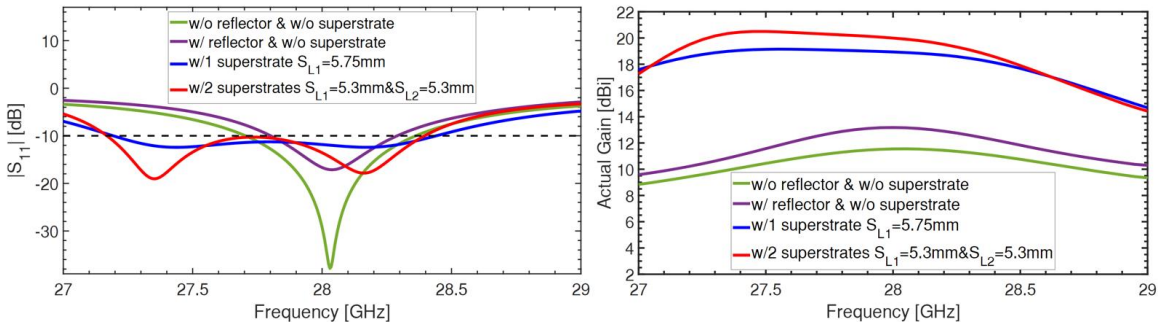

Figure5. 11 Actual gain and $|S_{11}|$ comparison after two superstrate layers are used.

From analysis results in Figure5. 11, it can be seen that −10dB impedance bandwidth of the slot antennas array with two layers of dielectric superstrate occupies the frequency range

of 27.17GHz to 28.39GHz which is about 1.22GHz, whereas −10dB impedance bandwidth of the slot antenna array with one layer of dielectric superstrate occupies frequency range of 27.19GHz to 28.49GHz, which is about 1.25GHz. Therefore, −10dB impedance bandwidth of the antenna structure has decreased around 30MHz, after two layers of dielectric superstrate are used. From analysis results, maximum actual gain in broadside direction is about 20.49dBi and −3dB gain bandwidth occupies the frequency range of 27.02GHz to 28.57GHz, which is about 1.55GHz. Thus, the −10dB impedance bandwidth is in the same band as −3dB gain bandwidth. Comparing to antenna structure with one layer of superstrate, actual gain increases around 2dB and −10dB impedance bandwidth decrease around 30MHz. Comparing to antenna structure with only reflector, actual gain increases around 7dB, and −10dB impedance bandwidth is around 800MHz wider. Therefore, the performance of antenna characteristics such as actual gain and impedance bandwidth has been enhanced after two layers of dielectric superstrate are arranged on the top linear array of 4 leaf-shaped bowtie slot antennas. The comparison of radiation pattern between the antenna structure with two layers of superstrate and one layer of superstrate are shown as in following Figure5. 12 and Figure5. 13. The radiation patterns are evaluated at 27GHz, 28GHz, and 29GHz by performing FDTD.

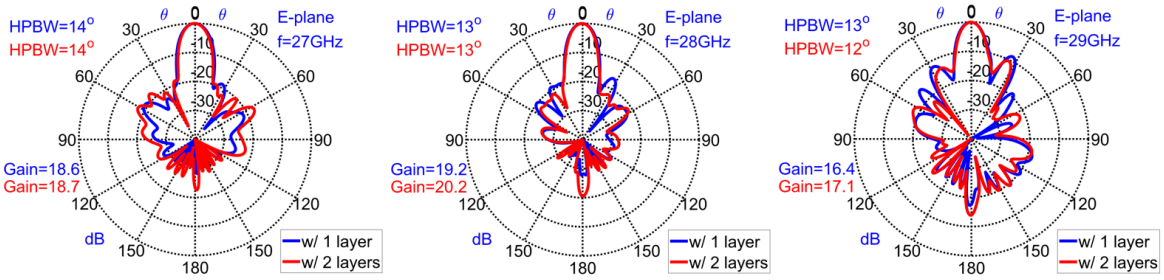

Figure5. 12 E-plane comparison between antenna structure with one superstrate layer and two superstrate layers.

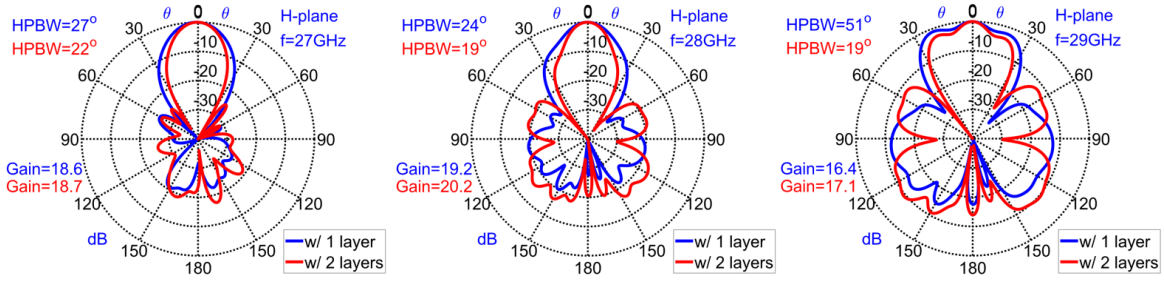

Figure5. 13 H-plane comparison between antenna structure with one superstrate layer and two superstrate layers

For antenna structure with two layers of superstrate, maximum sidelobe level is around −18dB at 27GHz, −20dB at 28GHz, and −10dB at 29GHz in E-plane. For antenna with one layer of superstrate, maximum sidelobe level is around −20dB at 27GHz, −16dB at 28GHz, and −10dB at 29GHz. Therefore, maximum sidelobe level has increased 2dB at 27GHz, decreased 4dB at 28GHz, and slightly changed at 29GHz in E-plane. However, both antenna

structures have almost the same HPBW along E-plane. However, in H-plane, HPBW has decreased 5° at 27GHz and 28GHz, and 32° at 29GHz.

To confirm that the element spacing between each adjacent slot is optimum for the case of the slot antenna array with 2 layers of superstrate, the actual gain and reflection coefficient are investigated by changing the element spacing d_s. The analysis results of antenna characteristics, which are evaluated by performing FDTD in commercial simulation software (Sim4Life), are shown as in the following Figure5. 14.

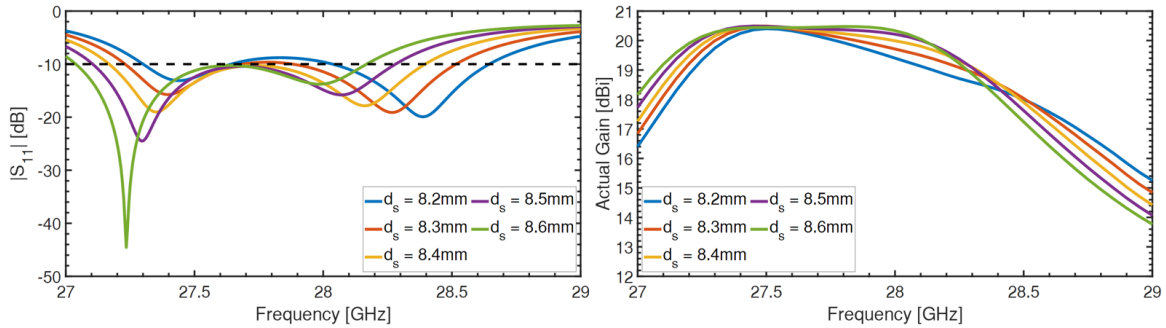

Figure5. 14 Actual gain and $|S_{11}|$ comparison of antenna structure with two superstrate layers by changing element spacing d_s

Table5. 3 Summary of −10dB impedance bandwidth and maximum actual gain of Figure5. 14

d_s(mm)	−10dB impedance bandwidth	Maximum actual gain
d_s = 8.2	0.34GHz (27.3 − 27.64GHz) 0.6GHz (28.04 − 28.64GHz)	20.4dBi
d_s = 8.3	0.45GHz (27.23 − 27.68GHz) 0.63GHz (27.88 − 28.51GHz)	20.47dBi
d_s = 8.4	1.22GHz (27.17 − 28.39GHz)	20.49dBi
d_s = 8.5	1.18GHz (27.1 − 28.28GHz)	20.49dBi
d_s = 8.6	1.12GHz (27.04 − 28.16GHz)	20.49dBi

The effect of the element spacing d_s on −10dB impedance bandwidth and maximum actual gain is summarized as in Table5. 3. The analysis results show that actual gain has maximum value at d_s=8.4mm, d_s=8.5mm, and d_s=8.6mm. The maximum −10dB impedance bandwidth is obtained at d_s=8.4mm. Therefore, the optimum element spacing for both −10dB impedance bandwidth and actual gain is d_s=8.4mm.

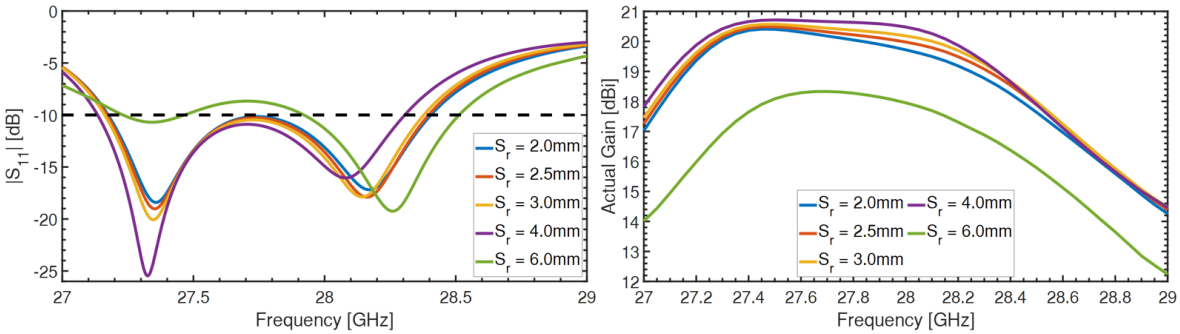

Figure5. 15 Comparison of actual gain and $|S_{11}|$ by varying separation S_r

To confirm that the separation (S_r) between dielectric substrate and reflector is optimum, the separation S_r is changed within 2mm to 6mm along z-direction. Actual gain and reflection coefficient are evaluated to investigate the effect of S_r. FDTD in commercial simulation software is performed to analyze the antenna characteristics. The simulated results of antenna characteristics are shown as in Figure5. 15. For analysis results, the optimum actual gain is obtained when S_r is chosen as S_r=4mm, and the optimum −10dB impedance bandwidth is obtained when S_r is chosen as S_r=2.5mm. However, the difference between actual gain at S_r=4mm and S_r=2.5mm is around 0.3dB to 0.5dB. Therefore, the separation between dielectric substrate and reflector is chosen as S_r=2.5mm. As the results, the optimum parameters which are chosen to design antenna prototype are shown as in Following Table.

Table5. 4 Optimized parameters for fabrication

d_s	S_r	S_{L1}	S_{L2}
8.4mm	2.5mm	5.3mm	5.3mm

C. Conductor Loss Investigation

The analysis results that have been previously shown in section5.4.1 are calculated without consideration of conductor loss. So far, only dielectric loss is included in the FDTD simulation. The conductor loss must be investigated because the antenna structure is designed to operate within millimeter wave frequency band. In this section, conductor loss is investigated by comparing magnitude of reflection coefficient and actual gain. To include conductor loss, the material of ground plane and feeding circuit is chosen copper (Cu) and the analysis results of actual gain and reflection coefficient are evaluated by performing Finite Element Method (FEM) in commercial simulation software EMPro. The analysis results are evaluated within frequency of 27GHz to 29GHz. The analysis results of actual gain are calculated with sampling frequency of 0.05GHz.

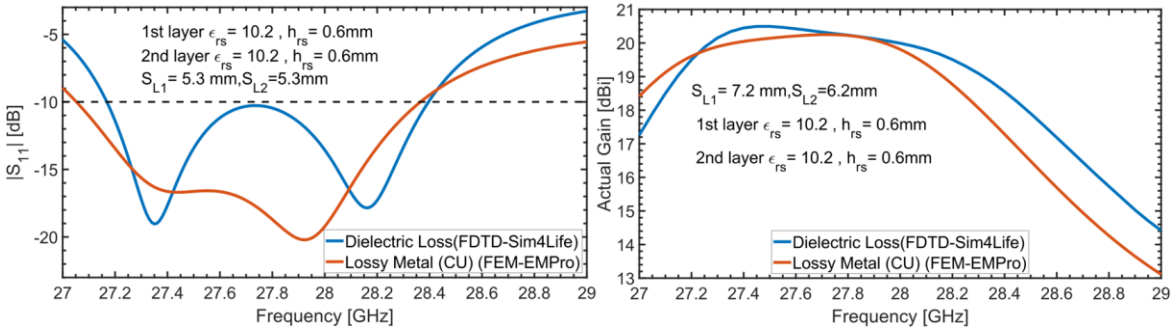

Figure5. 16 Comparison of actual gain and $|S_{11}|$ for investigation of conductor loss

From the analysis results in Figure5. 16, the −10dB impedance bandwidth from FEM are slightly wider than the −10dB impedance bandwidth from FDTD. In addition, the actual gain from FEM is slightly higher from 27GHz to 27.2GHz and slightly lower from 27.2GHz to 28GHz. Within 28GHz to 29GHz, the actual gain from FEM is around 1dB lower than

actual gain from FDTD. The discrepancy of −10dB impedance bandwidth could be from the error between FEM and FDTD simulation methods. The decrease in actual gain could be from the effect of conductor loss. Therefore, the actual gain has decreased around 1dB after the conductor loss is considered.

D. Comparison of total radiation efficiency

Finally, comparison of total radiation efficiency is performed as following. Total radiation efficiency, which will be evaluated, are calculated as in the following equations from FDTD simulation in commercial software Sim4Life.

$$\eta_{total} = \eta_{rad} \times \eta_{mis}$$
$$\eta_{mis} = \frac{P_{in}}{P_{av}}$$
$$\eta_{rad} = \frac{G_{max}}{D_{max}}$$

In these equations, η_{total} is total radiation efficiency, η_{mis} is mismatch efficiency, η_{rad} is radiation efficiency, P_{in} is total input power, P_{av} is total available power, G_{max} and D_{max} are maximum gain and maximum directivity, respectively. Figure5. 17 shows comparison of total radiation efficiency which is evaluated by performing FDTD in commercial simulation software (Sim4Life). Without using reflector, the slot antennas array has high total efficiency at 28GHz and low total efficiency when frequency is getting higher and lower. After a reflector is used, the trend of efficiency is not changed. However, performance of total efficiency is degraded. After one layer of dielectric superstrate is used, total efficiency is enhanced at lower frequency. Total efficiency is within 77% to 91% over 27GHz to 28.7GHz. After two layers of dielectric superstrate are used, total efficiency is within 86% to 95% over 27.17GHz to 28.4GHz. The total radiation efficiency has been improved by two layers of dielectric superstrate.

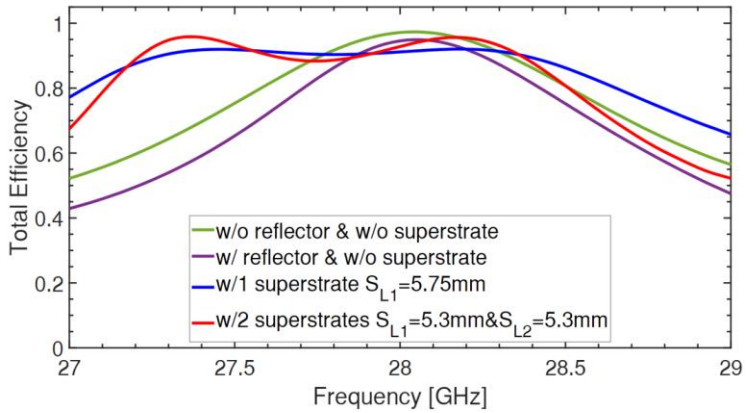

Figure5. 17 Comparison of raidiation efficiency of antenna structure with and without superstrate layer

5.4.2 Gain Enhancement of Leaf-Shaped Bowtie Slot Antenna Array Electromagnetically Fed by Microstrip Line

A. Antenna structure with one layer of dielectric superstrate (ε_{rs}=10.2 & h_{rs}=0.6mm)

Leaf-shaped bowtie slot antenna electromagnetically fed by microstrip line is also used as primary source for gain enhancement. The antenna structure is designed and optimized in section4.5.2 (Figure4. 30). The radiating slot of the array structure has element length L_e=4mm. The element spacing between adjacent radiating slot is D_s=8.3mm, and the separation between reflector and dielectric substrate is chosen as S_r=3mm. To investigate the effect of dielectric superstrate on actual gain and reflection coefficient of the slot antennas array, one layer of dielectric superstrate has been placed on the top of antenna ground plane. The relative permittivity and thickness of dielectric superstrate is ε_{rs}=10.2, and h_{rs}=0.6mm, respectively. The structure of the slot antennas array with one layer of dielectric superstrate is shown as in the following Figure5. 18.

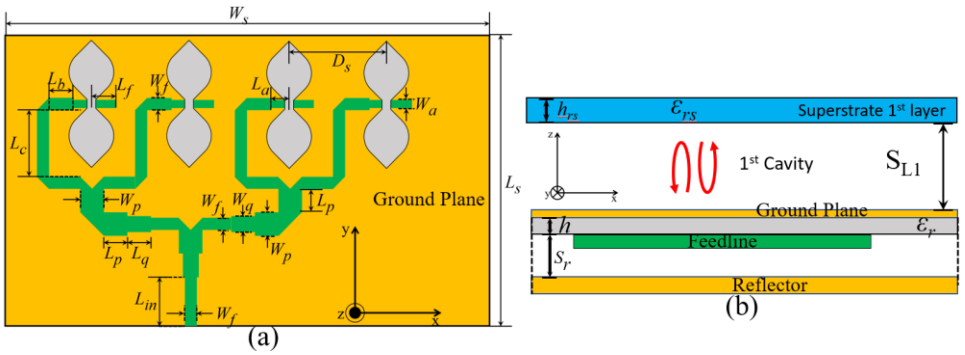

Figure5. 18 Slot antennas array fed by quarter wavelength matching circuit with one layer of superstrate

The separation between dielectric superstrate layer and ground plane is S_{L1}. A resonant cavity has been created between dielectric superstrate layer and ground plane of the slot antennas array. The thickness of resonant cavity is the separation between ground plane and superstrate layer S_{L1}. The antenna characteristics such as actual gain and reflection coefficients are depending on the thickness of cavity (S_{L1}). Therefore, the superstrate layer is shifted along z-direction to find the optimum results of actual again and −10dB impedance bandwidth. The actual gain and reflection coefficient are evaluated by performing FDTD in commercial simulation software. In FDTD simulation setting, grid size is chosen as Δx=0.05mm, Δy=0.05mm, and Δz=0.02mm for dielectric substrate, and Δz=0.05mm for dielectric superstrate layer. 10-layer uniaxial perfectly matched layer is used as absorbing boundary condition. The separation between antenna structure to absorbing boundary condition is 10mm in all direction, except in −z-direction. The distance between reflector to absorbing boundary condition is 5mm. Line source (delta gap source) has been placed at the edge of microstrip line and ground plane to excite gaussian signal with center frequency of 28GHz and 2GHz bandwidth. Dielectric loss and conductor loss are not included in this

simulation.The antenna's characteristics are evaluated with frequency range of 27GHz to 29GHz. The actual gain is calculated with sampling frequency of 0.05GHz. Reflection coefficient is calculated with reference impedance of 50Ω. The simulated results of actual gain and reflection coefficient are shown as in following Figure5. 19.

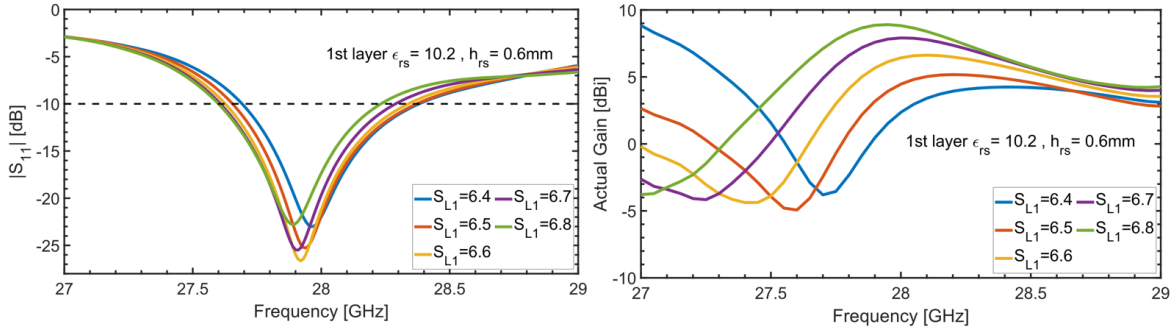

Figure5. 19 Actual gain and $|S_{11}|$ comparison by varying S_{L1}

From the simulated results in Figure5. 19, maximum −10dB impedance bandwidth is obtained at S_{L1}=6.6mm, and maximum actual gain is obtained at S_{L1}=6.8mm. The peak actual gain in broadside direction is around 9dBi at 28GHz. From both cases of impedance bandwidth and actual gain, characteristics of antenna is degraded after using one layer of dielectric superstrate. Comparison of radiation pattern is shown as in Figure5. 20 and Figure5. 21 below.

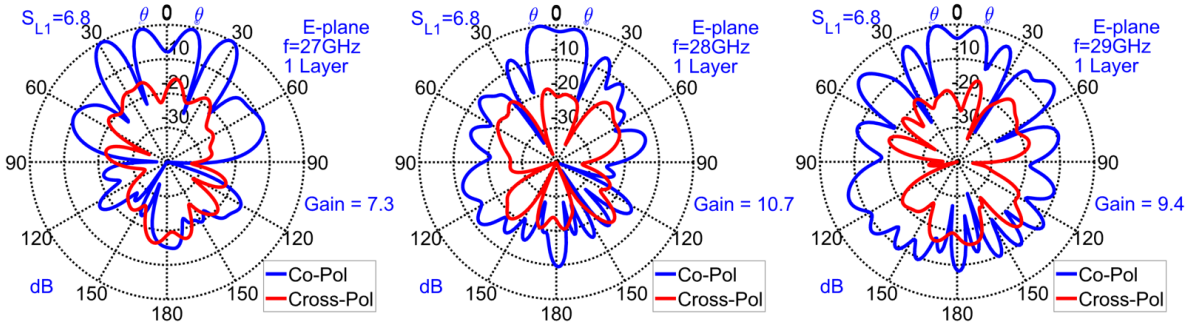

Figure5. 20 E-plane of slot antennas array fed by quarter wavelength matching circuit with one layer of superstrate.

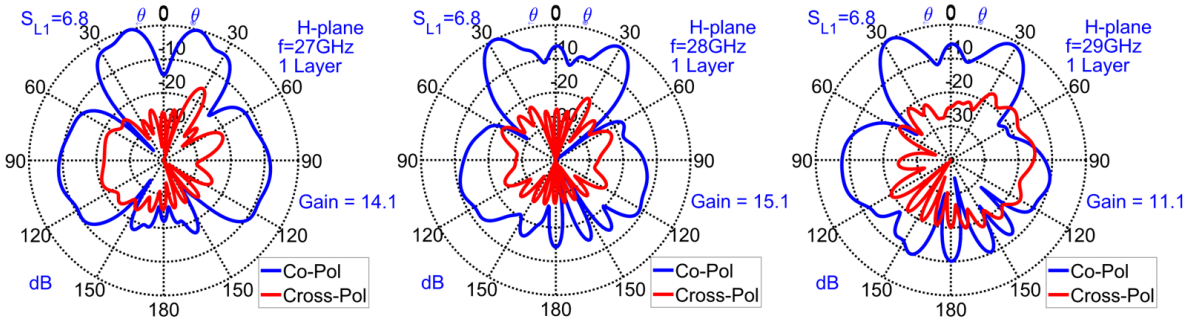

Figure5. 21 E-plane of slot antennas array fed by quarter wavelength matching circuit with one layer of superstrate

From the simulated results of radiation patter, the slot antennas array with one layer of dielectric superstrate has more than one main lobe in E-plane and H-plane. Comparing to radiation pattern of slot antenna array without dielectric superstrate layer, the radiation beam is splitting in H-plane which causes maximum gain in broadside direction decreasing. From [54][55], gain of antenna structure is enhanced when the reflecting electromagnetic wave from superstrate creates an in-phase contribution. However, the superstate can also cause the in part and out-of-phase contribution phenomena of the reflected electromagnetic wave, which causes the beam split as in Figure5. 21.

B. Antenna structure with two layers of dielectric superstrate (ε_{rs}=10.2 & h_{rs}=0.6mm)

To further investigate the effect of dielectric superstrate layer on characteristics of antenna structure, two layers of dielectric superstrate are arranged on top of ground plane of slot antenna array. The characteristics of first and second layer are identical. The relative permittivity and thickness of dielectric superstrate is ε_{rs}=10.2, and h_s=0.6mm, respectively. The antenna structure is shown as in Figure5. 22.

From Figure5. 22, the separation between ground plane and first superstrate layer is represented by S_{L1}, and the separation between first layer and second layer is represented by S_{L2}. After two layers of superstrate are arranged on top of the slot antennas array ground plane, two resonant cavities are created as shown in Figure5. 22. The thickness of first cavity and second cavity are represented by S_{L1} and S_{L2}, respectively. The antenna characteristics are highly depending on the thickness of each cavity. Therefore, the separation S_{L1} and S_{L2} are varied and precisely studied to obtain maximum gain and −10dB impedance bandwidth. The actual gain and reflection coefficient are evaluated by performing FDTD in commercial simulation software. In FDTD simulation setting, grid size is chosen as Δx=0.05mm, Δy=0.05mm, and Δz=0.02mm for dielectric substrate, and Δz=0.05mm for dielectric superstrate layer. 10-layer uniaxial perfectly matched layer is used as absorbing boundary condition. The separation between antenna structure to absorbing boundary condition is 10mm in all direction, except in −z-direction. The distance between reflector to absorbing boundary condition is 5mm. Line source (delta gap source) has been placed at the edge of microstrip line and ground plane to excite gaussian signal with center frequency of 28GHz and 2GHz bandwidth. Dielectric loss and conductor loss are not included in this simulation. The analysis results are shown as in Figure5. 23 and Figure5.24.

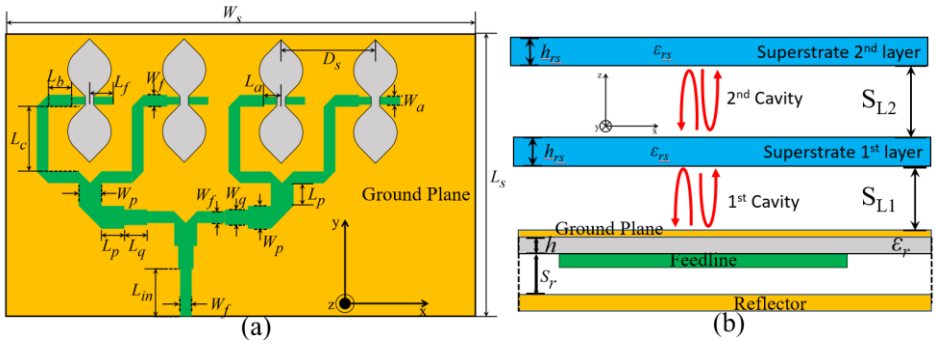

Figure5. 22 Slot antennas array fed by quarter wavelength matching circuit with two layers of superstrate

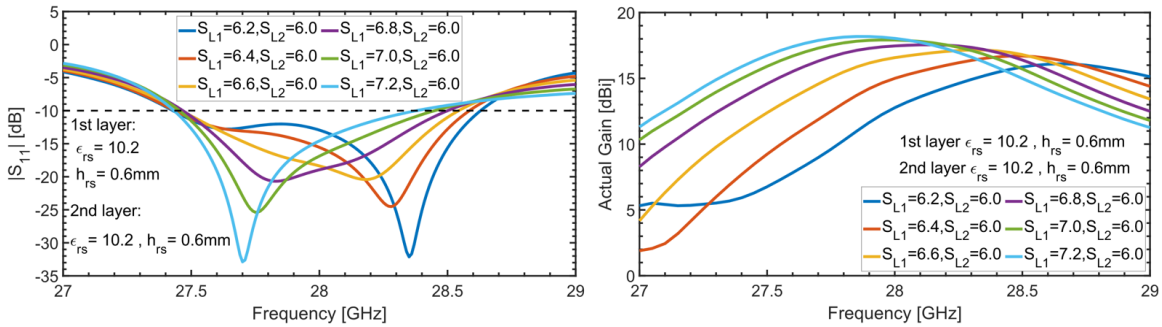

Figure5. 23 Actual gain and $|S_{11}|$ of slot antennas array with two layers of superstrate (ε_{rs}=10.2)

Firstly, the separation between first layer and second layer S_{L2} is chosen to be S_{L2}=6.0mm. The separation between ground plane and first layer S_{L1} is changed from 6.2mm to 7.2mm. The maximum actual gain is obtained when S_{L1} is chosen as S_{L1}=7.2mm, and S_{L2}=6.0mm. At this condition, the peak actual gain is obtained around 18dBi and −10dB impedance bandwidth occupies frequency range of 27.43GHz to 28.37GHz which is about 0.94GHz bandwidth.

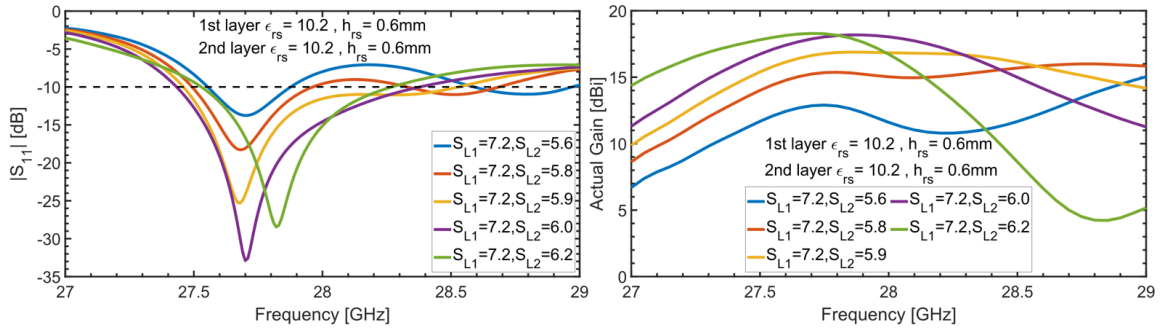

Figure5. 24 Actual gain and $|S_{11}|$ of slot antennas array with two layers of superstrate (ε_{rs}=10.2)

Secondly, the separation between ground plane and first layer S_{L1} is chosen as S_{L1}=7.2mm. The separation between first layer and second layer S_{L2} is changed from 5.6mm to 6.2mm. The maximum actual gain is obtained when S_{L2} is chosen as S_{L2}=6.0mm. Therefore, the optimum value of S_{L1} and S_{L2} are 7.2mm and 6.0mm, respectively. The

comparison of radiation patterns is shown as in following Figure5. 25 and Figure5. 26. The radiation patterns are evaluated at frequency of 27GHz, 28GHz, and 29GHz.

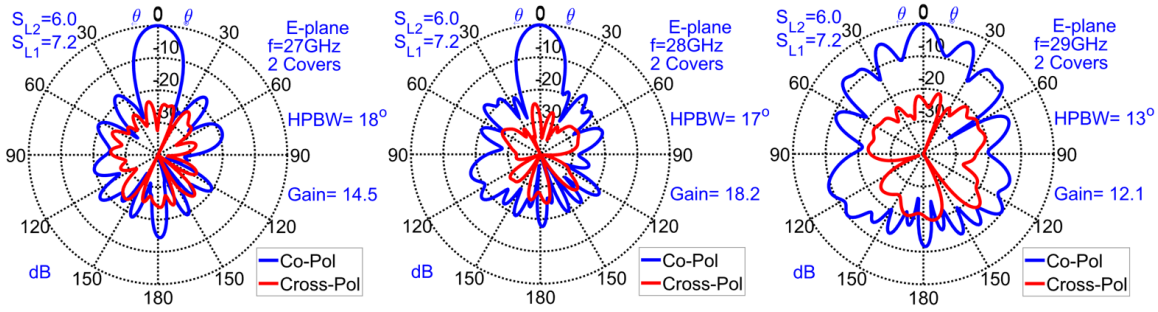

Figure5. 25 E-plane of slot antenna array with two layers of superstrate (ε_{rs}=10.2)

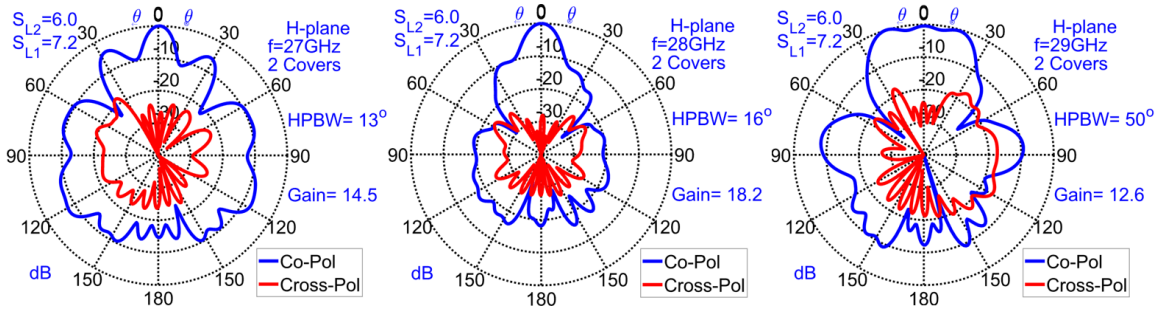

Figure5. 26 H-plane of slot antenna array with two layers of superstrate (ε_{rs}=10.2)

From the simulated results, the radiation pattern has been improved after two layers of dielectric superstrate are arranged on top of the slot antennas array. In E-plane, the radiation pattern has only one main lobe within 27GHz to 28GHz. Maximum gain has increased to 18.2dB at 28GHz in broadside direction. In H-plane, the beam split has been removed. Only one main beam is pointing in broadside direction at 28GHz. However, it turns out that high-side lobe has appeared at frequency of 29GHz along E-plane and at 27GHz along H-plane. From Equation5. 10 [54][55] , the power pattern of the antenna structure is depending on the separation S_{L1} and S_{L2}, which is represented by L_r in Equation5. 10, and the reflection coefficient of superstrate $R(\theta)$. The separation S_{L1} and S_{L2} is optimized for $|S_{11}|$. Therefore, the effect of superstrate will be investigated by changing the relative permittivity of superstrate (ε_{rs}) which is assumed to change the phase of reflecting and transmitting electromagnetic wave at the superstrate interface.

C. Antenna structure with one layer of dielectric superstrate (ε_{rs}=6 & h_{rs}=0.76mm)

Although the antenna characteristics such as actual gain and radiation pattern have been improved, the −10dB impedance bandwidth is relatively small comparing to the previous model in section5.4.1. The characteristics of resonant cavity antenna is also depending on relative permittivity of dielectric superstrate. As the relative permittivity of superstrate is changed, the reflection and transmission coefficients of superstrate is also assumed to change. To investigate the antenna characteristics, dielectric superstrate with relative permittivity of ε_{rs}=6.0 is used to enhance the actual gain and impedance bandwidth of the slot antennas array. The actual gain and reflection coefficient are evaluated by performing FDTD in commercial simulation software. In FDTD simulation setting, grid size is chosen as Δx=0.05mm, Δy=0.05mm, and Δz=0.02mm for dielectric substrate, and Δz=0.05mm for dielectric superstrate layer. 10-layer UPML (uniaxial perfectly matched layer) is used as absorbing boundary condition. The separation between antenna structure to absorbing boundary condition is 10mm in all direction, except in −z-direction. The distance between reflector to absorbing boundary condition is 5mm. Line source (delta gap source) has been placed at the edge of microstrip line and ground plane to excite gaussian signal with center frequency of 28GHz and 2GHz bandwidth. Dielectric loss and conductor loss are not included in this simulation. The analysis results are shown as in Figure5. 27.

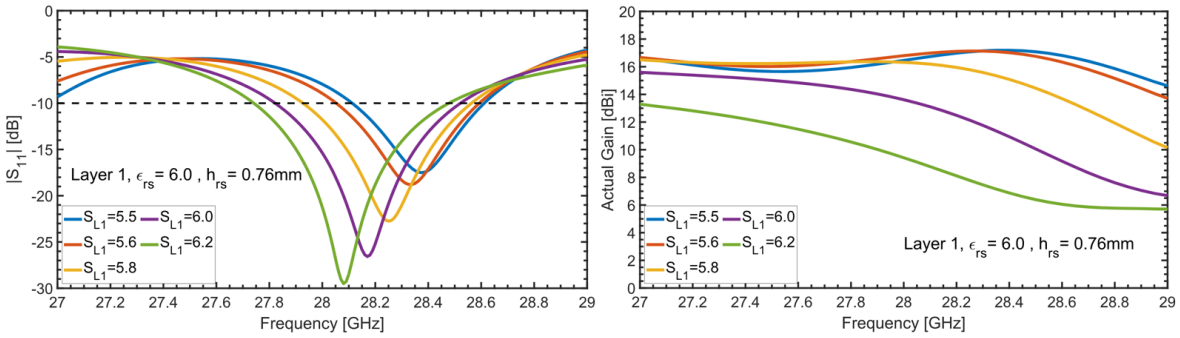

Figure5. 27 Actual gain and $|S_{11}|$ of slot antennas array with one layer of superstrate (ε_{rs}=6.0)

After one superstrate layer with relative permittivity of 6.0 is used, actual gain in broadside direction has been increased. For the case of S_{L1}=5.5, the maximum actual gain is around 17dBi. However, −10dB impedance bandwidth, which occupies frequency range of 28.1GHz to 28.6GHz, is relatively narrow. Therefore, one layer of superstrate with ε_{rs}=6.0 is not sufficient to improve actual gain and −10dB impedance simultaneously.

From analysis results of radiation pattern, the beam split characteristics disappear comparing to the results in Figure5. 21. In addition, the side lobe along both E-plane and H-plane has disappeared. Therefore, the characteristics (ε_{rs} & h_{rs}) of superstrate layer do effect on the antenna radiation pattern. The radiation pattern of antenna structure is improved by changing separation S_{L1} and superstrate characteristics ε_{rs} although the −10dB impedance bandwidth is narrow. In order to be useful in millimeter wave frequency band, antenna

structure must offer wide impedance bandwidth and high gain over the wide bandwidth simultaneously. The effect of dielectric superstrate must be further studied to get improvement on both −10dB impedance bandwidth and actual gain simultaneously over the same bandwidth.

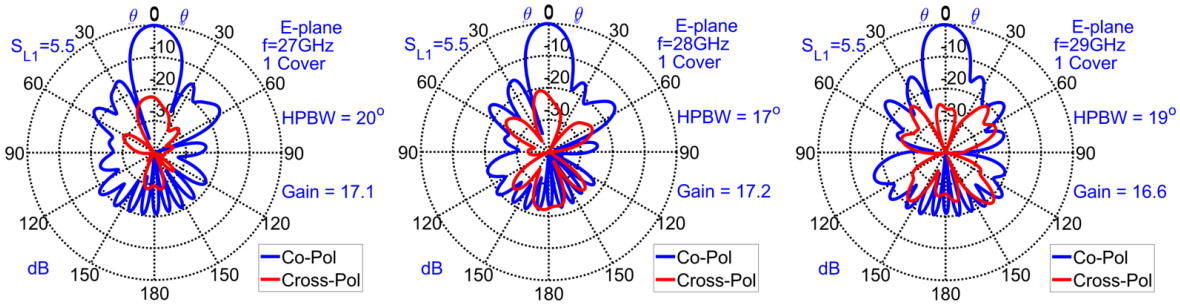

Figure5. 28 E-plane of slot antenna array with one layer of superstrate (ε_{rs}=6.0)

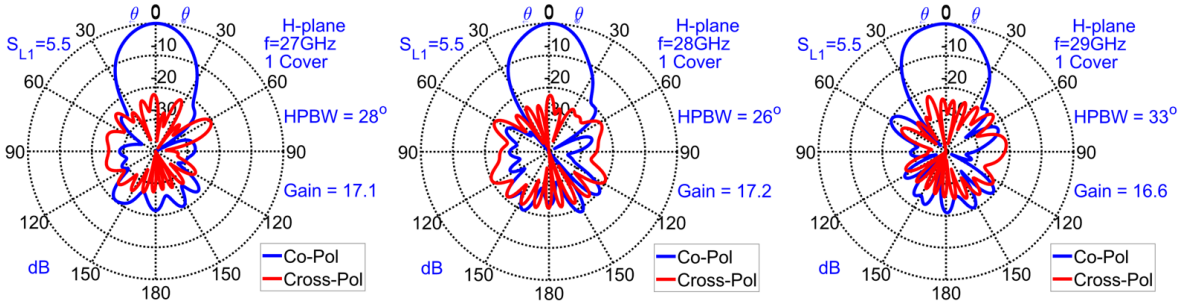

Figure5. 29 H-plane of slot antenna array with one layer of superstrate (ε_{rs}=6.0)

D. Antenna structure with two layers of dielectric superstrate (ε_{rs}=6 & h_{rs}=0.76mm)

Two layers of dielectric superstrate with ε_{rs}=6.0 are arranged on top of slot antennas array ground plane. Actual gain and reflection coefficient are evaluated to investigate the effect of superstrate layer. Firstly, the separation between first layer and second layer is chosen as S_{L2}=6.0mm. The separation between slot antennas array ground plane to first layer is changed within 6.0mm to 7.2mm. Antenna characteristics such as actual gain and reflection coefficient are evaluated by performing FDTD simulation in commercial simulation software. The setting of FDTD simulation is chosen the same as the setting in section5.4.2 (C). Antenna characteristics are evaluated over frequency range of 27GHz to 29GHz. Actual gain is calculated with frequency sampling of 0.05GHz. Reflection coefficient is calculated with reference impedance of 50Ω. The simulated results of actual gain and reflection coefficient are shown as in Figure5. 30.

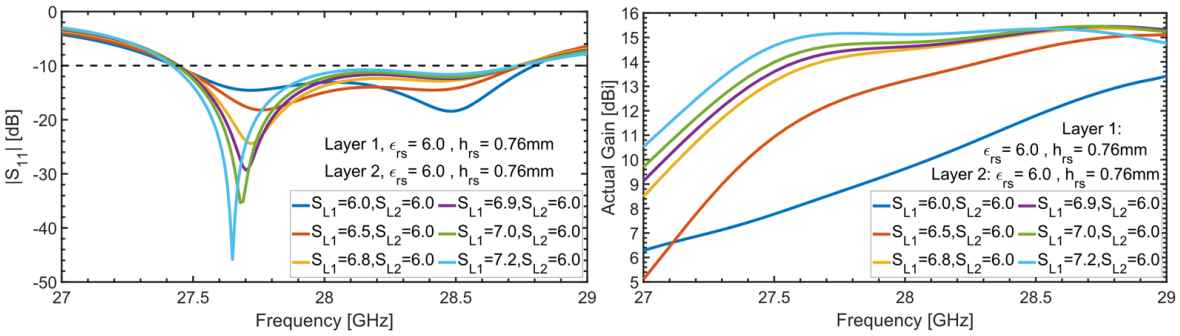

Figure5. 30 Actual gain and $|S_{11}|$ of slot antennas array with two layers of superstrate (ε_{rs}=6.0)

From the analysis results, the optimum −10dB impedance bandwidth and actual gain is obtain when S_{L1} and S_{L2} are chosen as S_{L1}=7.2mm and S_{L2}=6.0mm, respectively. As S_{L1} and S_{L2} are equal to 7.2mm and 6.0mm, the −10dB impedance bandwidth occupies frequency range from 27.42GHz to 28.74GHz which is about 1.32GHz. −10dB impedance bandwidth has increased around 0.38GHz comparing to the results in Figure5. 24. However, the peak actual gain is around 15dBi. Therefore, the optimum value of S_{L1} is 7.2mm. Secondly, separation between ground plane and first layer (S_{L1}) is fixed, and separation between first layer and second layer (S_{L2}) is changed within 5.9mm to 6.3mm. Antenna characteristics such as actual gain and reflection coefficient are evaluated by performing FDTD simulation in commercial simulation software. Antenna characteristics are evaluated over frequency range of 27GHz to 29GHz. Actual gain is calculated with frequency sampling of 0.05GHz. Reflection coefficient is calculated with reference impedance of 50Ω. The simulated results of actual gain and reflection coefficient are shown as in Figure5. 31. In addition, −10dB impedance bandwidth and −3dB gain bandwidth are summarized as in Table5. 5.

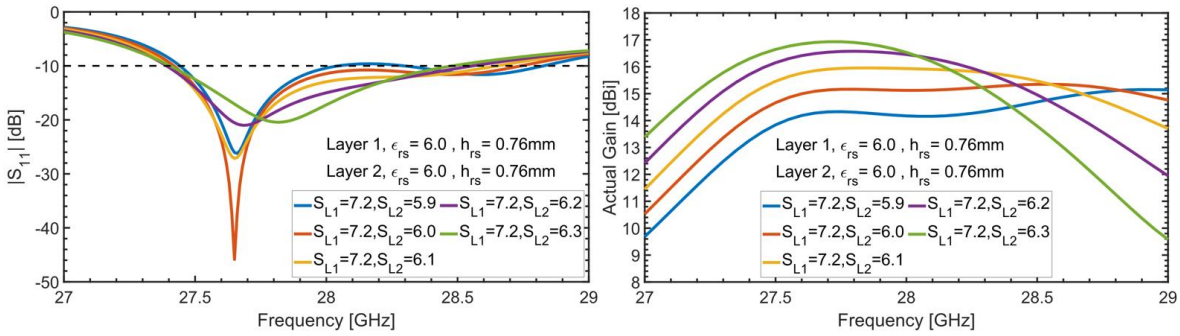

Figure5. 31 Actual gain and $|S_{11}|$ of slot antenna array with two layers of superstrate (ε_{rs}=6.0)

Table5. 5 Summary of −10dB impedance bandwidth and maximum actual gain of Figure5. 31

S_{L1} & S_{L2} (mm)	−10dB impedance bandwidth	Maximum actual gain (−3dB gain bandwidth)
S_{L1}=7.2, S_{L2}=5.9	0.61GHz (27.44−28.05GHz) 0.52GHz (28.30−28.82GHz)	15.51dBi (27.27−29GHz)
S_{L1}=7.2, S_{L2}=6.0	1.32GHz (27.42−28.74GHz)	15.31dBi (27.18−29GHz)
S_{L1}=7.2, S_{L2}=6.1	1.25GHz (27.40−28.65GHz)	15.95dBi (27.15−28.75GHz)
S_{L1}=7.2, S_{L2}=6.2	1.17GHz (27.39−28.56GHz)	16.57dBi (27.12−28.75GHz)
S_{L1}=7.2, S_{L2}=6.3	1.07GHz (27.41−28.48GHz)	16.92dBi (27.06−28.50GHz)

From the analysis results, 1.32GHz of impedance bandwidth and 15.3dBi of maximum actual gain are obtained when S_{L1} and S_{L2} are chosen as S_{L1}=7.2 and S_{L2}=6.0. In addition, 1.17GHz of impedance bandwidth and 16.5dBi of actual gain are obtain when S_{L1} and S_{L2} are chosen as S_{L1}=7.2 and S_{L2}=6.2. From actual gain comparison, the optimum condition is chosen as S_{L1}=7.2 and S_{L2}=6.2. Therefore, in the case of two layers of dielectric superstrate with relative permittivity of ε_{rs}=6.0 and thickness of h_{rs}=0.76mm, the optimum separation S_{L1} and S_{L2} are chosen as S_{L1}=7.2mm and S_{L2}=6.2mm.

Analysis results of radiation are shown in Figure5. 32 and Figure5. 33. From Figure5. 32, grating lobes do occur at high frequency. The radiation patterns are evaluated at frequency of 27GHz, 28GHz, 29GHz. The maximum gain is higher at 27GHz and 28GHz and lower at 29GHz. From Figure5. 33, the grating lobe do occur along E-plane at lower frequency after two layers of dielectric superstrate are used. Comparing to results in Figure5. 28, the radiation pattern has not been improved. Therefore, by using two layers of dielectric superstrate with relative permittivity of ε_{rs}=6.0, the −10dB impedance bandwidth of antenna structure has been widened although the actual gain has been decreasing and radiation pattern has been degraded. From Equation5. 12 and Equation5. 13 [54][55], radiation pattern is depending on separation S_{L1} and S_{L2}. However, the separation S_{L1} and S_{L2}, that offer good radiation, didn't offer a good impedance bandwidth. The purpose of this research is to design antenna structure that offers high performance of actual gain, impedance bandwidth and radiation pattern simultaneously. The effect of dielectric superstrate must be further investigated to improve antenna performance.

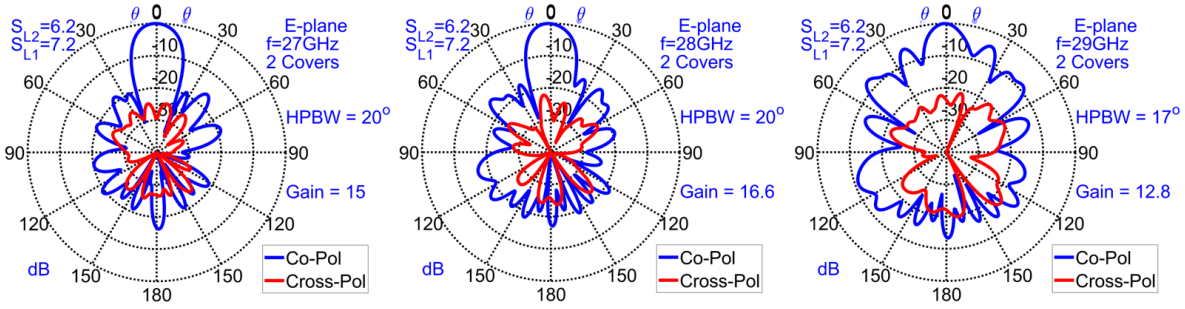

Figure5. 32 E-plane of slot antenna array with two layers of superstrate (ε_{rs}=6.0)

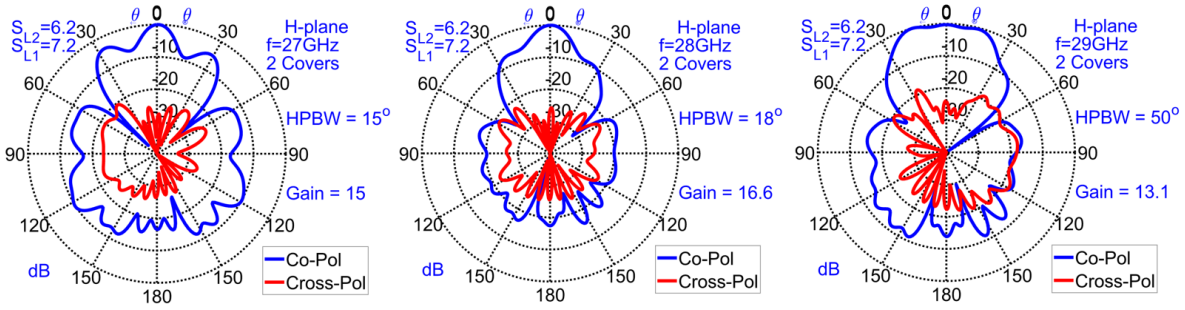

Figure5. 33 H-plane of slot antenna array with two layers of superstrate (ε_{rs}=6.0)

E. Antenna structure with two layers of dielectric superstrate with different characteristics (ε_{rs} & h_{rs})

From the previous sections, the antenna structure offers high gain but narrower impedance bandwidth after using two layers of superstrate with ε_{rs}=10.2. On the contrary, the antenna structure offers lower gain but wider impedance bandwidth after using two layers of superstrate with ε_{rs}=6.0. To further investigate the effect of resonant cavity as well as the effect of dielectric superstrate characteristics, two layers of dielectric superstrate with different characteristics (ε_{rs} & h_{rs}) are arranged on top of slot antennas array ground plane. The first superstrate layer has relative permittivity of ε_{rs}=6.0 and thickness h_{rs}=0.76mm. The second superstrate layer has relative permittivity of ε_{rs}=10.2 and thickness h_{rs}=0.6mm. The separation between ground plane and first layer is represented by S_{L1} and the separation between first layer and second layer is represented by S_{L2}. The structure of antenna is shown as in Figure5. 22.

Characteristics of antenna are evaluated within frequency range of 27GHz to 29GHz by performing FDTD simulation in commercial software. Antenna actual gain are calculated with sampling frequency of 0.05GHz. Reflection coefficient is calculated with reference impedance of 50Ω. In FDTD simulation setting, grid size is chosen as Δx=0.05mm, Δy=0.05mm, Δz=0.02mm for dielectric substrate, Δz=0.05mm for dielectric superstrate. Analysis results are shown as in Figure5. 34. In addition, 10-layer UPML (uniaxial perfectly matched layer) is used as absorbing boundary condition. The separation between antenna structure to absorbing boundary condition is 10mm in all direction, except in −z-direction. The distance between reflector to absorbing boundary condition is 5mm. Line source (delta gap source) has been placed at the edge of microstrip line and ground plane to excite gaussian signal with center frequency of 28GHz and 2GHz bandwidth. Dielectric loss and conductor loss are not included in this simulation. The previous cases have shown that the optimum value of S_{L1} and S_{L2} are around 7.2mm and 6.2mm with sampling point of 0.1mm. Therefore, in this case, S_{L1} is chosen between 6.9mm to 7.5mm and S_{L2} is chosen between 6.0mm to 6.3mm with sampling point of 0.1mm.

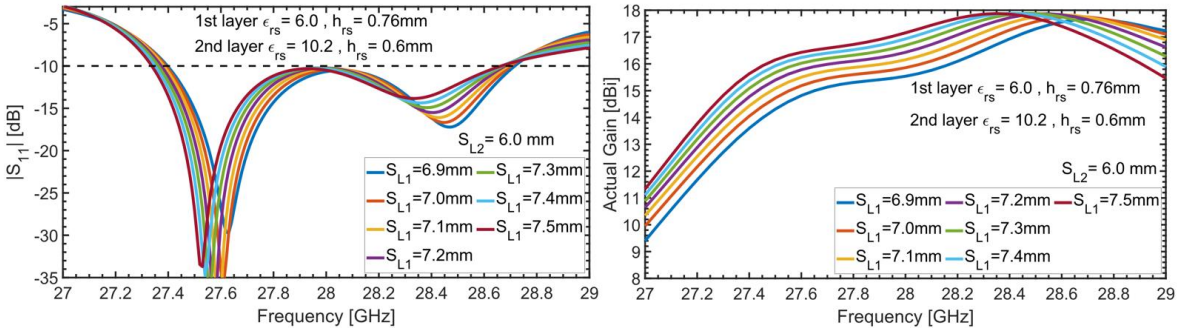

Figure5. 34 Actual gain and $|S_{11}|$ of slot antennas array with two layers of superstrate (ε_{rs}=6.0, ε_{rs}=10.2)

Table5. 6 Summary of −10dB impedance bandwidth and maximum actual gain of Figure5. 34

S_{L1} & S_{L2} (mm)	−10dB impedance bandwidth	Maximum actual gain (−3dB gain bandwidth)
S_{L1}=6.9, S_{L2}=6.0	1.32GHz (27.39 − 28.71GHz)	17.66dBi (27.6−29GHz)
S_{L1}=7.0, S_{L2}=6.0	1.31GHz (27.39 − 28.70GHz)	17.76dBi (27.55−29GHz)
S_{L1}=7.1, S_{L2}=6.0	1.31GHz (27.38−28.69GHz)	17.83dBi (27.5−29GHz)
S_{L1}=7.2, S_{L2}=6.0	1.3GHz (27.38−28.68GHz)	17.86dBi (27.45−29GHz)
S_{L1}=7.3, S_{L2}=6.0	1.31GHz (27.36−28.67GHz)	17.88dBi (27.4−29GHz)
S_{L1}=7.4, S_{L2}=6.0	1.31GHz (27.35−28.66GHz)	17.88dBi (27.35−29GHz)
S_{L1}=7.5, S_{L2}=6.0	1.32GHz (27.34−28.66GHz)	17.87dBi (27.3−29GHz)

Case I, S_{L2} is chosen as S_{L2}=6.0mm and S_{L1} is varied between 6.9mm to 7.5mm. Analysis results of actual gain and magnitude of reflection coefficient $|S_{11}|$ are shown and summarized as in Figure5. 34 and Table5. 6, respectively. From summarized results in Table5. 6, the optimum value of S_{L1} is chosen as S_{L1}=7.2mm. In Case I, 1.3GHz impedance bandwidth and 17.86dBi maximum actual gain are obtained when S_{L1} and S_{L2} are chosen as S_{L1}=7.2mm, and S_{L2}=6.0mm. To further investigate the antenna performance based on S_{L2}, another value of S_{L2} is chosen and fixed, the S_{L1} is varied within 6.9mm to 7.5mm.

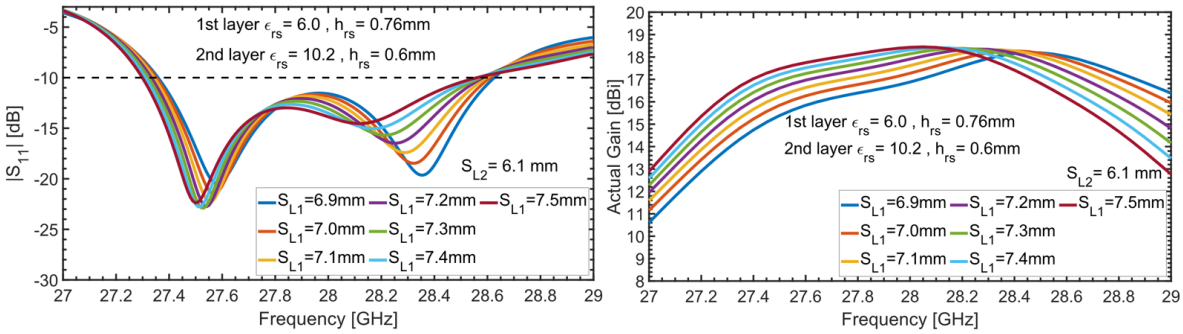

Figure5. 35 Actual gain and $|S_{11}|$ of slot antennas array with two layers of superstrate (ε_{rs}=6.0, ε_{rs}=10.2)

Table5. 7 Summary of −10dB impedance bandwidth and maximum actual gain of Figure5. 35

S_{L1} & S_{L2} (mm)	−10dB impedance bandwidth	Maximum actual gain (−3dB gain bandwidth)
S_{L1}=6.9, S_{L2}=6.1	1.26GHz (27.36−28.62GHz)	18.19dBi (27.5−29GHz)
S_{L1}=7.0, S_{L2}=6.1	1.26GHz (27.35−28.61GHz)	18.27dBi (27.4−29GHz)
S_{L1}=7.1, S_{L2}=6.1	1.25GHz (27.34−28.59GHz)	18.31dBi (27.35−29GHz)
S_{L1}=7.2, S_{L2}=6.1	1.25GHz (27.33−28.58GHz)	18.35dBi (27.35−28.9GHz)
S_{L1}=7.3, S_{L2}=6.1	1.25GHz (27.32−28.57GHz)	18.38dBi (27.3−28.85GHz)
S_{L1}=7.4, S_{L2}=6.1	1.25GHz (27.31−28.56GHz)	18.41dBi (27.25−28.75GHz)
S_{L1}=7.5, S_{L2}=6.1	1.26GHz (27.3−28.56GHz)	18.44dBi (27.25−28.7GHz)

Case II, S_{L2} is chosen as S_{L2}=6.1mm, and S_{L1} is varied between 6.9mm to 7.5mm. The analysis results of actual gain and magnitude of reflection coefficient $|S_{11}|$ are shown and summarized as in Figure5. 35 and Table5. 7, respectively. From the summarized results in Table5. 7, the optimum value of S_{L1} is chosen as S_{L1}=7.2mm. In Case II, 1.25GHz impedance bandwidth and 17.86dBi maximum gain are obtained when S_{L1} and S_{L2} are chosen as S_{L1}=7.2mm, and S_{L2}=6.1mm.

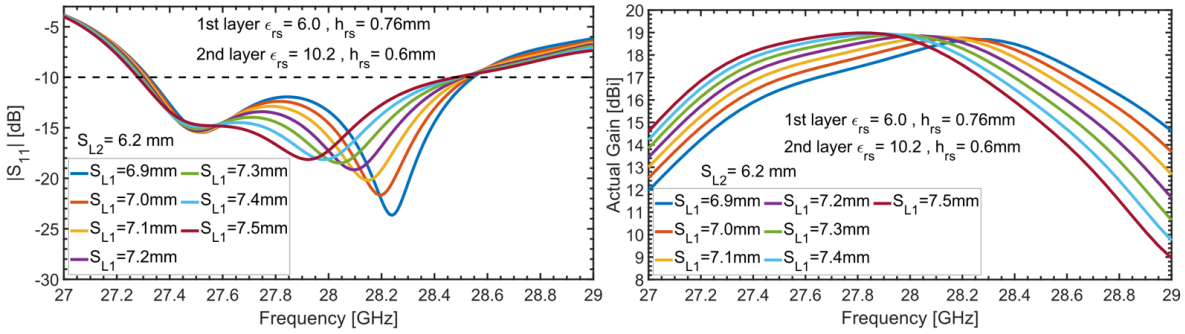

Figure5. 36 Actual gain and |S_{11}| of slot antennas array with two layers of superstrate (ε_{rs}=6.0, ε_{rs}=10.2)

Table5. 8 Summary of −10dB impedance bandwidth and maximum actual gain of Figure5. 36

S_{L1} & S_{L2} (mm)	−10dB impedance bandwidth	Maximum actual gain (−3dB gain bandwidth)
S_{L1}=6.9, S_{L2}=6.2	1.23GHz (27.32−28.55GHz)	18.69dBi (27.4−28.85GHz)
S_{L1}=7.0, S_{L2}=6.2	1.22GHz (27.32−28.54GHz)	18.75dBi (27.3−28.75GHz)
S_{L1}=7.1, S_{L2}=6.2	1.21GHz (27.31−28.52GHz)	18.80dBi (27.25−28.7GHz)
S_{L1}=7.2, S_{L2}=6.2	1.21GHz (27.30−28.51GHz)	18.84dBi (27.2−28.6GHz)
S_{L1}=7.3, S_{L2}=6.2	1.21GHz (27.29−28.50GHz)	18.90dBi (27.2−28.55GHz)
S_{L1}=7.4, S_{L2}=6.2	1.20GHz (27.29−28.49GHz)	18.94dBi (27.15−28.45GHz)
S_{L1}=7.5, S_{L2}=6.2	1.20GHz (27.28−28.48GHz)	18.98dBi (27.10−28.40GHz)

Case III, S_{L2} is chosen as S_{L2}=6.2mm, and S_{L1} is varied between 6.9mm to 7.5mm. The analysis results of actual gain and magnitude of reflection coefficient |S_{11}| are shown and summarized as in Figure5. 36 and Table5. 8, respectively. From the summarized results in Table5. 8, the optimum value of S_{L1} is chosen as S_{L1}=7.2mm. In Case III, 1.21GHz impedance bandwidth and 18.84dBi maximum actual gain are obtained when S_{L1} and S_{L2} are chosen as S_{L1}=7.2mm, and S_{L2}=6.2mm.

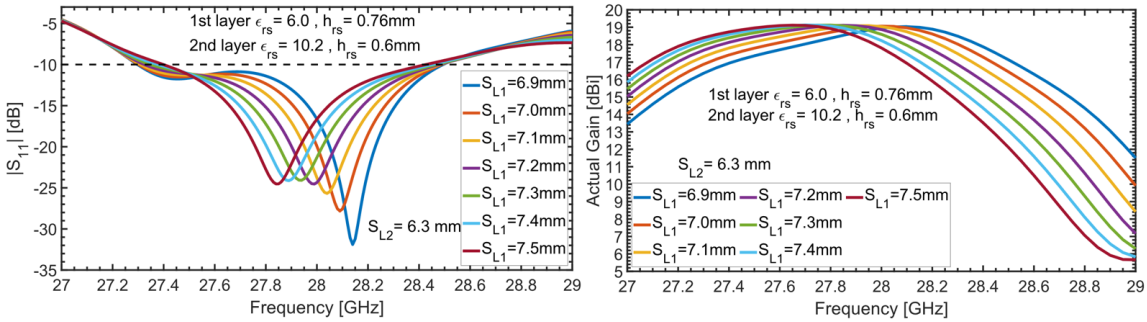

Figure5. 37 Actual gain and |S_{11}| of slot antennas array with two layers of superstrate (ε_{rs}=6.0, ε_{rs}=10.2)

Table5. 9 Summary of −10dB impedance bandwidth and maximum actual gain of Figure5. 37

S_{L1} & S_{L2} (mm)	−10dB impedance bandwidth	Maximum actual gain (−3dB gain bandwidth)
S_{L1}=6.9, S_{L2}=6.3	1.19GHz (27.30−28.49GHz)	19.03dBi (27.26−28.62GHz)
S_{L1}=7.0, S_{L2}=6.3	1.19GHz (27.30−28.49GHz)	19.06dBi (27.18−28.55GHz)
S_{L1}=7.1, S_{L2}=6.3	1.17GHz (27.31−28.48GHz)	19.08dBi (27.13−28.45GHz)
S_{L1}=7.2, S_{L2}=6.3	1.15GHz (27.32−28.47GHz)	19.11dBi (27.10−28.38GHz)
S_{L1}=7.3, S_{L2}=6.3	1.11GHz (27.35−28.46GHz)	19.12dBi (27.06−28.30GHz)
S_{L1}=7.4, S_{L2}=6.3	1.07GHz (27.38−28.45GHz)	19.12dBi (27.02−28.22GHz)
S_{L1}=7.5, S_{L2}=6.3	1.02GHz (27.40−28.42GHz)	19.11dBi (27.00−28.15GHz)

Case IV, S_{L2} is chosen as S_{L2}=6.3mm, and S_{L1} is varied between 6.9mm to 7.5mm. The analysis results of actual gain and $|S_{11}|$ are shown and summarized as in Figure5. 37 and Table5. 9, respectively. From the summarized results in Table5. 9, the optimum value of S_{L1} is chosen as S_{L1}=7.2mm. In Case IV, 1.15GHz impedance bandwidth and 19.11dBi maximum actual gain are obtained when S_{L1} and S_{L2} are chosen as S_{L1}=7.2mm, and S_{L2}=6.3mm. In Case IV, the −10dB impedance bandwidth occupies frequency range of 27.32GHz 28.47GHz and −3dB gain bandwidth occupy frequency range of 27.10 to 28.38GHz, which are smaller than bandwidth of previous three cases. Comparison of Case I, II, and III are shown in following Figure5. 38.

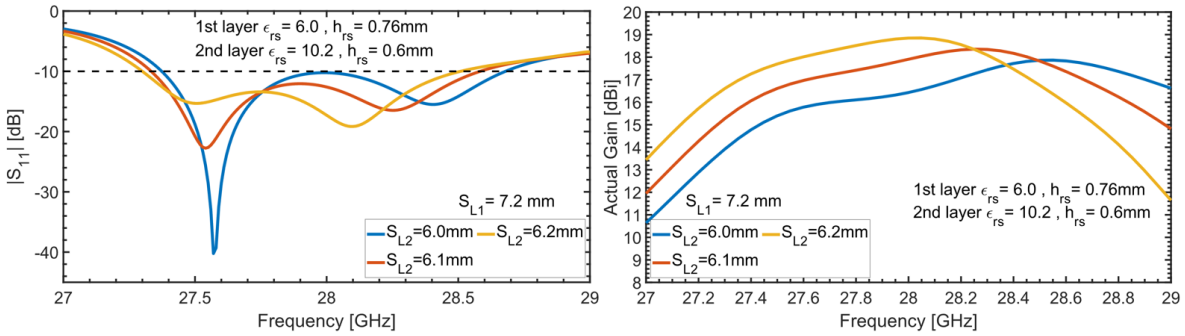

Figure5. 38 Actual gain and $|S_{11}|$ of slot antennas array with two layers of superstrate (ε_{rs}=6.0, ε_{rs}=10.2)

From the comparison of analysis results as shown in Figure3. 37, the antenna structure with two layers of dielectric superstrate with different characteristics has optimum value of S_{L1} and S_{L2} which is chosen as S_{L1}=7.2mm, and S_{L2}=6.2mm. −10dB impedance bandwidth occupies frequency range of 27.30GHz to 28.51GHz which is about 1.21GHz. Maximum actual gain is 18.84dBi and −3dB gain bandwidth occupies frequency range of 27.2GHz to 28.6GHz.

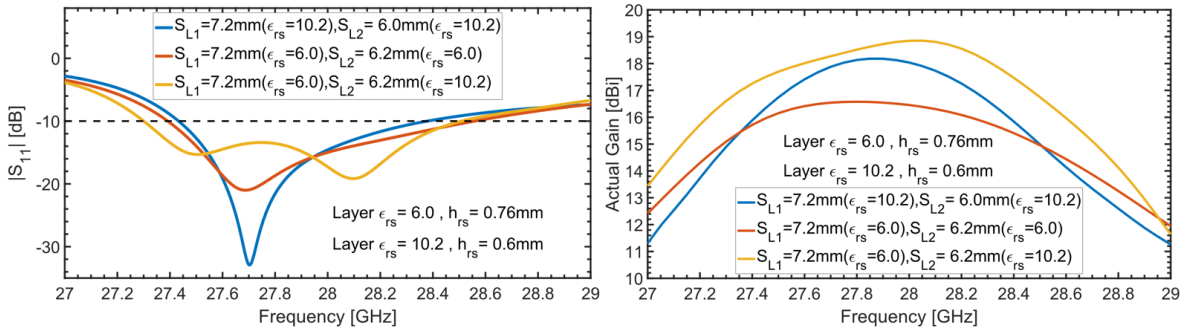

Figure5. 39 Actual gain and $|S_{11}|$ of slot antenna array with two layers of superstrate (ε_{rs}=6.0, ε_{rs}=10.2)

To confirm the effect of dielectric superstrate relative permittivity (ε_{rs}) on antenna characteristics, comparison of actual gain and reflection coefficient are shown as in Figure5. 39. Comparison between analysis of antenna structure with two superstrate layers having identical characteristics (ε_{rs}) and having different characteristics (ε_{rs}) are made. The analysis

results are evaluated by performing FDTD analysis in commercial simulation software. The analysis results in Figure5. 39 show that, antenna structure with two layers of dielectric superstrate, whose characteristics (ε_{rs} and h_{rs}) are different, has higher performance. Therefore, two dielectric superstrate layers with different characteristics are used to enhance actual gain in broadside direction of the slot antenna array. The first layer has relative permittivity of ε_{rs}=6.0 and thickness of h_{rs}=0.76mm. The second layer has relative permittivity of ε_{rs}=10.2 and thickness of h_{rs}=0.6mm. The separation between ground plane and first layer and first layer and second layer are chosen as S_{L1}=7.2mm and S_{L2}=6.2mm.

In addition, the separation between dielectric substrate and reflector (S_r) is also varied to investigate the effect on actual gain and −10dB impedance bandwidth. The separation S_r is varied from 2.0mm to 6mm. The antenna characteristics are evaluated within 27GHz to 29GHz by performing FDTD in commercial simulation software. The actual gain is evaluated with frequency sampling of 0.05GHz. The reflection coefficient is calculated with reference impedance of 50Ω. The analysis results are shown as in following Figure5. 40.

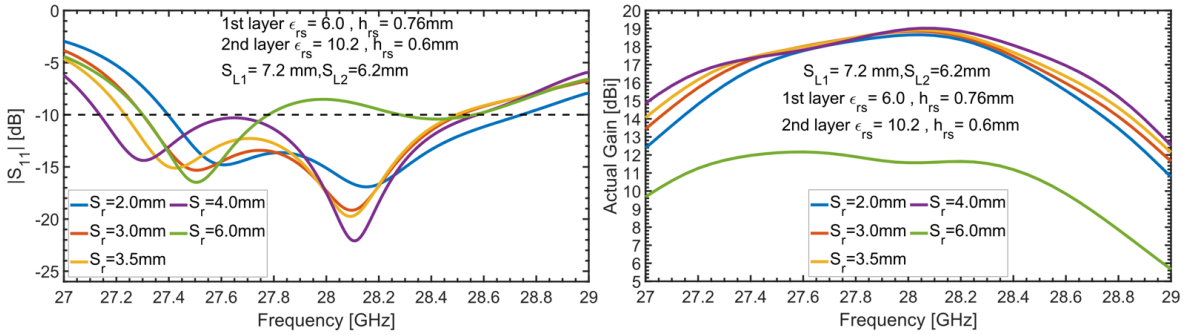

Figure5. 40 Actual gain and $|S_{11}|$ of slot antennas array with two layers of superstrate (ε_{rs}=6.0, ε_{rs}=10.2)

Table5. 10 Optimum parameters for antenna structure with quarter wavelength feeding circuit

1st layer	2nd layer	SL1	SL2	Sr	Ds
ε_{rs}=6.0	ε_{rs}=10.2	7.2mm	6.2mm	4mm	8.3mm

From the analysis results in Figure5. 40, −10dB impedance bandwidth is relatively depending on the separation S_r. The maximum −10dB impedance bandwidth is obtained when S_r is chosen as S_r=4.0mm. The −10dB impedance bandwidth occupies the frequency range of 27.13GHz to 28.58GHz which is about 1.45GHz bandwidth. The −10dB impedance bandwidth has increased around 0.23GHz. In addition, the actual gain in broadside direction has slightly increased when S_r is chosen as S_r=4.0mm. The maximum gain of 19dBi is obtained at 28GHz, and −3dB gain bandwidth occupies frequency range of 27.12GHz to 28.72GHz which is about 1.6GHz gain bandwidth. Figure5. 41 and Figure5. 42 show analysis results of radiation pattern of antenna structure with optimum parameters which is shown in Table5. 10. The results of radiation pattern are evaluated at frequency of 27.15GHz, 28GHz and 28.6GHz, which are within the operational impedance bandwidth. From Figure5. 41, E-plane has HPBW (Half-Power Beamwidth) within 14° to 20°. Maximum sidelobe level is around −15dB at 28.5GHz. Maximum gain of 19dB is obtained at 28GHz. From Figure5. 42,

H-plane has HPBW within 14° to 16°. Grating lobe has occurred at 27.15GHz along H-plane because the superstrate layers are trying to narrow down the beamwidth. At higher frequency, the grating lobe disappears. Comparing to radiation of antenna structure in Figure3. 34, those two layers of dielectric superstrate is trying to narrow down the beamwidth to increase gain in broadside direction that cause the occurrence of side lobe at lower frequency.

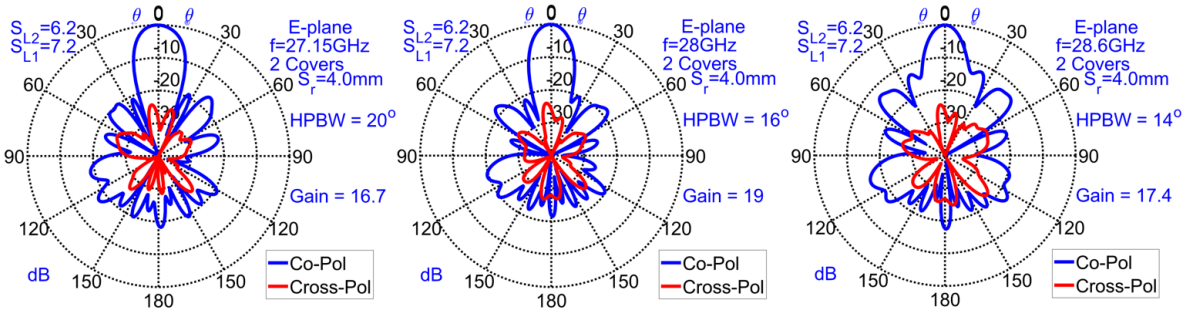

Figure5. 41 E-plane of slot antenna array with two layers of superstrate (ε_{rs}=6.0, ε_{rs}=10.2)

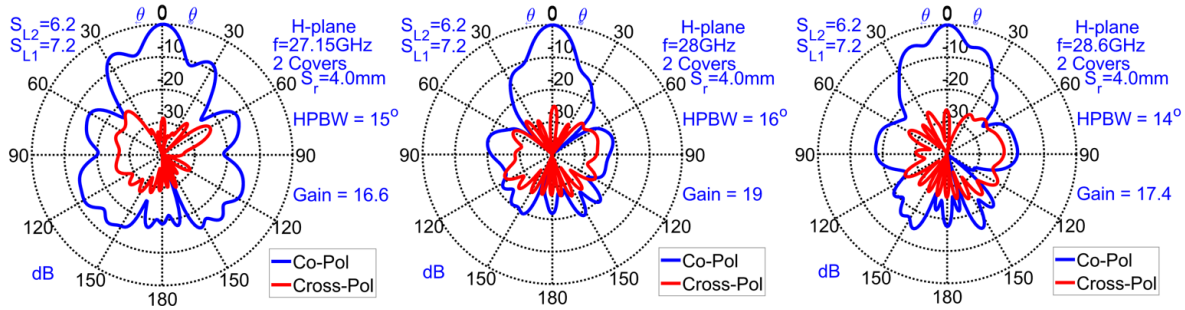

Figure5. 42 H-plane of slot antenna array with two layers of superstrate (ε_{rs}=6.0, ε_{rs}=10.2)

F. Effects of dielectric loss and conductor loss

So far, the analysis results of actual gain and magnitude of reflection coefficient are evaluated with condition of lossless material. Ground plane and feeding circuit are treated as PEC, and dielectric loss tangent of dielectric substrate and superstrate are not included. The effect of dielectric loss and conductor loss must be analyzed because the antenna structure is designed for use in millimeter wave frequency band. Previous analysis results (Section5.4.2) with lossless material are evaluated by performing FDTD analysis in commercial simulation software (Sim4life). Nevertheless, the antenna characteristics with lossy materials are evaluated by performing Finite Element Methos (FEM) in commercial simulation software EMPro. To include conductor loss in FEM (EMPro), ground plane and feeding circuit are treated as copper (Cu). To include dielectric loss, loss tangent of both dielectric superstrate and dielectric substrate are included in FEM (EMPro). The dissipation loss tangent of dielectric substrate is $tan\delta$=0.00085 and loss tangent of both superstrate layers are $tan\delta$=0.0023.

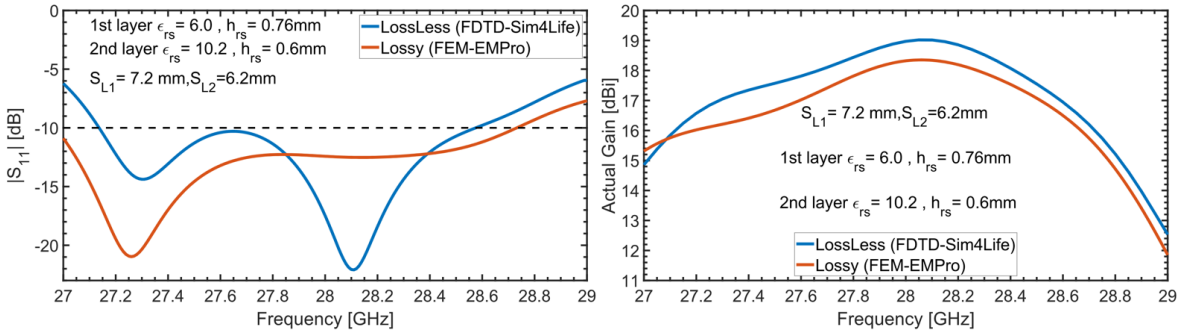

Figure5. 43 Comparison of |S_{11}| and actual gain between lossless and lossy material

The effect of conductor loss and dielectric loss are investigated by comparison of actual gain and magnitude of reflection coefficient between antenna structure with lossless and with lossy materials. The analysis results are evaluated within frequency band of 27GHz to 29GHz with sampling frequency of 0.05GHz. From analysis results in Figure5. 43, −10dB impedance bandwidth from FEM is wider than that from FDTD. However, the actual gain from FEM is smaller than that from FDTD. The actual gain of slot antenna is decreasing about 0.6dB after conductor loss and dielectric loss are included. The discrepancy between reflection coefficients may be from the effect computational error between FDTD and FEM. However, the discrepancy in actual gain could be from the effect of dielectric and conductor loss. Therefore, both dielectric and conductor loss cause the decrease in actual gain.

5.4.3 Gain enhancement of leaf-shaped bowtie slot antenna array fed by quarter wavelength matching circuit and microstrip taper line

The antenna structure in Figure4. 36 is used for gain enhancement investigation. To increase gain of the slot antenna array in Figure4. 36, superstrate layer is arranged on top of antenna ground plane. The superstrate layer has relative permittivity of ε_{rs}=6.0, and thickness of h_{rs}=0.72mm. The superstrate layer has the same dimension as ground plane. Two methods have been used as gain enhancement. The first method is one superstrate layer, and the second method is two superstrate layers.

A. Antenna structure with one superstrate layer

One superstrate layer with relative permittivity of ε_{rs}=6.0 and thickness of h_{rs}= 0.76mm is arranged on top of antenna ground plane. The antenna structure is shown as in Figure5. 44. The separation with superstrate layer to antenna ground plane is S_{L1}. To obtained maximum actual gain and impedance bandwidth, the separation S_{L1} is optimized. In addition, due to the effect of superstrate layer, the right-angle bends of microstrip line are not used in this structure. Moreover, the length of opened-circuit line is also re-adjusted to get maximum impedance bandwidth. The structural parameters of slot antenna array with one superstrate layer are shown in Table5. 11.

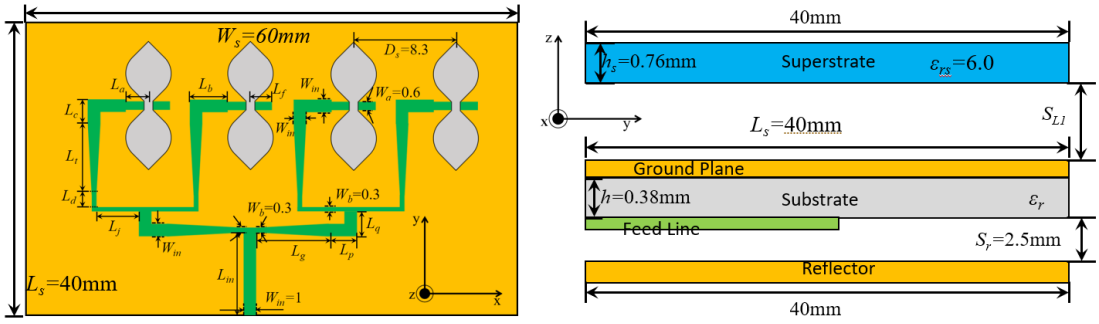

Figure5. 44 Slot antenna array fed by quarter wavelength matching circuit and tapered line with one superstrate layer

Table5. 11 Structural parameters of slot antenna array

L_a	L_b	L_f	W_{in}	W_a	L_c
2mm	2.55mm	2.4mm	1mm	0.6mm	2.3mm
L_t	L_d	L_j	L_{in}	W_b	L_q
5.5mm	2mm	2.5mm	7.75mm	0.3mm	3mm
L_p	L_g	L_k	D_s	S_{L1}	
3mm	5.3mm	1.3mm	8.3mm	5.6mm	

To optimize actual gain and impedance bandwidth, the separation S_{L1} is varied within 5.5mm to 5.9mm. The actual gain and reflection coefficient are analyzed by using FDTD in commercial simulation software. Actual gain is analyzed with sampling frequency of 0.05GHz and reflection coefficient is calculated with reference impedance of 50Ω. The analysis results are shown as in following Figure5. 45.

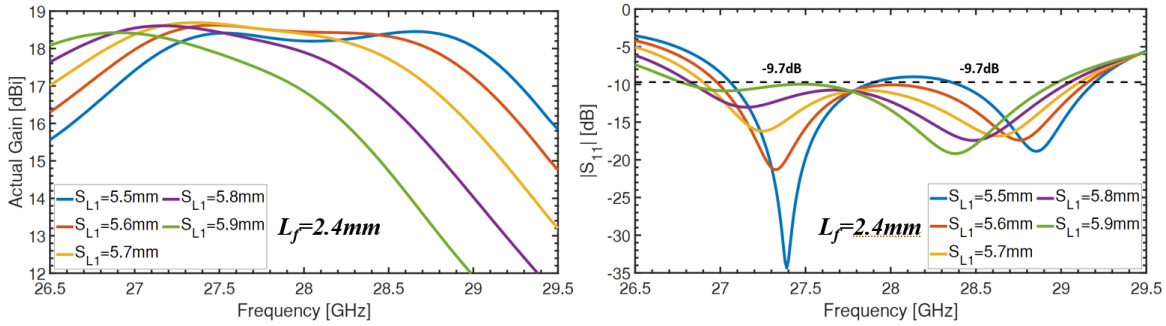

Figure5. 45 Actual gain and reflection coefficient of antenna structure with one superstrate layer

From the comparison of analysis results, the maximum impedance bandwidth and actual gain are obtained when the separation S_{L1} is chosen as S_{L1}=5.6mm. The analysis results in Figure5. 46 shows the reflection coefficient and actual gain of antenna structure with separation S_{L1}=5.6mm. In addition, the element spacing D_s is varied within 8.1mm to 8.5mm in order to optimize actual gain and impedance bandwidth. The analysis results are shown as in Figure5. 46. From the analysis results, as element spacing is getting smaller, the impedance bandwidth is shifting to higher frequency; and as element spacing is getting larger, the

impedance bandwidth is shifting to lower frequency. From the comparison, the optimum element spacing is chosen as D_s=8.3mm.

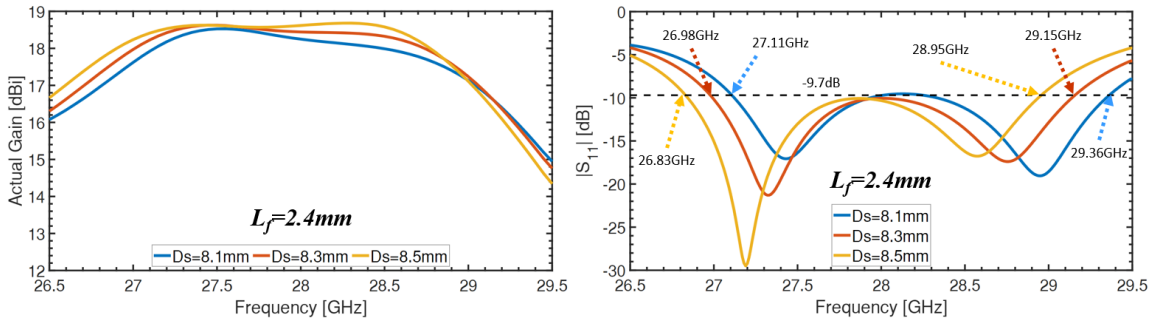

Figure5. 46 comparison of analysis results actual gain and $|S_{11}|$ with S_{L1}=5.6mm

From Figure5. 47, the maximum actual gain is around 18.5dBi and impedance bandwidth occupies frequency range of 26.98GHz to 29.15GHz which is about 2.15GHz. The −3dB gain bandwidth occupies frequency range of 26.5GHz to 29.35GHz. Therefore, the analysis results show that the antenna structure with one superstrate layer has high gain and wideband characteristic. The antenna bandwidth satisfies the target frequency band 27GHz to 29GHz.

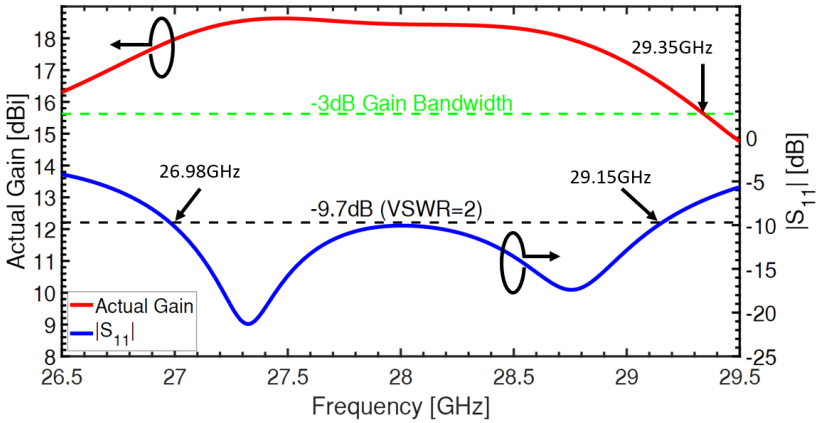

Figure5. 47 Analysis results of antenna characteristics with separation D_s=8.3mm, S_{L1}=5.6mm

The analysis results of radiation pattern are evaluated within frequency range of 27GHz to 29GHz with sampling frequency of 0.5GHz. From Figure5. 48, the radiation pattern in E-plane has maximum sidelobe level less than −10dB within 27GHz to 29GHz. The cross polarization is less than −20dB within the targeted bandwidth. In H-plane, there is no sidelobe and maximum cross polarization is less than −20dB within 27GHz to 28.5GHz. However, the cross polarization in H-plane is slightly increasing at higher frequency. The maximum cross polarization in H-plane at 29GHz is less than −18dB. Comparing to antenna structure in Figure5. 18 and Figure5. 22, the antenna structure in Figure5. 44 offers wider impedance bandwidth and higher actual gain. Moreover, the antenna structure in Figure5. 44 offers a wider −3dB gain bandwidth and better radiation pattern.

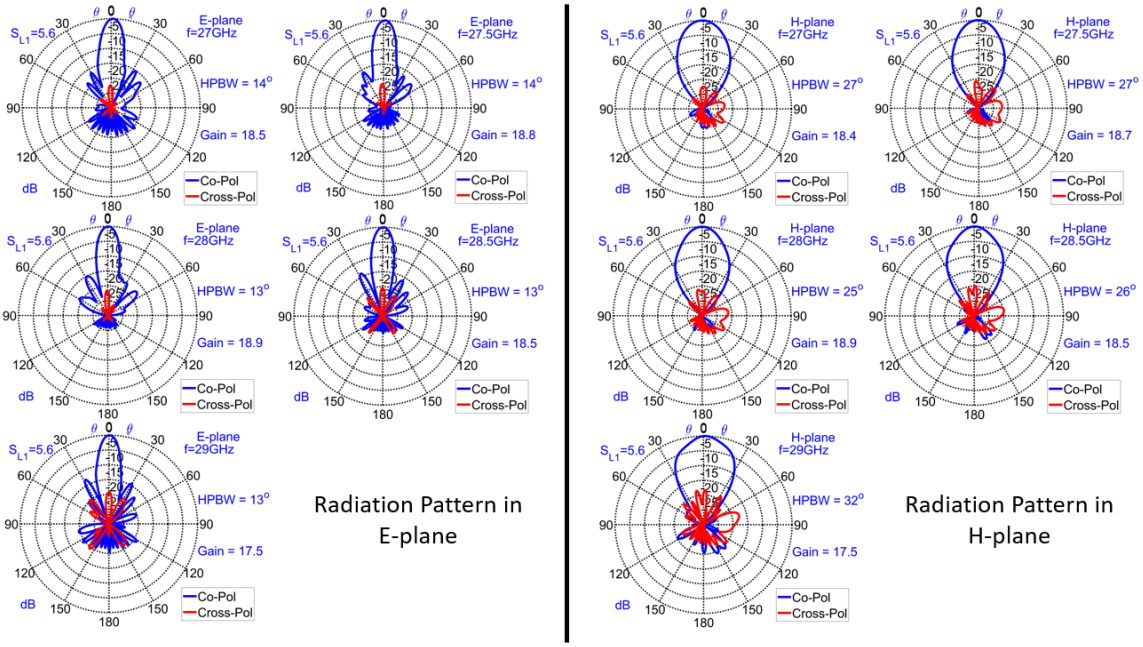

Figure5. 48 Radiation pattern of slot antenna array with quarter wavelength and tapered line D_s=8.3mm, S_{L1}=5.6mm

B. Antenna structure with two superstrate layers

To further study the effect of dielectric superstrate on slot antenna array, two superstrate layers are arranged on top of antenna ground. The completed antenna structure is shown as in Figure5. 49.

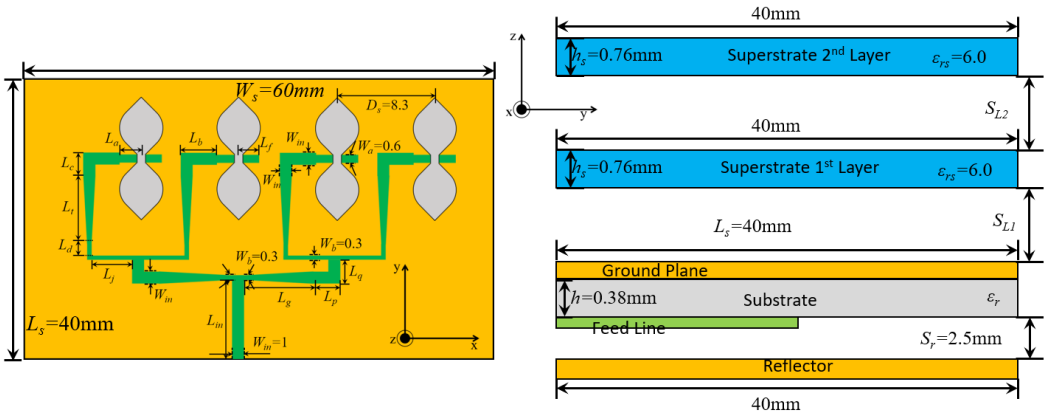

Figure5. 49 Leaf-shaped bowtie slot antenna array fed by quarter wavelength matching circuit and tapered line with two superstrate layers

The separation between superstrate 1st layer and superstate 2nd layer are represented by S_{L1} and S_{L2}. To maximize actual gain and impedance bandwidth, the separation S_{L1} and S_{L2} are reoptimized. The structural parameters of antenna structure in Figure5. 49 are shown as in following Table5. 12.

Table5. 12 Structural parameters of antenna structure in Figure5. 49

L_a	L_b	L_f	W_{in}	W_a	L_c
2mm	2.55mm	2.2mm	1mm	0.6mm	2.3mm
L_t	L_d	L_j	L_{in}	W_b	L_q
5.5mm	2mm	2.5mm	7.75mm	0.3mm	3mm
L_p	L_g	L_k	D_s	S_{L1}	S_{L2}
3mm	5.3mm	1.3mm	8.3mm	5.2mm	5.2mm

To obtain the maximum actual gain and impedance bandwidth, the separation S_{L1} and S_{L2} are varied within 5.1mm to 5.3mm. The analysis results are evaluated by using FDTD method in commercial simulation software. From the comparison of analysis results in Figure5. 50 and Figure5. 51, the maximum actual gain and impedance bandwidth is obtained when S_{L1} and S_{L2} are chosen as S_{L1}=5.2mm, and S_{L2}=5.2mm. In addition, length of the open-circuited line is re-adjusted to obtain impedance bandwidth which occupies frequency range of 27GHz to 29GHz. With S_{L1}=5.2mm and S_{L2}=5.2mm, the optimum length of open-circuited stub is chosen as L_f=2.2mm.

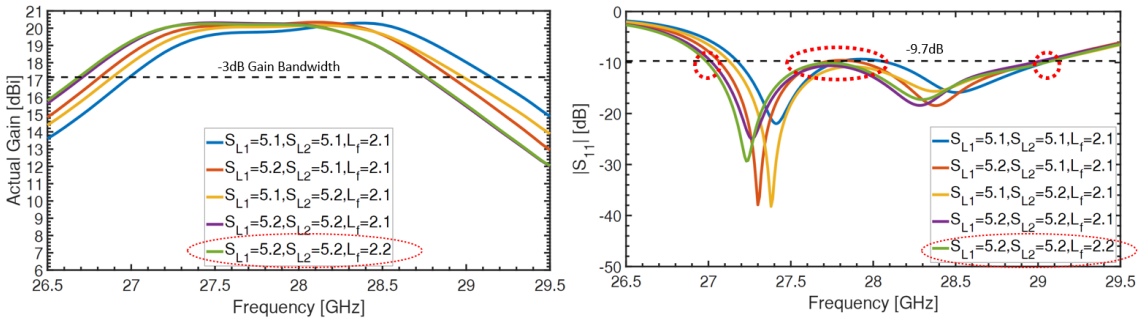

Figure5. 50 Actual gain and $|S_{11}|$ with S_{L1} and S_{L2} varied within 5.1mm to 5.2mm (D_s=8.3mm)

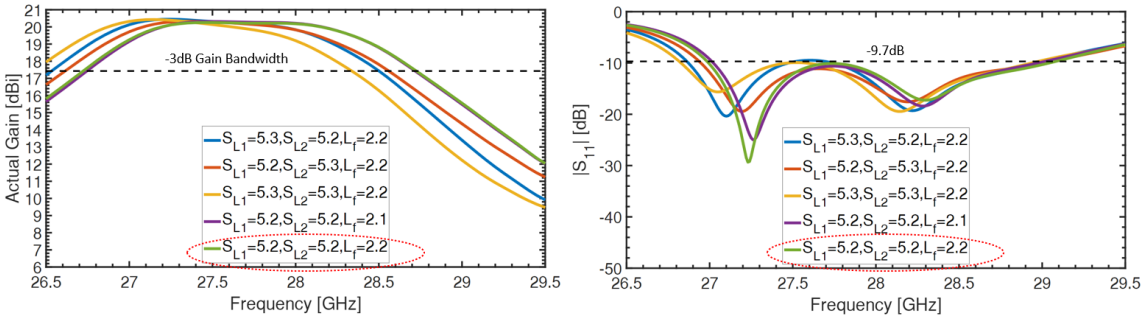

Figure5. 51 Actual gain and $|S_{11}|$ with S_{L1} and S_{L2} varied within 5.2mm to 5.3mm (D_s=8.3mm)

In addition to the optimization of separation S_{L1} and S_{L2}, the antenna element spacing is also varied within 8.1mm to 8.5mm to obtain maximum actual gain and impedance bandwidth. Similarly, the impedance bandwidth is shifting to lower frequency when element spacing is getting larger, and the impedance bandwidth is shifting to higher frequency when element spacing is getting smaller. From the comparison of analysis results in Figure5. 52, the optimum element spacing for maximum actual gain and impedance bandwidth is chosen as D_s=8.3mm.

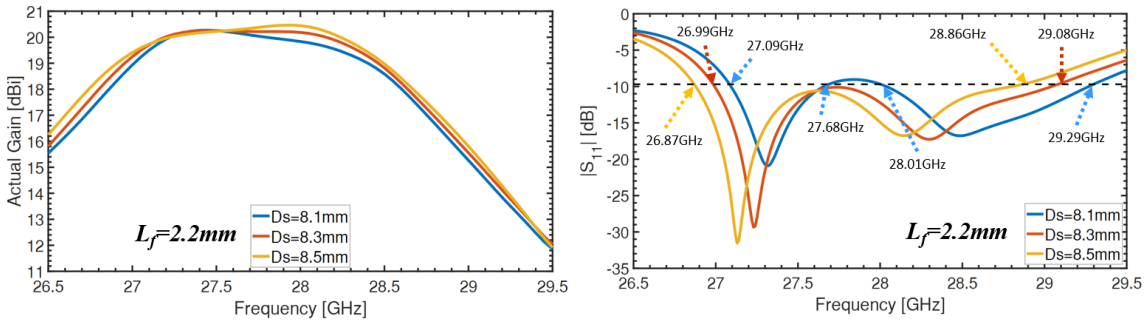

Figure5. 52 Actual gain and $|S_{11}|$ with element spacing D_s varied within 8.1mm to 8.5mm (S_{L1}=S_{L2}=5.2mm)

The maximum actual gain and impedance bandwidth are obtained when S_{L1} and S_{L2} are chosen as S_{L1}=S_{L2}=5.2mm, L_f is chosen as L_f=2.2mm, and D_s is chosen as D_s=8.3mm. The optimized results are shown as in Figure5. 53. The antenna structure in Figure5. 49 offers impedance bandwidth which occupies frequency range of 27GHz to 29GHz. The maximum actual gain is around 20dBi with −3dB gain bandwidth which occupies frequency range of 26.7GHz to 28.75GHz. From Figure5. 53, the impedance bandwidth and −3dB gain bandwidth are in the same band; especially, the −3dB gain bandwidth does not satisfy the targeted bandwidth 27GHz to 29GHz.

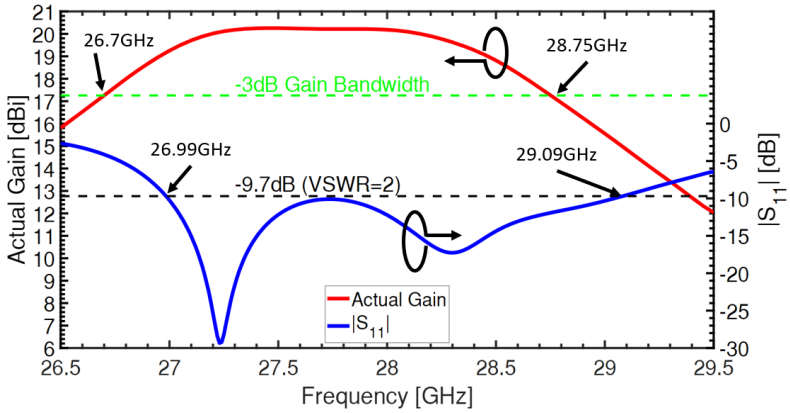

Figure5. 53 Actual gain and $|S_{11}|$ of antenna structure with D_s=8.3mm, L_f=2.2mm, S_{L1}=S_{L2}=5.2mm

From the radiation pattern analysis in Figure5. 54, sidelobe level in E-plane is increasing as frequency is getting higher. Comparing to radiation pattern in Figure5. 48, the sidelobe level at 29GHz is slightly higher. However, the cross polarization in E-plane is lower than radiation pattern in Figure5. 48. In H-plane, the beam width is smaller than radiation pattern in Figure5. 48 within 27GHz to 28.5GHz. At 29GHz, the beamwidth is wider than the result in Figure5. 48. Gain in broadside of radiation pattern in Figure5. 54 is greater than that of radiation pattern in Figure5. 48 within 27GHz to 28.5GHz. At 29GHz, gain in broadside of radiation pattern in Figure5. 48 is greater than that of radiation pattern in Figure5. 54. The reason maybe the reflection coefficient of superstrate is changed with frequency. The reason maybe, in broadside direction, the reflected field from 2nd layer are out of phase comparing to field transmitted from 1st layer.

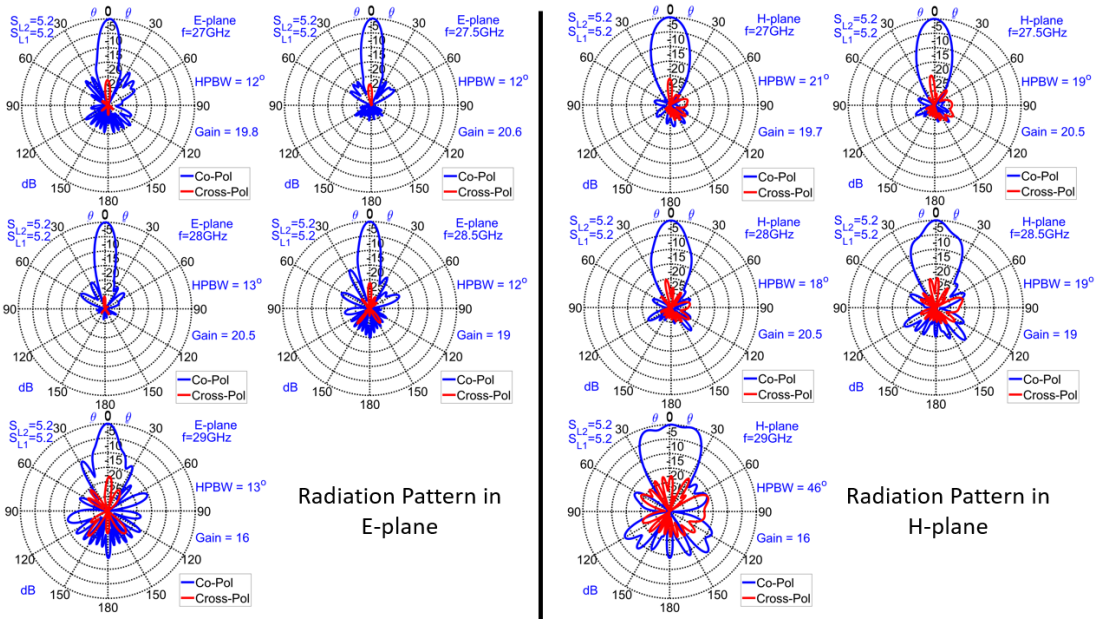

Figure5. 54 Radiation of slot antenna fed by quarter wavelength matching circuit and tapered line with two superstrate layers

Figure5. 55 shows the comparison of antenna characteristics between antenna structure with one superstrate layer and antenna with two superstrate layers. From the comparison, by using two superstrate layers, the maximum actual is increasing around 1.5dB; however, the antenna structure with one superstrate layer has wider −3dB gain bandwidth than the antenna with two superstrate layers. Both antenna has almost the same impedance bandwidth, although impedance bandwidth of antenna structure with one superstrate layer is slightly wider than antenna structure with two superstrate layers. As the results, both antenna structure offers high gain and wide band characteristics.

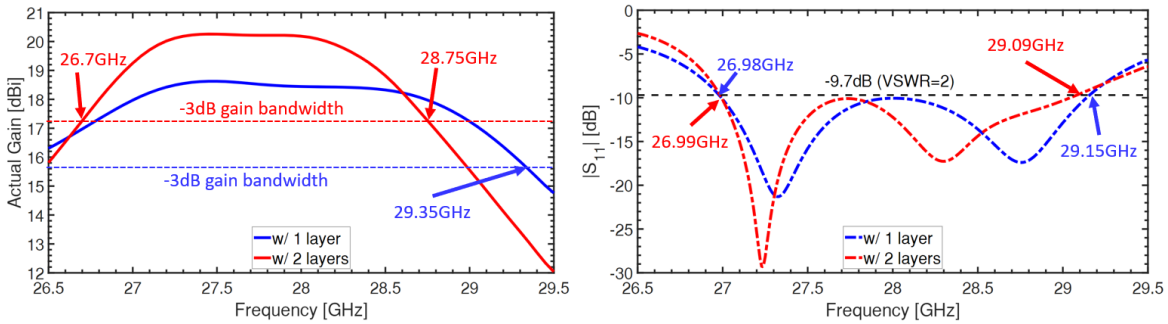

Figure5. 55 Comparison of actual gain and $|S_{11}|$ between antenna structure with one superstrate layer and two superstrate layers

5.5 Gain Enhancement of Leaf-Shaped Slot Antenna Array with 4×4 Butler Matrix

In addition to the linear array of leaf-shaped bowtie slot antenna for broadside radiation, 4×4 microstrip-based Butler Matrix has been designed and connected to the slot antenna array to perform beam-scanning. The antenna structure, which is used in beam-scanning, is the same as in section 5.4.1. The element length of radiating slot is L_e=2.7mm and R_s=1.8mm. 4×4 butler matrix [59] feeding network is connected to ground plane vicinity of radiating slot through conductor probe. In addition, two layers of dielectric superstrate are arranged on top of slot antenna ground plane to improve actual gain and reflection coefficient. The antenna structures are shown as in Figure5. 44 and Figure5.45. In this structure, the separation between ground plane and first layer (S_{L1}) and separation between first layer and second layer (S_{L2}) are chosen as S_{L1}=5.3mm, and S_{L2}=5.3mm, which are optimized as in the previous section5.4.1. The element spacing between adjacent radiating slot d_s is chosen as d_s=7.6mm. Dielectric substrate of antenna structure has relative permittivity of ε_r=2.17 and h_r=0.38mm. The Butler matrix feeding network are printed on the bottom of antenna substrate. After flat reflector is placed at separation of S_r=2.5mm, which is optimized in section5.4.1. The characteristics of both dielectric superstrate layers are identical. The relative permittivity and thickness of dielectric superstrate are ε_{rs}=10.2 and h_{rs}=0.6mm. The unit of structural parameters in Figure5. 44 is "*mm*".

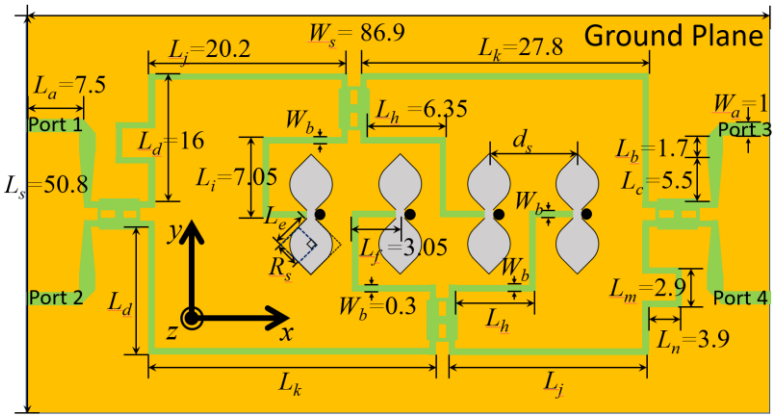

Figure5. 56 Linear array of 4 leaf-shaped bowtie slot antenna in connection with 4x4 Butler matrix

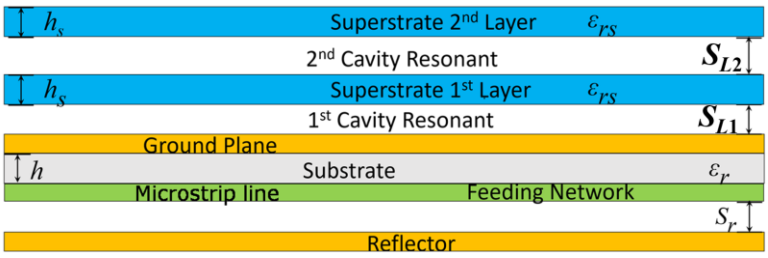

Figure5. 57 side view of antenna structure with two layers of superstrate

Characteristics of the designed antenna structure are evaluated by performing Finite-Difference Time-Domain (FDTD) simulation using commercial simulation software Sim4Life. The antenna characteristics are analyzed over the frequency range from 27GHz to 29GHz. In FDTD simulation, cell size for modelling structure of slot antenna array is set as following, Δx=0.05mm, Δy=0.05mm, and Δz=0.02mm. In addition, grid size of dielectric superstrate is set as Δx=0.05mm, Δy=0.05mm, and Δz=0.05mm. A 10-layer UPML (uniaxial perfectly matched layer) is employed as absorbing boundary condition for FDTD analysis. Simulated frequency response of reflection coefficients and actual gain in main beam direction of each port are shown as in Figure5. 46.

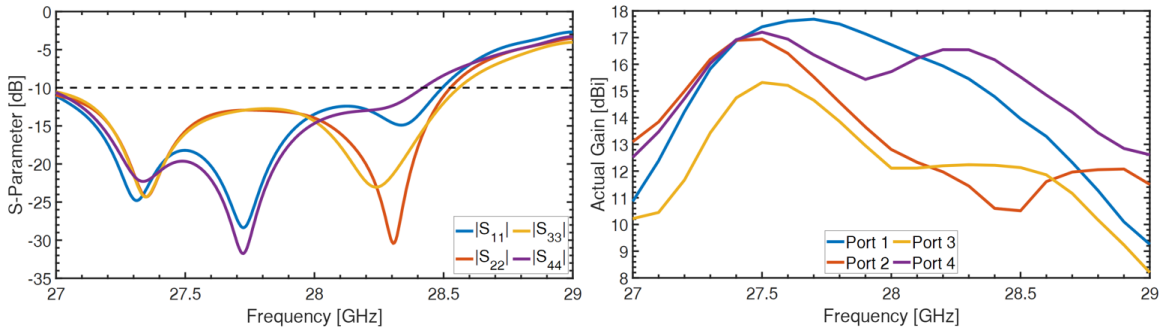

Figure5. 58 Magnitude of S-parameter and actual gain of each input port

For the evaluation of the reflection coefficients, reference impedance of each input port is chosen as 50Ω. The analysis results show that −10dB impedance bandwidth of Port#1 occupies frequency range of 27GHz to 28.5GHz, Port#2 occupies frequency range of 27GHz to 28.52GHz, Port#3 occupies frequency range of 27GHz to 28.56GHz, and Port#4 occupies frequency range of 27GHz to 28.42GHz. Therefore, −10dB impedance bandwidth of each input port is ranging from 5.2% to 5.8% within 28GHz band. The analytical results show that maximum actual gain from Port#1 is 17.68dBi, and −3dB gain bandwidth occupies frequency range of 27.22GHz to 28.42GHz. Peak actual gain from Port#2 is 16.9dBi, and −3dB gain bandwidth occupies frequency range of 27.1GHz to 27.88GHz. Peak actual gain from Port#3 is 15.3dBi, and −3dB gain bandwidth occupies frequency range of 27.23GHz to 27.98GHz. Peak actual gain of Port#4 is 17.2dBi, and −3dB gain bandwidth occupies frequency range of 27.15GHz to 28.7GHz.

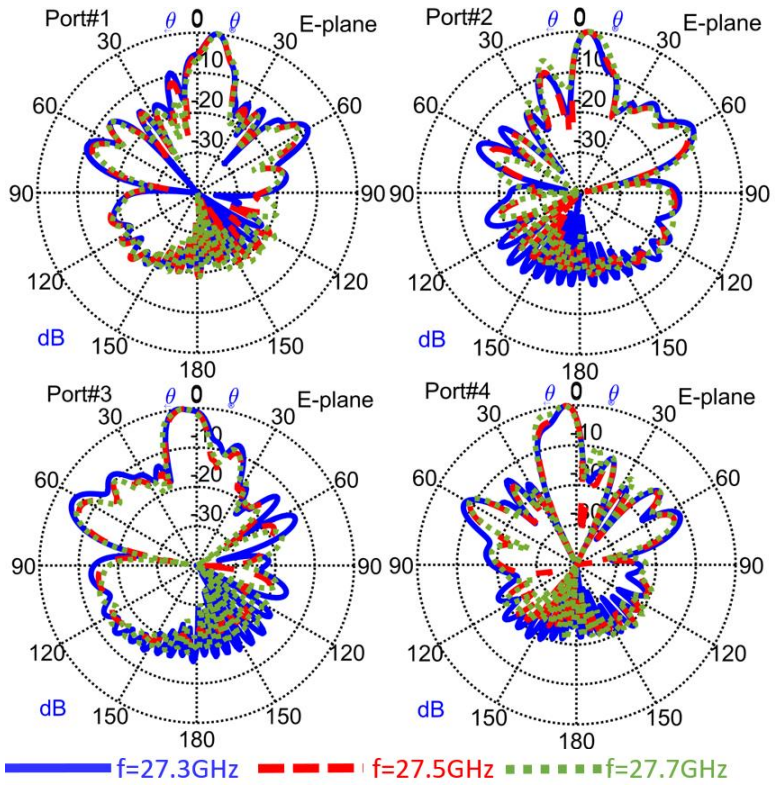

Figure5. 59 Radiation pattern of each input port

The analysis results of radiation pattern of each input port are shown as in Figure. The radiation patterns are evaluated at 27.3GHz, 27.5GHz, and 27.7GHz to observe the dependency of radiation pattern versus frequency. From Figure, half-power beamwidth of Port#1 is within 3° to 11° and maximum sidelobe level of Port#1 is −10dB at 27.5GHz. HPBW of Port#2 is within −12.5° to 2.5°, and maximum sidelobe level is −10dB at 27.5GHz. HPBW of Port#3 is within −12.5° to 2.5° and maximum sidelobe level is −8dB at 27.5GHz. HPBW of Port#4 is within −20° to −2°, and maximum sidelobe level is around −10dB at 27.5GHz. From Fig. 5, radiation beams are in the same angle when frequency is varying. Therefore, the proposed antenna structure has a good radiation pattern within 27.3GHz to 27.7GHz which is about 400MHz bandwidth.

Table5. 13 Summary of radiation pattern of each port

Frequency	f=27.3GHz	f=27.5GHz	f=27.7GHz
Port#1	Gain = 15.8dB Scanning Angle = 8°	Gain = 17.5dB Scanning Angle = 8°	Gain = 17.7dB Scanning Angle = 9°
Port#2	Gain = 16.2dB Scanning Angle = 4°	Gain = 17.1dB Scanning Angle = 4°	Gain = 15.8dB Scanning Angle = 5°
Port#3	Gain = 13.5dB Scanning Angle = −6°	Gain = 15.4dB Scanning Angle = −4°	Gain = 14.9dB Scanning Angle = −4°
Port#4	Gain = 16.1dB Scanning Angle = −3°	Gain = 17.2dB Scanning Angle = −3°	Gain = 16.4dB Scanning Angle = −4°

Summary

In Chapter 5, two layers of dielectric superstrate has been employed and arranged on the top of linear array of 4 leaf-shaped bowtie slot antennas. From FDTD analysis results, antenna characteristics have been improved. The actual gain in broadside radiation pattern has been increased by arranging two layers of dielectric superstrate on top of antenna ground plane. However, the performance of antenna characteristics is highly depending on the separation between antenna's ground plane and first layer and the separation between the first layer and second layer. In addition, the characteristics of superstrate layers (ε_{rs} and h_{rs}) also effect on performance of antenna for the case of antenna structure with feeding circuit as quarter wavelength matching circuit. From the analysis results, the structures of leaf-shaped bowtie slot antenna array with two layers of dielectric superstrate have been designed and optimized. On the hand, the antenna structure, whose feeding circuit consists of quarter wavelength matching circuit and microstrip tapered line, offers a wider impedance bandwidth and higher actual gain with wider −3dB gain bandwidth. From the FDTD analysis results, the impedance bandwidth and gain bandwidth can satisfy the targeted frequency band 27GHz to 29GHz. In terms of beam scanning, the structure of butler matrix is needed to be re-optimized.

Chapter 6
Antenna Prototype Measurement

6.1 Abstract

In Chapter 6, prototypes of antenna structures which are designed in Chapter 3 and Chapter 5 are fabricated. Characteristics of these antenna structures are measured and compared with analysis results to validate the designed model. Prototypes of antenna structures are fabricated by using conventional and low-cost method that is etching and engraving. The fabrication process has been done in Wireless Technology and EMC Research laboratory, Hokkaido University. Two antenna prototypes have been fabricated. First prototype is reflector backed leaf-shaped bowtie slot antenna fed by quarter wavelength matching circuit which is designed in Chapter 3. Second prototype is leaf-shaped bowtie slot antenna array with two layers of superstrate which is designed in Chapter 5.

6.2 Reflector Backed Leaf-Shaped Bowtie Slot Antenna Fed by Quarter Wavelength Transformer

The leaf-shaped bowtie slot antenna with a reflector designed in Chapter 3 is fabricated, and the antenna characteristics (magnitude of reflection coefficient and radiation pattern) were measured. A PTFE substrate NPC-H220A (relative permittivity: 2.17±0.05, dielectric loss tangent: 0.0006@10GHz) manufactured by Nippon Pillar Industry Co., Ltd was used as the reflector. The reflector was fixed to the antenna substrate by using holes made in the four corners of the antenna substrate and the reflector, and polycarbonate screws, spacer, and nuts. A female SMA connector is attached to the power supply port by soldering. Figure6. 1 shows an antenna prototype for measurement. Figure6. 2 shows a comparison between the analysis results of the reflection coefficient magnitude and the measured values. Reflection coefficient is shown in the frequency band of 5.9GHz to 10.4GHz.

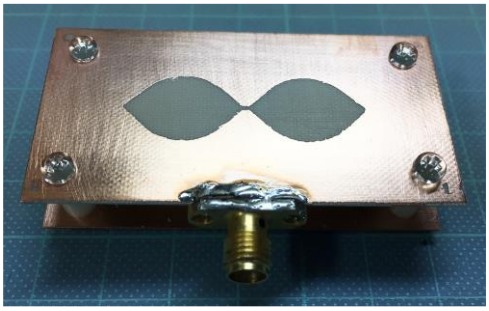

Figure6. 1 Prototype antenna for measurement

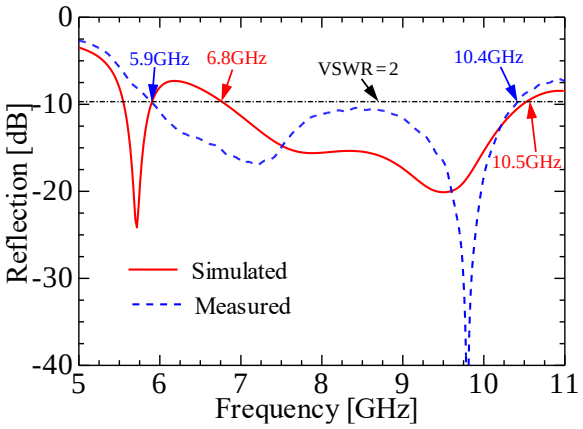

Figure6. 2 Comparison between simulated and measured reflection coefficient amplitude

From Figure6. 2, the measured amplitude of reflection coefficient is −9.7dB or less (standing wave ratio is 2 or less), and the same as analysis result, the characteristics that cover the band (7GHz to 10GHz) that is the design target in this research are obtained. Regarding to the upper limit frequency of the band where the standing wave ratio is 2 or less, the analysis value (10.5GHz) and the measurement result (10.4GHz) are almost the same. On the other hand, regarding to the lower limit frequency of the same band, the analysis result is 6.8GHz, while the measurement result is 5.9GHz, which is about 0.9GHz lower than the analysis result. The reason why the above discrepancy occurs between the analysis results of reflection coefficient amplitude and the measured value is the influence of the machining accuracy of the prototype antenna (the position of the microstrip line is misaligned, and the slot element dimensions F_a and F_b at the intersection with the line are in error. , etc.), the influence of the reflection by SMA connector.

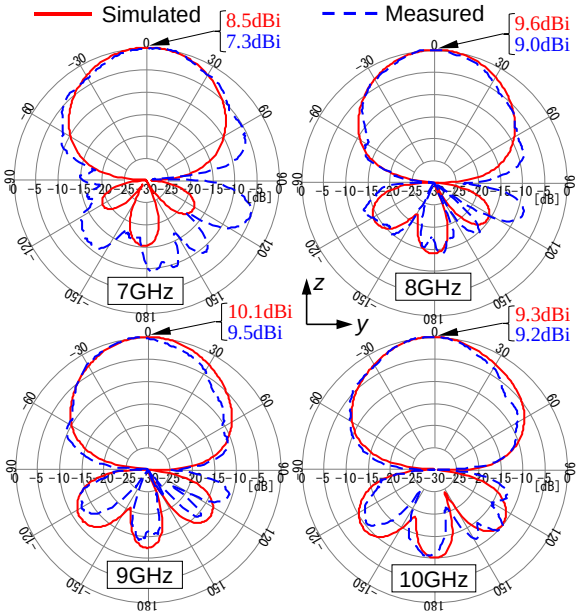

Figure6. 3 Comparison between simulated and measured E-plane pattern

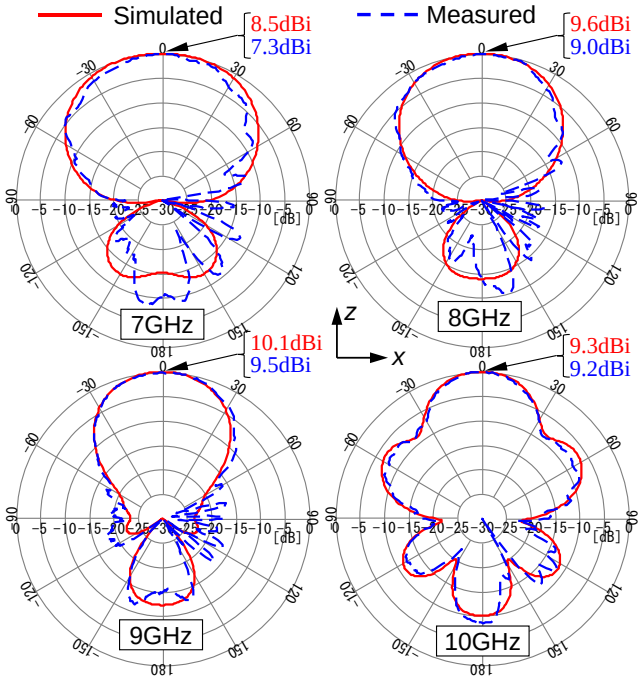

Figure6. 4 Comparison between simulated and measured H-plane pattern

Finally, Figure6. 3 and Figure6. 4 show the analysis and measurement results comparison of E-plane radiation pattern and H-plane radiation pattern from 7GHz to 10GHz, respectively. In these Figures, the result of normalizing the main polarization component with the maximum gain (value displayed in the 0° direction: red is analysis value, blue is the measured value) is displayed.

It can be confirmed that the measurement results of the radiation patterns at each frequency for both E-plane and H-plane are almost the same as the analysis results. On the E-plane, the pattern shape of the measurement results are distributed around 60° to 120°, but since it is the results of measurement with the SMA connector and the measurement cable in the direction corresponding to 90°. It is considered that the pattern shaped was distributed due to these effects. In addition, the reason why the error in the measurement results of E-plane radiation pattern at 7GHz, which is lower of the design band, is larger than that of other frequencies is that the dimensions of the ground conductor plate and the reflector with respect to wavelength are the smallest in the design band at the same frequency. Therefore, it possible that the influence of connectors, measurement cables, and screw holes will be greater than at other frequencies. The measurement results of the operating gain in the maximum radiation direction at each frequency was 7.3dBi to 9.5dBi, which was almost the same as or slightly lower than the analysis result (8.5dBi to 10.1dBi)

6.3 Leaf-Shaped Bowtie Slot Antennas Array with Two Layers of Superstrate

To validate the analysis results of antenna structure, which is designed in Chapter 5, the prototype of linear array of 4 leaf-shaped bowtie slot antennas is fabricated by using etching and engraving technique. The antenna characteristics such as actual gain and reflection coefficient and radiation pattern are measured and compared with analysis results.

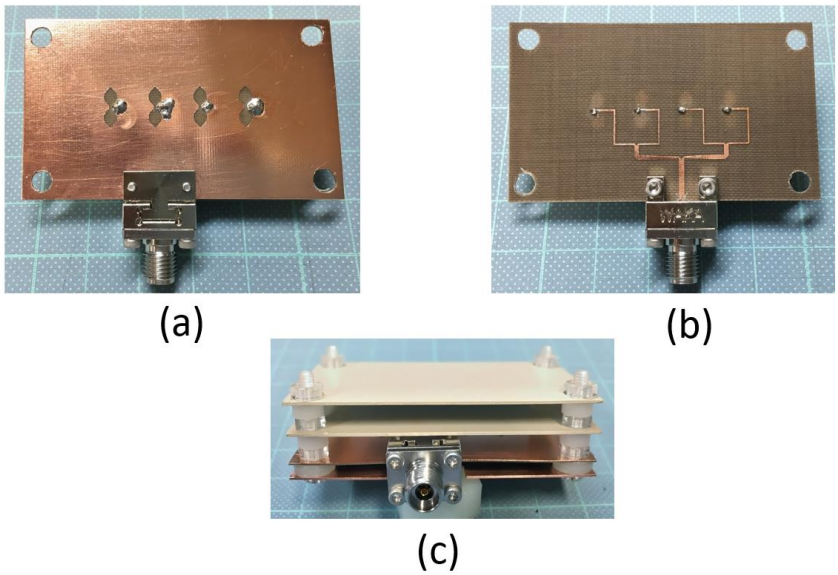

Figure6. 5 (a) antenna ground plane, (b) feeding circuit,
(c) antenna's side view with two layers of dielectric superstrate

Figure6. 5 show prototypes of the proposed antenna structure. The reflector, and two superstrate layers were fixed to the antenna substrate by using holes made in the four corners of the antenna substrate and the reflector, and polycarbonate screws, spacer, and nuts. A

female K-type connector is attached to the power supply input port by soldering. In addition, conducting post were connected to ground plane vicinity and microstrip line by soldering.

Figure6. 6 shows comparison between measured and simulated results of actual gain and $|S_{11}|$. From Figure6. 6 the measured −10dB impedance bandwidth occupies frequency range of 27.22GHz to 28.55GHz, and the simulated −10dB impedance bandwidth occupies the frequency range of 27.17GHz to 28.39GHz. Therefore, the measured −10dB impedance bandwidth is slightly shifting to higher frequency band. However, the discrepancies between the measured and simulated −10dB impedance bandwidth are small. In addition, −10dB impedance bandwidth is still in the same 28GHz band. From Figure6. 6, the measured actual gain is around 1.5dBi smaller than simulated actual gain at 28GHz. The discrepancies could be due to the conductor loss, fabrication error of the prototype antenna, and the disturbance of radiation characteristics which is caused by screws or connectors.

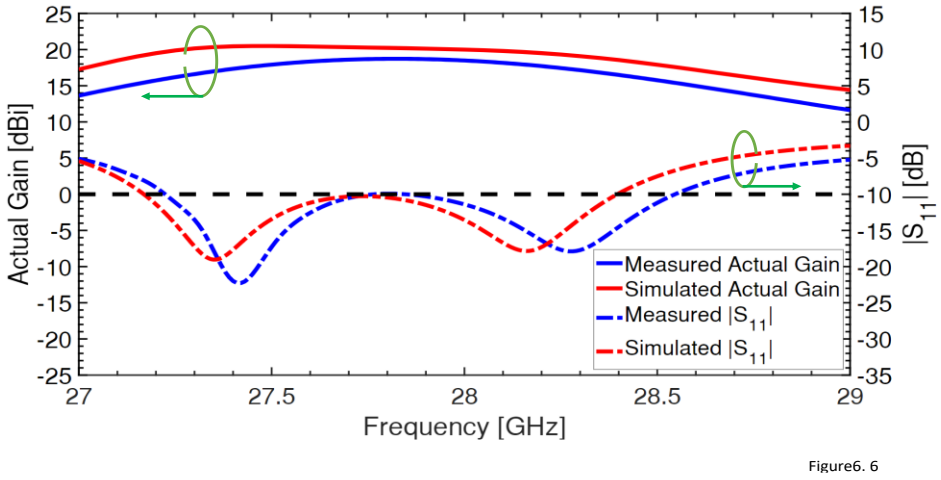

Figure6. 6

Figure6. 6 Comparison between measured and simulated actual gain and $|S_{11}|$

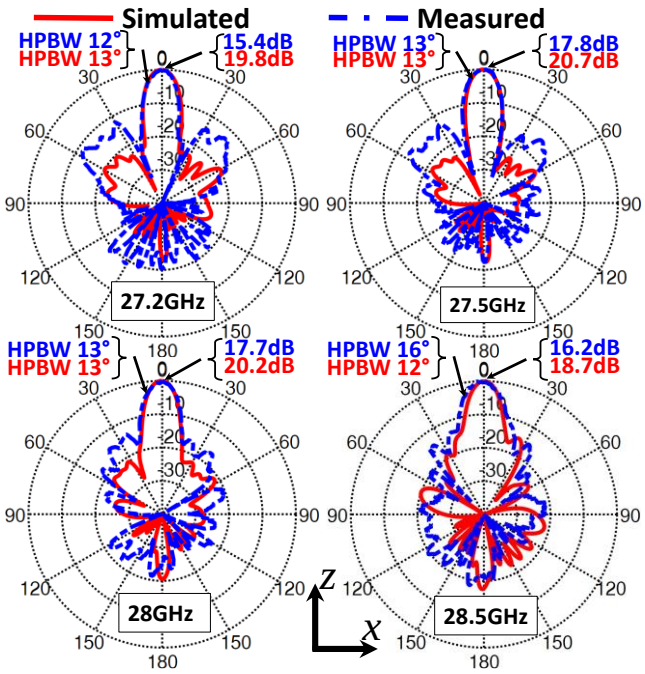

Figure6. 7 Comparison between measured and simulated E-plane pattern

Figure6. 7 and Figure6. 8 show comparison between measured and simulated radiation pattern at frequencies of 27.2GHz, 27.5GHz, 28GHz, and 28.5GHz, which are within −10dB impedance bandwidth (27.2GHz - 28.5GHz). In broadside direction, there are small discrepancies between measured and simulated results at 28.5GHz along both E-plane and H-plane. However, sidelobe level of measured radiation pattern along E-plane is slightly increasing at 27.2GHz, 27.5GHz and 28GHz. From Figure6. 7 and Figure6. 8, maximum gain of measured radiation pattern at 28GHz is around 2dB smaller than the maximum gain of simulated radiation pattern. The discrepancies could be due to the fabrication error of the prototype antenna, and the disturbance of radiation characteristics which is caused by screws or connectors. On the hand, the soldering, at the connection between conducting probe and ground plane and at the connection between conducting probe and microstrip line, may also cause the error of radiation pattern. In terms of HPBW, Figure6. 7 and Figure6. 8 show a good agreement between simulated and measured radiation patterns along both E-plane and H-plane. Therefore, both simulated and measured results confirm that the proposed antenna structure has good radiation pattern with 27.2GHz to 28.5GHz.

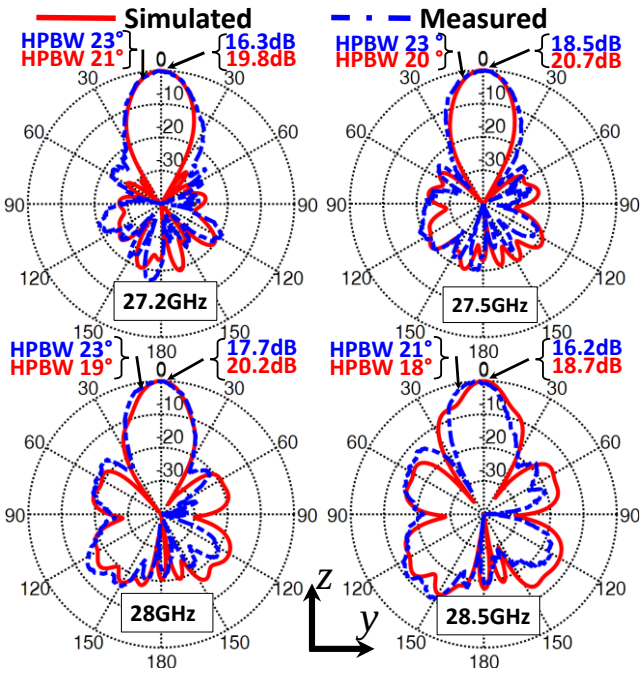

Figure6. 8 Comparison between measured and simulated H-plane pattern

Summary

Two antenna prototypes have been fabricated by using conventional and low-cost method which is etching and engraving. Characteristics of antenna structures, which are designed in this research, have been measured and compared with simulated results to validate the analysis model. From the comparison, both measured and simulated results are relatively in a good agreement. There are small discrepancies which is assumed to be caused from fabrication process, connector, screws, and soldering.

CHAPTER 7
Conclusion and Future Work

7.1 Conclusion

In Chapter 1, the background of this research has been discussed. The purpose of this research is to design antenna structure that has high gain, wide bandwidth, low cost of fabrication and low profile. In addition, the antenna is suitable for 28GHz frequency band in Japan which is within 27GHz to 29GHz.

In Chapter 2, a briefly review of computational method for electromagnetic is presented. From that review, it makes this research go smoothly because the review helps to utilize the commercial simulation software effectively and efficiently. In addition, Finite Difference Time-Domain (FDTD) Method are the main discussion point in Chapter 2. Understanding the main concept of FDTD in Chapter 2 is a base to use commercial simulation Sim4Life which is a FDTD based commercial simulation software. Therefore, selection of grid size, excitation source, Far-Field sensor in Sim4Life is based on review in Chapter 2.

In Chapter 3, the leaf-shaped bowtie slot antenna is specifically focused. wideband characteristics of leaf-shaped bowtie slot antenna is indispensable for the realization of a high-frequency band distributed antenna system and examined its design. When a reflector is added to make the bidirectional antenna become unidirectional, the design takes into consideration the influence of the reflector, and even if the reflector is added, the antenna characteristics were evaluated by numerical simulation (FDTD analysis) that the bandwidth of the antenna can be widened. It is also shown that quarter wavelength matching circuit is adopted as a component of the feeding circuit with an impedance matching function, and that a wideband of impedance characteristics was possible by obtaining double resonance characteristics.

In Chapter 4, leaf-shaped bowtie slot antenna is adopted in a linear array for use in millimeter wave frequency band. Comparing to single leaf-shaped bowtie slot antenna, the actual gain in broadside direction has increased around 6dB. However, the −10dB impedance bandwidth of the slot antenna array are depending on feeding circuit. Reflector backed leaf-shaped bowtie slot antennas array fed by microstrip line and conductor probe has −10dB impedance bandwidth of around 0.49GHz bandwidth. Reflector backed leaf-shaped bowtie slot antennas array electromagnetically fed by microstrip line and quarter wavelength matching circuit has −10dB impedance bandwidth of about 1.68GHz bandwidth. Therefore, the slot antennas array with quarter wavelength matching circuit has wider impedance bandwidth. In quarter wavelength feeding circuit, the quarter wavelength matching circuit has been used in seven locations which are at radiating slot, and T-junction. To improve impedance matching, right-angle bend of microstrip line and T-junction must be truncated.

The cutting ratio at each right-angle bend and T-junction must be properly chosen because it highly effects on impedance matching of whole slot antenna array structure. In this structure, conductor loss and dielectric loss are investigated by comparison of actual gain and impedance bandwidth. Actual gain has decreased around 0.3dB due to dielectric and conductor loss. To improve impedance bandwidth and actual gain, tapered lines are used to convert impedance at 50Ω line from feed point of antenna element and at T-junction to 100Ω line, to have balance of impedance within feeding circuit. The antenna structure, whose feeding circuit consists of quarter wavelength matching circuit and tapered line, offers high gain and wider impedance bandwidth.

In Chapter 5, gain enhancement technique has been applied to array of leaf-shaped bowtie slot antenna. Gain enhancement technique consists of one layer and two layers of dielectric superstrate are arranged on top of ground plane of slot antennas array. From analysis results in Chapter 5, dielectric superstrate layers effect not only actual gain in broadside but also −10dB impedance bandwidth of the antenna structure. Constructive and destructive effect are depending on the slot antenna structure and its feeding circuit. First case is antenna structure that has feeding circuit as microstrip line and conducting probe. After two layers of dielectric superstrate are arranged on top of ground plane, the actual gain has increased up to 20.5dBi which is a very high actual gain. In addition, −10dB impedance bandwidth has also increased from 0.49GHz to 1.22GHz. Therefore, two dielectric superstrate layers have constructive effect on both actual gain and −10dB impedance bandwidth. Second case is antenna structure that has feeding circuit as quarter wavelength matching circuit. Actual gain has increased up to 19dBi and −10dB impedance bandwidth has decreased from 1.68GHz to 1.45GHz after two layers of dielectric superstrate are arranged on top of antenna ground plane. Therefore, two dielectric superstrate layers has constructive effect on actual gain and destructive effect on −10dB impedance bandwidth. Comparison between the first and second case, the first case has higher actual gain and narrower −10dB impedance bandwidth than the second case. In another case, the antenna structure, whose feeding circuit consists of quarter wavelength matching circuit and tapered line, offers high gain and wide impedance bandwidth that satisfies targeted frequency band of 27GHz to 29GHz. From Chapter 5, high gain and wide band antenna structure have been designed. Using dielectric superstrate layer to increase gain in broadside direction is a very effective, low cost and low-profile technique because the slot antennas array that is used as radiating element is low cost and low profile and it can be fabricated by using conventional method such as etching and engraving.

In Chapter 6, antenna prototypes have been fabricated. The fabrication model is based on the analytical model in Chapter 3 and Chapter 5. In addition, antenna characteristics are measured and compared with simulated results to validate the analytical model. First case of antenna prototype is reflector backed leaf-shaped bowtie slot antenna electromagnetically fed by quarter wavelength matching circuit. There is some small discrepancy between the

simulated results and measures results of reflection coefficient magnitude. The discrepancy is assumed coming from the machining accuracy of antenna prototype (the position of microstrip line is misaligned, and the slot element dimensions F_a and F_b at the intersection with the line are in error., etc.), and the influence of the reflection by SMA connector. Although there is small discrepancy between measured and simulated results, the comparison can be concluded that both results are in a good agreement. These results prove that the proposed method is effective and useful to be investigated and that quarter wavelength matching circuit does increase the impedance bandwidth of antenna structure. The proposed antenna is designed to have a standard 50Ω connector. Therefore, the proposed antenna is applicable in real application. Second case of antenna prototype is leaf-shaped bowtie slot antenna array with two layers of dielectric superstrate. Comparing to simulated results, actual gain has decreased around 1.5dB at 28GHz. In addition, the −10dB impedance bandwidth has been slightly shifting to higher frequency. The decrease in actual gain could be caused by effect of conductor loss, or reflection from K-type connector. In addition, the soldering at conductor post may also effect on radiation characteristics. The shifting of reflection coefficient may result from fabrication error of radiating slot or microstrip line. Although there is small discrepancy between simulated and measured results, both simulated and measured results are in a good agreement.

From both simulated and measured results, the analysis models from FDTD method are validated. The proposed antenna structure in this research offers high gain, wide bandwidth, low profile, and low cost of fabrication. The proposed antenna structure is effective and useful. The proposed antenna is applicable in 28GHz band in Japan (27GHz to 29GHz). The proposed antenna structure will contribute to the future 5G communication.

7.2 Future Work

In this research linear of 4 leaf-shaped bowtie slot antennas has been proposed. In addition, the combination between linear array and 4×4 butler matrix has also proposed. From that, a beam scanning structure has been created. From the analysis results, the antenna beam is stable within 27.3GHz to 27.7GHz, which is in small bandwidth. Therefore, in order to utilize the capability of leaf-shaped bowtie slot antenna which are high gain, wide gain bandwidth and wide impedance bandwidth, a large-scale array of leaf-shaped bowtie slot antenna further study with 28GHz band for future work. As the results of this research, the −10dB impedance bandwidth of the antenna structure doesn't occupy the whole band which is 27GHz to 29GHz. Therefore, extra impedance matching circuit and feeding circuit should be studied in the future to make −10dB impedance bandwidth wider that can occupy the whole frequency band 27GHz to 29GHz. However, the −3dB gain bandwidth must be stable with 27GHz to 29GHz band. Moreover, the application of leaf-shaped bowtie slot antenna in beam scanning should be further studied to have beam that is stable within a wider band.

REFERENCES

[1] Bernhard Raaf, Wolfgang Zirwas, Karl-Josef Friederichs, Esa Tiirola, Matti Laitila, Patrick Marsch and Risto Wichman. *Vision for beyond 4G broadband radio systems*. in *2011 IEEE 22nd International Symposium on Personal, Indoor and Mobile Radio Communications*. 2011. IEEE.

[2] TS Rappaport. *Special session on mmWave communications*. in *Proc. ICC*. 2013.

[3] A. Ghosh, T. A. Thomas, M. C. Cudak, R. Ratasuk, P. Moorut, F. W. Vook, T. S. Rappaport, G. R. MacCartney, S. Sun and S. Nie, *Millimeter-Wave Enhanced Local Area Systems: A High-Data-Rate Approach for Future Wireless Networks.* IEEE Journal on Selected Areas in Communications, 2014. **32**(6): p. 1152-1163.

[4] Satoshi Suyama Yoshihisa Kishiyama. *History of 5G Initiatives*. Available from: https://www.ntt-review.jp/archive/ntttechnical.php?contents=ntr202012fa11_s.html#Author01.

[5] Juho Lee, Erika Tejedor, Karri Ranta-aho, Hu Wang, Kyung-Tak Lee, Eliane Semaan, Eiman Mohyeldin, Juyeon Song, Christian Bergljung and Sangyeob Jung, *Spectrum for 5G: Global status, challenges, and enabling technologies.* IEEE Communications Magazine, 2018. **56**(3): p. 12-18.

[6] Shinsuke Sawamukai Yuta Sagae, Yusuke Ohwatari,Kohei Kiyoshima, Keiichi Kanbara, and Jo Takahashi. *5G Network*. Available from: https://www.ntt-review.jp/archive/ntttechnical.php?contents=ntr202012fa13.html.

[7] Ramadan A Alhalabi and Gabriel M Rebeiz, *Differentially-fed millimeter-wave Yagi-Uda antennas with folded dipole feed.* IEEE Transactions on Antennas and Propagation, 2009. **58**(3): p. 966-969.

[8] Guohua Zhai, Yong Cheng, Qiuyan Yin, Shouzheng Zhu and Jianjun Gao, *Gain enhancement of printed log-periodic dipole array antenna using director cell.* IEEE Transactions on Antennas and Propagation, 2014. **62**(11): p. 5915-5919.

[9] Jang-Soon Park, Jun-Bong Ko, Heon-Kook Kwon, Byung-Su Kang, Bonghyuk Park and Dongho Kim, *A tilted combined beam antenna for 5G communications using a 28-GHz band.* IEEE Antennas and Wireless Propagation Letters, 2016. **15**: p. 1685-1688.

[10] Osama M Haraz, Ayman Elboushi, Saleh A Alshebeili and Abdel-Razik Sebak, *Dense dielectric patch array antenna with improved radiation characteristics using EBG ground structure and dielectric superstrate for future 5G cellular networks.* IEEE access, 2014. **2**: p. 909-913.

[11] Yujian Li and Kwai-Man Luk, *Wideband perforated dense dielectric patch antenna array for millimeter-wave applications.* IEEE Transactions on Antennas and Propagation, 2015. **63**(8): p. 3780-3786.

[12] Junfeng Xu, Wei Hong, Hongjun Tang, Zhenqi Kuai and Ke Wu, *Half-mode substrate integrated waveguide (HMSIW) leaky-wave antenna for millimeter-wave applications.* IEEE Antennas and Wireless Propagation Letters, 2008. **7**: p. 85-88.

[13] Mohsen Khalily, Rahim Tafazolli, TA Rahman and MR Kamarudin, *Design of phased arrays of series-fed patch antennas with reduced number of the controllers for 28-GHz mm-wave applications.* IEEE Antennas and Wireless Propagation Letters, 2015. **15**: p. 1305-1308.

[14] Mohsen Khalily, Rahim Tafazolli, Pei Xiao and Ahmed A Kishk, *Broadband mm-wave microstrip array antenna with improved radiation characteristics for different 5G applications.* IEEE Transactions on Antennas and Propagation, 2018. **66**(9): p. 4641-4647.

[15] Chun-Xu Mao, Mohsen Khalily, Pei Xiao, Tim WC Brown and Steven Gao, *Planar sub-millimeter-wave array antenna with enhanced gain and reduced sidelobes for 5G broadcast applications.* IEEE Transactions on Antennas and Propagation, 2018. **67**(1): p. 160-168.

[16] Hanieh Aliakbari, Abdolali Abdipour, Rashid Mirzavand, Alessandra Costanzo and Pedram Mousavi. *A single feed dual-band circularly polarized millimeter-wave antenna for 5G communication*. in *2016 10th European conference on antennas and propagation (EuCAP)*. 2016. IEEE.

[17] Mehrdad Nosrati and Negar Tavassolian. *A single feed dual-band, linearly/circularly polarized cross-slot millimeter-wave antenna for future 5G networks*. in *2017 IEEE International Symposium on Antennas and Propagation & USNC/URSI National Radio Science Meeting*. 2017. IEEE.

[18] Seong-Jin Park and Seong-Ook Park, *LHCP and RHCP substrate integrated waveguide antenna arrays for millimeter-wave applications.* IEEE Antennas and Wireless Propagation Letters, 2016. **16**: p. 601-604.

[19] Hussam Al-Saedi, Wael M Abdel-Wahab, Suren Gigoyan, Raj Mittra and Safieddin Safavi-Naeini, *Ka-band antenna with high circular polarization purity and wide AR beamwidth.* IEEE Antennas and Wireless Propagation Letters, 2018. **17**(9): p. 1697-1701.

[20] Abdolmehdi Dadgarpour, Milad Sharifi Sorkherizi and Ahmed A Kishk, *Wideband low-loss magnetoelectric dipole antenna for 5G wireless network with gain enhancement using meta lens and gap waveguide technology feeding.* IEEE Transactions on Antennas and Propagation, 2016. **64**(12): p. 5094-5101.

[21] Milad Sharifi Sorkherizi, Abdolmehdi Dadgarpour and Ahmed A Kishk, *Planar high-efficiency antenna array using new printed ridge gap waveguide technology.* IEEE Transactions on Antennas and Propagation, 2017. **65**(7): p. 3772-3776.

[22] Philip Ayiku Dzagbletey, Kwang-Seon Kim, Woo-Jin Byun and Young-Bae Jung, *Stacked microstrip linear array with highly suppressed side-lobe levels and wide bandwidth.* IET Microwaves, Antennas & Propagation, 2017. **11**(1): p. 17-22.

[23] Samuel Afoakwa and Young-Bae Jung, *Wideband microstrip comb-line linear array antenna using stubbed-element technique for high sidelobe suppression.* IEEE Transactions on Antennas and Propagation, 2017. **65**(10): p. 5190-5199.

[24] Binqi Yang, Zhiqiang Yu, Yunyang Dong, Jianyi Zhou and Wei Hong, *Compact tapered slot antenna array for 5G millimeter-wave massive MIMO systems.* IEEE Transactions on Antennas and Propagation, 2017. **65**(12): p. 6721-6727.

[25] Shuangshuang Zhu, Haiwen Liu, Zhijiao Chen and Pin Wen, *A compact gain-enhanced Vivaldi antenna array with suppressed mutual coupling for 5G mmWave application.* IEEE Antennas and Wireless Propagation Letters, 2018. **17**(5): p. 776-779.

[26] Tarek Djerafi and Ke Wu, *Corrugated substrate integrated waveguide (SIW) antipodal linearly tapered slot antenna array fed by quasi-triangular power divider.* Progress In Electromagnetics Research C, 2012. **26**: p. 139-151.

[27] Anthony Ghiotto, Frédéric Parment, Tan-Phu Vuong and Ke Wu, *Millimeter-wave air-filled SIW antipodal linearly tapered slot antenna.* IEEE Antennas and Wireless Propagation Letters, 2016. **16**: p. 768-771.
[28] Atef Z Elsherbeni and Veysel Demir, *The finite-difference time-domain method for electromagnetics with MATLAB® simulations*. Vol. 2. 2015: IET.
[29] Sim4Life. Available from: https://zmt.swiss/sim4life/.
[30] Jean-Pierre Berenger, *A perfectly matched layer for the absorption of electromagnetic waves.* Journal of computational physics, 1994. **114**(2): p. 185-200.
[31] Jean-Pierre Berenger, *Three-dimensional perfectly matched layer for the absorption of electromagnetic waves.* Journal of computational physics, 1996. **127**(2): p. 363-379.
[32] Yasuto Mushiake, *Self-complementary antennas.* IEEE Antennas and Propagation Magazine, 1992. **34**(6): p. 23-29.
[33] M Ameya. *An omnidirectional UWB printed dipole antenna with small waveform distortion*. in *Proc. of Progress In Electromagnetics Research Symposium 2006, Aug.* 2006.
[34] Michitaka Ameya, Manabu Yamamoto, Toshio Nojima and Kiyohiko Itoh, *Leaf-shaped element bowtie antenna with flat reflector for UWB applications.* IEICE transactions on communications, 2007. **90**(9): p. 2230-2238.
[35] Tomoyuki KOYANAGI, Manabu Yamamoto and Toshio Nojima, *A Study of a Leaf-Shaped Bowtie Antenna Backed by an Electromagnetic Band Gap Structure.* IEICE Proceedings Series, 2010. **52**(4FA3-2).
[36] Michitaka Ameya, Yoshinori Ito, Manabu Yamamoto and Toshio Nojima. *2-element UWB array antenna using leaf-shaped bowtie element*. in *2007 IEEE Antennas and Propagation Society International Symposium*. 2007. IEEE.
[37] Yoshinori Ito, Michitaka Ameya, Manabu Yamamoto and Toshio Nojima. *A study of unidirectional UWB array antenna using leaf-shaped bowtie elements and a flat reflector*. in *Proceedings of ISAP2007*. 2007.
[38] Soh Fujita, Manabu Yamamoto and Toshio Nojima. *A study of a leaf-shaped bowtie slot antenna for UWB applications*. in *2012 International Symposium on Antennas and Propagation (ISAP)*. 2012. IEEE.
[39] Manabu Yamamoto and Toshio Nojima. *Design of a leaf-shaped bowtie slot antenna electromagnetically fed by a microstrip line*. in *2014 International Symposium on Antennas and Propagation Conference Proceedings*. 2014. IEEE.
[40] Manabu Yamamoto, Soh Fujita, Jun Kimura and Toshio Nojima. *Design of a leaf-shaped bowtie slot antenna array for wide band applications*. in *2013 IEEE-APS Topical Conference on Antennas and Propagation in Wireless Communications (APWC)*. 2013. IEEE.
[41] 伊藤禎宣, 飴谷充隆, 山本学 and 野島俊雄, *UWB 用反射板付き葉状ボウタイアンテナの二次元アレー化に関する検討.* 電子情報通信学会論文誌 B, 2008. **91**(9): p. 1029-1036.
[42] 山本学, 棟形丈仁 and 野島俊雄, *直並列給電回路と葉状ボウタイ素子を用いた広帯域アレーアンテナ.* 電子情報通信学会論文誌 C, 2015. **98**(12): p. 447-450.
[43] 前田将平, 山本学 and 野島俊雄, *葉状ボウタイ素子を用いた 4 ポート広帯域 MIMO アンテナ.* 電子情報通信学会論文誌 B, 2015. **98**(9): p. 886-895.

[44] 山本学, *プリントアンテナの基礎と実際.* 電子情報通信学会論文誌 B, 2014. **97**(9): p. 714-730.
[45] 山本学, 藤田壮 and 野島俊雄, *UWB 無線用葉状ボウタイスロットアンテナ.* 電子情報通信学会論文誌 B, 2012. **95**(9): p. 1181-1184.
[46] 伊藤敦, 永利美緒, 田中信吾 and 森下久, *小型端末搭載を考慮した給電線付広帯域折返しダイポールアンテナの特性.* 電子情報通信学会技術研究報告. A・P, アンテナ・伝播, 2012. **112**(149): p. 75-80.
[47] 鳴原達郎, 野村早希 and 山本学. *誘電体基板上に配置された広帯域ループアンテナに関する基礎検討*. in *IEICE Conferences Archives*. 2019. The Institute of Electronics, Information and Communication Engineers.
[48] Yoshikazu Yoshimura, *A microstripline slot antenna (short papers).* IEEE Transactions on Microwave Theory and Techniques, 1972. **20**(11): p. 760-762.
[49] David M Pozar, *Microwave engineering*. 2011: John wiley & sons.
[50] Muftah Asaadi and Abdelrazik Sebak, *High-gain low-profile circularly polarized slotted SIW cavity antenna for MMW applications.* IEEE Antennas and Wireless Propagation Letters, 2016. **16**: p. 752-755.
[51] Manabu Yamamoto, Daisuke Tokuyama and Toshio Nojima. *Design of quasi-millimeter wave leaf-shaped bowtie array antenna for UWB applications*. in *2010 IEEE Antennas and Propagation Society International Symposium*. 2010. IEEE.
[52] Manabu Yamamoto, Tomoyuki Koyanagi, Soh Fujita and Toshio Nojima. *Quasi-millimeter wave leaf-shaped bowtie array antenna backed by an EBG substrate*. in *Proceedings of the 2012 IEEE International Symposium on Antennas and Propagation*. 2012. IEEE.
[53] Takehito Munekata, Manabu Yamamoto and Toshio Nojima. *A wideband 16-element antenna array using leaf-shaped bowtie antenna and series-parallel feed networks*. in *2014 IEEE International Workshop on Electromagnetics (iWEM)*. 2014. IEEE.
[54] G Von Trentini, *Partially reflecting sheet arrays.* IRE Transactions on antennas and propagation, 1956. **4**(4): p. 666-671.
[55] Az P Feresidis and JC Vardaxoglou, *High gain planar antenna using optimised partially reflective surfaces.* IEE Proceedings-Microwaves, Antennas and Propagation, 2001. **148**(6): p. 345-350.
[56] M. A. Al-Tarifi, D. E. Anagnostou, A. K. Amert and K. W. Whites, *Bandwidth Enhancement of the Resonant Cavity Antenna by Using Two Dielectric Superstrates.* IEEE Transactions on Antennas and Propagation, 2013. **61**(4): p. 1898-1908.
[57] Muftah Asaadi and Abdelrazik Sebak, *Gain and bandwidth enhancement of 2× 2 square dense dielectric patch antenna array using a holey superstrate.* IEEE Antennas and Wireless Propagation Letters, 2017. **16**: p. 1808-1811.
[58] Takuma Makanae and Manabu Yamamoto. *A Study on Gain Enhancement of a Leaf-Shaped Bowtie Slot Antenna Array Employing Dielectric Superstrates*. in *2019 International Symposium on Antennas and Propagation (ISAP)*. 2019. IEEE.
[59] C. Dall'Omo, T. Monediere, B. Jecko, F. Lamour, I. Wolk and M. Elkael, *Design and realization of a 4 × 4 microstrip Butler matrix without any crossing in millimeter waves.* Microwave and Optical Technology Letters, 2003. **38**(6): p. 462-465.

Appendix

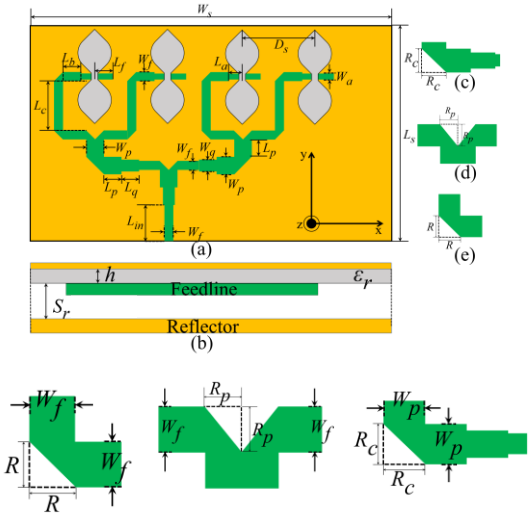

The −10dB impedance bandwidth of antenna structure in Figure4. 26 is highly depending on the cutting ratio at right angle bend and T-junction.

A. Right Angle Bend

In this structure, there are two categories of right-angle bend. First category, whose cutting ration is represented by η_R, is right-angle bend along microstrip line form radiating slot. Second category, whose cutting ration is represented by η_{Rc}, is right angle bend at T-junction. η_R and η_{Rc} are calculate as in following formula:

$$\eta_R = \frac{R}{W_f} \quad and \quad \eta_{Rc} = \frac{R_c}{W_p}$$

B. T-Junction

In addition, the cutting ratio at T-junction also effects on the impedance bandwidth of antenna structure. The cutting ratio at T-junction is represented by η_T which is calculated as following:

$$\eta_T = \frac{R_p}{W_f}$$

In this research, cutting ratio η_R and η_T are optimized with the value of:

$$\eta_R = \frac{R}{W_f} = \frac{0.7}{1.1} = 0.6363$$

$$\eta_T = \frac{R_p}{W_f} = \frac{1.2}{1.1} = 1.0909$$

List of Publications

Full Papers (Peer Review)

[1] Mangseang HOR, Takashi HIKAGE and Manabu YAMAMOTO, “A Study on Gain Enhanced Leaf-Shaped Bow-Tie Slot Array Antenna within Quasi-Millimeter Wave Band”, IEICE Transactions on Communications. (Accepted for publication in vol.E-105B, no.3, March 2022.)

[2] ホー メィンシェン，山本 尚也，日景 隆，山本 学，内田 大誠，白戸 裕史，北直樹，“1/4 波長整合回路を用いた反射板付葉状ボウタイスロットアンテナ”，電子情報通信学会論文誌 B.（2022 年 J-105B 巻 3 月号掲載決定）

Proceedings of International Conference (Peer Review)

[1] Mangseang Hor, Takashi Hikage and Manabu Yamamoto, “Leaf-Shaped Bowtie Slot Antenna Array for Application in Beam Scanning,” Proceedings of 2020 International Symposium on Antennas and Propagation (ISAP2020), 4B3-5, pp.777-778, Jan. 2021.

[2] Mangseang Hor, Takashi Hikage, Manabu Yamamoto, “Linear Array of Leaf-Shaped Bowtie Slot Antenna Electromagnetically Fed by Microstrip Line”, Proceedings of The 26th International Symposium on Antennas and Propagation (ISAP2021), no.220053, Oct. 2021.

Lectures (No Peer Review)

[1] Mangseang Hor, Takashi Hikage, and Manabu Yamamoto, “A Study on Increasing of Gain of Leaf-Shaped Bow-Tie Array Antenna within Quasi-Millimeter Wave Band”, 令和元年度電気・情報関係学会北海道支部連合大会，no.57，2019 年 11 月.

[2] Mangseang Hor, Takuma Makanae, Takashi Hikage, and Manabu Yamamoto, “A Study on Gain Enhancement of Leaf-Shaped Bow-Tie Slot Array Antenna within Quasi-Millimeter Wave Band”, 2020 年電子情報通信学会総合大会, B-1-70, 2020 年 3 月.

[3] Mangseang Hor, Takashi Hikage, Manabu Yamamoto, “A Study on Application of Leaf-Shaped Bow-Tie Antenna for Beamforming Array Antenna within Millimeter Wave Frequency”, 令和 2 年度 電気・情報関係学会北海道支部連合大会, no.93, 2020 年 11 月.

[4] Mangseang Hor, Takashi Hikage, Manabu Yamamoto, “Study of Gain Enhancement of Leaf-Shaped Bowtie Slot Antenna Array Electromagnetically Fed by Microstrip Line”, 令和 3 年度 電気・情報関係学会北海道支部連合大会, no.54, 2020 年 11 月.